UNIVERSIDADE DE LISBOA

FACULDADE DE CIÊNCIAS

Studies of Polymorphs and Solvates of Molecular Organic Solids

Doutoramento em Química
Especialidade em Química-Física

Abhinav Joseph

Tese orientada por:
Prof. Dr. Manuel E. Minas da Piedade

Documento especialmente elaborado para a obtenção do grau de doutor

2016

UNIVERSIDADE DE LISBOA

FACULDADE DE CIÊNCIAS

Studies of Polymorphs and Solvates of Molecular Organic Solids

Doutoramento em Química
Especialidade em Química-Física

Abhinav Joseph

Tese orientada por:
Prof. Dr. Manuel E. Minas da Piedade

Júri:
Presidente:
- Prof. Dr. Ana Maria Jara Ponces da Costa Freire

Vogais:
- Prof. Dr. Maria Ermelinda da Silva Eusébio
- Prof. Dr. Ricardo António Esteves de Castro
- Prof. Dr. Luís Manuel das Neves Belchior Faia dos Santos
- Prof. Dr. José Artur de Sousa Martinho Simões
- Prof. Dr. Manuel Eduardo Ribeiro Minas da Piedade
- Dr. Carlos Eduardo Sabino Bernardes

Documento especialmente elaborado para a obtenção do grau de doutor

Fundação para a Ciência e a Tecnologia (SFRH/BD/90386/2012)

2016

The research work presented in this thesis was essentially carried out at the Molecular Energetics Group (CQB-FCUL) and was financially supported by Foundation for Science and Technology (FCT), Portugal through doctoral fellowship (SFRH/BD/90386/2012).

To my Parents

Mr. and Mrs. Anil and Lalita Joseph

and

To my sister

Sakshi.

Acknowledgements

First and foremost, I would like to thank my supervisor, Prof. Dr. Manuel Eduardo Minas da Piedade, for the opportunity to work in his group. I express my sincere gratitude to him for his excellent guidance and motivation during the entire course of Ph.D. His expertise and incisive insight had both been inspiring and critical in the completion of this work. I also thank him deeply for all the support during these years of my stay in Lisbon.

I would like to thank, the members of the Molecular Energetics Group at CQB-FCUL, namely Prof. Dr. José Artur Martinho Simões, Prof. Dr. João Paulo Leal, Prof. Dr. Rui Borges, Dr. Rui Centeno, Dr. Elsa Gonçalves, Dr. Filipe Agapito, Dr. Ricardo Simões, Dr. Joana Vitorino, Valdir Semedo, Rafael Bento, Cátia Lopes, Mariana Donato and Miguel Rendas for being such wonderful colleagues. A special thanks to Dr. Carlos Bernardes, for his support in computational experiments and several helpful discussions throughout this work.

Most of the results described in this thesis would not have been obtained without contribution from other people. I take this opportunity to say heartfelt thanks to Prof. Dr. Hermínio Diogo from IST-UL for granting me access to his laboratory and helping me in HSM experiments; Prof. Dr. Fátima Piedade from DQB-UL and Dr. Franziska Emmerling from Federal Institute for Materials Research and Testing (BAM), Germany for SC-XRD and crystal structure analysis, Prof. Dr. Maria da Conceição Oliveira from IST-UL for LC-MS analysis, Dr. Ana Viana from CQB-FCUL for performing AFM experiments, Prof. Dr. Matthias Epple and his group at the University of Duisburg-Essen, Germany for SEM experiments, late Prof. Dr. Raisa Varushchenko and Dr. Anna Druzhinina from Moscow State University, Russia for adiabatic calorimetry experiments and Prof. Dr. Gérard Coquerel from Université de Rouen, France for his advice and for helpful discussions. I also take this opportunity to sincerely acknowledge the Foundation for Science and Technology (FCT), Portugal, for providing financial assistance in the form of doctoral fellowship (SFRH/BD/90386/2012).

Thanks to my landlady Mrs. Aurora Maria, for providing me a comfortable accommodation.

My deepest gratitude to Pastor Emmanuel Amissah, Mrs. Teresa Amissah, Mr Wesley Mathew and Mrs. Anila Wesley for their hospitality, counselling and support.

My time in Lisbon was enjoyable at large due to the friends that became part of my life. I came across people from different nationalities and cultures and shared some delightful moments with them. I would like to extend my kind regards to Dr. Emily Lange, Dr. Filmon Grehabmikhan, Talita Silva Rego, Smiljan Slukan, Pedro Favale, Rachel Mainland, Arjan Van der Laan, Ato Mensah, Rahul Ramchandran, Nana Kankam and Felix Diawuo.

I extend my gratitude to IAESTE India KU and Prof. Dr. Vasanth Kumar, Head Dept. of Chemistry, Karunya University for providing me a valuable opportunity to undertake internship at CQB-FCUL. I would also like to thank my teachers and colleagues from the Department of Chemistry, Karunya University for their love and encouragements.

I would like to extend my sincere thanks to Mr Subhash Chand, Mrs. Baby Chand, Sneha and Himanshu for all the support and confidence you placed in me.

Last but not least a special thanks to my family. Words cannot express how grateful I am to you for all the sacrifices you have made for me. You were always there for me and it was your love that sustained me thus far

Thank you all !

ABHINAV

Resumo

O trabalho apresentado nesta tese foi realizado no Grupo de Energética Molecular do Centro de Química e Bioquímica (CQB), Faculdade de Ciências da Universidade de Lisboa (FCUL).

Compreender a relação entre a energética de moléculas ou grupos de moléculas e sua estrutura e reactividade tem sido um objetivo central da investigação levada a cabo no Grupo de Energética Molecular. Nos últimos anos, esse interesse tem sido estendido ao estudo do polimorfismo e à formação/decomposição de solvatos em sólidos moleculares orgânicos, com ênfase em substâncias com interesse farmacêutico e sistemas modelo que possam ser usados para entender os dois fenómenos.

Hoje em dia, a maior parte dos compostos orgânicos com importância comercial, são produzidos na forma de sólidos cristalinos. A maioria deles tem capacidade de adotar mais do que uma estrutura cristalina, um fenómeno conhecido como polimorfismo. Diferentes polimorfos podem apresentar diferenças significativas nas propriedades físicas, pelo que cada polimorfo é, de facto, um material diferente. O polimorfismo proporciona, assim, por uma lado, uma oportunidade única para selecionar formas sólidas com características ideais para uma determinada aplicação sem alterar a molécula envolvida. Mas, por outro lado, a falta de controlo do polimorfismo pode complicar seriamente o fabrico de um produto com propriedades reprodutíveis. O controlo do polimorfismo é, assim, um objetivo muito importante em indústrias como a farmacêutica, onde a segurança e eficácia de um princípio ativo farmacêutico sólido depende significativamente da produção de materiais com propriedades constantes. De um ponto de vida mais académico o polimorfismo permite, também, investigar, por exemplo, o modo como diferentes interações intermoleculares determinam uma dada estrutura cristalina.

Uma estratégia alternativa para modificar as características de um produto, sem alterar a sua molécula essencial é a produção de solvatos. Com efeito, a inclusão de moléculas de solvente na rede cristalina pode alterar significativamente o empacotamento molecular relativamente a uma forma não solvatada. Os hidratos são os solvatos encontrados com mais

frequência durante o isolamento e processamento de sólidos orgânicos moleculares. A avaliação de sua tendência para formação/decomposição é, assim, de particular interesse quando se pretende um controlo apertado sobre a produção e processamento de produtos orgânicos cristalinos.

Duas grandes questões são geralmente relevantes quando se lida com polimorfos ou solvatos: (1) Quais são os seus domínios de estabilidade? (2) Quanto tempo pode uma forma metaestável permanecer inalterada quando sujeita a determinadas condições ambientais? A termodinâmica fornece o enquadramento adequado para discutir a primeira pergunta. A segunda questão cai no domínio da cinética de transições de fase e formação/decomposição de solvatos. Um aspeto importante relacionado com ambas as perguntas é a compreensão dos mecanismos das transições entre polimorfos e dos processos de formação/decomposição de solvatos.

Nesta tese foram realizados estudos estruturais, termodinâmicos e cinéticos relacionados com polimorfismo e formação/decomposição de solvatos para uma série de sólidos orgânicos moleculares. O trabalho foi centrado (1) no ácido nicotínico e alguns dos seus derivados hidroxilados (ácidos 4- e 5-hidroxinicotínico); (2) na simvastatina; e (3) na 4-hidroxiacetofenona. Estas moléculas fazem parte do portfólio de compostos investigados no Grupo de Energética Molecular. Foram selecionadas devido à sua relevância do ponto de vista farmacêutico, ou à sua importância como sistemas modelo para entender as relações estrutura-energética no âmbito do polimorfismo e da ocorrência de solvatos.

O ácido nicotínico (NA), também designado por vitamina B3 ou niacina, tem bastante importância biológica e diversas aplicações, tais como o tratamento de hiperlipidemia. Vários aspetos termodinâmicos do ácido nicotínico tinham sido previamente abordados no Grupo de Energética Molecular (e.g., entalpia de formação, solubilidade, pK_a). Conhecia-se também a existência de duas formas polimórficas relacionados por uma transição de fase sólido-sólido a 455 K, embora apenas a estrutura molecular e cristalina do polimorfo de baixa temperatura (forma II) fosse conhecida. A transição entre as formas II e I não tinha sido convenientemente caracterizada, nomeadamente a avaliação da sua reversibilidade. Este aspeto é particularmente importante, uma vez que determina se os dois polimorfos podem coexistir à pressão e

temperatura ambiente, exigindo assim um controlo rigoroso polimorfismo se o ácido nicotínico for usado como princípio ativo farmacêutico. A termodinâmica do ácido nicotínico numa gama de temperatura compreendendo a transição de fase foi, por conseguinte, investigada no presente trabalho, através de medições de capacidade calorífica. Este estudo (Capítulo 3) permitiu determinar os domínios de estabilidade dos dois polimorfos, e exprimi-los na forma de um diagrama energia de Gibbs vs temperatura. Demostrou, ainda, que a transição forma II → forma I pode ser revertida, indicando, assim, que apenas a forma II irá prevalecer à temperatura e pressão ambientes. As mudanças estruturais que acompanham a transição de fase não puderam, no entanto, ser avaliadas uma vez que, conforme acima mencionado, a estrutura cristalina da fase de alta temperatura (estável acima de 455 K) não é conhecida.

No caso da simvastatina, que é um medicamento amplamente prescrito para controlar a hiperlipidemia, tinham sido observadas duas transições de fase reversíveis numa gama de temperatura sub-ambiente (III → II e II → I) e investigados alguns aspetos estruturais e energéticos do seu comportamento nos estados sólido, líquido e gás. Esses estudos sugeriram que as transições III → II e II → I estavam essencialmente relacionadas com alterações de liberdade conformacional da "cauda éster" da simvastatina. A investigação termodinâmica destas transições de fase, com base em medições de capacidade calorífica, está descrita no capítulo 4. Os resultados mostraram que as entalpias dos processos III → II e II → I são pequenas, em bom acordo com a conclusão acima mencionada de que as transformações ocorrem sem mudanças significativas de empacotamento cristalino.

A 4'-hidroxiacetofenona tem sido largamente estudada no Grupo de Energética Molecular, pois tem provado ser um sistema muito rico em termos da diversidade de formas sólidas (pelo menos dois polimorfos e três hidratos identificados), mecanismo de cristalização, etc.. Um dos objetivos desta tese foi determinar a temperatura de equilíbrio da transição de fase forma II → forma I utilizando estudos de solubilidade. Verificou-se que o valor obtido (T_{trs} = 300,1 K) é inferior em cerca de 60 K à temperatura (357 K) a que a transição é normalmente observada por calorimetria diferencial de varrimento (DSC) usando uma velocidade de aquecimento de baixa (e.g. 1 $K \cdot min^{-1}$). Esta determinação permitiu também redesenhar o diagrama de fases energia de Gibbs vs temperatura ilustrando os domínios de estabilidade dos dois polimorfos anidros da 4'-hidroxiacetofenona. Os estudos de solubilidade

mostraram, ainda, que a interconversão dos dois polimorfos é possível sob controlo termodinâmico, indicando assim que a hipótese avançada por G. R. Desiraju, segundo a qual, polimorfos com Z' > 1 (forma II da HAP) são necessariamente menos estáveis do que polimorfos com Z' = 1 (forma I da HAP), não pode ser universalmente verdadeira. As diferenças moleculares entre as duas formas foram, também, analisadas por cálculos ab-initio e superfícies de Hirshfeld. Verificou-se que as duas conformações moleculares presentes na forma II são menos estáveis do que a existente na forma I, mas favorecem a formação de ligações de hidrogénio mais fortes no estado sólido. Isto pode explicar o facto de a energia de rede da forma II ser ligeiramente mais elevada do que a da forma I.

A presente Tese incluiu ainda estudos de três solvatos de ácidos hidroxinicotínicos: um hemi-hidrato do ácido 4-hidroxinicotínico (4HNA·0,5H_2O) anteriormente obtido no nosso laboratório e dois novos solvatos do ácido 5-hidroxinicotínico (5HNA·H_2O e 5HNA·DMSO). Num trabalho anterior tinha sido verificado que o hemi-hidrato do ácido 4-hidroxinicotínico era estável em condições normais de temperatura, pressão e humidade ambiente, apesar de um estudo termodinâmico prever que a desidratação devia ocorrer espontaneamente, a 298 K, mesmo para uma humidade relativa de 100%. Foi, por conseguinte, concluído que a robustez do 4HNA·0,5H_2O relativamente à desidratação devia ser de origem cinética. O estudo cinético da desidratação de 4HNA·0,5H_2O usando termogravimetria (TGA) é descrito no capítulo 6. Os resultados indicaram que o processo envolve, de facto, uma energia de ativação (E_a) significativa, que aumenta entre 85 kJ·mol^{-1} e 133 kJ·mol^{-1} quando o tamanho das partícula aumenta de 177 μm a > 707 μm. Os valores de E_a obtidos para diferentes tamanhos de partícula são comparáveis, ou superiores, à energia/entalpia necessária para cindir as quatro ligações de hidrogénio de tipo OH···O e NH···O (~20-30 kJ·mol^{-1} cada) formadas pelas moléculas de água na rede cristalina. Verificou-se ainda que a cinética de desidratação obedece ao modelo de Avrami-Erofeev A2, que corresponde a um mecanismo de nucleação e de crescimento. A conclusão de que o mecanismo envolve um processo de nucleação e de crescimento foi também sugerida por observações microscópicas e análise de empacotamento molecular. Finalmente, uma análise estatística das relações de Arrhenius obtidas para amostras com diferentes tamanhos de partículas evidenciou a existência de um efeito isocinético, sugerindo que o mecanismo de desidratação é independente do tamanho de partícula.

O mono-hidrato (5HNA·H_2O) e o solvato (5HNA·DMSO) do ácido 5-hidroxincotinico foram sintetizados pela primeira vez. A respetiva caracterização estrutural por difracção de raios-X de cristal único revelou que a molécula de 5HNA adopta uma conformação zwitteriónica no 5HNA·H_2O e uma conformação hidroxilica no 5HNA·DMSO. Estas conformações correspondem às formas tautoméricas mais prováveis nas soluções de água e DMSO a partir das quais os dois compostos são cristalizados. A termodinâmica dos processos de desidratação/dessolvatação foi também investigada. Verificou-se que, em condições isotérmicas, a 298 K, a entalpia de desidratação do 5HNA·H_2O ($\Delta_r H_m^\circ$ = 51,1 kJ·mol^{-1}) é, aproximadamente, duas vezes superior à entalpia de desidratação do 4HNA·0,5H_2O ($\Delta_r H_m^\circ$ = 22,0 kJ·mol^{-1}). Este resultado é coerente com as razões molares H_2O:xHNA existentes em cada um dos compostos. Concluiu-se, também, que o valor da entalpia de dessolvatação do 5HNA·DMSO a 298 K ($\Delta_r H_m^\circ$ = 83,7 kJ·mol-1) é consideravelmente maior que a entalpia de desidratação do 5HNA·H_2O ($\Delta_r H_m^\circ$ = 51,1 kJ·mol^{-1}), apesar de na rede cristalina o DMSO estar envolvido numa única ligação de hidrogénio enquanto a água está envolvida em três ligações de hidrogénio. A estrutura cristalina do 5HNA·H_2O é, para além disso, mais compacta que a do 5HNA·DMSO. Isto sugere que a diferença de entalpia de dessolvatação entre as duas formas deve estar sobretudo relacionada com diferenças nas interações de van der Waals. Outra conclusão interessante é o facto de as entalpias de rede de 5HNA·H_2O e 5HNA·DMSO serem aproximadamente aditivas, uma vez que são próximas, dentro da incerteza experimental, dos valores obtidos adicionando as entalpias de sublimação do 5HNA e do solvente respetivo. Finalmente análises de LC-MS mostraram que, embora o grau de pureza do material de partida utilizado para produzir os solvatos de 5HNA fosse de 93% (percentagem molar), a purezas dos produtos de dessolvatação correspondiam a 99,03% e 99,95%, respetivamente. Isto permitiu sugerir a formação/dessolvatação de 5HNA·H_2O ou 5HNA·DMSO como um método simples e expedito de obter 5HNA com elevada pureza.

Palavras-chave: Polimorfismo, solvatos, capacidade de calorífica, energia de Gibbs, ácido nicotínico, simvastatina, 4'-hidroxiacetofenona, ácido 4-hidroxinicotínico, ácido 5-hidroxinicotínico, tautomerismo.

Abstract

The work presented in thesis was carried out at the Molecular Energetics Group of Centro de Química e Bioquímica (CQB), Faculdade de Ciências da Universidade de Lisboa (FCUL).

Understanding the relationship between the energetics of molecules, or groups of molecules, and their structure and reactivity has been a central research goal of the Molecular Energetics Group. In recent years, this interest has been extended to polymorphism and solvate formation in organic molecular solids, with emphasis on substances of pharmaceutical interest or model systems which can be used to better understand both phenomena.

Most organic compounds of commercial importance today are marketed as crystalline solids. The majority of them have the ability to exist in more than one crystal structure, a phenomenon known as 'polymorphism'. Different polymorphs may exhibit significant differences in physical properties, so that each polymorph should be regarded as a different material. Thus, on one hand, polymorphism provides a unique opportunity to find and select a solid form with optimal characteristics for a given application without changing the molecule involved. But, on the other hand, uncontrolled polymorphism can seriously affect the manufacture of a product with highly reproducible properties. Achieving polymorph control is, therefore, of major importance for industries such as pharmaceuticals, where the safe use and efficacy of a solid dosage form strongly depends on the consistent production of materials with constant properties. From a more academic point of view polymorphism also offers an opportunity to investigate, for example, how the interplay of different intermolecular interactions determines a given crystal structure.

An alternative approach for changing the characteristics of a product without changing the molecule involved is the production of solvates. Indeed, the inclusion of solvent molecules in the crystal lattice can significantly change both the packing, and the physical properties of a solvate, relative to an unsolvated crystal form. Hydrates are the most commonly occurring solvates during the isolation and processing of organic molecular solids. Thus the evaluation of

their tendency to form and to desolvate is of particular interest if tight control over the production and processing of crystalline organic products is to be achieved.

Two major questions are generally relevant when polymorphs or solvates are identified: (1) What are their stability domains? (2) How long can a metastable form remain unaltered under a given set of ambient conditions? Thermodynamics provides the framework to discuss the first question whereas the second question lies in the realm of kinetics of phase transitions and solvate formation/desolvation. An important aspect related with both questions is to understand the mechanisms behind polymorphic phase transitions and solvation/desolvation processes.

In this thesis structural, thermodynamic and kinetic studies related to polymorphism or solvate formation/desolvation were carried out for a number of molecular organic solids. The work was centered on nicotinic acid and some of its hydroxyl derivatives (4- and 5-hydroxynicotinic acid), simvastatin and 4-hydroxyacetophenone. These compounds are part of the molecular portfolio investigated at the Molecular Energetics Group. They were selected due to their actual or potential pharmaceutical relevance, or to their importance as model systems to understand structure-energetics relationships within the scope of polymorphism and solvate occurrence.

Nicotinic acid (NA), also known as niacin or vitamin B3, has a considerable biological importance and diverse applications, such as the treatment of hyperlipidemia. Various thermodynamic aspects of nicotinic acid had been previously studied at the Molecular Energetics Group (e.g. enthalpy of formation, solubility, pK_a). The compound was also reported to exist in two polymorphic forms related by a solid-solid phase transition at 455 K. Only the molecular structure of the low temperature polymorph (form II) was known. The form II $\rightarrow$ form I process had not been accurately characterized. Particularly interesting was the evaluation of its reversibility, since this determines if both polymorphs can coexist under ambient pressure-temperature conditions, thus requiring strict polymorphism control if nicotinic acid is used as an active pharmaceutical principle (API). The thermodynamics of nicotinic acid in a temperature range comprising the phase transition was therefore investigated in the present thesis through heat capacity measurements. This study (chapter 3) led to the

determination of the Gibbs energy vs temperature phase diagram showing the relative stability domains of the two polymorphs. It also showed that the form II → form I transition is reversible and occurs with little hysteresis, thus indicating that only the form II polymorph will prevail at normal ambient temperature and pressure. The structural changes accompanying the phase transition could not, however, be elucidated since the crystal structure of the high temperature phase, which becomes stable above 455 K, is not known.

Two sub-ambient reversible phase transitions (III→II and II→I) had been reported for simvastatin, which is also a widely prescribed hyperlipidemia medicine. Some structural and energetic aspects of solid, liquid, and gaseous simvastatin had been previously studied at the Molecular Energetics Group. From those studies, it was concluded that the phase transitions were essentially related with changes in the conformational freedom of the simvastatin "ester tail". The thermodynamic investigation of these phase transitions, based on heat capacity measurements, is described in chapter 4. The results showed that the enthalpies of the form III→ form II and form II→ form I processes are small, thus supporting the above mentioned conclusion that the transformations occur without significant packing changes.

4-Hydroxyacetophenone (HAP) has been extensively studied at the Molecular Energetics Group, and has proved to be a very rich system in terms of solid form diversity (two polymorphs and three hydrates identified) and crystallization features. A major goal of this thesis was to determine the equilibrium temperature of the form II → form I phase transition, using solubility studies. It was found that the obtained value (T_{trs} = 300.1 K) is lower by ~60 K than the temperature of ~357 K at which the transition is normally observed by differential scanning calorimetry (DSC) using a low heating rate (e.g. 1 K·min^{-1}). This allowed a redetermination of the Gibbs energy vs temperature diagram highlighting the stability domains of the two HAP polymorphs. The solubility studies also demonstrated that the interconversion of the two polymorphs is possible under thermodynamic control, thus indicating that the hypothesis put forward by G. R. Desiraju that Z′ > 1 polymorphs (form II HAP) are necessarily less stable than their corresponding Z′ = 1 counterparts (form I HAP) cannot be universally true. The molecular differences between both forms were also examined by ab-initio calculations and Hirshfeld surface analysis. It was found that the two molecular conformations present in form II are less stable than the single molecular conformation existing in form I, but

favor the formation of stronger hydrogen bonds in the solid state. This may explain why the lattice energy of form II is slightly higher that of form I.

Three solvates were also explored in this thesis: a hemihydrate of 4-hydroxynicotinic acid (4HNA·0.5H_2O) previously obtained at the Molecular Energetics Group, and two new solvates of 5-hydroxynicotinic acid (5HNA·H_2O and 5HNA·DMSO). The 4-hydroxynicotinic acid hemihydrate had been found to be stable under ambient temperature, pressure and humidity conditions, although thermodynamic studies predicted that spontaneous dehydration should occur at 298 K, even for a relative humidity of 100%. It was, therefore, concluded that the observed robustness of 4HNA·0.5H_2O should be of kinetic origin. The kinetic study of the dehydration of 4HNA·0.5H_2O using thermogravimetry (TGA) is described in chapter 6. The results indicated that the resilience of 4HNA·0.5H_2O to water loss is indeed of kinetic origin, and involves a significant activation energy, E_a, which increased from 85 kJ·mol^{-1} to 133 kJ·mol^{-1} with the increase in particle size from 177 μm to > 707 μm. The obtained E_a values for different particle sizes are all comparable to, or larger, than the energy/enthalpy necessary to cleave the four ~20-30 kJ·mol^{-1} OH···O and NH···O H-bonds holding the water molecules in the crystal lattice. The dehydration kinetics conformed to the Avrami-Erofeev A2 model, corresponding to a nucleation and growth mechanism, a conclusion which was also supported by structural and microscopic observations. Finally, a statistical analysis of Arrhenius plots for samples with different particle sizes evidenced the existence of an isokinetic relationship between the activation parameters, which suggested that the dehydration mechanism is always the same regardless of the particle size.

The 5-hydroxyncotinic acid monohydrate (5HNA·H_2O) and DMSO solvate (5HNA·DMSO) were previously unknown. Their characterization by single crystal X-ray diffraction analysis revealed that the 5HNA molecule adopts a zwitterionic conformation in 5HNA·H_2O and a hydroxyl conformation in 5HNA·DMSO. These conformations correlate with the tautomeric forms that are expected to prevail in the water and DMSO solutions from which the solvates are crystallized. The thermodynamics of the dehydration/desolvation processes was also investigated. It was found that under isothermal conditions, at 298 K, the enthalpy of dehydration of 5HNA·H_2O ($\Delta_r H^\circ_m$ = 51.1 kJ·mol^{-1}) was approximately twice the

enthalpy of dehydration of 4HNA·0.5H_2O ($\Delta_r H_m^\circ$ = 22.0 kJ·mol^{-1}). This is in consistent with the fact that the H_2O:xHNA molar ratio in 4HNA·0.5H_2O is half that in 5HNA·H_2O. A considerably larger enthalpy of desolvation ($\Delta_r H_m^\circ$ = 83.7 kJ·mol^{-1}) was found for 5HNA·DMSO at 298 K, albeit, in this case, DMSO is only engaged in one hydrogen bond while three hydrogen bonds need to be cleaved to remove water from 5HNA·H_2O. The crystal lattice of 5HNA·H_2O is, also, closely packed compared to that of 5HNA·DMSO. It can therefore be concluded that the larger enthalpy of desolvation observed for 5HNA·DMSO ($\Delta_r H_m^\circ$ = 83.7 kJ·mol^{-1}) compared to 5HNA·H_2O ($\Delta_r H_m^\circ$ = 51.1 kJ·mol^{-1}) is necessarily due to stronger van der Walls interactions. Another interesting conclusion is the fact that the lattice enthalpies of 5HNA·H_2O and 5HNA·DMSO are approximately additive, since they are close within the experimental uncertainty to the corresponding values obtained by adding the enthalpies of sublimation of 5HNA and the solvent. Finally LC-MS analysis showed that while the purity of the starting material used to produce the 5HNA solvates was 93% (mole percentage), the purities of the dehydrated and desolvated products were 99.03% and 99.95%, respectively. A new and simple method to produce high purity 5HNA through solvate formation/desolvation was, therefore, developed.

Keywords: Polymorphism, solvates, heat capacity, Gibbs energy, nicotinic acid, simvastatin, 4-hydroxyacetophenone, 4-hydroxynicotinic acid, 5-hydroxynicotinic acid, polymorphic tautomerism.

Index

Chapter 7

Chapter 1

Introduction

This chapter describes the scope of the present work and gives an overview of the research carried out throughout this thesis.

Many organic compounds can exist in different solid forms. Depending on the arrangement of the molecules, the solid form can be either amorphous i.e., disordered state or crystalline i.e., ordered state. Crystalline solids are usually highly stable and most compounds of industrial relevance are used in crystalline form, although, in some cases, the use of amorphous phases may be advantageous (e.g. solubility enhancement of active pharmaceutical ingredients).[1-5] Diverse types of crystalline forms are also possible such as polymorphs, solvates and co-crystals.[6-8] Polymorphs differ only in the packing arrangement of the molecules in the crystal lattice. In solvates and co-crystals, however, the solvent molecules or molecules of a co-former are also incorporated in the crystal lattice.[6-7] Solvates or co-crystals may also exist in different polymorphic forms.[7]

A change in crystalline form can affect the stability of a compound and often also results in variations of physical properties, such as fusion temperature, compressibility, solubility or dissolution rate.[6, 9-12] From an industrial point of view, this may have a considerable impact on the manufacture, effectiveness and shelf-life of a given product. This aspect is particularly important for the pharmaceutical industry. Indeed, the effective and safe use of a medicine requires that an active pharmaceutical ingredient (API) be reproducibly manufactured in the desired solid form which should not transform over time. A critical goal in this regard is to control polymorphism and solvate formation during the entire drug development stage and select the solid form with the optimal characteristics for the intended use.[1, 7, 13]

From a more fundamental point of view, the occurrence of different crystal forms offers a unique possibility of investigating how the intermolecular interactions involved in molecular packing may determine the occurrence of a given packing architecture. The understanding of these interactions is the basis of Crystal Engineering which, in the words of Desiraju, Vittal and Ramanan,[14] aims at "the understanding of intermolecular interactions in the context of crystal packing and the utilization of such understanding in the design of new solids with desired physical and chemical properties".

A key aspect of crystal form control is the identification and understanding of transformations relating different phases such as solid-solid transitions, desolvations or co-crystal decompositions. This involves both thermodynamic and kinetic approaches.

Thermodynamics dictates that, for example, the relative stability of two coexisting polymorphs depends upon their Gibbs energies, the most stable being the one with the lowest Gibbs energy. On thermodynamic grounds there will always be a tendency for the least stable form under a given set of pressure-temperature conditions to transform into the most stable one. Kinetic factors may, however, prevent the transformation, thus allowing the coexistence of both forms, albeit one being *metastable*.[8, 15] The metastable form may eventually remain indefinitely metastable if the kinetic barrier preventing its transformation is sufficiently high.[16]

The main focus of this thesis was the relationship between structural, thermodynamic and kinetic aspects of the two most important transformations generally encountered in the pharmaceutical and fine chemical industries, namely those involving polymorphism and solvate formation/desolvation.[6-8]

1.1 Polymorphism

The term polymorphism is derived from two Greek words, *poly* = many and *morph* = form. This designation first appeared in 1656 in the Oxford English Dictionary and was ascribed to diversity in fashion.[8] Polymorphism in the context of crystallography was first reported in 1821 by Mitscherlich who recognized two different crystalline forms of sodium phosphate.[17-18] The first reported example of polymorphism in organic compounds refers to the polymorphs of benzamide, discovered by Woehler and Liebig.[18] The term polymorphism has been under scrutiny since it was coined, even though the basic concept behind it has always been the difference in packing of the same molecule in a solid form. The question of how similar the molecule can be and how different the packing must be in order to qualify two solids as polymorphic, has been at the center of this debate.[19] According to the most widely recognized and used definition of polymorphism by the McCrone,[17, 20] *'A polymorph is a solid crystalline phase of a given compound resulting from the possibility of at least two different arrangements of the molecules of that compound in the solid state. The molecule itself may be of different shape in the two polymorphs, but that is not necessary and, indeed, certain changes in shape (involving dynamic isomerism or tautomerism) involve formation of different molecules and hence do not constitute polymorphism.'*

Polymorphism is very common in organic solids and in recent years there has been renewed interest in its study due to its implications to the fine chemical industry, in particular pharmaceuticals. As mentioned above, different crystal forms of a compound may exhibit different physical properties, such as those listed in Table 1.1, which needs to be controlled if the safe and reproducible manufacture of a product is to be achieved. The search for the new polymorphs has, therefore, become an integral part of API development and quality control, given the economic pressure faced by the pharmaceutical industry and the greater awareness of the effect of polymorphism on the bioavailability and stability of a drug [21-22] This can be illustrated by the well-documented case of ritonavir.[22-23]

Table 1.1 Physical properties that differ among the crystal forms of a polymorphic system.[6]

Packing properties	Molar volume and density Refractive index Conductivity: electrical and thermal Hygroscopicity
Thermodynamic properties	Fusion and sublimation temperatures Lattice energy Enthalpy Heat capacity Entropy Gibbs energy and chemical potential Thermodynamic activity Vapour pressure Solubility
Spectroscopic properties	Electronic state transitions Vibrational state transitions Nuclear spin state transitions
Kinetic properties	Dissolution rate Rate of solid state reactions Stability
Surface properties	Surface Gibbs energy Interfacial tension Crystal habit

Ritonavir ($C_{37}H_{48}N_6O_5S_2$, CAS No. [155213-67-5], Figure 1.1) is a protease inhibitor which was marketed under the trade name 'Norvir' as an oral liquid and semi-solid capsule for the treatment of Acquired Immunodeficiency Syndrome (AIDS).[22] Since ritonavir is not bioavailable from the solid-state, both formulations were based on an ethanol/water solution. Because ICH (International Conference on Harmonisation of Technical Requirements for Registration of Pharmaceuticals for Human Use) guidelines stated that "For a drug product, that is a solution, there is a little scientific rationale for polymorph control",[22-23] no polymorph control strategy was applied during development and production stages. Only one crystal form of ritonavir (form I) was identified during the development stage and 240 lots of Norvir capsules were produced without any stability problems.[22] Two years later, however, several lots failed the dissolution requirements and, when examined, it was found that a new polymorph (form II) with greatly reduced solubility compared to the original form I had formed. Within weeks this new polymorph began to appear throughout the bulk drug and formulations.[22]

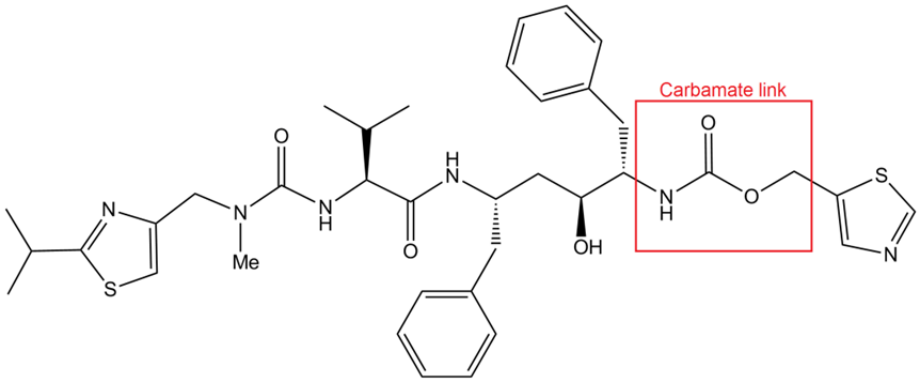

Figure 1.1 Molecular structure of ritonavir with indication of the carbamate linkage involved in polymorphism.

The two polymorphs, differed in the conformation around the carbamate linkage (trans conformation in form I and cis conformation in form II) leading to two unique crystal lattices with significantly different solubility (Figure1.2). The unforeseen appearance and dominance of this new polymorph with considerably less solubility halted the manufacture of Norvir

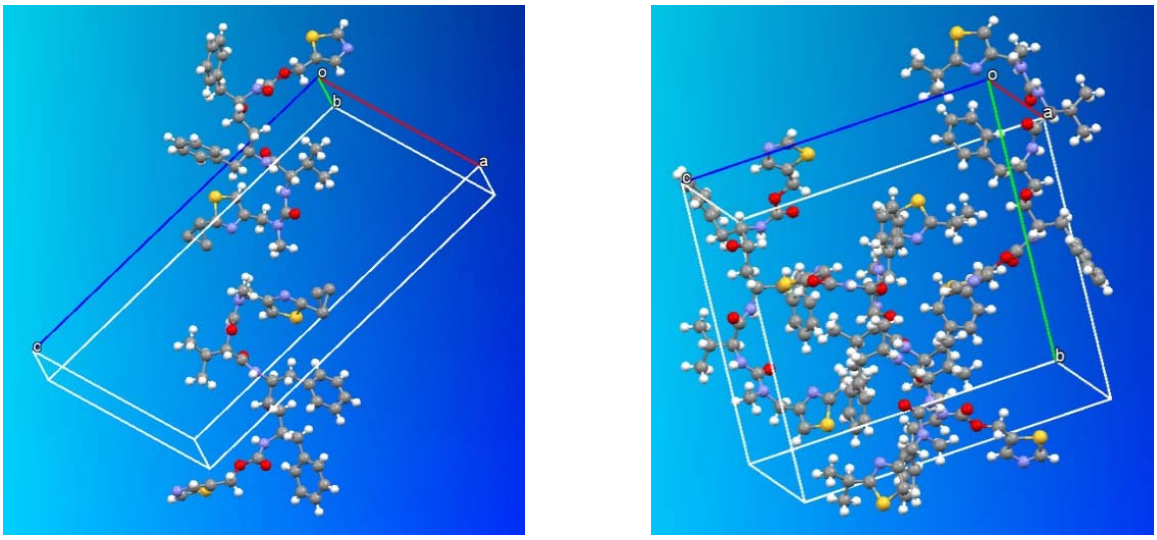

Figure 1.2 Unit cell of the two conformational polymorphs of ritonavir (a) Form I (monoclinic $P2_1$, Z = 2) and Form II (orthorhombic, $P2_12_12_1$, Z = 4).

semi-solid capsules. Additionally, the Norvir oral solution could no longer be stored at low temperatures without risk of crystallization. This created a serious threat to the supply of this lifesaving drug until a new formulation could be developed.[22-23]

Polymorphism is not only relevant for the pharmaceutical industry but also, for example, in the case of explosives, dyes, photography and agrochemical industries, where its occurrence can challenge the reliability, effectiveness and safety of products.[8]

If a compound exists in more than one crystal form, it becomes essential to address two important questions: (1) what are their relative pressure-temperature stability domains, as well as the conditions and directions in which polymorphic conversions may occur and (2) which form will be prepared and how long it can survive.[15] Thermodynamics provides the framework to discuss the first question. The second one lies in the realm of kinetics which allows quantification of the energetic barriers and rate of transformations between crystal forms.

1.1.1 Thermodynamics of polymorphic phase transitions

The thermodynamic property that governs the tendency for spontaneous conversion of one form to another under a given set of pressure-temperature conditions is the Gibbs energy (G). As postulated by Willard Gibbs, a system will tend to spontaneously evolve in the direction that leads to a reduction in Gibbs energy, which is defined as

$$G = U + pV - TS = H - TS \tag{1.1}$$

where the enthalpy H is the sum of internal energy U and the product of the pressure, p and volume V. T is the temperature and S is the entropy. In order to calculate the temperature dependency of the Gibbs energy it is necessary to predict the temperature dependency of enthalpy and entropy. Under constant pressure, the integration of heat capacity data with respect to temperature can be used to calculate the enthalpy and entropy at a temperature T according to eqs.:

$$H(T) = H(T_0) + \int_{T_0}^{T} C_{p,\mathrm{m}}\,\mathrm{d}T \tag{1.2}$$

$$S(T) = S(T_0) + \int_{T_0}^{T} \frac{C_{p,\mathrm{m}}}{T}\,\mathrm{d}T \tag{1.3}$$

The relative thermodynamic stability between the two forms and the driving force for the spontaneous transformation of one into another, at constant pressure and temperature, is determined by the difference in Gibbs energy between the two forms

$$\Delta G = \Delta H - T\Delta S \qquad (1.4)$$

where ΔH is the corresponding enthalpy change, which reflects the lattice energy difference, and ΔS is the entropy difference which is related to disorder and lattice vibrations.[15]

Depending upon the algebraic sign of the ΔG value relating the two phases, three possibilities can be envisioned:[15]

1. If ΔG is negative, i.e., when the Gibbs energy decreases, the transformation will spontaneously occur, unless hindered by a kinetic barrier.
2. If ΔG is zero, i.e., when Gibbs energy of the distinct forms are the same, the system is in equilibrium.
3. If ΔG is positive, i.e., when the Gibbs energy increases, the reverse transformation will tend to spontaneously occur.

Gibbs energy vs. temperature (*G-T*) phase diagram

G-T phase diagrams provide the most complete and quantitative information on the relative stability of polymorphs.[6] The utility of such a diagram is that it contains a considerable amount of information in a compact form, and provides a visual and readily interpretable summary of what can be complex interrelationships among polymorphic modifications.[8] The heat capacity data and other thermodynamic functions necessary for the construction of this diagram are obtained by variety of calorimetric and computational methods. A typical *G-T* phase diagram is represented in Figure 1.3.

The intersection points of the *G-T* curves in Figure 1.3 represent conditions where phases co-exist in equilibrium. Thus T_{fus}(I), T_{fus}(II) and T_{fus}(III) correspond to the fusion temperatures of forms I, II and III, respectively; T_{trs}(II→I) is the transition temperature between forms II and form I and T_g is the glass transition temperature where the amorphous solid and

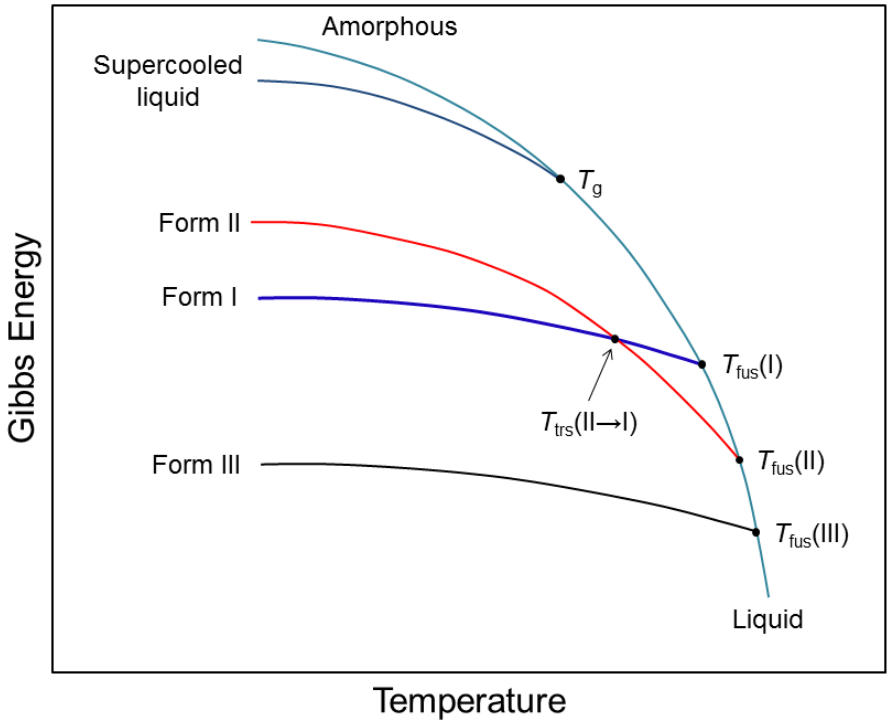

Figure 1.3 Schematic Gibbs energy vs. temperature (*G*-*T*) diagram for a hypothetical single component system that exhibit crystalline and amorphous phases (adapted from reference 15).

supercooled liquid converts to liquid. The figure also reveals that, for example, form III is always more stable than form I as ΔG = *G*(form III) – *G*(form I) is negative and thus, in the absence of kinetic barriers, the form I → form III transition will occur spontaneously.

Two different polymorphic behaviors are illustrated in Figure 1.3: (a) form III remains the most stable polymorph in the entire temperature range and subsequently melts and (b) for form I and II there is a transition temperature T_{trs}(II→I) before fusion where the stability order is reversed. Form III is said to be *monotropically* related to forms I and II, whereas there is an *enantiotropic* relationship between forms I and II.

The assignment of a given polymorphic pair as monotropic or enantiotropic, may be aided based on a set of rules proposed by Burger and Ramberger.[24] Three of the most useful rules are as follows:

Heat of transition rule. This rule states that if an endothermic phase transition occurs between two polymorphs at a certain temperature, the thermodynamic transition point lies at or below this temperature. The two polymorphs are, thus, enantiotropically related. If an exothermic phase transition is observed at a certain temperature, there is no thermodynamic transition point below this temperature and the two polymorphs are monotropically related.

Heat of fusion rule. This rule states that if the polymorph with the higher fusion temperature has the lowest enthalpy of fusion, the two polymorphs are enantiotropically related.

Density rule: This rule is based on Kitaigorodskii's principle of close packing for molecular crystals and states that for a non-hydrogen bonded system at 0 K, usually the most stable polymorph will have the highest density because of stronger intermolecular van der Waals interactions. The polymorph with most efficient packing will also have the lowest Gibbs energy.

1.2 Solvates

The term 'solvate' is used as a general designations for those crystalline compounds in which the crystallization solvent is incorporated into the crystal host lattice.[25] When the incorporated solvent is water, the term 'hydrate' is used to be more specific. Solvates are also often divided into two main classes: stoichiometric solvates and non-stoichiometric solvates. Stoichiometric solvates are characterized by a fixed, although not necessarily integral, molar ratio of solvent to compound. In these types of solvates, the solvent is an intrinsic part of crystal lattice and is essential for sustaining the molecular network. Desolvation of stoichiometric solvates always leads to a different crystal structure or an amorphous state. Non-stoichiometric solvates, on the other hand, are inclusion compounds. In this case, the solvent molecules are located in structural voids (often channels) and act like space fillers. The solvent content in the structure depends on the corresponding partial pressure in the environment at a given temperature and can take a range of values between zero and multiples of the molar solvent:compound ratio. Unlike stoichiometric solvates, the structure of the non-stoichiometric solvate is generally retained after desolvation.[7]

Solvates, and in particular hydrates, commonly occur during the isolation and processing of organic molecular solids.[26] For example, a survey within the European Pharmacopeia indicates that at least one-third of the listed compounds form hydrates and more than 90 hydrates are listed in United States Pharmacopeia.[27] The behavior of hydrates has become the object of increasing attention over the last decades, primarily due (directly or indirectly) to their potential impact in the development process and dosage form performance of an API. Hydrates are an integral part of the pharmaceutical industry. Hydration may occur during unit operations such as crystallization, milling, lyophilization, wet granulation or under normal storage conditions. Moreover many formulated drugs, are solvates, mainly hydrates.[28] On the other hand, a hydrate can dehydrate during processing or storage. The dehydrated form may differ significantly in stability, solubility, dissolution rate, bioavailability, tableting behavior, and other physicochemical properties.[29-30] Dehydration may also result in the formation of an amorphous material or a chemically labile compound. For example, cephradine dihydrate is an antibiotic which dehydrates into an amorphous form that is further oxidized.[28]

The examples illustrate why it has become important to understand the stability of hydrates and their dehydration under various experimental conditions if tight control over the production and processing of some crystalline organic products has to be achieved.[28] Assessment of the kinetics of dehydration is one way of gaining an understanding of the robustness of a given hydrate and this approach has, therefore, attracted pharmaceutical researchers since the 1970s.[26] Since then, many studies have been reported on hydrates and dehydration processes. Moreover, dehydration itself constitutes an important class of reactions which has contributed significantly to the provision of a theoretical foundation for the understanding of solid-state reactions.[31]

The presence of solvent molecules in the crystal lattice influences the intermolecular interactions and confers unique physical properties to each solvate. Therefore, a solvate has its own characteristic values of internal energy, enthalpy, entropy and Gibbs energy, [7] Also the resulting solvent free solids can be different when the original lattice solvent or the desolvation conditions change. Desolvation has thus been used for polymorph screening or to prepare novel solid forms.[32]

1.3 Overview

This thesis was centered on the study of nicotinic acid and some of its hydroxy derivatives, simvastatin and 4'-hydroxyacetophenone (Figure 1.4). These systems belong to families of compounds which are part of the ongoing research on polymorphism at the Molecular Energetics Group of CQB. Besides their importance as APIs or for other applications, the study of their polymorphism is intrinsically relevant from a crystal engineering point of view.

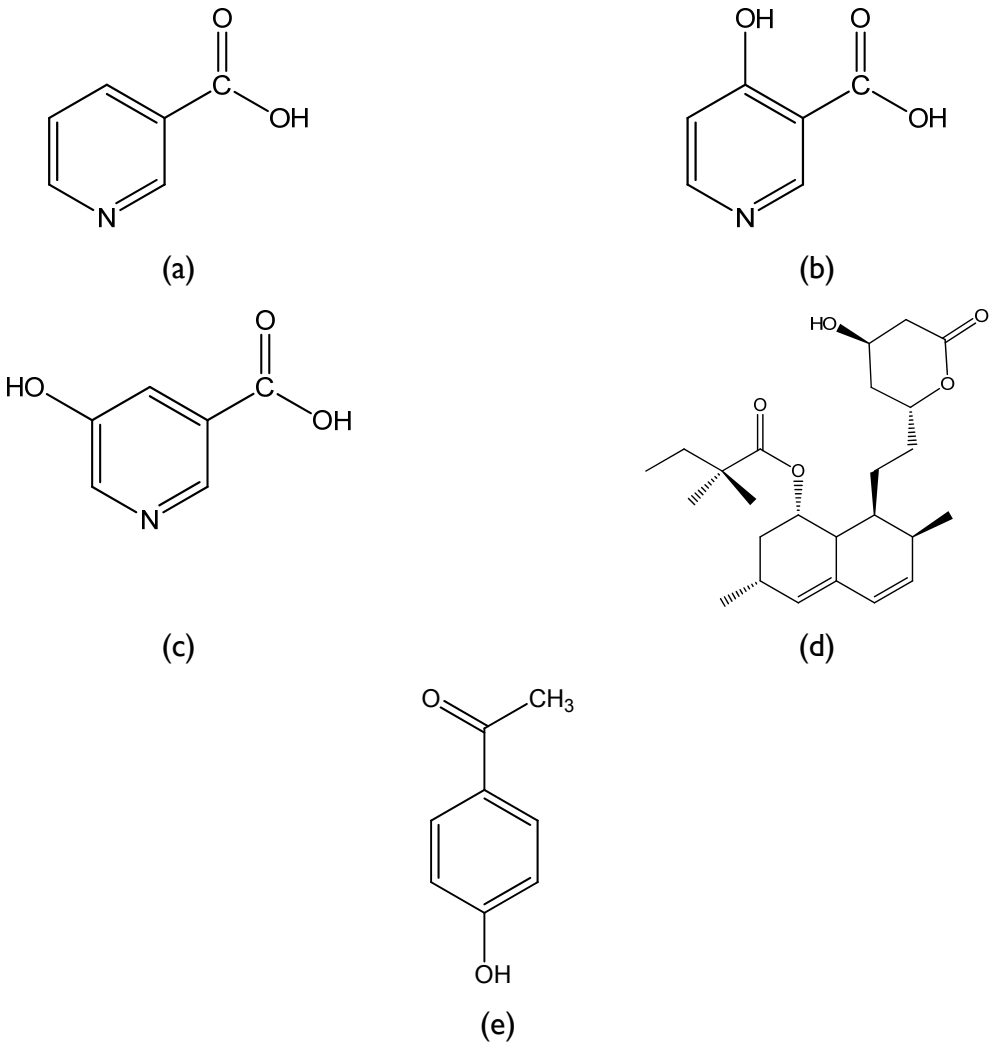

Figure 1.4 Compounds studied in this thesis, (a) nicotinic acid, (b) 4-hydroxynicotinic acid, (c) 5-hydroxynicotinic acid, (d) simvastatin, (e) 4'-hydroxyacetophenone.

Nicotinic acid (NA, CAS number [59-67-6], Figure 1.4a) also known as pyridine-3-carboxylic acid and niacin, is one of eight water-soluble B vitamins. It has received considerable attention over the years due to its importance in chemical, dietetic and therapeutic applications.[33] Some of the noteworthy applications of nicotinic acid are the preparation of matrices for matrix-assisted laser desorption ionization (MALDI) mass spectroscopy analysis of the large polypeptides[34], the use as reference material for combustion calorimetry,[35-36] and, particularly, as an API in the treatment of hypercholesterolemia and atherosclerosis.[37-38] The demands for nicotinic acid and its derivatives have raised from 8500 t per year in 1980s to more recently 35,000 t to 40,000 t.[39-41]

The 4- and 5-hydroxy derivatives of nicotinic acid have also some pharmaceutical importance. 4-Hydroxynicotinic acid (4HNA; 4-hydroxypyridine-3-carboxylic acid; CAS number [609-70-1] Figure 1.4b) and some of its salts have been explored in the treatment of rheumatism and nasal congestion and hoarseness typical of the common cold.[42-43] 5-Hydroxynicotinic acid (5HNA, 5-hydroxypyridine-3-carboxylic acid CAS number [27828-71-3] Figure 1.4c) has been found to have potential inhibitory effect on the metabolism of nicotinic acid by human platelets.[44] It is also used in the investigation of the hydroxylation mechanism of the flavoprotein 2-methyl-3-hydroxypyridine-5-carboxylic acid oxygenase (MHPCO).[45]

Simvastatin ($C_{25}H_{38}O_5$, CAS number [79902-63-9], Figure 1.4d), belongs to the statin family, a group of active pharmaceutical ingredients (APIs) widely prescribed for the treatment of hypercholesterolemia.[46-49] It is included in the World Health Organisation's list of essential medicines, which records all drugs needed in a basic healthcare system given their efficacy, safety, and cost.[50]

4'-Hydroxyacetophenone or piceol[51] (HAP, CAS number [99-93-4], Figure 1.4e) is a versatile compound with significant commercial applications and additional potential end uses. Its applications include rubber and plastics, pharmaceuticals, agricultural chemicals, flavor and fragrances, and cosmetics.[52]

As mentioned above this thesis is a continuation of previous work carried out on these systems at the Molecular Energetics Group. The reversible and fast solid-solid phase transitions

in nicotinic acid (chapter 3) and simvastatin (chapter 4) were studied by heat capacity measurements using differential scanning calorimetry and Calvet microcalorimetry. The polymorphic phase transition involving the two polymorphs of 4'-hydroxyacetophenone, (a model system which has been extensively investigated in the Molecular Energetics Group laboratories) [52-56] was also studied (chapter 5) to: (i) analyze the structure and energetic features behind the occurrence of $Z' = 1$ or $Z' = 2$ polymorphs; (ii) determine equilibrium temperature of the form II $\rightarrow$ form I phase transition through solubility studies, (iii) revisit the $\Delta_f G_m^\circ$-T phase diagram that highlights the stability domains of the two forms at ambient pressure (1 bar); and (iv) evaluate the activation energy of the phase transition.

The investigation of the kinetic barrier behind the robustness of a metastable hemihydrate of 4-hydroxynicotinic acid (4HNA·0.5H_2O) by thermogravimetric analysis and differential scanning calorimetry is described in chapter 6. The dehydration mechanism is addressed by combining structural and microscopic observations and was found to occur by rare one dimensional nucleation and growth. Finally, chapter 7 reports studies on two new solvates of 5-hydroxynicotinic acid: a monohydrate (5HNA·H_2O) and a DMSO solvate (5HNA·DMSO). These compounds were characterized both from structural and thermodynamic points of view. This work also led to the development of a new methodology to obtain highly pure 5HNA based on solvate formation/desolvation.

References

1. Hancock, B. C.; Parks, M. *Pharmaceut. Res.* **2000**, *17,* 397-404.
2. Ambike, A. A.; Mahadik, K. R.; Paradkar, A. *Drug. Dev. Ind. Pharm.* **2005**, *31,* 895-899.
3. Pokharkar, V. B.; Mandpe, L. P.; Padamwar, M. N.; Ambike, A. A.; Mahadik, K. R.; Paradkar, A. *Powder. Technol.* **2006**, *167,* 20-25.
4. Graeser, K. A.; Patterson, J. E.; Zeitler, J. A.; Gordon, K. C.; Rades, T. *Eur. J. Pharm. Sci.* **2009**, *37,* 492-498.
5. Alonzo, D. E.; Zhang, G. G. Z.; Zhou, D. L.; Gao, Y.; Taylor, L. S. *Pharmaceut. Res.* **2010**, *27,* 608-618.
6. Brittain, H. G., *Polymorphism in Pharmaceutical Solids*, 2nd ed.; Informa Healthcare USA, Inc: New York, 2009.
7. Hilfiker, R., *Polymorphism: In Pharmaceutical Industry*; Wiley-VCH: Weinheim, 2006.
8. Bernstein, J. *Polymorphism in Molecular Crystals; IUCr Monographs on Crystallography;* 14th, Ed.; Oxford University Press: Oxford, 2002.
9. Mullin, J. W., *Crystallization*, 4th ed.; Butterworth Heinemann: Oxford, 2001.
10. Gu, C. H.; Young, V.; Grant, D. J. W. *J. Pharm. Sci.* **2001**, *90,* 1878-1890.
11. Ferrari, E. S.; Davey, R. J.; Cross, W. I.; Gillon, A. L.; Towler, C. S. *Cryst. Growth. Des.* **2003**, *3,* 53-60.
12. Llinas, A.; Goodman, J. M. *Drug. Discov. Today.* **2008**, *13,* 198-210.
13. Chow, K.; Tong, H. H. Y.; Lum, S.; Chow, A. H. L. *J. Pharm. Sci.* **2008**, *97,* 2855-2877.
14. Desiraju, G. R.; Vittal, J. J.; Ramanan, A. *Crystal Engineering: A Textbook*; World Scientific: Singapore, 2011.
15. Rodriguez-Spong, B.; Price, C. P.; Jayasankar, A.; Matzger, A. J.; Rodriguez-Hornedo, N. *Adv. Drug. Deliver. Rev.* **2004**, *56,* 241-274.
16. Desiraju, G. R. *J. Chem. Sci.* **2010**, *122,* 667-675.
17. McCrone, W. C., *Polymorphism*; Wiley: New York, 1965; Vol. 2.
18. Reffner, J. A.; Ferrillo, R. G. *J. Therm. Anal.* **1988**, *34,* 19-36.
19. Threlfall, T. L. *Analyst* **1995,** *120,* 2435-2460.
20. Haleblia, J.; Mccrone, W. *J. Pharm. Sci.* **1969**, *58,* 911-&.
21. Raw, A. S.; Yu, L. X. *Adv. Drug. Deliver. Rev.* **2004**, *56,* 235-236.
22. Bauer, J.; Spanton, S.; Henry, R.; Quick, J.; Dziki, W.; Porter, W.; Morris, J. *Pharmaceut. Res.* **2001**, *18,* 859-866.
23. Chemburkar, S. R.; Bauer, J.; Deming, K.; Spiwek, H.; Patel, K.; Morris, J.; Henry, R.; Spanton, S.; Dziki, W.; Porter, W.; Quick, J.; Bauer, P.; Donaubauer, J.; Narayanan, B. A.; Soldani, M.; Riley, D.; McFarland, K. *Org. Process. Res. Dev.* **2000**, *4,* 413-417.
24. Burger, A.; Ramberger, R. *Mikrochim. Acta.* **1979**, *2,* 259-271.
25. Haleblian, J. K. *J. Pharm. Sci.* **1975**, *64,* 1269-1288.
26. Koradia, V.; de Diego, H. L.; Elema, M. R.; Rantanen, J. *J. Pharm. Sci.* **2010**, *99,* 3966-3976.
27. Sheng, J.; Venkatesh, G. M.; Duddu, S. P.; Grant, D. J. W. *J. Pharm. Sci.* **1999**, *88,* 1021-1029.
28. Khawam, A.; Flanagan, D. R. *J. Pharm. Sci.* **2006**, *95,* 472-498.
29. Zhou, D. L.; Schmitt, E. A.; Zhang, G. G. Z.; Law, D.; Wight, C. A.; Vyazovkin, S.; Grant, D. J. W. *J. Pharm. Sci.* **2003**, *92,* 1367-1376.
30. Khankari, R. K.; Grant, D. J. W. *Thermochim. Acta.* **1995**, *248,* 61-79.

31. Petit, S.; Coquerel, G. *Chem. Mater.* **1996**, *8,* 2247-2258.
32. Li, Y. H.; Han, J.; Zhang, G. G. Z.; Grant, D. J. W.; Suryanarayanan, R. *Pharm. Dev. Technol.* **2000**, *5,* 257-266.
33. Joseph, A.; Bernardes, C. E. S.; Minas da Piedade, M. E. *J. Chem. Thermodyn.* **2012**, *55,* 23-28.
34. Karas, M.; Hillenkamp, F. *Anal. Chem.* **1988**, *60,* 2299-2301.
35. Marsh, K. N., *Recommended Reference Materials for the Realization of Physicochemical Properties*; IUPAC-Blackwell Scientific Publications: Oxford, 1987.
36. Sabbah, R.; An, X. W.; Chickos, J. S.; Leitão, M. L. P.; Roux, M. V.; Torres, L. A. *Thermochim. Acta.* **1999**, *331,* 93-204.
37. Carlson, L. A. *J. Intern. Med.* **2005**, *258,* 94-114.
38. Gille, A.; Bodor, E. T.; Ahmed, K.; Offermanns, S. *Annu. Rev. Pharmacol.* **2008**, *48,* 79-106.
39. Shimizu, S., *Vitamins and Related Compounds: Microbial Production. In Biotechnology: A Multi-Volume Comprehensive Treatise*, 2nd Completely Rev. ed.; Rehm, H.J.; Reed, G.; Puhler, A.; Stadler, P.J.W.; Eds.; VCH: Weinheim, 2001.
40. Weissermel, K.; Arpe, H. J.; *Industrial Organic Chemistry*, 4th ed.; Wiley-VCH: Weinheim, 2003.
41. Cantarella, M.; Cantarella, L.; Gallifuoco, A.; Intellini, R.; Kaplan, O.; Spera, A.; Martinkova, L. *Enzyme. Microb. Tech.* **2008**, *42,* 222-229.
42. Hardy, J. D.; Wolff, H. G.; Goodell, H. *J. Clin. Invest.* **1940**, *19,* 649-657.
43. Tendeloo, H. J. C.; Broekman, F. W.; Stsiemelink, J. J. *Analgesic and Antiphlogistic Compositions*. 1974-08-07, 1974.
44. Gaut, Z. N.; Solomon, H. M. *Biochim. Biophys. Acta.* **1970**, *201,* 316-&.
45. Chaiyen, P.; Brissette, P.; Ballou, D. P.; Massey, V. *Biochemistry* **1997**, *36,* 2612-2621.
46. Li, J. J., *Triumph of the heart. The Story of Statins*; Oxford University Press: New York, 2009.
47. Taylor, F. Ward, K.; Moore, T. H. M.; Burke, M.; Davey Smith, G.; Casas, J. P.; Ebrahim, S., *Statins for the Primary Prevention of Cardiovascular Disease*, John Wiley: New York, 2012.
48. Tiwari, R.; Pathak, K. *J. Pharm. Pharmacol.* **2011,** *63,* 983-998.
49. Baxendale, I. R.; Hayward, J. J.; Ley, S. V.; Tranmer, G. K. *ChemMedChem.* **2007**, *2,* 768-788.
50. Tan, N. Y.; Zeitler, J. A. *Mol. Pharmaceut.* **2015**, *12,* 810-815.
51. Lokke, H. *Ecotox. Environ. Safe.* **1990**, *19,* 301-309.
52. Bernardes, C. E. S.; Piedade, M. F. M.; Minas da Piedade, M. E. *Cryst. Growth Des.* **2008**, *8,* 2419-2430.
53. Bernardes, C. E. S.; Piedade, M. F. M.; Minas da Piedade, M. E. *Cryst. Growth Des.* **2010**, *10,* 3070-3076.
54. Bernardes, C. E. S.; Minas da Piedade, M. E.; Lopes, J. N. C. *J. Phys. Chem. B* **2012**, *116,* 5179-5184.
55. Bernardes, C. E. S.; Minas da Piedade, M. E. *Cryst. Growth Des.* **2012**, *12,* 2932-2941.
56. Bernardes, C. E. S.; Lopes, M. L. S. M.; Ascenso, J. R.; Minas da Piedade, M. E. *Cryst. Growth Des.* **2014**, *14,* 5436-5441.

Chapter 2

Methods

The work described in this thesis required the use of variety of experimental methods. The methods which were most often used are described in this chapter.

2.1 General

2.1.1 X-ray Diffraction

Principle: When an electromagnetic radiation whose wavelength is comparable to atomic spacing, interacts with a periodic structure such as crystals (Figure 2.1), the constructive interference of the scattered beam yields diffraction. The constructive interference of the scattered beam occurs only when it satisfies Bragg's law:[1]

$$n\lambda = 2d\ \mathrm{Sin}\theta \qquad (2.1)$$

where, n is an integer, λ is the wavelength of the electromagnetic radiation, θ is the angle of incidence and d is the lattice spacing in a crystalline sample.

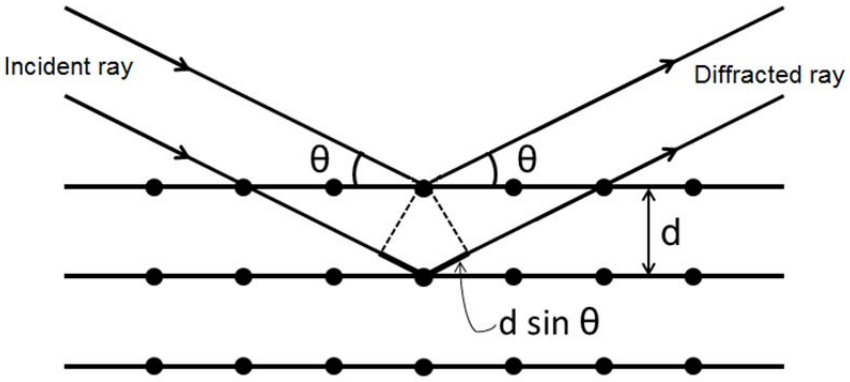

Figure 2.1 Condition for X-ray diffraction (adapted from reference 2).

X-rays have wavelength of order of a few angstrom (1 Å = 0.1 nm). This is the typical inter-atomic distance in crystalline solids, making X-rays the right choice for diffraction by atoms in crystalline materials.[2]

Powder X-ray diffraction (PXRD).

All the PXRD measurements were made on either a Philips 1730 diffractometer or on a Philips X'Pert PRO diffractometer (Figure 2.2).

(a) (b)

Figure 2.2 (a) Philips 1730 diffractometer and (b) Philips X'Pert PRO diffractometer at FCUL.

A PXRD apparatus consists of a source of X-ray radiation, a goniometer, a X-ray detector and a counting equipment.[1] X-ray radiation source generates the X-ray, filters to produced monochromatic radiation, collimates to concentrate and then directs the radiation to the sample. The goniometer performs the precise mechanical movement of the detector and sample with respect to the X-ray radiation source. In practice the X-ray radiation source remains stationary while the sample is rotated by the angle θ and the detector by the angle 2θ.[3]

The detectors used in PXRD are based on the ability of X-ray to ionize matter.[1] When the diffracted X-rays, from the sample are absorbed by the detector they generates a pulse of current. The counting equipment consists of a pulse amplifier which shapes the pulse from the detector into a convenient waveform and gives it a fixed time and voltage dimension.[1]

In a typical experiment, the grounded sample was placed in the sample holder. In case of solvates, the crystals were grounded minimally to prevent the desolvation. The sample holder containing sample was then attached to the sample positioner in the diffractometer and the control program was run. The data obtained from the PXRD is displayed as a diffractogram in which the intensity of the X-ray detected is plotted as a function of the detector angle, 2θ.

Unlike Single crystal X-ray diffraction (SC-XRD), PXRD obtains a diffraction pattern for the bulk crystalline material. While the single crystal data is used to determine the structure of material, it is the powder diffraction data which confirms if that single crystal is a true representative of the bulk sample. Thus powder X-ray diffraction is the method of choice to characterize the phase purity of a material.[2] For this purpose, the powder diffraction pattern of the bulk sample is compared with the simulated powder diffraction pattern obtained from single crystal data of the same sample and indexed. Indexing is the process of determining the unit cell dimensions from the peak positions in the diffractogram. Successful indexation of a powder pattern is considered a strong evidence for the phase purity. This method comes handy to confirm the phase purity of polymorphs and solvates and thus was extensively used throughout this work.

Another important conclusion which can be derived from PXRD analysis is the preferential orientation of the sample. Conventional theory of powder diffraction assumes completely random distribution of the orientations among the infinite number of crystallites in a sample which is used to obtain the powder diffraction pattern.[1] However it has been shown that there is a relationship between crystal morphology and XRD peak intensity.[4] When the shapes of crystallites are isotropic, random distribution of their orientations is not a problem and deviations from an ideal sample are usually negligible. However, quite often the shapes are anisotropic, e.g. plate-like or needle-like and this results in the introduction of distinctly non-random crystallite orientations due to natural preferences in packing of the anisotropic

particles. The non-random particle orientation is called preferential orientation and it may cause considerable distortions of the scattered intensity.[2] This feature was used in chapter 6 of the thesis to confirm the preferential orientation adopted by hemihydrate of 4-hydroxynicotinic acid (4HNA·0.5H_2O).

2.1.2 Infrared Spectroscopy

Principle: The Infrared (IR) region of electromagnetic spectrum consists of radiation with slightly lower energy (longer wavelength: 700 nm - 1 mm) than visible light (400 nm - 700 nm). The energy associated with this radiation is not large enough to excite electrons, but can induce vibrational excitation of heteronuclear diatomic molecules. When the vibration frequency corresponding to a bond in a molecule matches the specific frequency of the incident IR radiation, the bond absorbs energy and is promoted to an excited state. This event generates a peak in the IR spectrum which corresponds to the frequency of a vibration of a part of a sample molecule.[5] Different functional groups in a molecule absorb characteristic frequencies of IR radiation and hence have characteristic peak values.

A typical IR spectrum is essentially a graph which relates the IR radiation absorbed (or transmitted), to the corresponding frequency or wavelength of IR radiation. The ordinate scale is generally presented in percentage transmittance (%*T*). It measures the amount of IR radiation absorbed by a sample by comparing the intensities of incident radiation (I_0) and transmitted radiation (I) and is given by equation:

$$\%T = \frac{I}{I_0} \times 100 \qquad (2.2)$$

The abscissa scale is represented in wavenumber ($\bar{\nu}$).The wavenumber is the number of waves in one centimeter and has the units of reciprocal centimeters (cm^{-1}). Since the wavenumber is

inversely proportional to the wavelength, it is directly proportional to frequency and energy which makes it more convenient to use.

Diffuse Reflectance Infrared Fourier Transform (DRIFT) Spectroscopy

All IR measurements were made by the DRIFT technique on a Nicolet 6700 spectrometer equipped with a Smart Diffuse Reflectance (SDR) kit (Thermo Electron Corp.). (Figure 2.3)

Figure 2.3 Nicolet 6700 spectrometer at FCUL fitted with a Smart Diffuse Reflectance kit.

An infrared spectrometer is a device which passes the infrared radiation through the sample and subsequently scans the desired frequency (or wavelength) region using a monochromator. Most of the analytical applications are confined to the mid-IR region (4000-400 cm^{-1}), as the absorption of organic molecules are high in this region. Alternatively, the frequency range can be measured simultaneously using an interferometer in a Fourier transform instrument. A detector is used to examine the light transmitted from the sample, which responds to changes in temperature as the intensity of IR radiation falling on them varies. The result of the measurements is generated in the form of an IR spectrum.

Conventional transmittance methods such as the KBr pellet method usually requires sample manipulation, such as grinding and compressing the sample into a transparent pellet. This preparation method can result in irreversible changes in sample properties such as phase transition or desolvation. Thus, minimizing sample manipulation becomes an important consideration when sample properties are investigated.[6]

Reflectance techniques are used for samples that are difficult to analyze by the conventional transmittance methods. In Diffuse Reflectance Infrared Fourier Transform, commonly called DRIFT the sample is composed of small particles of diluent (here KBr) and analyte. The infrared radiation that is reflected from the sample is composed of two components: specular component and diffuse component (Figure 2.4).

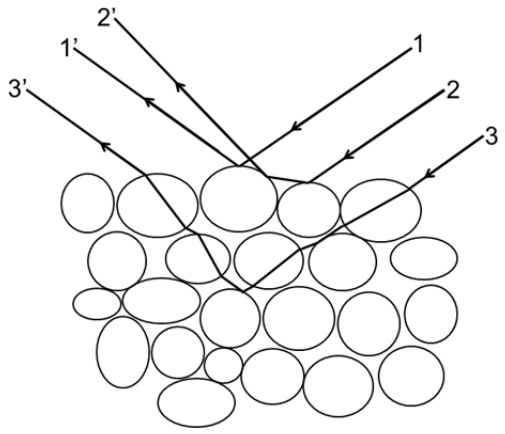

Figure 2.4 Illustration of reflections from the surface of the sample (adapted from reference 6): 1, 1') Fresnel specular reflectance; 2, 2') Fresnel diffuse reflectance and 3, 3') Kubelka-Munk diffuse reflectance.

When a simple reflection of the infrared radiation occurs from the surface of a particle parallel to the macroscopic surface of the sample, it is called Fresnel specular reflectance **(1, 1')**. This reflection from the top surface of the sample retains the polarization of the incident beam and has equal angles of incidence and reflection relative to the macroscopic sample. In a sample however, many of the particle interfaces are not parallel to the macroscopic

surface. In such scenario, the angle of reflection will be equal to the angle of incidence at the particle surface but not equal to the angle of incidence relative to the macroscopic sample. Multiple reflections also occur between the particles of the sample. The generated radiation which emerges from the sample is thus scattered and has a mixed polarity relative to incident radiation. This radiation is called Fresnel diffuse reflectance **(2, 2')**. This component like specular reflectance carries no information about the analyte as it has not been transmitted through any sample particle.

The third type of reflectance is similar to the Fresnel diffuse reflectance accept that the radiation has been transmitted through at least one sample particle. This component is called Kubelka-Munk reflectance **(3, 3')** and carries all information regarding the analyte. The intensity of this component obeys the Kubelka-Munk relation for the intensity of analyte absorption bands relative to concentration of the absorber, under the limitations.[6]

The Fresnel reflectance components in the radiation reflected from the sample, cause changes in band shapes, their relative intensities and in some cases it is responsible for complete band inversions called 'reststrahlen' bands. Well grinded and diluted analytes can reduce the contribution of Fresnel reflectance in the reflected radiation.

In a typical DRIFT experiment first the background spectrum of the diluent KBr was collected with a DRIFT accessory. The analyte was then gently grounded and diluted to a suitable concentration (2% w/w) in KBr. In case of solvates, in order to prevent desolvation, the crystals were grinded minimally. This diluted sample was then placed in the sample holder and the surface was levelled by scrapping away the excess sample. The sample holder along with the sample was inserted into the DRIFT accessory, and the sample measurement program was run.

The data obtained from the DRIFT spectroscopy was displayed as a diffuse reflectance spectrum, in which the Kubelka-Munk transformation function is plotted as a function of the wavenumber (cm^{-1})

Infrared spectroscopy is often employed to complement PXRD in characterizing the sample. It becomes particularly useful to characterize polymorphic sample with <5% mixture of phases, which is typically beyond the detection limit of PXRD. It had been shown recently that

the structural difference between the two 4'-hydroxyacetophenone polymorphs is reflected clearly in their DRIFT spectra.[7] This feature was thus used in chapter 5 of this thesis to characterize the polymorphic phases.

2.2 Thermal Analysis and Calorimetry

Principle: The terms thermal analysis and calorimetry denotes a variety of experimental methods, which involve a change in the temperature of the sample to be investigated.[8] The modern instrumentation used for any experiment in thermal analysis and calorimetry is usually made up of four major parts:[9]

- The sample holder;
- Sensor to detect and measure a particular property of the sample and to measure temperature;
- An enclosure within which the experimental parameter (e.g. temperature, pressure, gas atmosphere) may be controlled;
- A computer to control the experimental parameters, such as the temperature programme to collect the data from the sensors and to process the data to produce meaningful results and records.

2.2.1 Thermogravimetric Analysis (TGA)

Thermogravimetric Analysis (TGA) or Thermogravimetry (TG) is an experimental technique in which the weight change of a sample is measured as a function of temperature or time, whilst the sample is subjected to a controlled temperature program in a controlled atmosphere. Weight loss is observed only when a volatile component is lost.

Instrumentation

All the measurements were performed on a TGA 7 apparatus from Perkin Elmer (Figure 2.5).

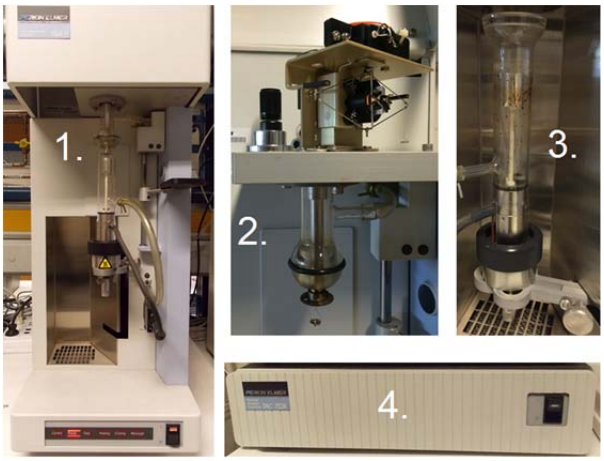

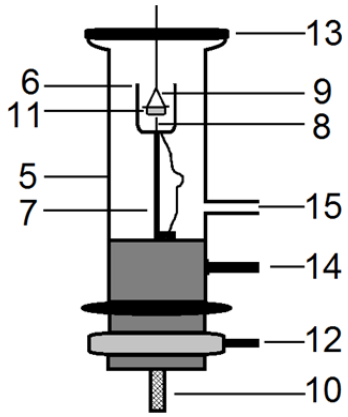

(a) (b)

Figure 2.5 (a) TGA 7 thermogravimetric apparatus from Perkin Elmer at FCUL: 1) The TGA 7; 2) the microbalance unit; 3) the furnace unit; 4) TAC 7/DX thermal analysis instrument controller and (b) Schematic representation of furnace unit: 5) Pyrex glass enclosure; 6) furnace tube; 7) shaft; 8) measuring thermocouple; 9) crucible stirrup; 10) knob for adjusting measuring thermocouple; 11) crucible; 12) furnace base; 13) rubber O-ring; 14) cable; 15) purge gas outlet.

The apparatus, **1**, consists of a microbalance unit, **2**, which supports a crucible stirrup via a hangdown wire and a furnace unit, **3**, positioned around the crucible stirrup and below the microbalance unit. The apparatus is controlled by a TAC 7/DX thermal analysis instrument controller, **4**, that in turn is controlled by the Pyris software from Perkin Elmer.

The microbalance unit features a null balance design that compensates for weight changes in the sample. In this type of balance, the control system varies the current passing

through the balance in an attempt to keep the beam of the balance in the zero position. This has the advantage that the sample maintains the same position in the furnace throughout the run. The whole unit is inserted in a sealed enclosure.

The furnace unit consists of a pyrex glass enclosure, **5**, which incorporates a small furnace tube, **6**. This furnace tube is made of a resistive alloy wire wound on a ceramic tube. The winding is coated with furnace cement to hold the wires in place because they expand greatly in length during heating. The furnace tube rests on a shaft, **7**, which is fixed at the base of the furnace unit. A measuring thermocouple, **8**, is located just below the crucible stirrup, **9**, at the base of the furnace tube in which the sample is lowered during experiments. It can be adjusted manually by a knob, **10**, located at the base of furnace unit, so that it is positioned as near as possible to the crucible, **11**, but not quite touching it. The furnace unit is capable of being moved away from the balance unit to allow access to the sample. The furnace base, **12**, allows it to move up, down or sideways as required. A rubber O-ring, **13**, produces a gas tight seal between the furnace unit and the microbalance unit. The furnace unit is connected to TGA electronics through a cable, **14**. The furnace unit along with the microbalance unit is called 'thermobalance'.

The atmosphere in the sample chamber was always purged with an inert gas (here nitrogen). This prevents oxidation and other undesired reactions by eliminating the gaseous product through an outlet, **15**. The balance chamber was always kept at a positive flow of nitrogen so as to prevent the back diffusion of gaseous products into the microbalance compartment.

The apparatus was calibrated prior to the experiments. Calibration was performed in three stages. Firstly balance calibration was performed in which the balance was first zeroed and then a standard weight (100 mg in this case) was added. The observed mass was then implemented in the calibration routine of the software. It was followed by temperature calibration which makes use of 'Curie point transitions' in reference transition metals.[10] Certain metals and alloys are ferromagnetic at room temperature. When these materials are heated, at a temperature characteristic for each, the material becomes diamagnetic. When a magnet is placed below the crucible holding the sample, the sample experiences the magnetic flux in the

same direction as gravity. At low temperatures this causes a pull on the sample and a higher weight is recorded. At the Curie temperature there is a sudden loss in apparent weight. Two metals, alumel alloy (PerkinElmer, T_C = 427.35 K) and nickel (PerkinElmer, mass fraction 0.9999, T_C = 628.45 K) were used for this purpose. These measurements resulted in the observed temperature of the thermocouple which was then implemented in the calibration routine. Third step involved furnace calibration which calibrates furnace for the programmed nine temperature points. This is a self-contained routine which automatically calibrates the furnace.

Briefly the experiment can be described as follows. The empty crucible was loaded on the stirrup and the furnace unit was raised to seal with microbalance unit. Zero weight was obtained to subtract the tare weight of the empty crucible. Thereafter the furnace unit was lowered and the crucible was removed. The solvate crystals were carefully removed from the mother liquor and dried over a filter paper. The crucible filled with the sample was loaded on stirrup and the starting weight of the sample was obtained in an identical procedure. The starting weight was always confirmed to be 100% for the precise measurements. Control program was then run to measure the weight loss of the sample as a function of time (isothermal) or temperature (non-isothermal). The data obtained from the TGA was displayed as a thermogram (Figure 2.6).

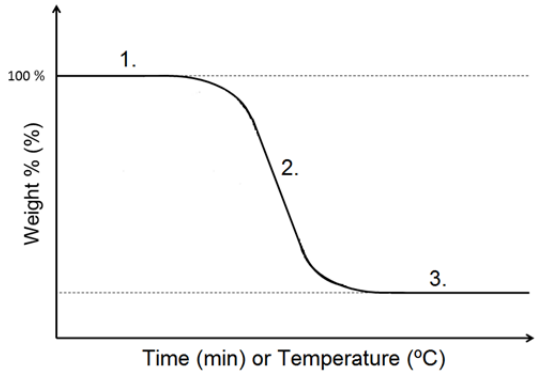

Figure 2.6 A typical TGA curve of a mass loss process indicative of: 1) constant weight; 2) rate of mass loss; 3) completion of mass loss process.

The following features of the TGA curve may be identified: An initial horizontal portion or plateau, **1**, which is indicative of constant weight, a curved portion, **2**, which is indicative of the loss of volatile component say solvent of crystallization, and a final horizontal portion, **3**, which indicates the completion of the mass loss process. In the curved portion, **2**, the steepness of curve gives an indication of the rate of mass loss and depends on several factors such as heating rate, sample type, crucible and atmosphere.[11]

The mass loss can be followed throughout the process as the sample is heated or held at constant temperature and the data can be expressed as conversion fraction (α).[12] This feature was used in chapter 6 of the thesis to calculate conversion fraction (α), under isothermal condition which is given by equation

$$\alpha = \frac{m_0 - m}{m_0 - m_f} \tag{2.3}$$

where m_0 and m_f are the initial and final masses of the sample respectively and m is the mass of the sample at a given time.

TGA can also be used to confirm the stoichiometry of solvates and, to judge if the desolvation process has been completed. It can be done by determining the amount of substance, n, of the solvent of crystallization in the solvate and is expressed by equation

$$n = \frac{\left(m_f - m_i\right) / M_{SC}}{m_f / M_{DS}} \tag{2.4}$$

where m_i and m_f are the initial and final mass corresponding to mass of solvated and desolvated sample respectively. M_{SC} and M_{DS} are the molar mass of the solvent of crystallization and desolvated sample respectively. This feature was used in chapter 6 and 7 of this thesis.

2.2.2 Hot Stage Microscopy (HSM)

Hot Stage Microscopy (HSM), is an analytical technique which combines microscopy and thermal analysis to enable the characterization of the physical properties of a material as a function of time or temperature. The temperature of the sample in a specified atmosphere is programmed.[13]

Instrumentation

Hot Stage Microscopy (HSM) (Figure 2.7) was used in chapter 5 and 6 to visualize the thermal events. The HSM system, **1**, used in this work consisted of an Olympus BX 51 microscope, coupled with a Linkam LTS350 temperature controlled stage, **2**, and an Olympus SC-30 digital camera. The temperature of the stage, was controlled by Linkam TMS 94 controller, **3**.

The Linkam LTS350 temperature controlled stage,[14] **2**, is made up of lid assembly and stage assembly. The lid assembly consists of a stage lid, **4**, with a lid insert, **5**. The lid insert incorporates a viewing window, **6**, and holes, **7**, for tube clip holders or for window removal tool. The stage assembly consist of a stage chamber, **8**, which incorporates a heating/cooling block (43×53 mm), **9**, The block, is heated by a heating element, **10** and it's temperature is monitored by a Pt100 platinum temperature sensor, **11**. A small aperture (2.5 mm), **12**, is located in the block. This aperture is for placing the sample in the field of view. On top of the block rests a microscope sample slide holder, **13**, and is fixed on the other end of stage chamber aligned in X or Y directions by X-manipulator, **16** or Y-manipulator, **17**, respectively. The stage assembly is outfitted with a lemo connector, **18**, for stage lead, a set of bypass stage body water cooling connector, **19**, a set of liquid nitrogen cooling connector, **20**, which is

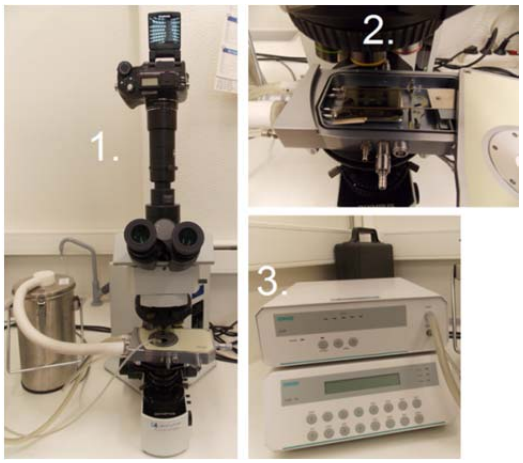

(a)

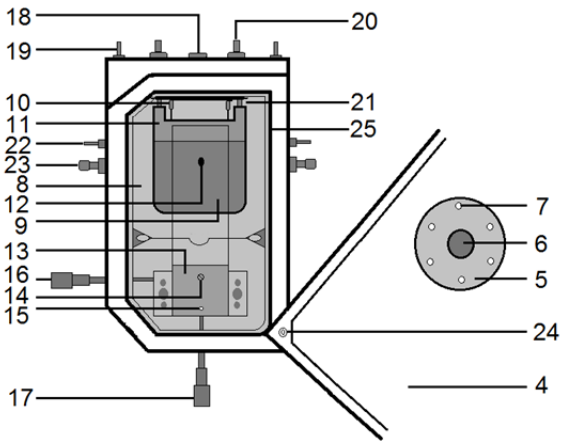

(b)

Figure 2.7 (a) Hot Stage Microscopy apparatus at IST: 1) Olympus BX 51 microscope, coupled with a Linkam LTS350 temperature controlled stage and an Olympus SC-30 digital camera.; 2) Linkam LTS350 temperature controlled stage; 3) Linkam TMS 94 controller and (b) Schematic representation of Linkam LTS350 temperature controlled stage (adapted from reference 14): 4) stage lid; 5) lid inserts; 6) viewing window; 7) lid holes; 8) stage chamber; 9) heating cooling block; 10) heating element; 11) Pt100 platinum temperature sensor; 12) block aperture; 13) microscope sample slide holder; 14) screw; 15) alignment peg; 16) X-manipulator; 17) Y-manipulator; 18) lemo connector; 19) bypass stage body water cooling connector; 20) liquid nitrogen cooling connector; 21) stainless steel tubes; 22) stage body water cooling connector; 23) gas purge valve; 24) hinge; 25) rubber O-ring.

attached to the block by a set of stainless steel tubes, **21**, a set of stage body water cooling connector, **22** and a set of gas purge valve, **23**. The lid assembly can rotate via a hinge, **24**, to cover and uncover the stage chamber. A rubber sealing O-ring, **25**, produces a tight seal between stage lid and stage chamber.

In a typical experiment a good quality single crystal was isolated from the batch and then placed gently on the glass slide. The stage lid was opened and the glass slide with sample crystal was loaded on the microscopic sample slide holder of the stage. The position of the crystal was adjusted by X and Y manipulators so that it comes within the field of view of the

heating/cooling block's aperture. The stage lid was then closed and the tube blowing warm nitrogen was attached to the lid window by the tube clip holder. This was to prevent condensation on the viewing window surface.[14] Microscopic focusing combined with stage movements were used to acquire good images of the sample crystal. The stage temperature control parameters were then programmed in the controller and the experiments were run either at a given rate or at a fixed temperature. Images were recorded at regular intervals on detection of a thermal event. Hot stage microscopy was used in this thesis to visualize the thermal events of phase transition (chapter 5) and dehydration (chapter 6).

2.2.3 Calorimetry

A typical calorimeter is made up of two regions:[9, 15] (1) A calorimetric vessel, which holds the sample and all the necessary accessories to investigate the process under study and (2) the surrounding, which refers to the controlled region around the calorimetric vessel whose temperature control is either active (as in the case of a Peltier unit) or passive (as in the case of a heat sink).

Calorimeters can be classified on three primary criteria,[8-9]

- The principle of measurement
- The mode of operation
- The construction principle

According to the principle of measurement, calorimeters can be heat compensating type which determines the energy (power) required for compensating the heat (heat flow rate) to be measured; heat accumulating type which measures the temperature change caused by the heat to be measured; or heat exchanging type which measures the temperature difference between sample and surroundings caused by the heat to be measured.

Based on the mode of operation, calorimeters can be isothermal, where sample and surrounding are held at constant temperature, isoperibol, where surrounding stays at constant temperature while sample temperature may vary or adiabatic, where ideally no heat exchange

takes place between the sample and surrounding because they both are maintained at the same temperature, which may increase during the process under study.

Based on the principles of construction, calorimeters can have a single measuring system or a twin or differential measuring system.

All calorimeters must be calibrated either by an electrical method which is available as an overall package or by comparison with the standard systems.[16]

2.2.3.1 Differential Scanning Calorimetry (DSC)

Differential Scanning Calorimetry (DSC) is a technique where the power input to the sample and a reference is measured as a function of temperature or time, while they are subjected to a temperature variation.[8, 17] The term "differential" emphasizes on the fact that the signal from the instrument depends on the difference between the response of the measuring sensors for sample and reference. In this way the signal is representation of the thermal event alone and is free from diverse thermal effects which influence both sensors equally. This allows high sensitivities to be devised into instruments.[9]

Unlike thermogravimetry this technique is not limited to mass loss and so can be applied to variety of thermal events occurring in the sample such as polymorphic phase transitions, fusion, glass transition etc.

Instrumentation

All the measurements were performed on either a DSC 7 from Perkin Elmer, a Netzsch DSC 204 F1 Phoenix or on a TA Instruments 2920 MTDSC apparatus. Depending on the method of measurement, these DSC fall under following two categories;[8]

(a) Power compensation
(b) Heat flux

(a) Power Compensation

DSC 7 from Perkin Elmer is a power compensation type DSC and is controlled by a TAC 7/DX thermal analysis instrument controller, (Figure 2.8).

Figure 2.8 Images of DSC 7 differential scanning calorimeter from Perkin Elmer at FCUL.

The measuring system of power compensation type DSC is described in Figure 2.9. In this type of DSC, the crucible, **1**, containing the sample and the reference crucible, **2**, are placed in two small furnaces, **3** and **3'** respectively. The furnaces are equipped with heat source, **4**, **4'** and temperature sensor, **5**, **5'** both located inside the cell, **6**, whose temperature is monitored.

The system of furnace is controlled by two separate loops, one for average temperature control and another for differential temperature control. The average temperature control loop ensures that the average of the sample and reference temperatures is increased at the programmed rate β. When the sample undergoes change in heat capacity or endothermic or exothermic transformations (eg. phase transition or desolvation) the temperature difference tends to develop between two furnaces, **3** and **3'**. At this point the differential control loop automatically adjusts the power supplied to each furnace so that the temperature difference is maintained as small as possible during the experiment. The recorded output signal of the calorimeter is proportional to the difference $\Delta\phi$ between the heat flow rates supplied to the sample and the reference.

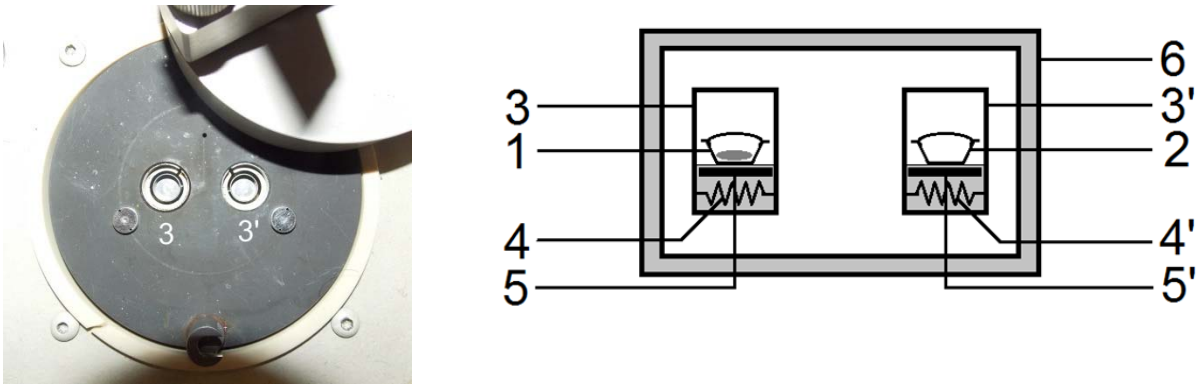

(a) (b)

Figure 2.9 (a) The two furnaces of the power compensation DSC 7 and (b) Schematic representation of a power compensation apparatus (adapted from reference 18): 1), sample crucible; 2) reference crucible; 3, 3') furnace; 4, 4') heat source; 5, 5') temperature sensor; 6) cell.

(b) Heat Flux

Netzsch DSC 204 F1 Phoenix and TA Instruments 2920 MTDSC apparatuses (Figure 2.10) are of disc type heat flux DSC. The MTDSC apparatus from TA instruments was operated as a conventional DSC in this work.

(a) (b)

Figure 2.10 (a) Netzsch DSC 204 F1 Phoenix at FCUL and (b) TA Instruments 2920 MTDSC apparatus at IST.

The measuring system of disc type heat flux DSC (Netzsch DSC 204 F1 Phoenix) is described in Figure 2.11. In this type of DSC, both the crucible, **1**, containing a sample and a empty reference crucible, **2**, are placed on a supporting disc, **3** and **3'** respectively, inside a block furnace, **4**, whose temperature is monitored. When the sample undergoes a thermal event, the temperature difference developed between the two crucibles **1** and **2** is measured by heat flux sensor, **5**, embedded in the supporting disc. This temperature difference is recorded and converted to a difference in heat flow rate to the sample and to the reference, using a suitable calibration factor.

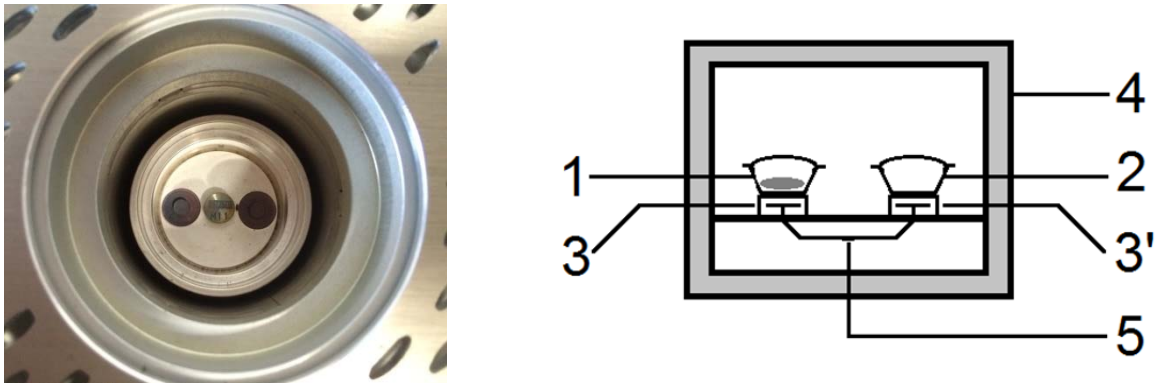

(a) (b)

Figure 2.11 (a) Image of a furnace of the disc type heat flux DSC (Netzsch DSC 204 F1 Phoenix) used in this work. (b) Scheme of a heat flux apparatus (adapted from reference 18): 1) sample crucible; 2) reference crucible; 3, 3') supporting disc; 4) block furnace: 5) heat flux sensor.

The temperature scale and the energy equivalent of the calorimeters were determined through calibration, which was based on the fusion of standard substances. This calibration was always performed prior to experimental runs.

In a typical DSC experiment a sample was sealed in air in an aluminum crucible and was weighed with a precision of ±0.1 μg on either a Mettler XP2U or a Mettler UMT2 ultra-micro balance. When studying solvates, the lid of the crucible was punctured in order to prevent

pressure build-up inside the crucible during desolvation. This crucible was then either placed in one furnace (power compensated DSC) or kept on one disc (disc type heat flux DSC) while the other furnace or disc held the reference crucible. The control parameters were then programmed in the program setup and the experiments were run either at a given rate or at a fixed temperature. The result from the DSC experiment was displayed as a thermogram in which the differential heat flow rate ($\Delta\phi$) is plotted against sample temperature or time. By convention positive heat flow rates were assigned to endothermic events while negative heat flow rates were assigned to exothermic events.

During a thermal event such as fusion, the difference in heat flow rates between the sample and crucible is recorded as a peak in the thermogram (Figure 2.12).

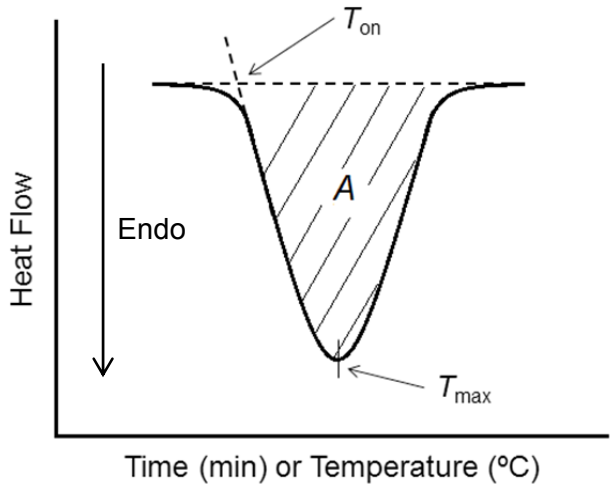

Figure 2.12 A typical DSC curve of an endothermic event.

To analyse the peak an approximate baseline was introduced by the software which connects the start and finish of the transformation. This allowed the determination of the extrapolated onset temperature (T_{on}) and the peak temperature (T_{max}) for the process. The area

(*A*) of the peak under the baseline corresponds to $\Delta_{fus}h^{\circ}$ from which the value of $\Delta_{fus}H_m^{\circ}$ was calculated as

$$\Delta_{fus}H_m^{\circ} = \Delta_{fus}h^{\circ} \times M \qquad (2.5)$$

where *M* is the molar mass of the sample.

Heat capacity measurements were performed in the continuous mode.[18] The experiments were carried out either in a single temperature interval or the temperature interval was divided into several overlapping segments. The temperature program consisted of an isothermal baseline of 15 minutes at the initial temperature, followed by dynamic scan at the rate of 2 or 10 $K \cdot min^{-1}$ and finally an isothermal baseline of 15 minutes at the final temperature.

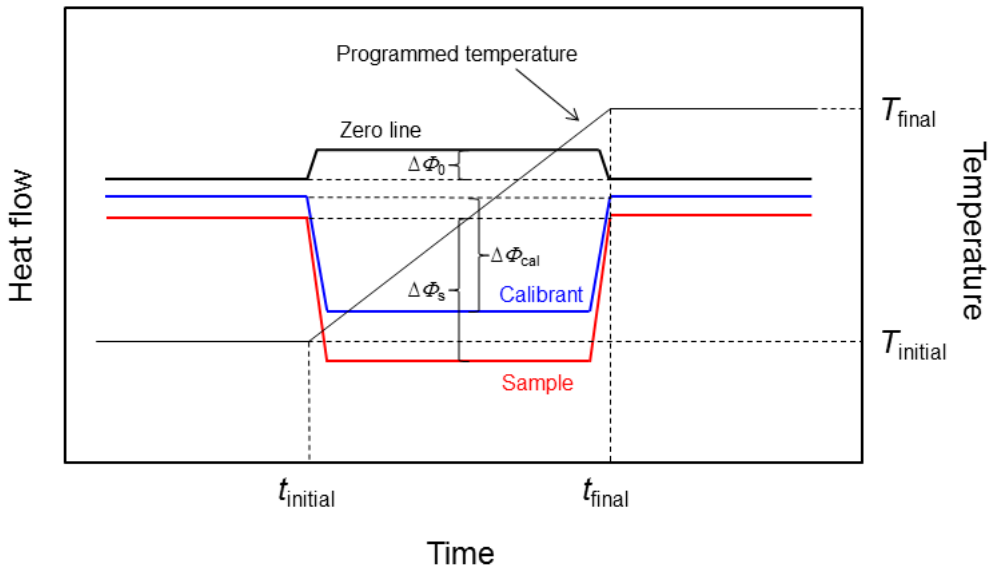

Figure 2.13 Measurement of heat capacity by DSC in continuous mode (adapted from reference 18).

'*C*p ratio method' was used to determine heat capacities.[18] This method consists of three consecutive measurements in each temperature interval/segment using the similar temperature program (Figure 2.13). In the sequence of measurement, first a zero baseline was recorded with two empty crucibles with difference in mass of < 0.01 mg. Next, a calibrant (alumina, i.e., synthetic sapphire) was placed in the sample crucible and the temperature program was repeated. Finally the calibrant was replaced by the sample under study and the temperature program was run the third time. The reference crucible was left untouched in the furnace during all three measurements.

Determination of heat capacity by DSC 7 required curve manipulations which were done manually using Pyris software from Perkin Elmer. Firstly the curve alignment was made so that the initial isothermal segment of zero line and say for e.g. calibrant curve get overlaid upon each other. This was followed by curve subtraction and endpoint alignment. The slope of the dynamic segment of the resultant curve was used to calculate $\Delta\phi_{\text{cal}}$ for the given temperature range. The standard molar heat capacity of the calibrant $C^{\circ}_{p,\text{m}}\left(\text{calibrant}\right)$ at a given temperature was calculated as

$$C^{\circ}_{p,\text{m}}\left(\text{calibrant}\right) = \frac{M}{m\beta}\Delta\phi_{\text{cal}} \tag{2.6}$$

where *m* and *M* are the mass and molar mass of the calibrant respectively and β is the heating rate.

This observed heat capacity was then compared with the reference value to obtain the calibration factor *k,* which was then applied to the measured heat capacity of the sample (obtained using similar procedure) in order to arrive at the corrected heat capacity of the sample. This routine was implemented in the Netzsch Proteus Analysis software Version 6.1.0 and the curve manipulations and calculations were performed automatically.

2.2.3.2 Calvet Drop Microcalorimeter

This is the twin cell heat flow type calorimeter where the instrument signal is obtained by measuring the heat flux between the sample and the reference inside a relatively massive calorimetric block which acts as a heat sink.[9] The apparatus shown in Figure 2.14 and illustrated in Figure 2.15 is based on DAM Calvet microcalorimeter, which can be used from room temperature to 473 K.[19-20]

Figure 2.14 The Calvet microcalorimeter at FCUL.

The apparatus (Figure 2.15) consists of four wells, **1**, **1'**, **2** and **2'**, each containing a microcalorimetric element, **3.** The microcalorimetric elements operate in pairs to allow differential measurement. Only one of these pairs was used in this work. The microcalorimetric elements are surrounded by a large furnace, **4**, whose temperature is controlled with a precision of ±0.1 K by a Eurotherm 2404 PID unit, and measured with a precision of ±0.1 K by a Tecnisis 100 Ω platinum resistance thermometer inserted into one of the unused microcalorimetric elements. Two identical glass cells, **5**, (9 mm external diameter × 800 mm

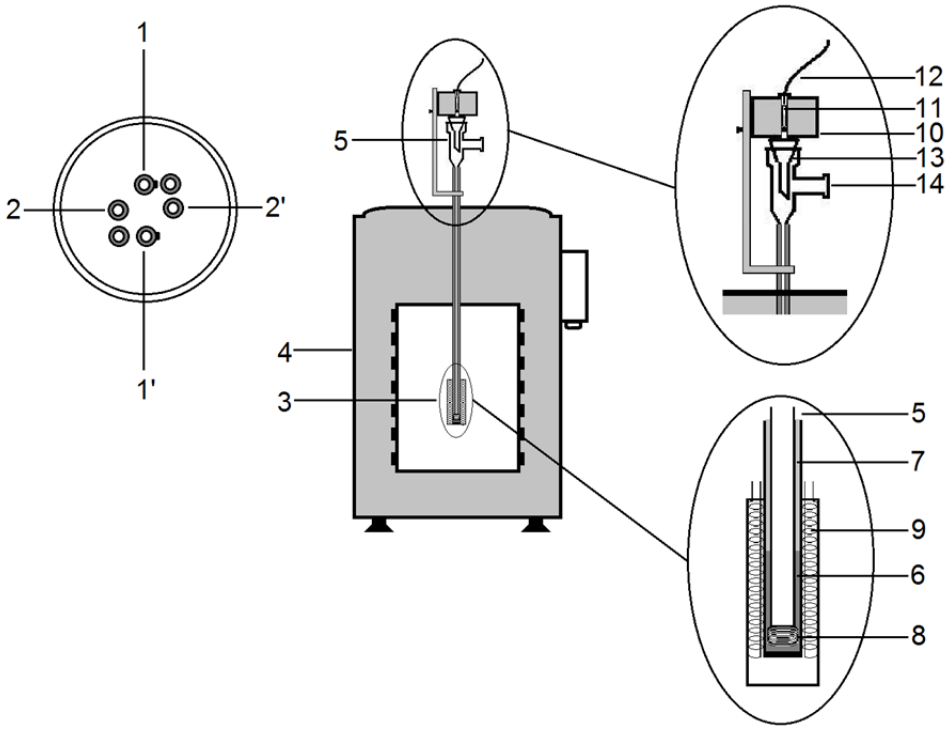

Figure 2.15 Schematic representation of Calvet microcalorimeter at FCUL. (adapted from references 19 and20): 1, 1', 2 and 2'), wells; 3) microcalorimetric element; 4) furnace; 5) glass cell; 6) brass cylinder; 7) teflon tube; 8) brass piece; 9) thermopile; 10) furnace; 11) sample; 12) platinum resistance sensor; 13) guide funnel; 14) vacuum/inert gas (N_2) inlet.

height) are inserted into the calorimetric wells, and are enveloped by the microcalorimetric element at the bottom. One cell is used for measurement while another cell acts as a reference. Each microcalorimetric element, consist of a brass cylinder, (17 mm external diameter × 100 mm height), **6**, which is closed at the bottom and is screwed at the base of Teflon tube (17 mm external diameter × 600 mm height), **7**. The brass cylinder rests on a brass piece, **8**, which is a Manganin wire resistance (200 Ω).This resistance is used for calibration of apparatus by Joule effect. The heat flow in and out of the cell is detected by thermopile, **9**, that surrounds the brass cylinder. The differential heat flow across the thermopiles of the microcalorimetric elements is measured as a potential difference by using a Hewlett-Packard 34420A nanovoltmeter.

Positioned above the inlet of glass cell is a furnace, **10**, which holds the sample, **11**, initially. The temperature of this furnace is measured by a miniature platinum resistant sensor (Labfacility, 1/10), **12**, which is placed in the central well of the furnace. The sample rests on a small pin in the furnace well. Pulling the pin allows the sample to be dropped into the glass cell of the calorimeter through a guide funnel, **13**. The cell can then be closed and if necessary, evacuated through inlet, **14**, which is connected to a vacuum/inert gas (N_2) line.

The pumping system includes an alcatel Adixen Pascal series 2005SD rotary pump and an Edwards E02 oil diffusion pump with a liquid nitrogen trap. A second liquid nitrogen trap separates the vacuum system from the sublimation cell. The ultimate vacuum, measured between the two traps, when pumping the glass cells, is 4×10^{-3} Pa. Only the rotary pump, which can reach an ultimate pressure of ~ 0.13 Pa, was necessary to perform the experiments described in this thesis.

The sensors used to measure the temperature of the sample in the dropping furnace and in the calorimetric cell are both connected in a four-wire configuration to a Hewlett Packard 34401A multimeter. The two sensors were calibrated against a standard platinum resistant thermometer, which in turn had been calibrated at an accredited facility in accordance with the International temperature Scale ITS-90. The data acquisition and the electrical calibration are computer controlled by the CBCAL 1.0 program.[21]

The electrical calibration circuit consists of the Manganin resistance referred above, connected in a four-wire configuration to a Hewlett Packard 6611 DC power supply and a Hewlett Packard 34401A multimeter. The power supply is used to supply and measure the current intensity across the Manganin resistance and the corresponding potential drop is measured with the multimeter.

In a typical experiment, the sample was introduced to a small glass capillary and was weighed with a precision of ±0.1 μg on a Mettler XP2U ultra-micro balance. This glass capillary with the sample was then introduced into the furnace preset at the desired temperature. The initial baseline of the measuring curve was recorded while the sample was left equilibrating in the furnace. After the equilibration period the pin was pulled allowing the sample to fall into the calorimetric cell through the guide funnel. The output of a thermal event is displayed as a plot

where the difference in heat flow rate $\Delta\phi$ between the sample and reference cell is plotted as a function of time, *t*. The measuring curve obtained was monitored until it returned to the base line.

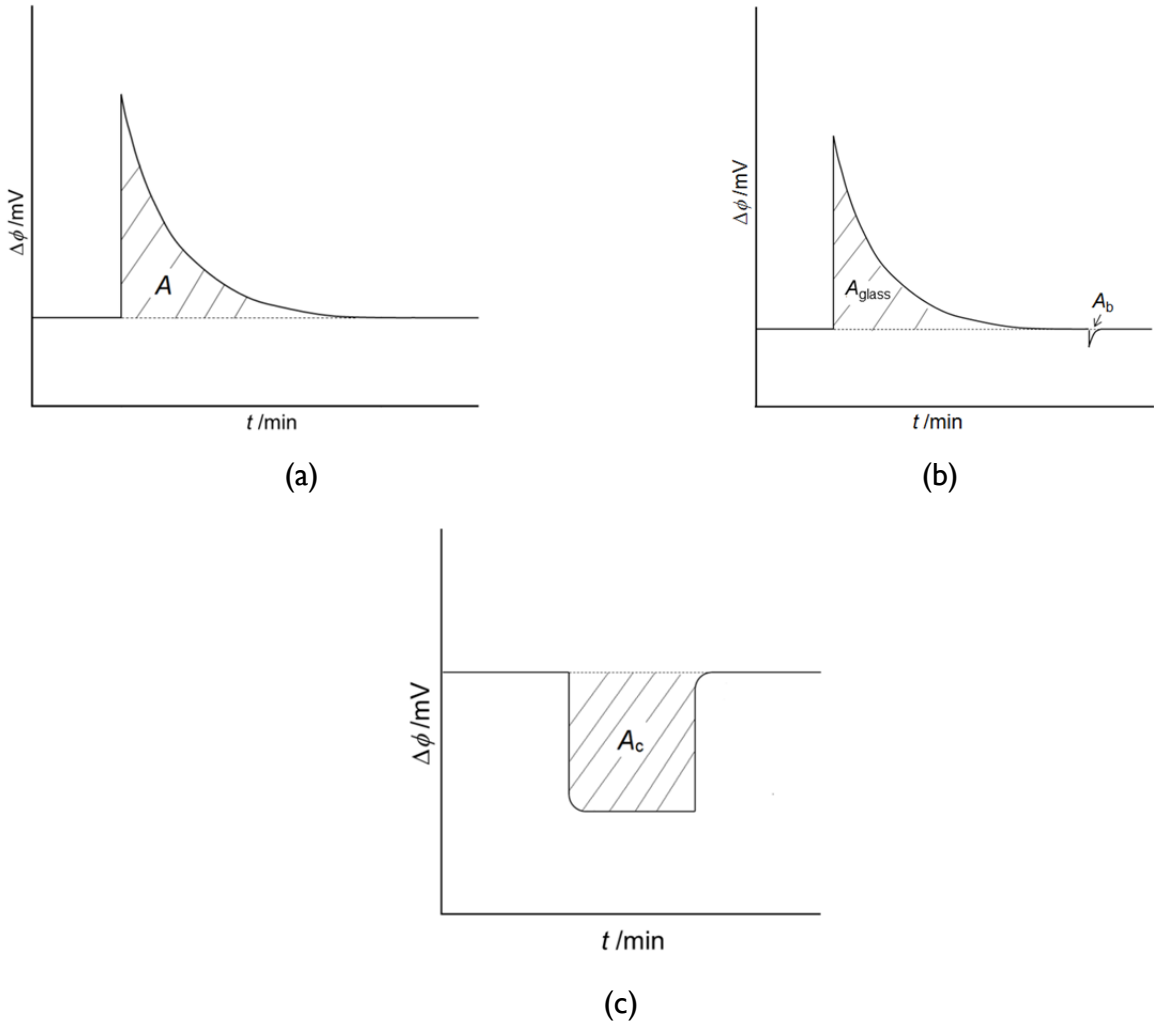

Figure 2.16 Measuring curves for (a) overall experiment; (b) determination of contribution from glass and cell evacuation and (c) calibration.

The area *A* of the measuring curve (Figure 2.16a) corresponding to the overall experiment has the contribution from the glass capillary and the sample. In the experiments carried out in vacuum, where the sample and reference cells were evacuated simultaneously

following the drop of capillary, the measuring curve area, *A*, also has the contribution from the evacuation process.

In order to determine the glass and vacuum contributions, a separate set of experiments were performed. Typically, an empty glass capillary was dropped into the calorimetric cell and following the baseline stabilization, the cells were subsequently evacuated to 0.13 Pa. The observed area A_{glass} and A_b corresponds to the contributions from glass and vacuum respectively (Figure 2.16b).

The area (A_{glass}) corresponding to measuring curve of glass was used to calculate the heat capacity of the glass which is given by equation:

$$C_p^{\circ}\left(\text{glass}\right) = \frac{A_{glass} / \varepsilon}{m_{glass}(T_f - T_i)} \tag{2.7}$$

where ε is the energy equivalent of calorimeter obtained from the set of electrical calibrations, m_{glass} is the mass of the glass capillary and T_i and T_f are the initial and final temperature of the process.

This heat capacity was then used to calculate the enthalpic contribution of the glass to the process and is given by equation

$$\Delta H_{glass} = m_{glass} C_p^{\circ}(\text{glass})(T_f - T_i) \tag{2.8}$$

The electrical calibration of the instrument was performed in a separate set of experiments where a known amount of heat was dissipated inside the cell by Joule effect. The

area (A_c) of the observed measuring curve (Figure 2.16c) was used to calculate ε through the equation

$$\varepsilon = \frac{A_c}{VIt} \tag{2.9}$$

where V and I are the voltage and intensity of the current applied to the Manganin wire resistance during the time period t.

The standard molar enthalpy of the calorimetric process $\Delta_r H_m^\circ$ was thus obtained from

$$\Delta_r H_m^\circ = \frac{M}{m}\left[\frac{A - A_b}{\varepsilon} - \Delta H_{glass}\right] \tag{2.10}$$

where m and M are the mass and molar mass of the sample respectively.

Calvet drop microcalorimetry was used in chapter 3 of this thesis to test the accuracy of heat capacity of nicotinic acid, measured by DSC. This test was based on determination of the enthalpy change associated with the cooling of the sample[19] from 357.9 K to 305.6 K.

This was also used in chapter 7, to measure the enthalpy change associated with the decomposition of 5HNA·H_2O and 5HNA·DMSO. For this purpose the sample and reference cells were simultaneously evacuated to 0.13 Pa following the drop of capillary containing sample, so that the solvent can be removed.

2.3 Equilibrium Solubility Studies

In equilibrium solubility studies the solubility of a solid in equilibrium with the solution is determined as a function of temperature. The solid (slurry) can be isolated and characterized for 'solution mediated transformations'[22] such as solvation and polymorphic transformations.

Instrumentation

The assembly used for equilibrium solubility studies in chapters 5 and 6 is described in Figure 2.17.

(a) (b)

Figure 2.17 (a) Assembly for equilibrium solubility studies: 1) a measurement unit; 2) thermostatic bath and (b) Schematic representation of a measurement unit; 3) jacketed glass cell; 4) suspension; 5) magnetic bar; 6) magnetic stirrer; 7) Pt100 sensor; 8) Agilent 34970A digital multimeter.

The assembly consists of a measurement unit, **1**, connected to a thermostatic bath, **2**. The measurement unit consists of a Schelnk tube like jacketed glass cell, **3**, holding the suspension, **4**, which is stirred by a magnetic bar, **5,** using a magnetic stirrer, **6**. The temperature of the suspension is monitored with a resolution of ± 0.01 K by a Pt100 sensor, **7**

and an Agilent 34970A digital multimeter, **8**. The Pt sensor has been previously calibrated against a reference platinum resistance thermometer, calibrated at an accredited facility in accordance to the International temperature Scale ITS-90. The temperature of the suspension was maintained constant within ±0.01 K by circulating water from the thermostatic bath through the cell jacket. The bath temperature was controlled by a Julabo MB unit and a Julabo FT200 immersion cooler. Depending on the experimental need more measurement units could be interconnected to perform experiments on different solvent-sample systems, simultaneously.

In a typical experiment, the excess amount of solid was allowed to equilibrate in a solvent for a period of one week. After the equilibration period, stirring was stopped and a sample of saturated solution (~ 3 cm^3) was extracted by a preheated syringe fitted with a Hamilton 7748-06 stainless steel needle. This aliquot was transferred to a previously weighed vial through a micro filter (Whatman Puradisc 25 TF, 0.2 µm PTFE membrane) adapted to syringe. The solubility of the solid in the solvent was analyzed by the 'solid residue method'[23] and the mole fraction of the solid in the saturated solution was calculated from

$$x_{\text{solid}} = \frac{M_{\text{solvent}}\left(m_3 - m_1\right)}{M_{\text{solvent}}\left(m_3 - m_1\right) + M_{\text{solid}}\left(m_2 - m_3\right)} \tag{2.11}$$

where m_1 is the mass of the empty vial, m_2 is the mass of the vial containing the solution aliquot, m_3 is the mass of the vial plus the solid residue left after evaporation of the solvent, and M_{solid} and M_{solvent} are the molar masses of solid and solvent, respectively. This was used to construct a solubility profile of the solid in one or more solvents where mole fraction solubility of solid in a solvent is plotted as a function of temperature. The solid phase in contact with solution can be analyzed for any possible solution mediated phase transformations (SMPTs). These transformations involve dissolution of metastable phase and subsequent precipitation of the thermodynamically most stable phase at the end of equilibration period.[24-25]

References

1. Jenkins, R.; de. Vries, J. L., *An Introduction to X-ray Powder Diffractometry*; Eindhoven, Holland.: Philips Gloeilampenfabrieken.
2. Pecharsky, V. K., *Fundamentals of Powder Diffraction and Structural Characterization of Materials*; Springer: New York, 2005.
3. Fultz, B.; Howe, J. M. *Transmission Electron Microscopy and Diffractometry of Materials*; Springer: Heidelberg, 2013.
4. Inoue, M.; Hirasawa, I. *J. Cryst. Growth* **2013**, *380,* 169-175.
5. Stuart, B., *Infrared Spectroscopy: Fundamentals and Applications.*, Wiley 2004.
6. Mitchell, M. B., *Fundamentals and Applications of Diffuse Reflectance Infrared Fourier Transform (DRIFT) Spectroscopy;* Advances in Chemistry; American Chemical Society: Washington DC, 2009; Vol. 236.
7. Bernardes, C. E. S.; Ilharco, L. M.; Minas da Piedade, M. E. *J. Mol. Struct.* **2014**, *1078,* 181-187.
8. Hemminger, W.; Sarge, S. M. In *Handbook of Thermal Analysis and Calorimetry: Principles and Practise*; Brown, M.E., Ed., Elsevier:Amsterdam, 1998 Vol. 1.
9. Haines, P. J., In *Principles of Thermal Analysis and Calorimetry*; Haine, P. J.; Ed.; RSC Paperbacks: Manchester, UK, 2002.
10. Thermogravimetric Analysis: A Beginner's Guide. Perkin Elmer: Waltham.
11. Coats, A. W.; Redfern, J. P. *Analyst* **1963**, *88,* 906-&.
12. Khawam, A.; Flanagan, D. R. *J. Pharm. Sci.* **2006**, *95,* 472-498.
13. Vitez, I. M.; Newman, A. W.; Davidovich, M.; Kiesnowski, C. *Thermochim. Acta* **1998**, *324,* 187-196.
14. Linkam LTS350 Temperature Controlled Stage User Guide. Linkam Scientific Instruments Ltd.:England
15. Zielenkiewicz, W.; Margas, E. *Theory of Calorimetry*; Kluwer Academic Publisher: Dordrecht, 2002.
16. Willson, R. J., In *Principles of Thermal Analysis and Calorimetry*; Haines, P. J.; Ed.; RSC Paperbacks: Manchester, UK, 2002.
17. Hatakeyama, T.: Liu, Z., *Handbook of Thermal Analysis*; John Wiley & Sons Ltd: England, 1998.
18. Martinho Simões, J. A.; Minas da Piedade, M. E. *Molecular Energetics, Condensed-Phase Thermochemical Techniques;* Oxford University Press: USA, 2008.
19. Bernardes, C. E. S.; Santos, L. M. N. B. F.; Minas da Piedade, M. E. *Meas. Sci. Technol.* **2006**, *17,* 1405-1408.
20. Kiyobayashi, T.; Minas da Piedade, M. E. *J. Chem. Thermodyn.* **2001**, *33,* 11-21.
21. Bernardes, C. E. S. *CBCAL*, FCUL: Lisbon, Portugal, 2008.
22. Brittain, H. G., *Polymorphism in Pharmaceutical Solids*, 2nd ed.; Informa Healthcare USA, Inc: New York, 2009.
23. Gonçalves, E. M.; Minas da Piedade, M. E. *J. Chem. Thermodyn.* **2012**, *47,* 362-371.
24. Cardew, P. T.; Davey, R. J. *P. Roy. Soc. Lond. A. Mat.* **1985**, *398,* 415-428.
25. Simões, R. G.; Bernardes, C. E. S.; Minas da Piedade, M. E. *Cryst. Growth. Des.* **2013**, *13,* 2803-2814.

Chapter 3

Heat Capacity and Thermodynamics of Solid and Liquid Pyridine-3-Carboxylic Acid (Nicotinic Acid) Over the Temperature Range 296 K to 531 K.

Abhinav Joseph, Carlos E. S. Bernardes, Manuel E. Minas da Piedade

Article published in:
J. Chem. Thermodyn., **2012,** *55*, 23-28
DOI: 10.1016/j.jct.2012.06.010

This chapter describes the heat capacity measurements of nicotinic acid in the temperature range 296 K to 531 K using differential scanning calorimetry. The obtained results were combined with other thermodynamic data (e.g. enthalpy of formation, entropy) to determine the $\Delta_f G_m^\circ$ vs. T phase diagram of the system in the temperature range studied. This diagram evidences the stability domains of the two polymorphic forms related by a reversible solid-solid phase transition occurring at 455 K

DSC studies and heat capacity measurements on nicotinic acid were performed by me. I also carried out the accuracy test to the DSC measurements by Calvet drop microcalorimetry. The quantum chemistry calculations mentioned in the text were performed in our laboratory by Dr. Carlos Bernardes. Finally, I contributed in the discussion of the results and the construction of the phase diagram.

After publication of our work,[1] Knyazev *et al.*[2] reported an adiabatic calorimetry study of the heat capacity of nicotinic acid in the temperature range 5 K to 346 K. These data were also included in the present chapter.

Abstract

The molar heat capacity of pyridine-3-carboxylic acid (nicotinic acid) for T = 296 – 531 K was investigated by differential scanning calorimetry (DSC) and Calvet-drop microcalorimetry. The measurements extended up to the liquid range and also covered the interval where a reversible and fast solid-solid (cr II $\rightarrow$ cr I) phase transition occurs. The molar enthalpies and entropies of that phase transition and of fusion were obtained as T_{trs} = 455.0±0.2 K, $\Delta_{trs}H^{\circ}_{m}$ = 0.90±0.10 kJ·mol^{-1}, $\Delta_{trs}S^{\circ}_{m}$ = 1.98±0.22 J·K^{-1}·mol^{-1}, T_{fus} = 509.91±0.04 K, $\Delta_{fus}H^{\circ}_{m}$ = 28.2±0.1 kJ·mol^{-1}, and $\Delta_{fus}S^{\circ}_{m}$ = 55.30±0.16 J·K^{-1}·mol^{-1}.

By combining these experimental results with the previously reported $\Delta_{sub}H_{m}$(NA, cr II) at T = 366.5 K, the corresponding entropy in the gaseous state calculated at the B3LYP/ 6-31+G(d,p) level of theory, and $\Delta_{f}H^{\circ}_{m}$(NA, cr II) at T = 298.15 K, it was possible to estimate the standard molar Gibbs energy of formation functions necessary for the construction of the $\Delta_{f}G^{\circ}_{m}$ vs. T diagram illustrating the enantiotropic nature of this system.

3.1 Introduction

Pyridine-3-carboxylic acid (Figure 3.1, CAS number [59-67-6]), generally known as nicotinic acid (NA), is a compound of considerable importance in terms of chemical, dietetic and therapeutic applications. It has for example been used in matrices for matrix-assisted laser desorption ionization (MALDI) mass spectrometry analyses of large polypeptides[3], as a reference material for combustion calorimetry[4-5], and particularly as an active pharmaceutical ingredient (API) in the treatment of hypercholesterolemia and atherosclerosis.[6-7] It has also long been recognized as a water-soluble vitamin (vitamin B_3 or niacin)[8-9] indispensable in the diet of humans and animals and, as such, widely used as additive in food, forage, and cosmetics.[10-11] Some recent estimates of the world demand for compounds of the nicotinic acid family point to 35,000 t to 40,000 t.[12-14]

In a series of previous publications we have reported on various aspects of the thermodynamics of nicotinic acid and some of its derivatives, namely (i) the relationship between structure and energetics of both the isolated molecules and anhydrous or hydrate forms of nicotinic acid, 2-, 4-, 5-, and 6-hydroxy nicotinic acids, and 5-chloro-6-hydroxynicotinic acid[15-17]; (ii) the concentration dependence of the enthalpy of solution of nicotinic acid in water[18]; (iii) the solubility of nicotinic acid in a series of solvents differing in polarity, polarizability and hydrogen-bonding ability[19]; (iv) the influence of temperature and ionic strength on the acidity constants of nicotinic acid in aqueous solution[20]; and (v) the determination of the

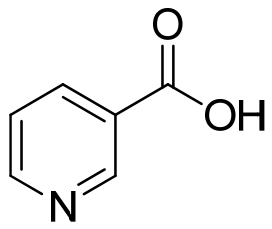

Figure 3.1 Molecular structure of pyridine-3-carboxylic acid (nicotinic acid, NA).

standard molar enthalpies of formation of the three nicotinic acid species involved in aqueous protonation/deprotonation equilibria at infinite dilution.[18]

The present study was motivated, in part, by the fact that the two previous reported measurements of the standard molar heat capacity of nicotinic acid at constant pressure ($C^{\circ}_{p,m}$) by adiabatic calorimetry, refer to the temperature interval 79 K to 400 K,[21-22] which does not cover the range where the compound undergoes a transition from a monoclinic phase (here designated as form II; $P2_1/c$, Z = 4, Z' = 1, a = 7.186 Å, b = 11.688 Å, c = 7.231 Å, β = 113.55°)[23-24] to a phase of unknown crystal structure (here designated as form I) and subsequently melts.[15, 21, 25-33] Moreover, those determinations show inconsistencies of over 10%, which are significantly larger than the 1% to 5% accuracy that can typically be achieved in routine DSC experiments, provided that an adequate methodology is followed.[34] The main objectives of this work were, therefore: (i) to obtain the heat capacity of nicotinic acid from T = 296 K up to the liquid range based on DSC and Calvet-drop microcalorimetry experiments; (ii) the thermodynamic study of the form II → form I solid-solid phase transition and of fusion; and (iii) the determination of the $\Delta_f G^{\circ}_m$ vs T phase diagram illustrating the stability domains of the solid and liquid nicotinic acid phases over the temperature range 296 K to 531 K, by combining the obtained $C^{\circ}_{p,m}$ results with the previously reported $\Delta_f H^{\circ}_m$ (NA, cr II) at 298.15 K[15] and entropy data for the ideal-gas state derived from statistical mechanics and density functional theory calculations.

3.2 Materials and Methods

3.2.1 Materials

The sample (NIST SRM 2151)[35] used in the experiments was the same as previously employed on the re-evaluation of the standard molar enthalpies of formation and sublimation of nicotinic acid at T = 298.15 K.[15] The compound had been characterized in terms of chemical purity, phase purity, and morphology by elemental analysis, diffuse reflectance infrared Fourier-transform (DRIFT) spectroscopy, ^{1}H- and ^{13}C-NMR, GC-MS, X-ray powder diffraction (XRPD), and scanning electron microscopy (SEM).[15] The chemical analyses showed no evidence of impurities (mass fraction > 0.999). No mixtures of phases were also detected by XRPD. The obtained powder pattern corresponded to the monoclinic phase (space group $P2_1/c$, with a = 7.181 Å, b = 11.679 Å, c = 7.233 Å, and β = 113.49°)[15] previously characterized by single crystal X-ray diffraction[23-24] which, as mentioned above, is designated here as crystal form II.

Table 3.1 Provenance and mass fraction purity of the materials used in this work.

Material	Supplier	Reference	Mass fraction purity
Pyridine-3-carboxylic acid	NIST	SRM 2151	>0.999[a]
Benzoic acid	NIST	SRM 39j	0.999996[b]
Sapphire (α-Al_2O_3 disks)	Perkin Elmer	0219-1483	0.9998[b]
Indium	Perkin Elmer	0319-0033	0.99999[b]
Tin	Goodfellow	SN006110	0.99995[b]
Lead	Goodfellow	PB006100	0.99995[b]
Zinc	Perkin Elmer	0319-0036	0.99999[b]

[a] Reference 15; [b]Given by the supplier.

The calibration of the temperature or heat flow scales of the DSC apparatus was performed by using benzoic acid (NIST SRM 39j; mass fraction 0.999996)[36], sapphire (Perkin Elmer; mass fraction 0.9998) , indium (Perkin Elmer; mass fraction 0.99999), tin (Goodfellow; mass fraction 0.99995), lead (Goodfellow; mass fraction 0.99995), and zinc (Perkin Elmer; mass fraction 0.99999). Table 3.1 summarizes relevant information on the provenance and mass fraction purity of all the materials used in this work.

3.2.2 Differential Scanning Calorimetry (DSC)

The DSC studies on nicotinic acid were carried out on a Perkin-Elmer DSC 7 apparatus. The samples with masses of ~5 mg were sealed in aluminum crucibles and weighed with a precision of ±0.1 μg on a Mettler XP2U ultra-micro balance. The experiments were performed in the approximate range 296 K to 531 K under a flow of nitrogen (Air Liquide N45) of 25 $cm^3 \cdot min^{-1}$. The heating rate was β = 2 $K \cdot min^{-1}$. The temperature scale of the apparatus was calibrated at the same heating rate based on the onsets of the fusion peaks of the benzoic acid (T_{fus} = 395.52 K)[37], indium (T_{fus} = 429.78 K), tin (T_{fus} = 505.08 K)[37], lead (T_{fus} = 600.61 K)[37], and zinc (T_{fus} = 692.65 K) samples indicated in Table 3.1.

The general procedure followed in the heat capacity measurements was as described elsewhere.[38-39] The complete temperature range of the determinations was divided into thirteen intervals of approximately 25 K, overlapping by 5 K. Within each interval, a blank run with the reference and sample cells loaded with two empty crucibles was initially performed. This was followed by a replicate run where one of the crucibles was filled with nicotinic acid.

The molar heat capacity of the sample at a given temperature, under the saturation pressure and approximately constant volume conditions $C_{s,m}(\mathrm{NA})$, was calculated from:

$$C_{s,m}(\mathrm{NA}) = k \frac{M_{\mathrm{NA}}}{m_{\mathrm{NA}} \beta} \Delta\phi \qquad (3.1)$$

where m_{NA} and M_{NA} are the mass and the molar mass of nicotinic acid, respectively, β is the heating rate, $\Delta\phi$ is the difference in heat flow rate between the main and blank runs obtained at a given temperature, and k is a calibration factor defined as:

$$k = \frac{C_{p,m}(\alpha - Al_2O_3)_{Ref}}{C_{p,m}(\alpha - Al_2O_3)_{obs}} \tag{3.2}$$

Here $C_{p,m}(\alpha\text{-}Al_2O_3)_{obs}$ represents the molar heat capacity of sapphire at a given temperature obtained in a run mimicking that for nicotinic acid and $C_{p,m}(\alpha\text{-}Al_2O_3)_{Ref}$ is the corresponding heat capacity of sapphire reported by Archer. [40]

An accuracy test carried out with benzoic acid within the temperature range 300 K to 352 K showed a maximum deviation between the $C^{\circ}_{p,m}$ results obtained in this work and those recommended by Furukawa *et al.*[41] of 2.8 %. Detailed results of this test and of the determination of k are given as Supporting Information.

3.2.3 Calvet-drop microcalorimetry

A further accuracy test to the DSC measurements was performed by determining the standard molar enthalpy change associated with the cooling of nicotinic acid form II from T_i = 357.9 K to T_f = 305.6 K, $\Delta^{305.6K}_{357.9K}H^{\circ}_m\left(\text{NA, cr II}\right)$ by Calvet-drop microcalorimetry. The apparatus and methodology have been previously described.[42] A sample with ~4.5 mg mass was sealed into a small glass capillary (Kontes; ~20 mm length, 1.5 mm OD, 0.94 mm ID) and weighed with a precision of ±0.1 μg on a Mettler XP2U ultra-micro balance. The sample was equilibrated for approximately one hour at T = 357.9 K inside the drop furnace and then dropped into the calorimetric cell kept at T = 305.6 K. The value of $\Delta^{305.6K}_{357.9K}H^{\circ}_m\left(\text{NA, cr II}\right)$ was calculated from:

$$\Delta_{357.9K}^{305.6K} H_m^o \left(\text{NA, cr II}\right) = \frac{M}{m}\left[\frac{A}{\varepsilon} - \Delta H_{glass}\right] \tag{3.3}$$

where m and M are the mass and molar mass of nicotinic acid, respectively, A is the area of the measuring curve, ε is the calibration constant, and ΔH_{glass} is the contribution of the glass tube to the total enthalpy change observed in the experiment. The value of ε = 63.922 ± 0.035 $mV \cdot W^{-1}$ was obtained from ten independent runs (the indicated uncertainty is the standard error of the mean) where a potential of V volts was applied to the Manganin resistance inside the measuring cell, causing a current of intensity I amperes to flow for t seconds. In this case:

$$\varepsilon = \frac{A_c}{VIt} \tag{3.4}$$

where A_c is the area of the measuring curve obtained in the calibration. The ΔH_{glass} term was calculated from:

$$\Delta H_{glass} = m_{glass} C_p^o \left(\text{glass}\right)\left(T_f - T_i\right) \tag{3.5}$$

where m_{glass} is the mass of the glass tube and $C_p^o\left(\text{glass}\right)$ is the corresponding average specific heat capacity in the temperature range of the experiments. Five independent runs where empty glass tubes with m_{glass} ~ 45 mg were dropped into the calorimetric cell under conditions

mimicking as much as possible those of the main experiments led to $C_p^\circ(\text{glass})$ = 0.858 ± 0.002 $J \cdot K^{-1} \cdot g^{-1}$, where the assigned uncertainty represents the standard error of the mean (see Supporting Information for details).

3.2.4 Computational details

Density functional theory (DFT)[43] was applied to obtain the vibration frequencies used in the statistical thermodynamics calculation of the standard molar entropy of gaseous nicotinic acid at T = 366.5 K. Full geometry optimization and frequency predictions were carried out with the B3LYP[44-45] hybrid functional using the 6-31+G(d,p)[46] basis set. The DFT calculations were performed with the Gaussian-03 package[47] and refer to the nicotinic acid conformation which was previously found to be more stable by a variety of levels of theory.[15] The statistical thermodynamics calculations[48] were made under the rigid rotor and harmonic oscillator approximations and using DFT vibration frequencies scaled by 0.964.[49]

3.3 Results and Discussions

All molar quantities were based on the molar mass of nicotinic acid M_{NA} = 123.1094 $g \cdot mol^{-1}$, which was calculated from the standard atomic masses recommended by the IUPAC Commission in 2007.[50]

3.3.1 Heat capacity

The results of the heat capacity measurements on nicotinic acid obtained in this work by DSC are listed in Table 3.2 and illustrated in Figure 3.2. Also shown in Figure 3.2 are the $C_{p,m}^\circ(\text{NA})$ values published by Wang *et al.*[21], Di *et al.*[22] and Knyazev *et al.*[2]

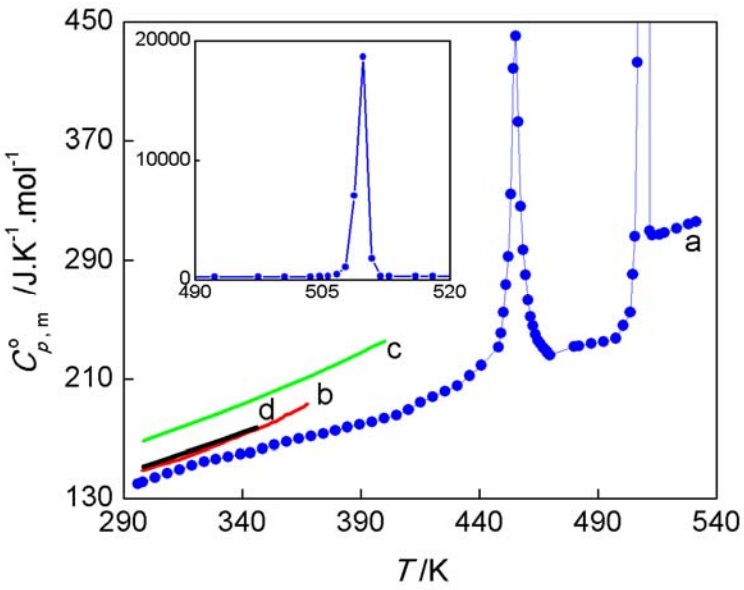

Figure 3.2 Comparison of the heat capacities of nicotinic acid obtained in this work for T = 296 to 531 K (curve a) with those previously reported by Wang *et al.*[21] (curve b), Di *et al.*[22] (curve c) and Knyazev *et al.*[2] (curve d). The fusion range is shown in the inset.

Each $C^{\circ}_{p,m}(\mathrm{NA})$ entry in Table 3.2 refers to the mean of five independent determinations and the assigned uncertainty is twice the standard error of the mean. The $C^{\circ}_{p,m}(\mathrm{NA})$ values were assumed identical to the corresponding $C_{s,m}(\mathrm{NA})$ data given by eq. 3.1. Indeed, the difference $C^{\circ}_{p,m}(\mathrm{NA}) - C_{s,m}(\mathrm{NA}) \sim T(\partial V_m / \partial T)_p (\partial p / \partial T)_{V_m}$ estimated for T = 290 to 400 K, varied in the range (6×10^{-11} to 1×10^{-5}) J·K^{-1}·mol^{-1} and was therefore well within the uncertainty of the determinations. This estimate was based on the published vapor pressures of form II nicotinic acid for T = 350 to 380 K[15] and on the variation of the corresponding unit cell volume with the temperature in the range 293 K to 403 K (see Supporting Information for details).

Two singularities can be noted in Figure 3.2: (i) a broad peak with a maximum at T_{max} = 455.3 K corresponding to the previously reported cr II → cr I phase transition[15, 21, 25-33] and (ii) a sharp peak due to fusion with a maximum located at T_{max} = 509.8 K. The apparent heat

Table 3.2 Standard molar heat capacities of nicotinic acid for T = 296.01 to 531.37 K.

T /K	$C^{\circ}_{p,m}$ /J·K^{-1}·mol^{-1}	T /K	$C^{\circ}_{p,m}$ /J·K^{-1}·mol^{-1}	T /K	$C^{\circ}_{p,m}$ /J·K^{-1}·mol^{-1}
296.01	139.9±5.7	420.35	198.0±3.9	468.66	227.8±5.4
298.06	141.2±5.5	425.49	201.7±3.9	469.69	226.1±3.6
303.20	144.2±4.9	430.63	205.3±3.4	479.97	231.6±5.9
308.34	147.0±4.6	435.77	212.1±7.4	482.03	232.2±5.1
313.48	149.4±4.6	440.91	219.1±6.5	487.17	233.6±3.7
318.62	152.3±2.0	448.1	231.3±8.8	492.31	235.1±4.0
323.76	154.8±4.2	449.13	240.6±6.2	497.45	237.2±4.5
328.90	156.5±4.7	450.16	254.7±5.5	500.53	245.9±6.7
334.04	158.2±5.2	451.19	273.6±8.5	503.62	254.7±10.1
339.18	159.8±5.9	452.22	292.5±12.6	504.65	280.5±25.5
343.24	160.4±6.0	453.24	334.7±19	505.67	306.3±41.3
348.38	163.3±6.1	454.27	418.6±18.7	506.70	422.7±125.1
353.52	165.9±3.2	455.3	440.3±6	507.73	1073.5±774.4
358.66	167.9±3.1	456.33	382.6±20.4	508.76	7052.2±5458.9
363.80	170.0±3.1	457.36	326.3±16.3	509.79	18653.4±7223.5
368.94	171.5±3.1	458.38	297.2±13.9	510.81	1773.6±6149.4
374.08	173.2±4.2	459.41	280.2±11.0	511.84	309.8±14.6
379.22	175.4±4.0	460.44	263.1±8.0	512.87	307.2±10.6
384.37	177.6±3.8	461.47	251.7±6.6	515.95	307.4±3.5
389.51	179.4±3.6	462.5	245.7±7.1	518.01	308.6±3.4
394.65	181.2±5.9	463.52	239.8±8.0	523.15	311.5±3.6
399.79	183.5±6.2	464.55	235.7±8.5	528.29	314.4±4.2
404.93	185.8±6.5	465.58	233.6±8.6	531.37	316.2±4.8
410.07	189.4±4.7	466.61	231.4±8.7		
415.21	194.3±3.9	467.64	229.5±7.7		

capacities obtained over the ranges of these phase transitions were also included Table 3.2 and in Figure 3.2. The data in Table 3.2 was fitted to polynomial equations of the type:

$$C^{\circ}_{p,m}/\mathrm{J\cdot K^{-1}\cdot mol^{-1}} = a + b(T/\mathrm{K}) + c(T/\mathrm{K})^2 + d(T/\mathrm{K})^3 + e(T/\mathrm{K})^4 \quad (3.6)$$

in different temperature intervals. The corresponding parameters, range of application and regression coefficients are summarized in Table 3.3. Also shown in Table 3.3 are the analogous values for C(graphite), H_2(g), N_2(g), and O_2(g) used in the calculation of the $\Delta_f G^{\circ}_m$ vs T phase diagram of nicotinic acid described in section 3.3.3. These were obtained by fitting eq. 3.6 to data retrieved from the JANAF tables.[51]

Table 3.3 Coefficients of eq. 3.6 for different species, temperature ranges of application (T range), and regression coefficients (R^2).

Species	a	$b\times10^3$	$c\times10^6$	$d\times10^9$	$e\times10^{10}$	T range/K	R^2
NA, cr II	−57.4472	866.867	−664.911			296 to 400	0.998
NA, cr I	81.2192	313.090				479 to 498	0.992
NA, l	13.9742	568.728				516 to 531	0.99997
C, graphite[a]	−4.02995	49.3147	−24.1565			250 to 600	0.99995
H_2, g[a]	14.8587	117.156	−360.535	493.855	−2.52356	250 to 600	0.99994
N_2, g[a]	29.5379	−2.83035	3.29280	5.02824		250 to 600	0.9990
O_2, g[a]	31.3350	–21.8534	63.8195	−42.1671		250 to 600	0.999998

[a]Based on data from reference 51, see text.

Where comparison is possible the $C^{\circ}_{p,m}(\mathrm{NA})$ values published by Wang *et al.*[21], Di *et al.*[22] and Knyazev *et al.*[2] (Figure 3.2) exhibit deviations of 5% to 11% (curve b) and 16% to 22% (curve c), and 6% to 8% (curve d) respectively, from those here reported. The published data by Wang *et al.* and Di *et al.* were obtained with two different versions of the same adiabatic calorimeter and the authors favour the higher values (curve c in Figure 3.2) which refer to the latest version of the apparatus.[22] Because the nature of the above mentioned deviations was impossible to assess Calvet drop microcalorimetry experiments were also carried out to test the accuracy of the DSC results. The experiments consisted in the direct measurement of the standard molar enthalpy change associated with the cooling of nicotinic acid form II from T = 357.8 K to T = 305.6 K (see Supporting Information for details). The mean of five independent determinations with the assigned uncertainty (twice the standard error of the mean) is compared in Table 3.4 with the corresponding DSC result obtained by integration of eq. 3.6 using the coefficients in Table 3.3. Also included in Table 3.4 are the $\Delta^{305.6\mathrm{K}}_{357.9\mathrm{K}}H^{\circ}_{\mathrm{m}}(\mathrm{NA,cr\ II})$ values computed from the heat capacity data reported by Wang *et al.* [21], Di *et al.* [22] and Knyazev *et al.*[2] (see Supporting Information for details). The results in Table 3.4 correspond to the mean $C^{\circ}_{p,m}(\mathrm{NA})$ values 157.9± 2.0 J·K^{-1}·mol^{-1} (Calvet-drop microcalorimetry), 156.8 J·K^{-1}·mol^{-1} (DSC), 168.2 J·K^{-1}·mol^{-1} (Wang *et al.*)[21], 188.4 J·K^{-1}·mol^{-1} (Di *et al.*)[22] and 169.5 J·K^{-1}·mol^{-1} (Knyazev *et al.*)[2] within the temperature interval 305.6 K to 357.8 K.

Table 3.4 Standard molar enthalpy change associated with the cooling of nicotinic form II from T = 357.8 to 305.6 K

Method	$-\Delta^{305.6\mathrm{K}}_{357.9\mathrm{K}}H^{\circ}_{\mathrm{m}}(\mathrm{NA,cr\ II})$ /J·mol^{-1}
Calvet-drop microcalorimetry[a]	8258±105
DSC[a]	8200
Adiabatic calorimetry[b]	8795
Adiabatic calorimetry[c]	9852
Adiabatic calorimetry[d]	8864

[a]This work, [b]Wang *et al.*, [c]Di *et al.*, [d]Knyazev *et al.*

The DSC and Calvet-drop microcalorimetry results obtained in this work are in good agreement within the uncertainty of the determinations and are closer to the result by Wang *et al.*[21] and Knyazev *et al.*[2]

3.3.2 Enthalpies, entropies and temperatures of phase transition

The two peaks observed in the heat capacity determinations, with maxima at temperatures 455.3 K and 509.8 K, respectively, were also detected in normal DSC scans carried out at a heating rate of 2 K·min^{-1} (Figure 3.3).

In this case the onset (T_{on}) and maximum (T_{max}) temperatures of the cr II → cr I transition peak were T_{on} = 452.8±0.3 K and T_{max} = 455.0±0.2 K, and the corresponding standard molar enthalpy change was $\Delta_{trs}H^{o}_{m}$ = 0.86±0.10 kJ·mol^{-1}. The transition was reversible and fast, being completed in ~150 s when heating or cooling the sample at β = 2 K·min^{-1}.

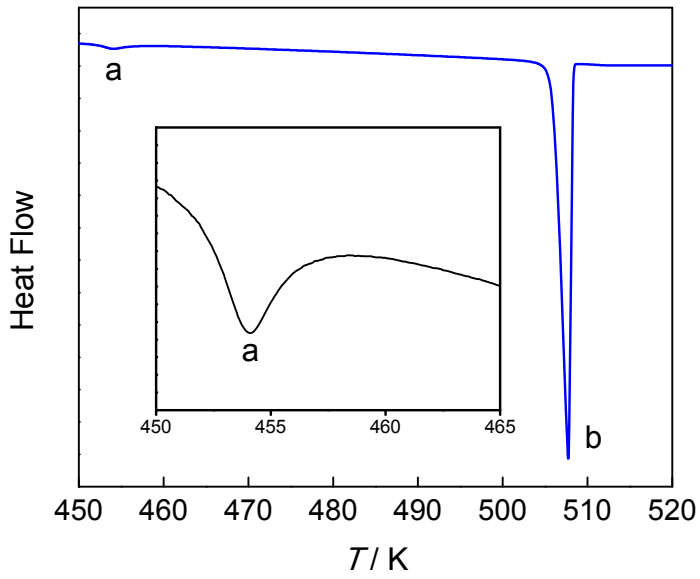

Figure 3.3 Typical differential scanning calorimetry measuring curve obtained for nicotinic acid in the range 450 K to 520 K, at a scan rate of 2 K·min^{-1}. Peak a corresponds to the cr II → cr I phase transition (see also inset) and peak b to fusion.

Although the T_{max} values observed on cooling (using the temperature calibration of the apparatus obtained on heating mode) were systematically ~ 1.5 K lower than those obtained in the heating, the corresponding $\Delta_{trs}H^{\circ}_{m}\left(\text{cr I} \rightarrow \text{cr II}\right)$ = -1.01±0.16 kJ·mol^{-1} is consistent with the above mentioned $\Delta_{trs}H^{\circ}_{m}\left(\text{cr II} \rightarrow \text{cr I}\right)$ = 0.86±0.10 kJ·mol^{-1} within the experimental error. For fusion T_{on} = 508.5±0.2 K, T_{max} =509.9±0.3 K, and $\Delta_{fus}H^{\circ}_{m}$ = 28.24±0.08 kJ·mol^{-1}. The uncertainties indicated for T_{on}, T_{max}, $\Delta_{trs}H^{\circ}_{m}$ and $\Delta_{fus}H^{\circ}_{m}$ correspond to twice the standard error of the mean of five determinations. As for the heat capacity, the differences between the experimentally determined enthalpies of phase transition under saturation conditions and the corresponding standard molar quantities were assumed to be negligible.

The above results are in reasonable agreement with those previously obtained for the same sample in DSC experiments carried out at a significantly higher heating rate (10 K·min^{-1}): for the $\text{cr II} \rightarrow \text{cr I}$ phase transition T_{on} = 452.9±0.5 K, T_{max} = 456.1±0.4 K, and $\Delta_{trs}H^{\circ}_{m}$ = 0.83±0.10 kJ·mol^{-1} and for fusion T_{on} = 507.3±1.4 K, T_{max} =509.9±0.9 K, and $\Delta_{fus}H^{\circ}_{m}$ = 27.8±0.2 kJ·mol^{-1}.[15]

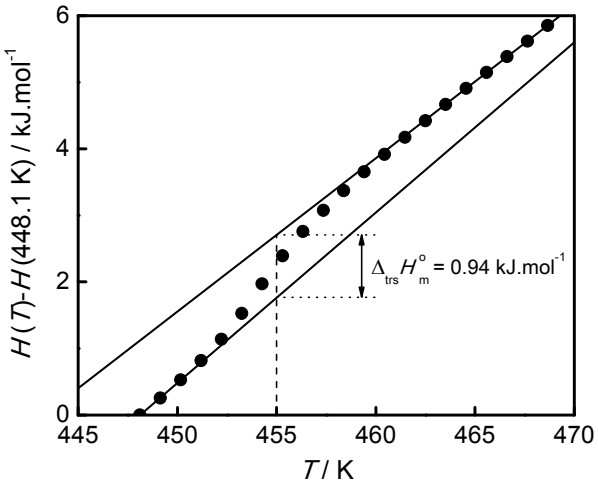

Figure 3.4 Enthalpy increments $H^{\circ}_{m}\left(T\right) - H^{\circ}_{m}\left(448.1\,\text{K}\right)$, in the range of the $\text{cr II} \rightarrow \text{cr I}$ phase transition.

Furthermore, integration of the heat capacity data in Table 3.2 over the cr II $\rightarrow$ cr I phase transition region led to the results in Figure 3.4, from which $\Delta_{trs}H^{\circ}_{m}$ = 0.94 kJ·mol^{-1} can be derived for T_{max} = 455.0 K. The agreement between this value and the above $\Delta_{trs}H^{\circ}_{m}$ = 0.86±0.10 kJ·mol^{-1} independently determined from normal DSC scans suggests good internal consistency for the results reported here. The mean of both results $\Delta_{trs}H^{\circ}_{m}$ = 0.90±0.10 kJ·mol^{-1} was selected in this work.

The temperature of fusion of nicotinic acid was also obtained by the method of fractional melting [52], which is based on a linear least squares fit of the equation:

$$T_j = T_{fus} - \frac{m}{F_j} \qquad (3.7)$$

to the DSC results. Here, $F_j = \left(A_j + c\right) / \left(A_{tot} + c\right)$ is the fraction melted up to a temperature T_j in the range limited by the initial, T_i, and maximum, T_{max}, temperatures of the fusion peak, A_j is the corresponding fraction of the total peak area, A_{tot}, and c is a linearization constant. The slope of eq. 3.7 is $m = RT^2_{fus}x_B / \Delta_{fus}H^{\circ}_{m}$ where R = 8.314472 J·K^{-1}·mol^{-1} is the gas constant, x_B is the mole fraction of impurities, and $\Delta_{fus}H^{\circ}_{m}$ = 28.24±0.08 kJ·mol^{-1} is the enthalpy of fusion of nicotinic acid at T_{fus}. The analysis of five independent DSC fusion peaks led to T_{fus} = 509.91±0.04 K and to a mole fraction purity of nicotinic acid x_{NA} = 0.997±0.020 (see Supporting Information for details). The T_{fus} value obtained by the method of fractional melting is in very good agreement to the above mentioned T_{max} = 509.9±0.9 K corresponding to the maximum of the DSC fusion peak.

As previously noted the temperatures and enthalpies of the cr II → cr I phase transition and, particularly, of fusion, reported for nicotinic acid vary within reasonable wide ranges, namely T_{trs} ~ (451 to 458) K,[21, 25, 29, 31-32] $\Delta_{trs}H^{\circ}_{m}$ ~ (0.6 to 0.8) kJ·mol^{-1}, [21, 25] T_{fus} ~ (507 to 516) K,[21, 25-32] and $\Delta_{fus}H^{\circ}_{m}$ ~ (12 to 30) kJ·mol^{-1}. [21, 25-26, 30, 33] Evidence from DSC and differential thermal analysis (DTA) studies suggested that this is probably due to changes in the crystallinity and particle size of the sample.[15, 25, 33] The fact that the T_{trs}, $\Delta_{trs}H^{\circ}_{m}$, T_{fus}, and $\Delta_{fus}H^{\circ}_{m}$ obtained in the present work are amongst the highest published indicates the sample to be significantly crystalline, in agreement with previous X-ray powder diffraction, SEM, and low temperature DSC results.[15]

The temperatures and enthalpies of the cr II → cr I phase transition and fusion recommended in this work are summarized in Table 3.5 along with the corresponding entropies calculated as $\Delta_{trs}S^{\circ}_{m} = \Delta_{trs}H^{\circ}_{m} / T_{trs}$ and $\Delta_{fus}S^{\circ}_{m} = \Delta_{fus}H^{\circ}_{m} / T_{fus}$, respectively.

Table 3.5 Temperatures and standard molar enthalpies and entropies of solid-solid phase transition and fusion for nicotinic acid.

cr II → cr I		Fusion (cr I → l)	
T_{trs}/K	455.0±0.2	T_{fus}/K	509.91±0.04
$\Delta_{trs}H^{\circ}_{m}$/kJ·mol^{-1}	0.90±0.10	$\Delta_{fus}H^{\circ}_{m}$/kJ·mol^{-1}	28.2±0.1
$\Delta_{trs}S^{\circ}_{m}$/J·K^{-1}·mol^{-1}	1.98±0.22	$\Delta_{fus}S^{\circ}_{m}$/J·K^{-1}·mol^{-1}	55.38±0.16

3.3.3 Standard molar thermodynamic functions of formation of solid and liquid nicotinic acid and the $\Delta_f G_m^\circ$ vs *T* phase diagram.

The standard molar Gibbs energy of formation functions necessary for the construction of the $\Delta_f G_m^\circ$ vs. *T* diagram illustrated in Figure 3.5 were obtained from:

$$\Delta_f G_m^\circ = \Delta_f H_m^\circ - TS_m^\circ \qquad (3.8)$$

using the corresponding enthalpy and entropy contributions.

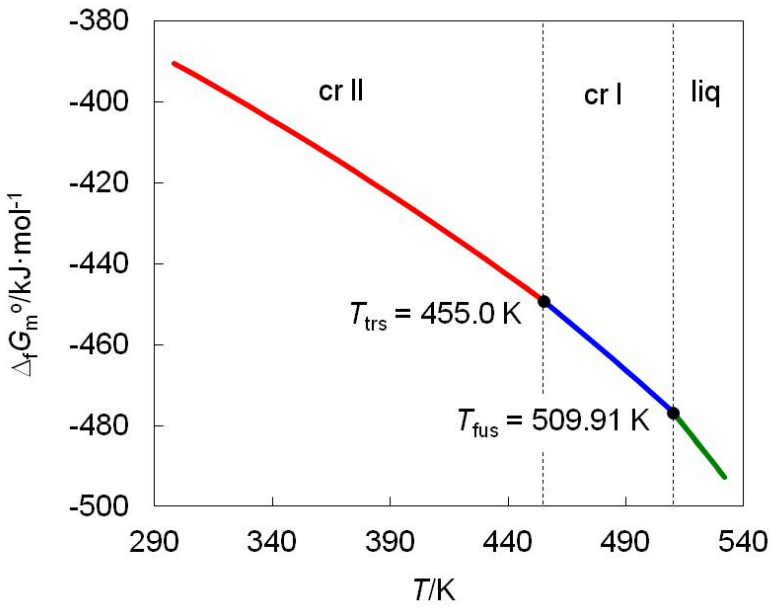

Figure 3.5 $\Delta_f G_m^\circ$-*T* diagram for the solid and liquid phases of nicotinic acid in the range 296 K to 531 K.

The enthalpies of formation of solid (forms II and I) and liquid nicotinic acid at different temperatures were calculated from:

$$\Delta_f H^\circ_m\left(\text{cr II}, T\right) = \Delta_f H^\circ_m\left(\text{cr II}, 298.15\ \text{K}\right) + \int_{298.15\text{K}}^{T} \Delta_f C^\circ_{p,m}\left(\text{cr II}\right) dT \qquad (3.9)$$

$$\Delta_f H^\circ_m\left(\text{cr I}, T\right) = \Delta_f H^\circ_m\left(\text{cr II}, T_{trs}\right) + \Delta_{trs} H^\circ_m\left(T_{trs}\right) + \int_{455.0\ \text{K}}^{T} \Delta_f C^\circ_{p,m}\left(\text{cr I}\right) dT \qquad (3.10)$$

$$\Delta_f H^\circ_m\left(\text{l}, T\right) = \Delta_f H^\circ_m\left(\text{cr I}, T_{fus}\right) + \Delta_{fus} H^\circ_m\left(\text{cr I}, T_{fus}\right) + \int_{509.91\ \text{K}}^{T} \Delta_f C^\circ_{p,m}\left(\text{l}\right) dT \qquad (3.11)$$

where $\Delta_f H^\circ_m\left(\text{cr II}, 298.15\ \text{K}\right)$ = –344.7±1.2 kJ·mol^{-1} [15] is the enthalpy of formation of the low temperature phase (cr II) of nicotinic acid at T = 298.15 K; T_{trs} = 455.0 K and T_{fus} = 509.91 K are the temperatures of the cr II → cr I phase transition and of fusion, respectively; and $\Delta_f C^\circ_{p,m}\left(\text{cr II}\right)$, $\Delta_f C^\circ_{p,m}\left(\text{cr I}\right)$ and $\Delta_f C^\circ_{p,m}\left(\text{l}\right)$ are the heat capacity changes associated with the formation of solid and liquid nicotinic acid from C(graphite), H_2(g), N_2(g), and O_2(g), respectively. These $\Delta_f C^\circ_{p,m}$ terms were calculated from eq. 3.6 using the data in Table 3.3.

The corresponding entropy contributions were derived from:

$$S^\circ_m\left(\text{cr II}, T\right) = S^\circ_m\left(\text{cr II}, T_m\right) + \int_{T_m}^{T} \frac{C^\circ_{p,m}\left(\text{cr II}\right)}{T} dT \qquad (3.12)$$

$$S_m^\circ\left(\text{cr I}, T\right) = S_m^\circ\left(\text{cr II}, T_{fus}\right) + \frac{\Delta_{trs}H_m^\circ\left(T_{trs}\right)}{T_{trs}} + \int_{T_{trs}}^{T} \frac{C_{p,m}^\circ\left(\text{cr I}\right)}{T} dT \quad (3.13)$$

$$S_m^\circ\left(\text{l}, T\right) = S_m^\circ\left(\text{cr I}, T_{fus}\right) + \frac{\Delta_{fus}H_m^\circ\left(T_{fus}\right)}{T_{fus}} + \int_{T_{fus}}^{T} \frac{C_{p,m}^\circ\left(\text{l}\right)}{T} dT \quad (3.14)$$

The term $S_m^\circ\left(\text{cr II}, T_m\right)$ in equation (3.12) is given by:

$$S_m^\circ\left(\text{cr II}, T\right) = S_m^\circ\left(g, T_m\right) - R\ln\frac{p_{sat}}{p^\circ} - \frac{\Delta_{sub}H_m\left(T_m\right)}{T_m} \quad (3.15)$$

where p_{sat} = 0.599 Pa is the saturation pressure of form II nicotinic acid at the reference temperature T_m = 366.5 K and $\Delta_{sub}H_m\left(T_m\right)$ = 109.2±2.3 kJ·mol^{-1} is the corresponding enthalpy of sublimation[15]. The selected $\Delta_{sub}H_m\left(T_m\right)$ value represents the weighted mean of three previously reported Knudsen effusion determinations and T_m is the average of the highest and lowest temperatures of the range covered in those experiments[15]. The value of p_{sat} corresponds to the average of the three saturation pressures at T_m obtained in those experiments. The calculation of $S_m^\circ\left(\text{cr II}, T_m\right)$ in eq. 3.15 and, hence, of all other entropy data, is anchored in $S_m^\circ\left(g, T_m\right)$ = 185.7888 J·K^{-1}·mol^{-1}. This value was obtained from statistical thermodynamics calculations[48], using structural and vibration frequency data predicted at the B3LYP/6-31G+(d,p) level of theory. The rigid rotor harmonic-oscillator-ideal gas model was assumed and the vibration frequencies were scaled by 0.964.[49]

3.4 Conclusion

Figure 3.5 highlights the enantiotropic nature of the nicotinic acid solid phases (i.e., there is transition temperature before fusion at which the stability order is reversed). As shown in Table 3.5 the cr II → cr I phase transition, which occurs at 455.0 K, is characterized by a small entropy change, $\Delta_{trs}S^{\circ}_{m}$ = 1.98±0.22 J·mol^{-1}·K^{-1}. The T_{max} value during cooling was found to be ~ 1.5 K lower than during heating. Since the transition is reversible and fast and occurs with a small undercooling, the kinetic barrier associated with this phase transition will be low. The structural features of this phase transition have yet to be determined. Indeed as mentioned above, although the structure of the lower temperature monoclinic cr II phase has been solved from single crystal X-ray diffraction results[23-24] the same is not true for the post-transitional cr I phase.

Supporting Information

1. Differential Scanning Calorimetry

Calibration. The molar heat capacity at a given temperature, under approximately constant volume and saturation pressure conditions, $C_{s,m}$, was calculated from:

$$C_{s,m} = k\frac{M}{m\beta}\Delta\phi \qquad \text{(S1)}$$

where m and M are the mass and the molar mass of the compound under study, respectively, β is the heating rate, $\Delta\phi$ is the difference in heat flow rate between the main and blank runs obtained at a given temperature, and k is a calibration factor defined as:

$$k = \frac{C_{p,m}(\alpha\text{-}Al_2O_3)_{Ref}}{C_{p,m}(\alpha\text{-}Al_2O_3)_{obs}} \qquad \text{(S2)}$$

Here $C_{p,m}(\alpha\text{-}Al_2O_3)_{obs}$ represents the molar heat capacity of sapphire obtained in a run mimicking that for the sample and $C_{p,m}(\alpha\text{-}Al_2O_3)_{Ref}$ is the heat capacity of sapphire used as reference. The values of $C_{p,m}(\alpha\text{-}Al_2O_3)_{obs}$ were calculated from:

$$C_{p,m}(\alpha\text{-}Al_2O_3)_{obs}/J\cdot K^{-1}\cdot mol^{-1} = -3.118942\times10^{-5}(T/K)^3 + 3.124643\times10^{-2}(T/K)^2 - 10.15507(T/K) + 1157.219 \quad (S3)$$

$$C_{p,m}(\alpha\text{-}Al_2O_3)_{obs}/J\cdot K^{-1}\cdot mol^{-1} = 4.281486\times10^{-7}(T/K)^3 - 1.020822\times10^{-3}(T/K)^2 + 7.705403\times10^{-1}(T/K) - 71.57305 \quad (S4)$$

for T = 296 to 343 K and T = 343 to 531 K, respectively. Equation S3 and S4 were obtained through a least squares fitting to the experimental data in Table S1, which represents the mean of three independent measurements. The assigned uncertainties are twice the standard deviation of the mean. The values of $C_{p,m}(\alpha\text{-}Al_2O_3)_{Ref}$ were calculated from:

$$C_{p,m}(\alpha\text{-}Al_2O_3)_{Ref}/J\cdot K^{-1}\cdot mol^{-1} = 6.602810\times10^{-7}(T/K)^3 - 1.131424\times10^{-3}(T/K)^2 + 7.150036\times10^{-1}(T/K) - 51.06011 \quad (S5)$$

derived from a least squares fit to the data reported by Archer for T = 280 to 540 K.[40] Equations S3 and S4 show regression coefficients R^2 = 0.9995 and R^2 = 0.991, respectively, for 95% probability, and reproduce the values in Table S1 with a maximum deviation of 1.6 $J\cdot K^{-1}\cdot mol^{-1}$. Equation S5 has R^2 = 0.999993, and reproduces the experimental values given by Archer[40] with a maximum deviation of 0.05 $J\cdot K^{-1}\cdot mol^{-1}$.

Table S1 Heat capacity of sapphire experimentally determined by DSC at different temperatures using the heating rate, β = 2 K·min^{-1}.

T/K	$C_{p,m}$ (α–Al_2O_3)$_{obs}$/ J·K^{-1}·mol^{-1}	T/K	$C_{p,m}$ (α–Al_2O_3)$_{obs}$ / J·K^{-1}·mol^{-1}	T/K	$C_{p,m}$ (α–Al_2O_3)$_{obs}$ / J·K^{-1}·mol^{-1}
296.01	80.04±6.61	374.08	96.96±2.90	456.33	108.96±2.55
298.06	80.48±6.27	379.22	97.81±2.86	461.47	109.54±2.55
303.20	81.47±5.51	384.37	98.59±2.74	466.61	110.05±2.55
308.34	82.45±4.73	389.51	98.95±3.28	471.75	109.06±2.55
313.48	83.47±4.08	394.65	99.34±3.98	476.89	109.71±5.40
318.62	84.71±3.37	399.79	100.16±3.87	482.03	110.58±4.36
323.76	86.29±6.27	404.93	101.04±3.90	487.17	111.75±1.96
328.90	87.69±4.55	410.07	102.30±1.29	492.31	112.56±0.73
334.04	89.08±3.06	415.21	103.35±2.43	497.45	110.52±0.70
339.18	90.47±2.27	420.35	104.03±2.93	502.59	111.27±0.85
342.27	91.32±2.46	425.49	104.68±3.35	507.73	111.981.12±
348.38	91.08±4.53	430.63	104.70±2.32	512.87	112.67±1.34
353.52	92.03±4.65	435.77	104.41±2.47	518.01	113.62±0.24
358.66	92.92±4.73	440.91	104.82±2.31	523.15	113.72±0.12
363.80	93.87±4.87	447.08	107.98±2.45	528.29	113.86±0.23
368.94	95.49±3.89	451.19	108.42±2.55	531.37	113.92±0.31

Finally, the temperature dependency of k obtained from equations S2 – S5 is given by the equations:

$$k = 4.16667\times10^{-7}\,(T/\mathrm{K})^3 - 4.19214\times10^{-4}\,(T/\mathrm{K})^2 + 0.139574(T/\mathrm{K}) - 14.4092 \quad \text{(S6)}$$

$$k = -3.36712\times10^{-10}\,(T/\mathrm{K})^3 + 2.24856\times10^{-6}\,(T/\mathrm{K})^2 - 1.89241\times10^{-3}\,(T/\mathrm{K}) + 1.37370 \quad \text{(S7)}$$

which are valid for T = 293 to 343 K and T = 343 to 531 K, respectively.

Heat capacity of benzoic acid. The accuracy of the heat capacity measurements was tested for benzoic acid (BA) in the temperature range 300 K to 351 K. The obtained results are compared in Table S2 with those calculated from[42]:

$$C^{\circ}_{p,\mathrm{m}}(\mathrm{BA})_{\mathrm{ref}} = -1.24935\times10^{-6}(T/\mathrm{K})^3 + 1.20038\times10^{-3}(T/\mathrm{K})^2 + 8.13151\times10^{-2}(T/\mathrm{K}) + 48.9495 \quad \text{(S8)}$$

which was derived from a least squares fit to the data recommended by Furukawa *et al.*[41] for T = 273 to 350 K. The uncertainties quoted for the DSC results in Table S2 represent twice the standard deviation of the mean of five independent determinations. Figure S1 shows the deviations between the observed and recommended values in Table S2. Table S2 and Figure S1 indicate that the DSC results agree with recommended values within the experimental uncertainty and that the maximum deviation is 2.8%.

Table S2 Comparison of the heat capacity of benzoic acid obtained in this work (β = 2 K·min^{-1}) by DSC, $C^{\circ}_{p,m}(BA)_{obs}$, and given by equation (S8).

T/K	$C^{\circ}_{p,m}(BA)_{obs}$ / J·K^{-1}·mol^{-1}	$C^{\circ}_{p,m}(BA)_{ref}$ /J·K^{-1}·mol^{-1} [a]	Δ% [b]
300.99	150.9±5.3	148.1	1.9
306.13	153.3±4.5	150.5	1.9
311.27	155.4±4.1	152.9	1.6
316.41	157.3±3.6	155.3	1.3
321.55	158.9±3.5	157.7	0.8
326.69	160.3±3.5	160.1	0.1
331.83	161.7±3.8	162.5	0.5
336.97	163.0±4.3	164.9	1.1
342.11	164.3±4.9	167.2	1.7
347.25	165.6±5.5	169.6	2.4
352.39	167.1±6.2	172.0	2.8

[a] Reference 41 see text; $\Delta\% = 100 \times \left[C^{\circ}_{p,m}(BA)_{obs} - C^{\circ}_{p,m}(BA)_{ref} \right] / C^{\circ}_{p,m}(BA)_{obs}$

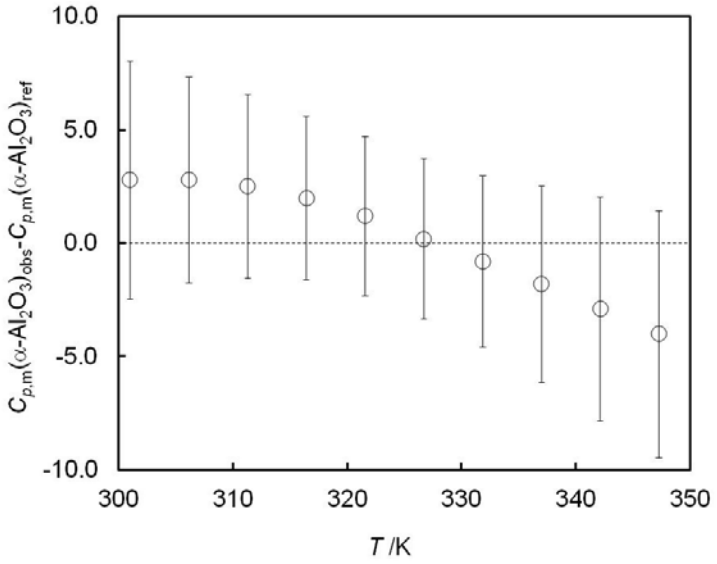

Figure S1 Differences between the heat capacity of benzoic acid obtained in this work by DSC, $C^{\circ}_{p,m}(\mathrm{BA})_{obs}$, and given by eq S8.

Calculation of $C_{p,m}(\mathrm{NA}) - C_{s,m}(\mathrm{NA}) \sim T(\partial V_m / \partial T)_p (\partial p / \partial T)_{V_m}$. The molar volumes of form II nicotinic acid (monoclinic, $P2_1/c$, $Z = 4$) calculated at different temperatures from the corresponding unit cell parameters retrieved from the literature[23] or obtained in this work from powder X-ray diffraction experiments are given in Table S3. A linear least squares regression to the data in that table led to:

$$V_m/\mathrm{m^3 \cdot mol^{-1}} = (2.66 \pm 0.77) \times 10^{-8} T + (7.63 \pm 0.26) \times 10^{-5} \qquad \text{(S9)}$$

from which $(\partial V_m / \partial T)_p = 2.66 \times 10^{-8}\ \mathrm{m^3 \cdot K^{-1} \cdot mol^{-1}}$ can be derived.

The vapor pressures of form II nicotinic acid for $T = 350$ to 380 K[15] are given by[15]:

$$\ln (p/\mathrm{Pa}) = -\frac{13143.5}{(T/\mathrm{K})} + 35.35 \qquad \text{(S10)}$$

From this equation it is possible to conclude that:

$$\left(\frac{\partial p}{\partial T}\right)_{V_m} = 13152.4\,\frac{p}{T^2} \qquad \text{(S11)}$$

The values of $C^{\circ}_{p,m}(\mathrm{NA}) - C_{s,m}(\mathrm{NA})$ obtained by combining $(\partial V_m / \partial T)_p$ = 2.66×10^{-8} m^3·K^{-1}·mol^{-1} mentioned above with the $(\partial p / \partial T)_{V_m}$ values calculated from eq. S11 are summarized in Table S4.

Table S3 Unit cell parameters (*a*, *b*, *c*, β) and molar volumes of form II nicotinic acid (monoclinic, $P2_1/c$, Z = 4) in the range 293 K to 403 K.

T/K	*a*/Å	*b*/ Å	*c*/ Å	β/°	V_m×10^5/m^3·mol^{-1}
293	7.186	11.688	7.231	113.55	8.38[a]
303	7.173	11.760	7.273	112.97	8.50[b]
353	7.193	11.713	7.281	112.94	8.51[b]
403	7.257	11.840	7.356	113.46	8.73[b]

[a] Reference 23. [b] This work.

Table S4 Estimated values of $C_{p,m}(NA) - C_{s,m}(NA)$

T/K	$(\partial p / \partial T)_{V_m}$ /Pa·K^{-1}	$C_{p,m}(NA) - C_{s,m}(NA)$ /J·K^{-1}·mol^{-1} [a]
290	7.29×10^{-6}	5.63×10^{-11}
298.15	2.38×10^{-5}	1.89×10^{-10}
300	3.09×10^{-5}	2.47×10^{-10}
305	6.13×10^{-5}	4.97×10^{-10}
310	1.19×10^{-4}	9.81×10^{-10}
315	2.26×10^{-4}	1.89×10^{-9}
320	4.20×10^{-4}	3.57×10^{-9}
325	7.65×10^{-4}	6.62×10^{-9}
330	1.37×10^{-3}	1.20×10^{-8}
335	2.41×10^{-3}	2.15×10^{-8}
340	4.16×10^{-3}	3.77×10^{-8}
345	7.08×10^{-3}	6.50×10^{-8}
350	1.19×10^{-2}	1.10×10^{-7}
355	1.96×10^{-2}	1.85×10^{-7}
360	3.18×10^{-2}	3.05×10^{-7}
365	5.10×10^{-2}	4.96×10^{-7}
370	8.08×10^{-2}	7.96×10^{-7}
375	1.26×10^{-1}	1.26×10^{-6}
380	1.95×10^{-1}	$1.97\cdot10^{-6}$
385	2.98×10^{-1}	3.05×10^{-6}
390	4.49×10^{-1}	4.67×10^{-6}
395	6.71×10^{-1}	7.06×10^{-6}
400	9.92×10^{-1}	1.06×10^{-5}

Fusion temperature and purity. The fusion temperature of form I nicotinic acid, T_{fus}, was obtained by the method of fractional melting[52], which is based on a linear least squares fit of the equation:

$$T_j = T_{fus} - \frac{m}{F_j} \qquad \text{(S12)}$$

to the DSC results in Table S5. Here, $F_j = (A_j + c)/(A_{tot} + c)$ is the fraction melted up to a temperature T_j in the range limited by the initial, T_i, and maximum, T_{max}, temperatures of the fusion peak, A_j is the corresponding fraction of the total peak area, A_{tot}, and c is a linearization constant. The slope of eq. S12 is $m = RT_{fus}^2 x_B / \Delta_{fus}H_m^\circ$ where R = 8.314472 J·K^{-1}·mol^{-1} is the gas constant, x_B is the mole fraction of impurities, and $\Delta_{fus}H_m^\circ$ = 28.24±0.08 kJ·mol^{-1} is the enthalpy of fusion of nicotinic acid at T_{fus}. The results given in Table S6 indicate that the sample used in the experiments has a temperature of fusion T_{fus} = 509.91±0.04 K of and a molar fraction purity of 0.997±0.018. This last value is compatible with the mass fraction purity (> 0.999) given in Table 3.1 of the main text.

Table S5 Temperatures and melting fractions used in the calculation of the fusion temperature and mole fraction purity of nicotinic acid.

F_j	T_j/K				
	Run 1	Run 2	Run 3	Run 4	Run 5
0.01	507.31	506.77	507.01	507.21	507.25
0.10	508.51	508.38	508.67	508.90	508.86
0.20	508.86	508.76	508.99	509.32	509.24
0.30	509.09	509.00	509.22	509.60	509.49
0.40	509.27	509.19	509.38	509.82	509.68
0.50	509.43	509.34	509.53	510.00	509.85
A_{tot}	228.1660	229.2064	230.5474	229.3725	229.4416

Table S6 Parameters of eq. S12, temperatures of fusion and mole fraction purities of nicotinic acid obtained from the data in Table S5.

Run	c	$-m$/K	T_{fus}/K	x_B	R^2
1	22.3897	0.2399±0.0079	509.80±0.04	0.003±0.053	0.996
2	16.0518	0.2124±0.0063	509.67±0.04	0.003±0.042	0.997
3	13.1864	0.1725±0.0055	509.78±0.04	0.002±0.037	0.996
4	17.8735	0.2540±0.0083	510.39±0.05	0.003±0.055	0.996
5	16.4189	0.2183±0.0071	510.18±0.05	0.003±0.047	0.996

$\langle T_{fus} \rangle$ = 509.91±0.02 K; $\langle x_B \rangle$ = 0.003±0.020

2. Calvet-drop microcalorimetry

The standard molar enthalpy changes associated with the cooling of nicotinic acid form II from T_i = 357.8 K to T_f = 305.6 K, $\Delta_{357.8\,K}^{305.6\,K}H_m^o(\text{NA, crII})$, determined by Calvet-drop microcalorimetry were calculated from:

$$\Delta_{357.8\,K}^{305.6\,K}H_m^o(\text{NA, crII}) = \frac{M}{m}\left[\frac{A}{\varepsilon} - \Delta H_{glass}\right] \quad \text{(S13)}$$

where m and M are the mass of and molar mass of nicotinic acid, respectively; A is the area of the measuring curve; ε = 63.922±0.035 mV·W^{-1} is the calibration constant obtained from a series of ten independent runs (the assigned uncertainty is the standard error of the mean); and ΔH_{glass} is the contribution of the glass tube to the total enthalpy change, ΔH_{tot}, observed in the experiment. The term ΔH_{glass} was calculated from:

$$\Delta H_{glass} = m_{glass}\, c_p^o(\text{glass})\,(T_f - T_i) \quad \text{(S14)}$$

where m_{glass} is the mass of the glass tube and $c_p^o(\text{glass})$ is the corresponding average specific heat capacity in the temperature range of the experiments. The value of $c_p^o(\text{glass})$ was obtained as:

$$c_p^o(\text{glass}) = \frac{\Delta_{T_i}^{T_f}H(\text{glass})}{m_{glass}(T_f - T_i)} \quad \text{(S15)}$$

from a series of drop runs where empty glass capillaries were dropped into the calorimetric cell under conditions mimicking as much as possible those of the main experiments.

The detailed results of the determination of c_p^o(glass) and $\Delta_{357.8\,K}^{305.6\,K}H_m^o$(NA, crII) are summarized in Tables S7 and S8 and lead to the mean values c_p^o(glass) = 0.858±0.002 J·K^{-1}·g^{-1} and $\Delta_{357.8\,K}^{305.6\,K}H_m^o$(NA, crII) = 8258±105 J·mol^{-1}. The assigned uncertainty for c_p^o(glass) represents the standard error of the mean and that for and $\Delta_{357.8\,K}^{305.6\,K}H_m^o$(NA, crII) is twice the standard error of the mean.

Table S7: Average massic heat capacity of the glass capillaries used in the Calvet-drop microcalorimetry experiments

Run	m_{glass}/mg	Area	T_i/K	T_f/K	$\Delta_{T_i}^{T_f}H$(glass /J)	c_p^o(glass) /J·K^{-1}·g^{-1}
1	46.7239	133.009	357.73	305.60	2.0808	0.854
2	45.3738	130.148	357.71	305.60	2.0360	0.861
3	47.9010	137.929	358.13	305.60	2.1578	0.858
4	45.6405	131.096	357.77	305.60	2.0509	0.861
5	47.4585	135.050	357.73	305.61	2.1127	0.854

$\langle c_p^o(\text{glass})\rangle$ = 0.858±0.002 J·K^{-1}·g^{-1}

Table S8 Results of the F = $\Delta_{357.8\,K}^{305.6\,K}H_m^o$(NA, crII) measurements by Calvet microcalorimetry

Run	m/mg	m_{glass}/mg	A	T_i/K	T_f /K	ΔH_{tot}/J	ΔH_{glass} /J	ΔH_{NA}/J	F/J·mol^{-1}
1	4.2263	40.3523	133.715	357.81	305.61	2.092	1.806	0.286	8326.5
2	4.7526	41.9806	140.904	358.10	305.61	2.204	1.89	0.314	8141.8
3	4.9810	45.7268	152.806	358.18	305.61	2.391	2.062	0.329	8119.3
4	4.7541	41.9806	140.447	357.66	305.61	2.197	1.874	0.323	8368.4
5	4.2286	40.3523	133.614	357.74	305.60	2.090	1.804	0.286	8334.2

$\left\langle \Delta_{357.8\,K}^{305.6\,K}H_m^o(\text{NA, crII}) \right\rangle$ = 8258±105 J·mol^{-1}

The calculation of the $\Delta_{357.8\,K}^{305.6\,K}H_m^o$(NA, crII) values from the $C_{p,m}^o$(NA) results given by Wang *et al.*[21] , Di *et al.*[22], and Knyazev *et al.*[2], (see Table 3.4 in the main text) were based on the following equations, respectively:

$$C_{p,m}^o/\text{J·K}^{-1}\text{·mol}^{-1} = 10.051 + 0.70853(T/\text{K}) - 1.8021\times10^{-3}(T/\text{K})^2 + 3.3162\times10^{-6}(T/\text{K})^3 \quad \text{(S16)}$$

$$C_{p,m}^o/\text{J·K}^{-1}\text{·mol}^{-1} = 25.814 + 0.47571(T/\text{K}) - 3.2458\times10^{-4}(T/\text{K})^2 + 1.1042\times10^{-6}(T/\text{K})^3 \quad \text{(S17)}$$

$$C_{p,m}^o/\text{J·K}^{-1}\text{·mol}^{-1} = -10.701 + 0.5432(T/\text{K}) \quad \text{(S18)}$$

Equations S16, S17 and S18 were obtained from linear least squares fits to the published data in the temperature range 305 K to 357 K.

3. Computational Details

Density functional theory (DFT)[43] was applied to obtain the vibration frequencies used in the statistical thermodynamics calculation of the standard molar entropy of gaseous nicotinic acid at 366.5 K. Full geometry optimization and frequency predictions were carried out with the B3LYP[44-45] hybrid functional using the 6-31+G(d,p)[46] basis set. The DFT calculations were performed with the Gaussian-03 package[47] and refer to the nicotinic acid conformation **I** which was previously found to be more stable by a variety of levels of theory.[15] The statistical thermodynamics calculations[48] were made under the rigid rotor and harmonic oscillator approximations and using DFT vibration frequencies scaled by 0.964.[49]

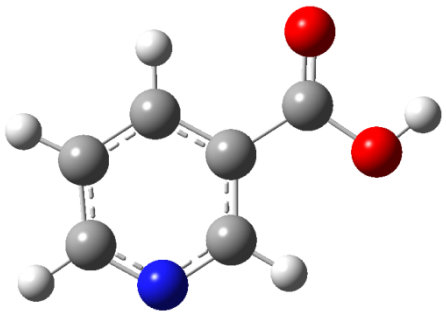

I

The standard molar entropy of nicotinic acid, S^{o}_{m}, in the gaseous phase at the temperature, *T*, was computed as:

$$S^{\circ}_{m} = S^{\circ}_{m,trans} + S^{\circ}_{m,rot} + S^{\circ}_{m,vib} \qquad \text{(S19)}$$

where $S^\circ_{m,trans}$, $S^\circ_{m,rot}$, and $S^\circ_{m,vib}$ are the corresponding translational, rotational and vibrational contributions calculated from:

$$S^\circ_{m,trans} = R\left[\frac{3}{2}\ln\left(\frac{2\pi m}{h^2}\right) + \frac{5}{2}\ln(kT) - \ln(p^\circ) + \frac{5}{2}\right] \quad \text{(S20)}$$

$$S^\circ_{m,rot} = R\left[\frac{3}{2}\ln\left(\frac{kT}{h}\right) - \frac{1}{2}\ln\left(\frac{ABC}{\pi}\right) - \ln(\sigma) + \frac{3}{2}\right] \quad \text{(S21)}$$

$$S^\circ_{m,vib} = -R\sum_i \ln\left(1 - e^{-h\nu_i/kT}\right) + R\sum_i \frac{h\nu_i}{kT}\frac{e^{-h\nu_i/kT}}{1 - e^{-h\nu_i/kT}} \quad \text{(S22)}$$

where R is the gas constant, m is the mass of nicotinic acid (123.03203 amu), h is Plank's constant, k is the Boltzmann constant, p° is the standard pressure, A = 3.935 GHz, B = 1.237 GHz and C = 0.941 GHz are the rotational constants calculated at the B3LYP/6-31+G(d,p) level of theory, σ = 1 denotes the rotational symmetry number of nicotinic acid and ν_i represent the vibration frequencies in Table S9. As mentioned above these were obtained by multiplying the ν_i values calculated at the B3LYP/6-31+G(d,p) level of theory by the recommended scaling factor 0.964[49].

Table S9 Vibration frequencies calculated for nicotinic acid at the theoretical level B3LYP/6-31+G(d,p).

ν /cm^{-1}	ν /cm^{-1}	ν /cm^{-1}	ν /cm^{-1}
63.888	152.98	201.887	371.16
375.392	413.151	475.353	576.459
601.127	632.094	688.703	729.033
762.175	813.389	927.978	961.789
979.377	1000.51	1020.57	1080.61
1094.91	1160.70	1184.58	1263.88
1313.90	1328.61	1402.77	1460.01
1558.35	1581.40	1729.63	3061.01
3089.36	3091.71	3105.47	3629.98

Acknowledgments

This work was supported by Fundação para a Ciência e a Tecnologia (FCT), Portugal through Projects PESt-OE/QUI/UI0612/2011 and PTDC/QUI-QUI/098216/2008. A Post Doctoral grant (SFRH/ BPD/43346/2008) awarded by FCT to C. E. S. Bernardes is also gratefully acknowledged.

References

1. Joseph, A.; Bernardes, C. E. S.; Minas da Piedade, M. E. *J. Chem. Thermodyn.* **2012**, *55,* 23-28.
2. Knyazev, A. V.; Smirnova, N. N.; Shipilova, A. S.; Shushunov, A. N.; Gusarova, E. V.; Knyazeva, S. S. *Thermochim. Acta* **2015**, *604,* 115-121.
3. Karas, M.; Hillenkamp, F. *Anal. Chem.* **1988**, *60,* 2299-2301.
4. Marsh, K. N., *Recommended Reference Materials for the Realization of Physicochemical Properties*; IUPAC-Blackwell Scientific Publications: Oxford, 1987.
5. Sabbah, R.; An, X. W.; Chickos, J. S.; Leitão, M. L. P.; Roux, M. V.; Torres, L. A. *Thermochim. Acta* **1999**, *331,* 93-204.
6. Carlson, L. A. *J Intern. Med.* **2005**, *258,* 94-114.
7. Gille, A.; Bodor, E. T.; Ahmed, K.; Offermanns, S. *Annu. Rev. Pharmacol.* **2008**, *48,* 79-106.
8. Elvehjem, C. A.; Teply, L. J. *Chem. Rev.* **1943**, *33,* 185-208.
9. Goldsmit, G. A. *J. Amer. Med. Assoc.* **1965**, *194,* 167-&.
10. Blum, R., Vitamins. In *Ulmann's Encyclopedia of Industrial Chemistry*, 5th ed.; Elvers, B.; Hawkins, S. Eds.; VCH: Weinheim, 1996; Vol. A27.
11. Block, J., Vitamins*, In Kirk-Othmer Encyclopedia of Chemical Technology*, 5th ed.; Seidel, S., Ed.; Wiley: Hoboken, 1996; Vol. 25.
12. Shimizu, S., Vitamins and Related Compounds: Microbial Production. *In Biotechnology: A Multi-Volume Comprehensive Treatise*, 2nd Completely Revised ed.; Rehm, H. J.; Reed, G.; Puhler, A.; Stadler P. J. W.; Eds.; VCH: Weinheim, 2001.
13. Weissermel, K.; Arpe, H. J., *Industrial Organic Chemistry*, 4th ed.; Wiley-VCH: Weinheim, 2003.
14. Cantarella, M.; Cantarella, L.; Gallifuoco, A.; Intellini, R.; Kaplan, O.; Spera, A.; Martinkova, L. *Enzyme. Microb. Tech.* **2008**, *42,* 222-229.
15. Gonçalves, E. M.; Bernardes, C. E. S.; Diogo, H. P.; Minas da Piedade, M. E. *J. Phys. Chem. B* **2010**, *114,* 5475-5485.
16. Santos, R. C.; Figueira, R. M. B. B. M.; Piedade, M. F. M.; Diogo, H. P.; Minas da Piedade, M. E. *J. Phys. Chem. B* **2009**, *113,* 14291-14309.
17. Matias, E. P.; Bernardes, C. E. S.; Piedade, M. F. M.; Minas da Piedade, M. E. *Cryst. Growth Des.* **2011**, *11,* 2803-2810.
18. Gonçalves, E. M.; Rego, T. S.; Minas da Piedade, M. E. *J. Chem. Thermodyn.* **2011**, *43,* 974-979.

19. Gonçalves, E. M.; Minas da Piedade, M. E. *J. Chem. Thermodyn.* **2012**, *47,* 362-371.
20. Gonçalves, E. M.; Joseph, A.; Conceição, A. C. L.; Minas da Piedade, M. E. *J. Chem. Eng. Data* **2011**, *56,* 2964-2970.
21. Wang, S. X.; Tan, Z. C.; Di, Y. Y.; Xu, F.; Wang, M. H.; Sun, L. X.; Zhang, T. *J. Therm. Anal. Calorim.* **2004**, *76,* 335-342.
22. Di, Y. Y.; Shi, Q.; Tan, Z. C.; Sun, L. X. *Acta Chim. Sinica* **2007**, *65,* 1940-1946.
23. Kutoglu, A.; Scheringer, C. *Acta Crystallogr. C* **1983**, *39,* 232-234.
24. Allen, F. H. *Acta Crystallogr. B* **2002**, *58,* 380-388.
25. Elmoussaoui, A.; Chauvet, A.; Masse, J. *J. Therm. Anal.* **1993**, *39,* 619-632.
26. Sabbah, R.; Ider, S. *Can. J. Chem.* **1999**, *77,* 249-257.
27. Gording, R.; Flexer, L. A. *J. Am. Pharm. Assoc.* **1940,** *5,* 230-231.
28. Spath, E.; Spitzer, H. *Ber Dtsch. Chem. Ges.* **1926**, *59,* 1477-1486.
29. Malaviolle, R.; Demaury, G.; Chauvet, A.; Terol, A.; Masse, J. *Thermochim. Acta.* **1987**, *121,* 283-294.
30. Allan, J. R.; Geddes, W. C.; Hindle, C. S.; Orr, A. E. *Thermochim. Acta* **1989**, *153,* 249-256.
31. Vora, P.; Menon, D.; Samtani, M.; Dollimore, D.; Alexander, K. *Instrum. Sci. Technol.* **2001**, *29,* 231-245.
32. Jingyan, S.; Jie, L.; Yun, D.; Ling, H.; Xi, Y.; Zhiyong, W.; Yuwen, L.; Cunxin, W. *J. Therm. Anal. Calorim.* **2008**, *93,* 403-409.
33. Rehman, M.; Shekunov, B. Y.; York, P.; Colthorpe, P. *J. Pharm. Sci.* **2001**, *90,* 1570-1582.
34. Rudtsch, S. *Thermochim. Acta* **2002**, *382,* 17-25.
35. NIST Certificate for Standard Reference Material 2151.
36. NIST Certificate for Standard Reference Material 39j.
37. Della Gatta, G.; Richardson, M. J.; Sarge, S. M.; Stolen, S. *Pure Appl. Chem.* **2006**, *78,* 1455-1476.
38. Martinho Simões, J. A.; Minas da Piedade, M. E. *Molecular Energetics: Condensed Phase Thermochemical Techniques*, Oxford University Press: New York, 2008.
39. Mraw, S. C.; Naas, D. F. *J. Chem. Thermodyn.* **1979**, *11,* 567-584.
40. Archer, D. G. *J Phys Chem Ref Data* **1993**, *22,* 1441-1453.
41. Furukawa, G. T.; Mccoskey, R. E.; King, G. J. *J. Res. Nat. Bur. Stand.* **1951**, *47,* 256-261.
42. Bernardes, C. E. S.; Santos, L. M. N. B. F.; Minas da Piedade, M. E. *Meas. Sci. Technol.* **2006**, *17,* 1405-1408.
43. Koch, W.; Holthausen, M. C. A.; *Chemist's Guide to Density Function Theory*, 2nd ed.; Wiley-VCH: Weinheim, 2002.
44. Becke, A. D. *J. Chem. Phys.* **1993**, *98,* 5648-5652.
45. Lee, C. T.; Yang, W. T.; Parr, R. G. *Phys. Rev. B* **1988**, *37,* 785-789.
46. Frisch, M. J.; Pople, J. A.; Binkley, J. S. *J. Chem. Phys.* **1984**, *80,* 3265-3269.
47. Frisch, M. J.; Trucks, G. W.; Schlegel, H. B.; Scuseria, G. E.; Robb, M. A.; Cheeseman, J. R.; Montogomery, J. A.; Vreven, A. T.; Kudin, K. N.; Burant, J. C.; Millam, J. M.; Iyengar, S. S.; Tomasi, J.; Barone V.; Mennucci, B.; Cossi, M; Scalmani, G.; Rega, N.; Petersson, G. A.; Nakatsuji, H.; Hada, M.; Ehara, M.; Toyota, K.; Fukuda, R.; Hasegawa, J.; Ishida, M.; Nakajima, T.; Honda, Y.; Kitao, O.; Nakai, H.; Klene, M.; Li, X.; Knox, J. E.; Hratchian, H. P.; Cross, J. B.; Adamo, C.; Jaramillo, J.; Gomperts, R.; Stratmann, R.E.; Yazyev, O.; Austin, A. J.; Cammi R.; Pomelli, C.; Ochterski, J. W.; Ayala, P. Y.; Morokuma, K.; Voth, G. A.; Salvador, P.; Dannenberg, J. J.; Zakrzewski, V. G.; Dapprich, S.; Daniels, A. D.; Strain, M. C.; Farkas, O.; Malick, D. K.;

Rabuck, A. D.; Raghavachari, K.; Foresman J. B.;. Ortiz, J. V.; Cui, Q.; Baboul A. G.; Clifford, S.; Cioslowski, J.; Stefanov, B. B.; G. Liu, G.; Liashenko, A.; Piskorz, P.; Komaromi, I.; Martin, R. L.; Fox, D. J.; Keith, T.; Al-Laham, M. A.; Peng, C. Y.; Nanayakkara, A.; Challacombe, M.; Gill, P. M. W.; Johnson, B.; Chen, W.; Wong, M. W.; Gonzalez, C.; Pople, J. A. *Gaussian* 03; Gaussian, Inc.: Wallingford CT, 2004.

48. Irikiura, K. K.; Frurip, D. J. *Computational Thermochemistry. Prediction and Estimation of Molecular Thermodynamics*, ACS Symposium No. 677, Washington, Washington, 1988.

49. Computational Chemistry Comparison and Benchmark Database. In *NIST Standard Reference Database 101*, (Release 15b) National Institute of Standards and Technology: Gaithersburg, 2011.

50. Wieser, M. E.; Berglund, M. *Pure Appl. Chem.* **2009**, *81,* 2131-2156.

51. Chase Jr, M. W. *NIST-JANAF, Thermochemical Table*s. 4th ed.; *J. Phys. Chem. Ref. Data* **1998**, Monograph 9.

52. Brown, M. E. *J. Chem. Educ.* **1979**, *56,* 310-313.

Chapter 4

Low Temperature Heat Capacity and Polymorphism in Simvastatin.

This chapter reports heat capacity measurements on simvastatin in the sub ambient temperature range (218 K to 297 K) using differential scanning calorimetry. Since this temperature zone is characterized by two solid-solid phase transitions, the structural features of these phase transitions are also discussed.

I performed all sub ambient heat capacity measurements on simvastatin mentioned in this chapter.

Abstract

The molar heat capacity of simvastatin in the range 218 K to 297 K was measured for the first time by differential scanning calorimetry (DSC). In this temperature interval simvastatin undergoes two reversible and fast solid-solid (III $\rightarrow$ II and II $\rightarrow$ I) phase transitions. Previously reported X-ray diffraction, solid state nuclear magnetic resonance (ssNMR), terahertz time-domain (THz-TDS) spectroscopies, and molecular dynamic simulations studies suggest that the structural changes accompanying those phase transitions are essentially related to the conformational mobility of the 'ester tail'. The fact that the stability of the phases are sequentially reversed before fusion, indicates the enantiotropic nature of this system.

4.1 Introduction

Simvastatin (Figure 4.1, CAS number [79902-63-9]), belongs to a group of drugs called "statins" which are used for lowering plasma levels of low density lipoprotein (LDL-c), commonly known as "bad cholesterol" in humans.[1-3] Simvastatin being one of the most prominent members of this family is widely prescribed for the treatment of hypercholesterolemia.[1-4] It is included in the World Health Organisation's list of essential medicines, which records all drugs needed in a basic healthcare system due to their efficacy, safety, and cost.[5] These drugs target hepatocytes and inhibit the HMG-CoA reductase enzyme, which is responsible for conversion of HMG-CoA into mevalonic acid, a cholesterol precursor.[6] Statins have also been shown to inhibit tumor cell growth and enhance intracellular calcium mobilization.[6-9]

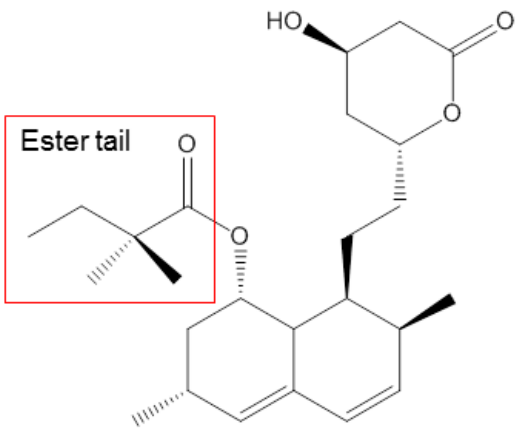

Figure 4.1 Molecular structure of simvastatin.

Simvastatin is administered orally as a lactone pro-drug, which upon dissolution at physiological pH hydrolyses into the analogous β-hydroxy acid form, an active metabolite (Scheme 1).[10]

Scheme 1

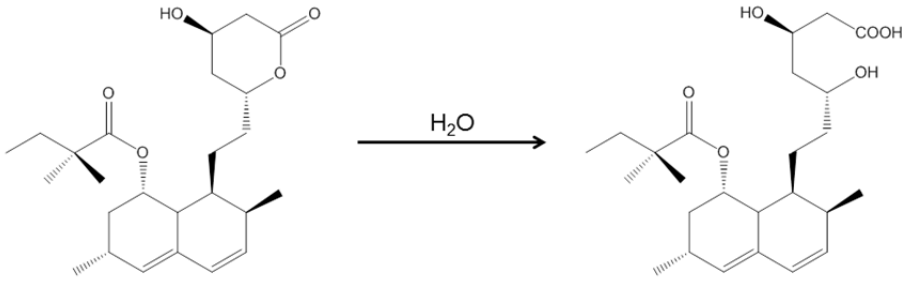

Simvastatin β- hydroxy simvastatin acid

This work is a continuation of systematic studies on simvastatin carried out in our group. In a previous publication, the characterization of simvastatin both from structural and energetic points of view was described.[11] This study, which also included heat capacity measurements, was focused on the crystalline form of simvastatin stable at ambient temperature (phase I). No phase transitions other than fusion were detected in the temperature range 293 – 423 K. The effect of different atmospheric conditions on the thermal stability of simvastatin was later studied and it was found that at or above 353 K the thermal degradation can rapidly occur in the presence of atmospheric or pure oxygen.[12] This led to the conclusion that simvastatin should be handled under nitrogen or inert gas in order to prevent thermal decomposition, particularly if processing requires heating above 353 K.

At sub-ambient temperatures, two solid-solid phase transitions have been reported for simvastatin:[13] phase III $\rightarrow$ II at ~232 K and phase II $\rightarrow$ I at ~272 K. The main objective of this work was to study those phase transitions through heat capacity measurements.

4.2 Materials and Methods

4.2.1 Materials

The simvastatin sample (Jubilant Organosys, 99.3%) used in the experiments was the same which was used to obtain the enthalpies of formation of solid (phase I), liquid and gaseous simvastatin, as well as the heat capacity in the range 293-388 K (solid) and 418-438 K (liquid).[11] This sample had been previously characterized in terms of chemical purity, phase purity and morphology by elemental analysis, HPLC-ESI/MS, diffuse reflectance infrared Fourier-transform (DRIFT) spectroscopy, ^{1}H and ^{13}C NMR, X-ray powder diffraction, scanning electron microscopy (SEM), differential scanning calorimetry (DSC) and thermogravimetry.[11] The X-ray powder pattern corresponds to orthorhombic phase (space group $P2_12_12_1$, with a = 6.123 (1) Å, b = 17.282 (3) Å, c = 22.395 (5) Å) previously analyzed by single crystal X-ray diffraction,[14-15] which as mentioned earlier is designated here as phase I. The HPLC-ESI/MS analysis led to molar percentage of 98.88±0.12 % (simvastatin, Figure 4.1), 0.030±0.004% (simvastatin hydroxyl acid, Figure 4.2a), 0.27±0.05% (anhydro simvastatin, Figure 4.2b), 0.38±0.03% (lovastatin, Figure 4.2c), 0.29±0.03% (epilovastatin, Figure 4.2d), 0.15±0.01% (unspecified impurity). Specific optical rotation measurements performed in a Atago AP300 automatic polarimeter, as recommended in the European Pharmacopeia 5.0, led to $[\alpha]^{16}$ = 276° indicating that the sample consisted of ~98% of the (+) isomer.

The sample used was always stored at 278 K under nitrogen in a Schelnk tube and was only taken out of the cold storage a few minutes before the experiments in order to minimize possible oxidation when exposed to air.

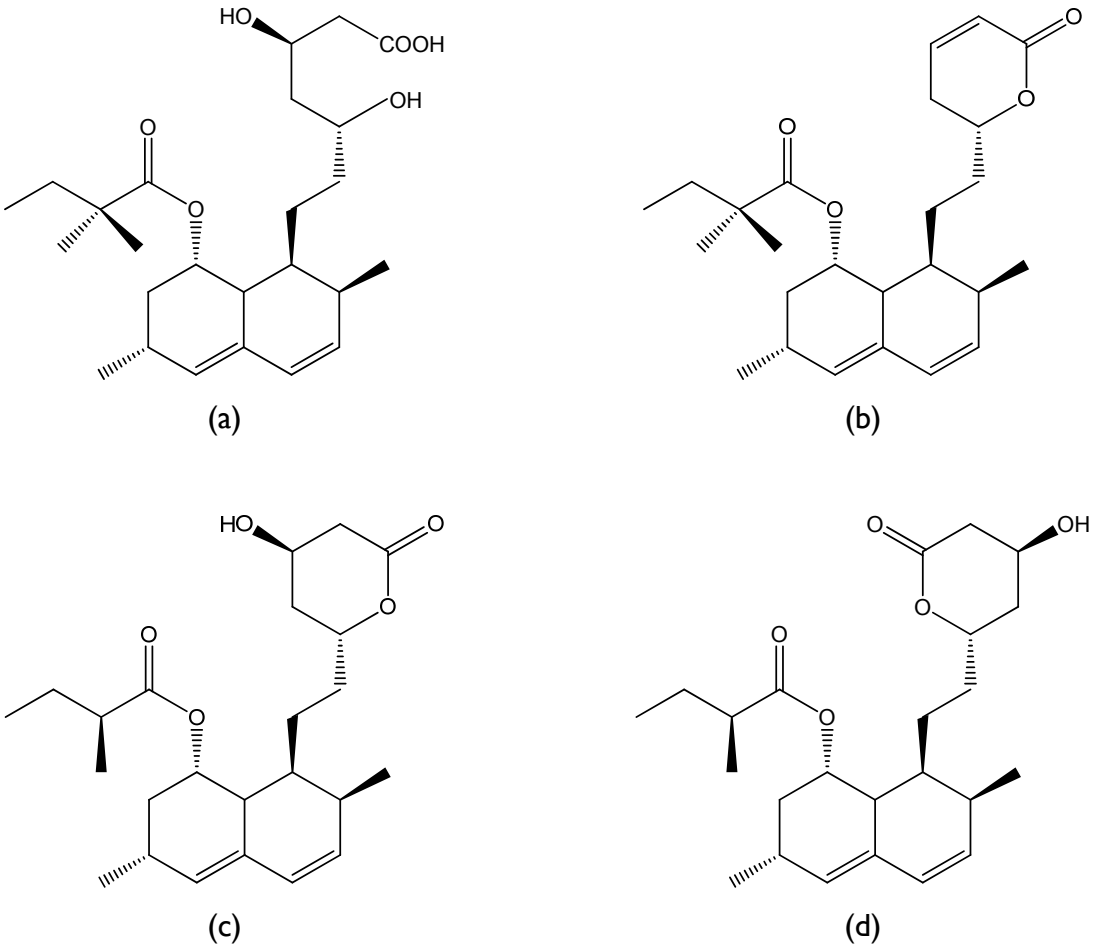

Figure 4.2 Simvastatin impurities detected by HPLC analysis: (a) simvastatin hydroxyl acid, (b) anhydro simvatstain, (c) lovastatin and (d) epilovastatin.

Table 4.1 Provenance and purity of the materials used in this work.

Material	Supplier	Reference	Purity (%)
Simvastatin	Jubilant Organosys	SMS/1001002	98.88*
Benzoic acid	Chem-Lab	CL00.0212.0250	99.9+#
Sapphire (α-Al_2O_3 disks)	Netzsch	6.239.2-91.5.00	99.99#
Indium	Netzsch	6.239.2-91.3.00	99.999#
Adamantan	Netzsch	6.239.2-91.3.00	≥99.0#

*determined by HPLC analysis; #given by the supplier.

4.2.2 Differential Scanning Calorimetry (DSC)

Low temperature heat capacity measurements on simvastatin were performed with a Netzsch DSC 204 F1 Phoenix apparatus equipped with an intracooler system. The samples with masses of ~13 mg were sealed in flat aluminum crucibles from Perkin Elmer and weighed with a precision of ±0.1 μg on a Mettler XP2U ultra-microbalance. The experiments were performed in the approximate range 218 K to 297 K under nitrogen (Linde N_2 5.0), at a flow rate of 30 $cm^3 \cdot min^{-1}$. The heating rate β = 10 $K \cdot min^{-1}$ was used. The temperature scale of the apparatus was calibrated at the same heating rate based on the onset of the fusion peak of the benzoic acid (T_{fus} = 395.52 K)[17], indium (T_{fus} = 429.75 K) and the onset of the low temperature phase transition peak of the adamantane (T_{trs} = 208.65 K). Table 4.1 summarizes the relevant information on the materials used in this work.

The heat capacity measurements were performed in the continuous mode.[18-19] The experiments were carried out in a single temperature interval (218 K to 297 K) covering 79 K. This consisted of recording a blank run, with two empty crucibles, followed by replicate runs involving sapphire and benzoic acid where the same set of crucibles were used each time. The heat capacities of simvastatin $C^{\circ}_{p,m}(\text{sim})$ were computed using the *C*p ratio method implemented in the Netzsch Proteus Analysis software Version 6.1.0.[18-19].The details on the *C*p ratio method can be found in chapter 2 of this thesis under the section on differential scanning calorimetry.

A test carried out with benzoic acid in the temperature range 219 K to 272 K using β = 10 $K \cdot min^{-1}$, showed a maximum deviation of 3.1% between the $C^{\circ}_{p,m}$ results obtained in this work and those recommended by Furukawa *et al.*[20] (see Supporting Information).

4.3 Results and Discussion

All molar quantities were based on the molar mass of simvastatin, M_{sim} = 418.5662 g·mol^{-1}, calculated from the standard atomic masses recommended by the IUPAC Commission in 2011.[21]

4.3.1 Heat capacity

The results of the low temperature heat capacity measurements on simvastatin obtained in this work by DSC are listed in Table 4.2 and illustrated in Figure 4.2. Also shown in Figure 4.2 are the heat capacity values for solid and liquid simvastatin reported by Simões *et al.*[11] and Nti-Gyabaah *et.al.*[22]

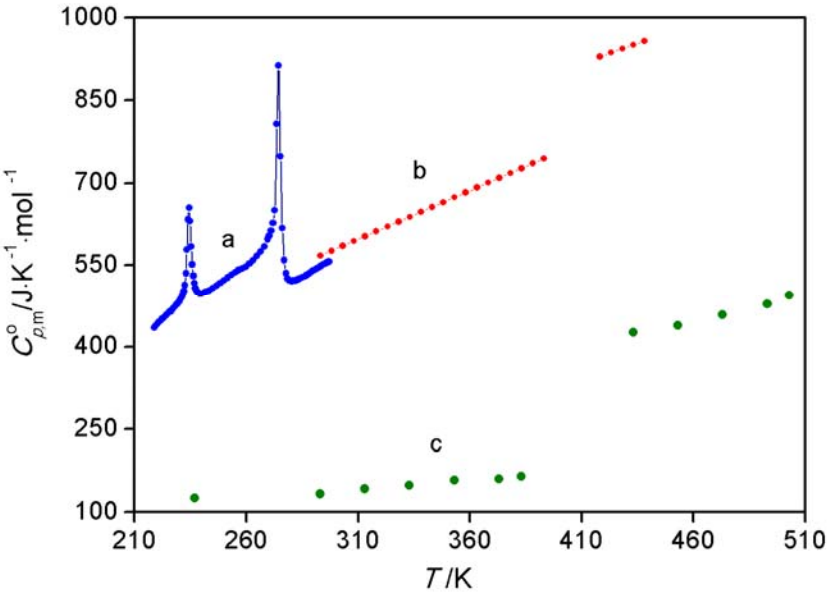

Figure 4.2 (a) Low temperature heat capacities (blue curve) of solid simvastatin obtained in this work for *T* = 218 K to 297 K, (b) heat capacities obtained by Simões *et al.*[11] (red curve) for phase I (*T* = 293 K to 388 K) and liquid (*T* = 418 K to 438 K) and (c) heat capacities previously reported by Nti-Gyabaah *et al.*[22] (green curve) for solid (*T* = 237 K to 383 K) and liquid (*T* = 433 K to 503 K) (see Supporting Information).

Table 4.2 Standard molar heat capacities of simvastatin for T = 218.71 to 297.17 K

T /K	$C^{\circ}_{p,m}$ /J·K^{-1}·mol^{-1}	T /K	$C^{\circ}_{p,m}$ /J·K^{-1}·mol^{-1}	T /K	$C^{\circ}_{p,m}$ /J·K^{-1}·mol^{-1}
218.71	435.3±14.2	237.70	503.0±13.5	276.85	559.7±8.1
219.45	438.7±14.8	238.18	500.4±13.9	277.67	535.19.2
220.19	441.7±14.8	238.65	498.3±14.2	278.49	525.1±10.0
220.93	445.0±14.8	239.12	497.6±14.1	279.31	521.7±10.3
221.67	447.7±14.7	239.59	497.2±14.1	280.01	521.1±10.2
222.41	451.0±14.8	240.06	497.4±14.1	280.71	521.2±10.0
223.14	453.6±14.7	241.70	500.5±13.7	281.41	521.7±10.0
223.88	456.8±14.4	243.35	503.8±13.4	282.11	522.4±10.1
224.61	459.3±14.7	244.99	508.3±12.8	282.81	523.6±10.7
225.34	462.4±14.5	246.64	512.5±11.9	283.51	524.8±10.5
226.06	464.6±14.3	248.28	517.5±12.1	284.21	526.3±10.7
226.79	467.6±13.9	249.92	521.9±11.6	284.91	527.4±11.0
227.51	470.5±13.6	251.57	526.9±12.0	285.61	528.7±11.1
228.23	474.1±13.4	253.21	532.7±12.2	286.31	530.1±11.4
228.95	477.5±13.5	254.85	536.8±12.0	287.01	532.0±11.6
229.66	481.6±13.3	256.49	540.9±12.1	287.71	533.7±11.6
230.14	484.2±13.6	258.13	543.4±12.7	288.41	536.0±11.7
230.62	487.3±13.9	259.77	547.0±12.5	289.11	538.1±11.9
231.09	490.5±13.5	261.41	553.4±12.6	289.81	539.8±11.7
231.57	495.1±13.6	263.05	559.1±13.1	290.51	541.3±11.7
232.04	501.8±14.0	264.69	566.9±12.8	291.21	543.1±11.6
232.51	513.1±14.7	266.33	575.0±12.6	291.91	544.7±10.9
232.99	535.1±15.3	267.96	584.6±12.2	292.61	546.4±10.2
233.46	578.0±17.7	269.60	597.7±12.6	293.31	548.9±10.0
233.93	633.8±19.2	270.30	604.3±12.4	294.02	550.3±9.5
234.40	655.5±18.5	271.12	613.5±12.3	294.72	552.3±8.7
234.88	631.1±14.3	271.94	627.0±12.3	295.42	553.7±8.3
235.35	584.5±13.2	272.76	650.1±12.8	296.12	554.8±7.9
235.82	551.5±13.3	273.57	807.0±22.5	296.58	556.0±7.9
236.29	530.3±13.4	274.39	913.2±19.9	297.17	556.9±7.6
236.76	517.2±13.4	275.21	749.1±7.2		
237.23	508.5±13.1	276.03	617.5±7.2		

Each $C^{\circ}_{p,m}$ data in Table 4.2 refers to the mean of six independent determinations (see Supporting Information). The uncertainties assigned for those determinations are twice the standard error of mean. Two solid-solid phase transition peaks can be noted in Figure 4.2: (i) a broad peak with a maximum at T_{max} = 234.4 K corresponding to the phase III → phase II transition and (ii) another broad peak with maximum at T_{max} = 274.4 K corresponding to the phase II → phase I transition. The heat capacities obtained over the ranges of these phase transitions are also included in Table 4.2 and shown in Figure 4.2. The data in Table 4.2 were fitted to the equation:

$$C^{\circ}_{p,m} / \mathrm{J \cdot K^{-1} \cdot mol^{-1}} = a(T/\mathrm{K}) + b \qquad (4.1)$$

in different temperature intervals outside the phase transition zones. The corresponding parameters, range of application and regression coefficient are summarized in Table 4.3.

As can be seen in Figure 4.2, where comparison is possible (293 to 297 K) the data reported here is in close proximity with that reported by Simões *et al.*[11] In the range 293 to 297 K where overlap is possible the discrepancy between data reported here and that obtained by Simões *et al.* is 3 to 3.5 %, which is within the uncertainty of the determinations. In contrast, the *C*p data published by Nti-Gyabaah and co-workers are considerably smaller than those obtained in this work. As pointed out by Simões *et al.*[11] these values are impossibly low since the result corresponding to phase I at 298 K (139 $\mathrm{J \cdot K^{-1} \cdot mol^{-1}}$) is smaller than the corresponding value for gas phase simvastatin (515.7 $\mathrm{J \cdot K^{-1} \cdot mol^{-1}}$) and thus are inconsistent with the expected order . $C^{\circ}_{p,m}(\mathrm{g}) < C^{\circ}_{p,m}(\mathrm{cr}) < C^{\circ}_{p,m}(\mathrm{l})$.

Table 4.3 Coefficients of equation 4.1 for different species of simvastatin, temperature range of application (*T* range/K) and regression coefficient (R^2).

Species	*a*	*b*	*T* range/K	R^2
Phase III	4.0118	-441.69	218 to 228	0.9991
Phase II	2.7299	-160.07	241 to 263	0.9972
Phase I	2.3823	-150.66	281 to 297	0.9958

4.3.2 Temperatures and enthalpies of phase transition

The peaks detected for the two solid-solid phase transitions in the heat capacity determinations with maxima at 234.4 K and 274.4 K were also observed in normal DSC scans carried out previously[23] at the heating rate of 10 K·min^{-1} (Figure 4.3). The figure clearly shows that the two phase transitions are reversible and occur with a very small undercooling (0.2-1.2 K) which points to low kinetic barrier associated with the phase transition. This conclusion can be justified on the fact that the crystal structures of the three phases are very similar as was observed previously[13] and is discussed in the next section.

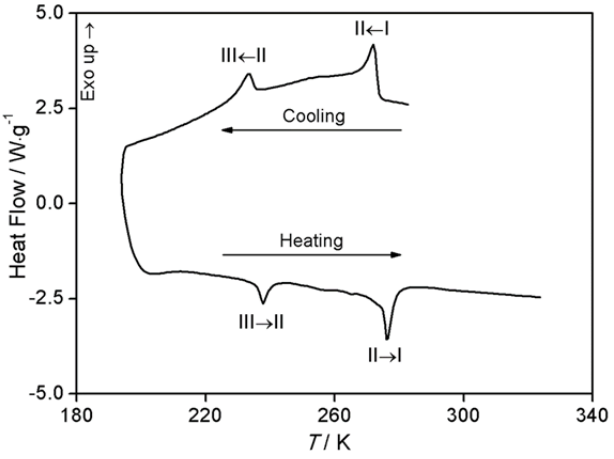

Figure 4.3 DSC measuring curve for the simvastatin (cooling/heating cycle) at a rate of 10 K·min^{-1} (adapted from reference 23)

The heat capacity data in Table 4.2 over the III→I and II→I phase transition regions were integrated (Figure 4.4) as described for nicotinic acid in chapter 3. This led to the determination of $\Delta_{trs}H_m$ (III→II) = 0.36 kJ·mol^{-1} for T_{max} = 234.37 K and $\Delta_{trs}H_m$ (II→I) = 0.55 kJ·mol^{-1} for T_{max} = 274.36 K.

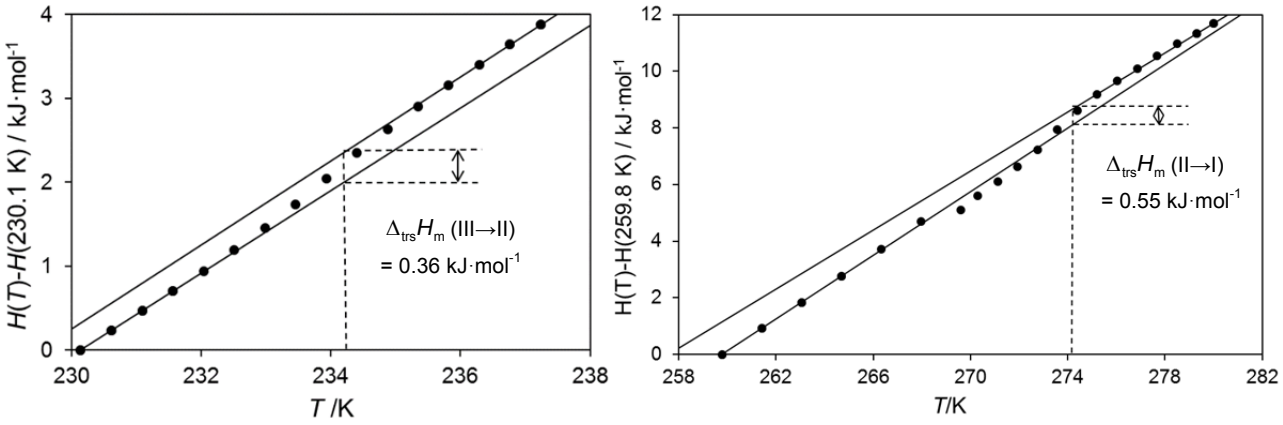

Figure 4.4 Enthalpy increment in the range of (a) III → II phase transition and (b) II → I phase transition.

4.3.3 Structural features of the phase transition

The structure solution carried out by Hušak *et al.*[13] for the two low temperature phases (phase III and phase II) led to the conclusion that while phases I and II were orthorhombic, space group ($P2_12_12_1$), and had one simvastatin molecule in the asymmetric unit (Z' = 1), phase III was monoclinic, space group $P2_1$ and had two molecules in the asymmetric unit (Z' = 2). The results also suggested that the transformation between the three phases is accompanied by the change in molecular conformation of the ester tail. Recently in an analysis carried out on the low temperature phase by using single crystal X-ray diffraction (SC-XRD), it was shown that all the three simvastatin phases are orthorhombic with only one molecule in the asymmetric unit (Z' = 1).[23] The structure solution of phase I and phase II are similar to the structures previously reported for phase I at 293 K[14] and for phase II at 258 K[14], however the results were different

for phase III. This discrepancy in the structure solution of the phase III was attributed to structural disorder due to ester tail getting frozen in different conformation as the temperature decreases.[23] This aspect was also studied by solid-state NMR (ssNMR)[13] molecular dynamic simulations (MD-simulations)[23] and terahertz time-domain spectroscopy (THz-TDS).[5] All these three methods suggested that the phase transition in simvastatin involves the conformational changes in the simvastatin ester tail. Thus it was concluded that (a) below III→II phase transition temperature, the ester tail remains essentially frozen, (b) between III→II and II→I phase transition temperatures, in the region of phase II, the ester tail experiences the rapid increase in rotational freedom as the temperature increases and (c) above II→I phase transition temperature in the region of phase I, the ester tail is freely rotating and therefore with the rise in temperature the ester tail experiences less rotational mobility compared to phase II.

The variation in lattice parameters obtained from the SC-XRD analysis of a simvastatin single crystal in the temperature range 167-291 K[23] is represented in Figure 4.5. As can be seen in Figure 4.5, the transformations in unit cell of simvastatin due to III→II and II→I phase transition is accompanied by continuous increase in molar volume (V_m) and unit cell length along *a* and *b* axis. However there is a sharp decrease in the unit cell length along *c* axis corresponding to II→I phase transition (Figure 4.5d).

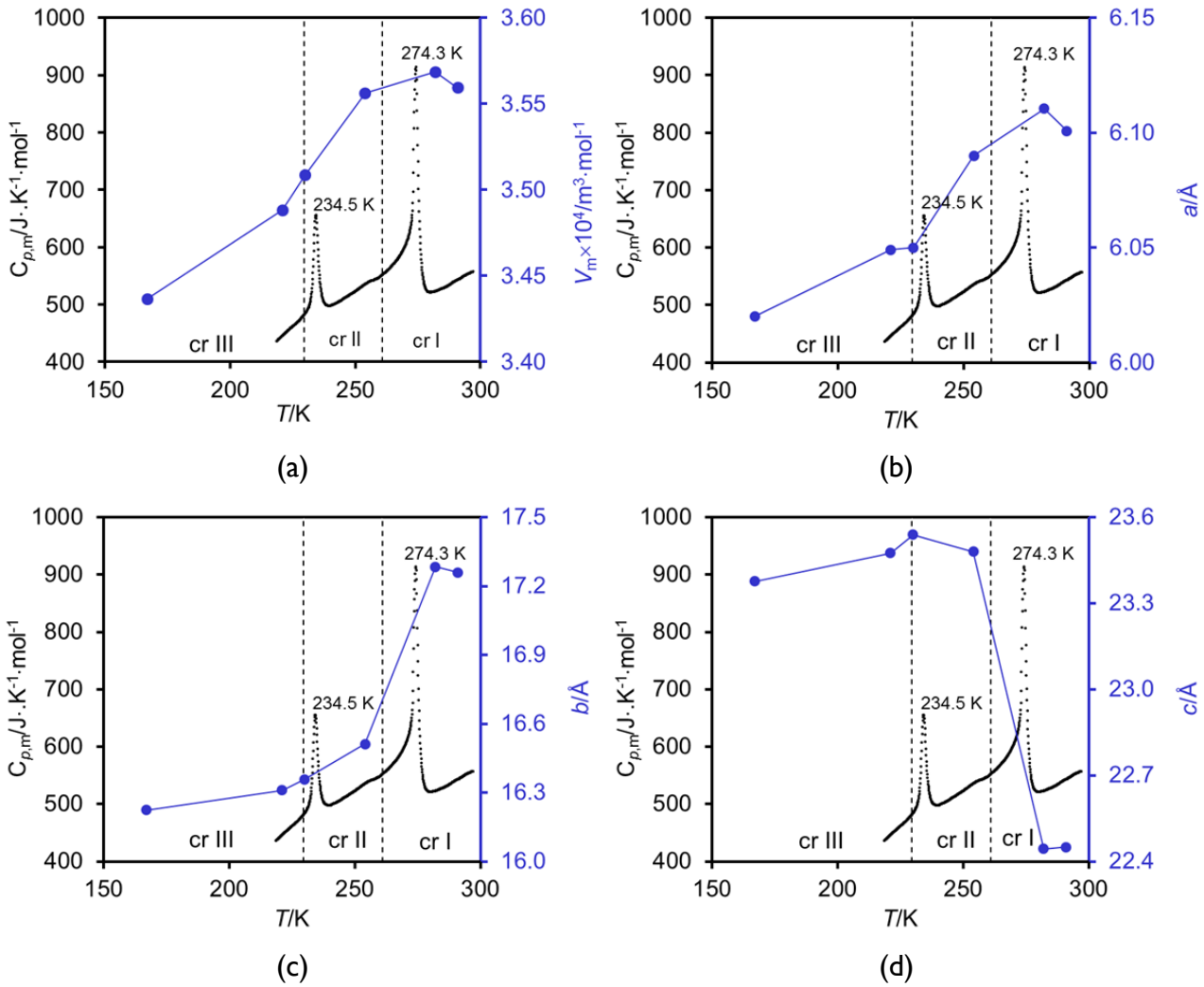

Figure 4.5 Variation of lattice parameters of simvastatin (blue curve) with temperature: (a) molar volume and cell lengths along (b) *a* axis, (c) *b* axis and (d) *c* axis. The corresponding variation of heat capacity in the given temperature interval is shown as black curve.

These three phase of simvastatin cannot be regarded as polymorphs in the classical sense of McCrone's defintition[24] which denies the possibility of polymorphism due to differences in shape such as those involving dynamic isomerism or tautomerism. However DSC experiments and heat capacity determinations clearly show the enantiotropic nature of the system i.e. there is a transition temperature relating III→II and II→I phase transition before fusion at which the stability order is reversed.

4.4 Conclusion

The heat capacity in the temperature range 218 K to 297 K is reported. The enthalpy of the two phase transitions were determined by integrating the heat capacity data over the III→II and II→I phase transitions region and were found to be 0.36 $kJ \cdot mol^{-1}$ and 0.55 $kJ \cdot mol^{-1}$ respectively. These values are smaller than the corresponding enthalpies ($\Delta_{trs}H_m$ (III→II) = 0.95±0.06 $kJ \cdot mol^{-1}$ and $\Delta_{trs}H_m$ (II→I) = 3.3±0.1 $kJ \cdot mol^{-1}$) obtained from DSC experiments at the same heating rate.[23] The enthalpy values obtained from DSC are large particularly in the case of II→I transition. This may be due to difficulty in assigning accurate integration limits and baseline type for these phase transition peaks. The smaller enthalpy values obtained from the heat capacity measurements are compatible with the fact that the crystal structure of the three phases are very similar and the phase transitions is essentially due to mobility of ester tail. The most significant change in the unit cell during II→I phase transition is due to contraction of lattice along *c* axis.

Supporting Information

Heat capacity of benzoic acid. The accuracy of the heat capacity measurements was tested for benzoic acid (BA) in the temperature range 219 K to 272 K. The obtained results are compared in Table S2 with those calculated from:[20]

$$C^{o}_{p,m}\left(\mathrm{BA}\right)_{\mathrm{ref}} / \left(\mathrm{J\cdot K^{-1}\cdot mol^{-1}}\right) = 0.45785 \pm 0.00082(T/\mathrm{K}) + (10.369 \pm 0.233) \qquad \text{(S1)}$$

which was derived from a least squares fit to the data recommended by Furukawa *et al.*[20] for T = 215 to 345 K. The uncertainties quoted for the DSC results in Table S2 represent twice the standard deviation of the mean of three independent determinations. Figure S1 shows the deviations between the observed and recommended values in Table S2 and is calculated from

$$s\% = 100\frac{\left\langle C^{o}_{p,m}\left(\mathrm{BA}\right)_{\mathrm{obs}}\right\rangle - C^{o}_{p,m}\left(\mathrm{BA}\right)_{\mathrm{ref}}}{C^{o}_{p,m}\left(\mathrm{Ref}\right)_{\mathrm{ref}}} \qquad \text{(S2)}$$

Table S1 and Figure S1 indicate that the DSC results agree with recommended values within the experimental uncertainty and that the maximum deviation is 3.1%.

Table S1 Comparison of the heat capacity of benzoic acid obtained in this work by DSC, $C^{\circ}_{p,m}(BA)_{obs}$, and that given by equation (S1).

T/K	$C^{\circ}_{p,m}(BA)_{obs}$ / J·mol^{-1}·K^{-1}	$C^{\circ}_{p,m}(BA)_{ref}$ /J·mol^{-1}·K^{-1} [a]	s%
219.22	108.4±4.28	110.7	2.1
223.22	110.1±4.14	112.6	2.2
227.22	111.8±4.02	114.4	2.3
231.22	113.5±3.88	116.2	2.3
235.22	115.2±3.74	118.1	2.4
239.21	116.9±3.62	119.9	2.5
243.21	118.6±3.48	121.7	2.6
247.21	120.3±3.36	123.6	2.7
251.21	121.9±3.24	125.4	2.7
255.21	123.6±3.12	127.2	2.8
259.21	125.3±3.00	129.0	2.9
263.20	127.0±2.90	130.9	3.0
267.20	128.7±2.78	132.7	3.0
272.20	130.8±2.66	135.0	3.1

[a]Reference 20

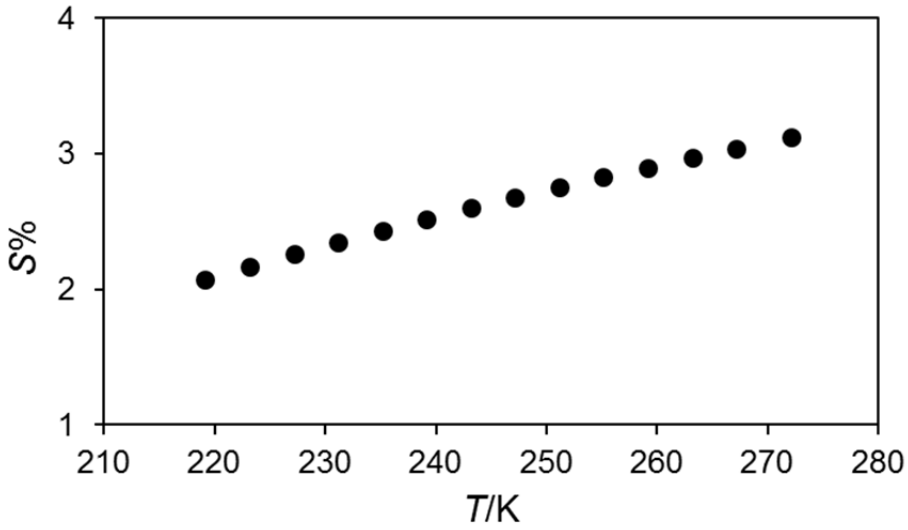

Figure S1 Deviation between the heat capacity of benzoic acid obtained in this work by DSC, and the reference value given by eq. S2.

Table S2 Heat capacity of simvastatin from six independent determinations in the temperature range 218 K to 297 K.

T/K	$C^{\circ}_{p,m}$ /J·K^{-1}·mol^{-1}					
	Exp-1	Exp-2	Exp-3	Exp-4	Exp-5	Exp-6
218.71	423.58	409.91	435.15	435.01	449.88	458.25
219.45	426.65	412.04	439.35	438.00	453.88	462.32
220.19	429.27	415.14	443.23	440.25	456.91	465.11
220.93	432.72	418.22	446.53	444.07	459.61	468.71
221.67	434.90	421.70	449.39	446.64	462.96	470.90
222.41	437.94	424.88	452.80	449.59	466.27	474.28
223.14	440.29	427.52	456.35	452.49	468.78	476.35
223.88	442.96	431.09	459.71	456.53	471.96	478.40
224.61	444.45	433.69	462.51	459.23	474.46	481.72
225.34	447.76	436.90	466.24	462.05	477.37	484.13
226.06	449.39	439.98	469.01	463.58	479.58	485.78
226.79	453.45	443.27	472.79	466.08	481.58	488.45
227.51	456.40	447.02	475.77	468.80	484.13	490.78
228.23	460.37	450.88	479.19	472.61	487.40	494.23
228.95	464.72	453.51	482.19	475.75	491.59	497.44
229.66	469.20	457.71	486.23	479.52	495.29	501.44
230.14	471.04	459.61	489.83	482.77	497.47	504.18
230.62	473.03	462.68	492.72	486.45	500.65	508.17
231.09	476.61	466.22	496.32	490.30	503.66	510.14
231.57	481.82	470.22	500.09	495.35	508.44	514.79
232.04	488.40	475.61	507.79	502.03	514.76	521.97
232.51	499.30	485.42	519.73	513.48	526.28	534.24
232.99	520.71	507.03	541.67	534.28	548.50	558.43
233.46	561.91	545.50	586.88	576.29	592.01	605.55
233.93	615.46	600.42	642.11	631.53	646.76	666.60
234.40	637.99	621.30	663.30	654.92	673.03	682.42
234.88	617.15	604.12	636.52	632.82	646.18	649.91
235.35	576.25	555.94	591.89	589.99	601.15	591.74
235.82	543.45	522.21	558.84	555.75	566.36	562.09
236.29	520.44	502.12	536.84	532.93	544.14	545.25
236.76	506.25	490.33	522.48	519.68	530.82	533.90
237.23	496.58	482.92	514.03	510.20	521.95	525.22
237.70	490.49	477.13	507.24	504.94	516.90	521.17
238.18	488.05	473.70	505.36	501.66	514.49	519.07
238.65	485.51	471.18	502.97	499.66	512.45	518.13
239.12	484.20	471.41	502.28	498.64	511.56	517.60
239.59	484.15	470.60	501.28	499.27	510.29	517.46
240.06	484.57	470.59	501.21	499.21	510.65	518.00
241.70	489.34	474.62	502.85	501.56	512.78	521.85
243.35	494.62	478.34	505.51	503.70	514.50	525.88
244.99	499.81	484.08	510.14	507.39	518.75	529.85
246.64	503.85	490.60	515.39	510.90	521.42	532.85
248.28	507.45	495.70	520.57	516.25	527.45	537.69
249.92	512.15	500.51	526.41	520.72	531.26	540.61

Continued….

T/K	$C^{\circ}_{p,m}$ /J·K^{-1}·mol^{-1}					
	Exp-1	Exp-2	Exp-3	Exp-4	Exp-5	Exp-6
251.57	515.78	505.46	532.20	524.97	536.51	546.43
253.21	520.75	511.38	538.50	530.65	542.91	552.28
254.85	523.92	516.34	540.98	536.27	547.39	556.06
256.49	528.97	519.92	543.96	540.16	551.52	560.93
258.13	529.97	522.02	547.85	541.80	555.91	563.01
259.77	533.89	525.95	552.66	545.43	556.83	567.43
261.41	540.72	532.25	557.90	550.58	565.49	573.56
263.05	546.45	536.55	562.69	557.44	570.48	580.78
264.69	556.30	544.29	568.70	565.63	577.35	589.13
266.33	565.65	552.14	576.53	573.45	585.66	596.41
267.96	578.62	561.47	585.27	582.77	592.82	606.53
269.60	590.77	574.13	599.29	595.51	606.35	620.01
270.30	596.83	581.83	605.83	601.88	612.49	627.23
271.12	605.69	591.38	615.34	611.26	621.76	635.83
271.94	617.38	605.18	628.91	626.50	634.29	649.50
272.76	640.78	627.10	652.13	649.65	656.69	674.00
273.57	794.77	769.70	809.62	804.58	808.95	854.47
274.39	892.32	882.34	919.06	909.29	925.79	950.33
275.21	744.60	735.68	754.58	753.90	760.22	745.38
276.03	611.21	602.77	620.95	621.71	626.51	621.74
276.85	551.69	544.71	562.57	560.07	567.87	571.04
277.67	525.56	519.53	537.64	534.37	543.22	550.42
278.49	515.33	508.59	527.74	522.78	534.40	541.84
279.31	510.51	505.14	524.75	519.81	530.73	539.04
280.01	510.11	504.74	524.40	518.89	530.53	538.09
280.71	510.80	504.61	524.85	518.70	531.12	537.04
281.41	512.17	504.55	525.46	519.08	532.09	536.96
282.11	512.85	505.18	526.32	519.16	533.01	538.06
282.81	513.99	504.80	528.52	520.14	534.64	539.63
283.51	514.90	507.04	531.00	520.72	534.07	541.22
284.21	516.37	508.17	533.24	521.87	535.17	543.22
284.91	517.59	508.77	534.88	522.14	536.08	544.69
285.61	518.89	509.92	536.52	522.94	538.26	545.61
286.31	520.09	510.66	538.09	524.32	539.82	547.77
287.01	520.99	512.53	540.19	526.94	541.13	550.02
287.71	522.51	514.71	542.43	528.21	542.54	551.98
288.41	525.07	516.57	545.06	530.14	545.30	554.04
289.11	528.64	517.22	548.08	532.50	545.90	556.53
289.81	532.32	517.97	549.64	534.53	547.02	557.40
290.51	535.28	518.76	550.20	535.48	548.94	559.01
291.21	537.95	520.55	551.12	537.12	551.25	560.44
291.91	540.03	522.96	551.50	539.58	553.84	560.46
292.61	541.70	525.70	552.27	542.83	555.09	560.90

Continued….

T/K	$C^{\circ}_{p,m}$ /J·K^{-1}·mol^{-1}					
	Exp-1	Exp-2	Exp-3	Exp-4	Exp-5	Exp-6
293.31	543.32	528.38	554.24	547.13	557.75	562.37
294.02	544.77	530.55	554.82	550.16	558.95	562.81
294.72	546.15	534.63	554.69	553.40	561.29	563.77
295.42	546.97	537.34	554.78	555.58	562.18	565.21
296.12	548.64	539.18	556.24	556.02	564.01	564.50
296.58	549.54	540.84	556.80	556.74	565.92	565.87
297.17	550.06	542.91	557.79	557.02	567.10	566.40

Table S3 Heat capacities of solid and liquid simvastatin reported by Nti-Gyabaah *et al.*[22]

	T/K	$C^{\circ}_{p,m}$ /J·K^{-1}·mol^{-1}
Solid	237	125±1
	293	133±2
	313	142±4
	333	148±3
	353	158±2
	373	160±3
	383	165±2
Liquid	433	426±6
	453	439±8
	473	459±8
	493	478±7
	503	495±10

Heat Capacities of phase I and liquid simvastatin reported by Simões *et al.*[11]

The heat capacities of solid phase I simvastatin in the temperature range *T* = 293-388 K can be calculated from:

$$C^{\circ}_{p,m}\,(\text{phase I})/\text{J}\cdot\text{K}^{-1}\cdot\text{mol}^{-1} = (1.7712\pm0.0171)(T/\text{K})+(48.429\pm5.840) \quad \text{(S3)}$$

and for liquid in the temperature range T = 418-438 K from:

$$C^{\circ}_{p,m}\,(\text{liquid})/\text{J}\cdot\text{K}^{-1}\cdot\text{mol}^{-1} = (1.4399\pm0.0001)(T/\text{K})+(327.20\pm0.02) \quad \text{(S4)}$$

Acknowledgements

This work was supported by the FCT doctoral grant (SFRH/ BD/90386/2012) awarded to A. Joseph.

References

1. Li, J. J., *Triumph of the Heart. The Story of Statins*; Oxford University Press: New York, 2009.
2. Taylor, F. Ward, K.; Moore, T.H.M.; Burke, M.; Davey Smith, G.; Casas, J.P.; Ebrahim, S., *Statins for the Primary Prevention of Cardiovascular Disease*; John Wiley: New York, 2012.
3. Tiwari, R.; Pathak, K. *J. Pharm. Pharmacol.* **2011**, *63,* 983-998.
4. Baxendale, I. R.; Hayward, J. J.; Ley, S. V.; Tranmer, G. K. *ChemMedChem* **2007**, *2,* 768-788.
5. Tan, N. Y.; Zeitler, J. A. *Mol. Pharmaceut.* **2015**, *12,* 810-815.
6. Stancu, C.; Sima, A. *J. Cell. Mol. Med.* **2001**, *5,* 378-387.
7. Warita, K.; Warita, T.; Beckwitt, C. H.; Schurdak, M. E.; Vazquez, A.; Wells, A.; Oltvai, Z. N. *Sci. Rep.* **2014**, *4*.
8. Hindler, K.; Cleeland, C. S.; Rivera, E.; Collard, C. D. *Oncologist* **2006**, *11,* 306-315.
9. Yokoyama, K.; Ishibashi, T.; Ohkawara, H.; Kimura, J.; Matsuoka, I.; Sakamoto, T.; Nagata, K.; Sugimoto, K.; Sakurada, S.; Maruyama, Y. *Circulation* **2002**, *105,* 962-967.
10. Hamelin, B. A.; Turgeon, J. *Trends. Pharmacol. Sci.* **1998**, *19,* 26-37.
11. Simões, R. G.; Bernardes, C. E. S.; Diogo, H. P.; Agapito, F.; Minas da Piedade, M. E. *Mol. Pharmaceut.* **2013**, *10,* 2713-2722.
12. Simões, R. G.; Diogo, H. P.; Dias, A.; Oliveira, M. C.; Cordeiro, C.; Bernardes, C. E. S.; Minas da Piedade, M. E. *J. Pharm. Sci.* **2014**, *103,* 241-248.
13. Husak, M.; Kratochvil, B.; Jegorov, A.; Brus, J.; Maixner, J.; Rohlicek, J. *Struct. Chem.* **2010**, *21,* 511-518.
14. Cejka, J.; Kratochvil, B.; Cisarova, I.; Jegorov, A. *Acta. Crystallogr. C* **2003**, *59,* O428-O430.
15. Allen, F. H. *Acta. Crystallogr. B* **2002**, *58,* 380-388.
16. Burla, M. C.; Caliandro, R.; Camalli, M.; Carrozzini, B.; Cascarano, G. L.; De Caro, L.; Giacovazzo, C.; Polidori, G.; Spagna, R. *J. Appl. Crystallogr.* **2005**, *38,* 381-388.
17. Della Gatta, G.; Richardson, M. J.; Sarge, S. M.; Stolen, S. *Pure. Appl. Chem.* **2006**, *78,* 1455-1476.
18. Joseph, A.; Bernardes, C. E. S.; Minas da Piedade, M. E. *J. Chem. Thermodyn.* **2012**, *55,* 23-28.
19. Martinho Simões, J. A. Minas da Piedade. M. E., *Molecular Energetics: Condensed-Phase Thermochemical Techniques;* Oxford University Press: New York, 2008.
20. Furukawa, G. T.; Mccoskey, R. E.; King, G. J. *J. Res. Nat. Bur. Stand.* **1951**, *47,* 256-261.
21. Wieser, M. E.; Coplen, T. B. *Pure Appl. Chem.* **2011**, *83,* 359-396.
22. Nti-Gyabaah, J.; Chan, V.; Chiew, Y. C. *Fluid Phase Equilibr.* **2009**, *280,* 35-41.

23. Simões, R. G., The Ambiguous Case of Polymorphism in Simvastatin: A Single Crystal X-ray Diffraction, Thermodynamic and MD Simulation Study, In Thermodynamics and Structural Studies of 4-Hydroxybenzaldehyde and Simvastatin; Ph.D Thesis, Lisbon, Portugal, 2013.
24. McCrone, W. C., *Polymorphism*; Wiley: New York, 1965; Vol. 2.

Chapter 5

Polymorphic Phase Transition in 4'-Hydroxyacetophenone and the Relative Stability of Z' = 1 and Z' = 2 Forms.

This chapter describes thermodynamic and kinetic studies of the solid-solid phase transition between the two known polymorphs of 4'-hydroxyacetophenone (HAP): form II (orthorhombic) and form I (monoclinic). The results from solubility and calorimetric studies, supplemented by other published thermodynamic data, allowed the redetermination of the $\Delta_f G_m^\circ$ vs. T diagram highlighting the enantiotropic nature of the HAP system and the stability domains of the two polymorphs. A kinetic analysis based on differential scanning calorimetry (DSC) measurements suggested that the form II → form I transition is irreversible in the solid state and characterized by a high activation barrier. Finally, as by-product of the solubility studies, a new procedure for the selective and reproducible synthesis of the two HAP polymorphs was developed.

I performed the synthesis of the two HAP polymorphs, the solubility experiments and all studies involving DSC, powder X-ray diffraction, diffuse reflectance infrared Fourier transform spectroscopy (DRIFT), and hot-stage microscopy (HSM). HSM experiments were carried out in collaboration with Professor Hermínio Diogo (IST-UL). The adiabatic calorimetry measurements were made by Dr. Anna Druzhinina and the late Prof. Raisa Varushchenko at Moscow State University, Russia. Raman spectroscopy experiments were performed by Dr. Carlos Bernardes at the group of Dr. Franziska Emmerling (BAM, Germany). All computational chemistry calculations were carried out in our laboratory by Dr. Carlos Bernardes. Finally, I contributed to the discussion of the results, the construction of phase diagram and the writing of the present text.

Abstract

The solid-solid phase transition involving the two polymorphic forms of 4'-hydroxyacetophenone (form II, orthorhombic, space group $P2_12_12_1$, Z' = 2; form I, monoclinic, space group $P2_1/c$, Z' = 1), was investigated from structural, thermodynamic, and kinetic points of view. The results of DSC, adiabatic calorimetry and solubility measurements, allowed the redetermination of the $\Delta_f G_m^\circ$ vs. T phase diagram highlighting the enantiotropic nature of the system i.e., form II is more stable than form I up to 300.1 K, and above this temperature the stability is reversed with fusion of form I subsequently occurring at 381.9 K. The phase transition was also found to be entropy driven. The solubility studies demonstrated that the equilibrium temperature of the phase transition (300.1 K) lies ~30-70 K below the temperature at which the form II → form I conversion is directly observed in the solid state using different techniques (calorimetry, Raman spectroscopy and hot stage microscopy) and heating rates. They also showed that, although the process is irreversible in the solid state, interconversion of the two forms under thermodynamic control is possible by solvent mediated dissolution/re-precipitation. The activation barrier behind the direct solid-solid form II → form I transformation was determined as E_a ~ 200 kJ·mol^{-1} by non-isothermal kinetic measurements using DSC. This high value must be taken with caution since it is larger than the lattice enthalpy of both HAP forms. Nevertheless, a large E_a value has at least the merit to be consistent with the fact that (i) a considerable overheating is necessary for the form II → form I to be observed, (ii) the reverse process was never found to occur and (iii) the two forms can indefinitely be stored at ambient temperature without change. All obtained evidence suggests that the transition involves a nucleation and growth mechanism and, despite the large E_a, hot stage microscopy experiments revealed that it can unequivocally occur under single crystal to single crystal conditions. Finally the structure/energetics features behind the occurrence of Z' = 1 (form I) or Z' = 2 (form II) structures in HAP were investigated from molecular and crystal packing points of view using ab-initio calculations and Hirshfeld surface analysis.

5.1 Introduction

Understanding the relationship between the structure and relative stability of polymorphic forms is at the heart of crystal engineering.[1-3] Polymorphs differ in their packing architecture and, sometimes, also in the conformation of the molecules in the crystal lattice. These differences are frequently large enough to affect the stability of the material in terms of chemical reactivity, compression, solubility and various other properties that need to be strictly controlled in industry sectors such as pharmaceuticals.[4-7] Uncovering structure-stability connections, and how polymorphs may interconvert through phase transitions, is therefore of considerable importance if the reproducible and selective preparation of crystal forms with the best properties for specific applications and manufacture processes is to be achieved using crystal engineering strategies.

The proposal that $Z' > 1$ polymorphs are metastable relative to $Z' = 1$, introduced about a decade ago,[8-9] carries deep meaning and, since then its degree of universality has been under scrutiny. The suggestion was born from the idea that from a crystallographic point of view clean-cut symmetry expression and stability should go hand in hand. High Z' structures might, therefore, correspond to arrested crystallization stages, originated by the non-equilibrium nature of the nucleation pathway, which would ultimately lead to a $Z' = 1$ form if thermodynamic control could be achieved.[8-9] Albeit, $Z' > 1$ cases represent only a small percentage of the structures deposited in the Cambridge Structural Database, which are mostly of $Z' = 1$ type,[10] they seem to be quite common for particular classes of compounds. In alcohols, for example, the frequent occurrence of high Z' structures has been assigned to the difficulty of balancing close molecular packing with hydrogen-bond formation.[11-13] There seems, in fact, to be a consensus that this type of conflict often leads to the formation of $Z' > 1$ structures.[9, 14-15] Other possible origins of $Z' > 1$ structures have, nevertheless, been considered along the years, such as modulation (i.e. structures in which small periodic changes in the position and or orientation of the independent molecules in the asymmetric unit can make them crystallographic equivalent),[16] local symmetry preferences that are incompatible with the space group symmetry,[17] differences in molecular conformation between different polymorphs,[18] the co-existence in the crystal lattice of a large number of energetically similar conformations of the same molecule,[19] or molecular shapes favoring the stacking of building

blocks composed of more than one molecule.[20-21] These aspects have all been addressed in a recent seminal review on high Z′ crystal structures,[22] which also highlights the fact that the debate on the relative stability of Z′ = 1 and Z′ > 1 polymorphs has been mostly centered on a structural perspective.[22]

The discussion should not, however, be divorced from thermodynamics, which provides the appropriate theoretical framework to assess the relative stability of molecular systems in general, and therefore also of polymorphs.[4, 23-25] Each crystalline form of a given molecule is characterized by a specific molar Gibbs energy value, G_m, which depends on the temperature (T) and pressure (p). The most stable form under a given set of p-T conditions is the one with the lowest Gibbs energy, all other forms being metastable relative to that one. The G_m value is necessarily linked to structure and that relationship can be evidenced by recalling that:[26]

$$G_m = H_m - TS_m \tag{5.1}$$

$$= U_m + pV_m - TS_m \tag{5.2}$$

where H_m, U_m, V_m and S_m are the molar enthalpy, internal or lattice energy, volume and entropy functions. All these functions are related to structure. The molar volume is, for example connected to the unit cell dimensions and the number of molecules it contains; the lattice energy is essentially determined by the van der Walls and hydrogen bond interactions between molecules in the lattice, which are influenced by the packing arrangement; and, in most cases, entropy essentially depends on molecular and lattice vibration modes albeit other contributions (e.g. rotational, electronic) may also be present.[27] Changing a particular molecular conformation or unit cell dimension will necessarily lead to a different G_m value and to a change in stability. Since stability increases as G_m decreases, eq. 5.2 indicates that the most stable structure will correspond to the packing arrangement that minimizes the U_m and V_m terms and

maximizes the S_m contribution in eq. 5.2. Adopting that crystalline arrangement will therefore involve an elaborate compromise between molecular constraints to close packing, maximization of intermolecular interactions and maximization of entropy. It is conceivable that in some cases this will require a departure from close packing and the adoption of a lower crystal symmetry. Close molecular packing may, for example, imply unfavorable molecular interactions, such as charge or dipole repulsions, and a strong hydrogen bonding pattern may require a loose molecular packing. Thus, as previously pointed out, there seems to be no obvious relationship between crystal symmetry and enthalpy or entropy.[28]

The fact that polymorph stability must be analyzed from a Gibbs energy point of view should be stressed. The issue has, for example, frequently been discussed from lattice energy considerations alone.[8, 18] The tendency for spontaneous conversion of a given polymorph into a more stable one is, however, determined by the Gibbs energy of the transformation, $\Delta_{trs}G_m$

$$\Delta_{trs}G_m = \Delta_{trs}U_m + p\Delta_{trs}V_m - T\Delta_{trs}S_m \qquad (5.3)$$

which in addition to the internal energy term ($\Delta_{trs}U_m$) representing the difference in lattice energy of the two forms, further includes volume ($\Delta_{trs}V_m$) and entropic ($\Delta_{trs}S_m$) contributions. Thus, a higher lattice energy does not necessarily corresponds to higher stability. It is also often overlooked that, because the Gibbs energy varies with pressure (p) and temperature (T) the conclusion that a less stable polymorph should spontaneously transform into a more stable one ($\Delta_{trs}G < 0$), may be overturned if T and/or p changes. In other words, the most stable polymorph may be different if different p-T domains are considered.

The thermodynamic investigation of enantiotropic systems involving two polymorphs with different Z′ is particularly interesting in this context since enantiotropy is characterized by the existence (at constant pressure) of a transition temperature before fusion at which the stability of the two forms is reversed. The determination of the accurate thermodynamic data

necessary to these studies usually requires slow painstaking procedures which are not devoid of pitfalls.[23, 25, 29-30] One important complication that often arises is the existence of kinetic barriers associated with solid-solid phase transitions. The observation of an enantiotropic phase transition on heating a sample at constant pressure requires the nucleation and growth of the high temperature polymorph within the precursor low temperature form. Conversely, in the cooling mode, the low temperature polymorph must be generated from the high temperature phase. Two important points should be kept in mind: (i) some degree of superheating or supercooling, respectively, is necessary for these processes to occur and (ii) the heating and cooling modes are not symmetrical. If true equilibrium conditions (T_{eq}) were achievable, both phases would be present in a proportion governed by the equilibrium constant of the process and no progress of the phase transition in the direct or reverse direction could be observed. Above T_{eq} the low temperature polymorph will tend to transform into the high temperature polymorph and below that temperature the opposite tendency prevails. According to classical nucleation theory the rates of the direct and reverse processes are both determined by the Gibbs energy barrier (ΔG_c) associated with the formation of a critical nucleus (i.e. a nucleus which further growth will originate the new phase) and the activation energy (E_a) for that nucleus to grow by transfer of molecules from the mother to the daughter phase, which may follow an Arrhenius relationship. The driving force for the formation of a critical nucleus increases as superheating or supercooling become more pronounced. In contrast, while heating favors overcoming E_a, the opposite occurs on cooling. This frequently leads to the observation of an enantiotropic phase transition well above or below its equilibrium temperature and without evidence of reversibility, when techniques such as differential scanning calorimetry (DSC) are used.[30-37] It may also happen that the transition may be undetected because, once the equilibrium temperature is surpassed, the transformation will slowly progress and become smeared throughout a large temperature range[34, 38] or it is ultimately be hindered up to fusion.[36]

Kinetic barriers are not exclusive of thermal activation processes and cases have been described where they were also most likely behind the detection of irreversible enantiotropic transformations of low-Z′ into high-Z′ polymorphs, using grinding or slurry tests.[39-42] Several molecular organic solid systems have, nevertheless, been reported where the interconversion

of enantiotropically related high-Z′ and low-Z′ forms due to temperature or pressure changes has unequivocally been demonstrated. Thus, for example, variable temperature X-ray diffraction (XRD) experiments carried out at ambient pressure, revealed a reversible [Z′ = 3] ⇌ [Z′ = 1] transition between two monoclinic polymorphs of 5,11-methano-2,8-diisopropyllethyl-5,6,11,12-tetrahydrodibenzo[*b*,*f*] [1,5]diazocin, at 130 K.[21] XRD and DSC studies evidenced a [Z′ = 1] ⇌ [Z′ = 2] transition, involving monoclinic and orthorhombic phases of dichloro-2',4',6'-triethylbenzophenone.[43] Using single crystal XRD analysis with synchrotron radiation at ambient temperature, methyl 2-(carbazol-9-yl) benzoate was found to undergo a reversible [Z′ = 8] ⇌ [Z′ = 2] phase transition between monoclinic and orthorhombic phases, upon pressurization to 5.3 GPa and depressurization to 4.9 GPa. A reversible thermally induced [Z′ = 0.5] ⇌ [Z′ = 1.5] transition involving two monoclinic polymorphs of 1,6-hexanedioic acid was observed at 130 K and characterized by variable temperature XRD.[44] Recently, two monoclinic forms of ciclopirox were also found to be related by a reversible [Z′ = 12] ⇌ [Z′ = 1] single crystal-to-single crystal transition which was investigated by a variety of structural, spectroscopic and thermoanalytical techniques.[45]

In the first three cases no strong directional contacts are present that could generate a conflict with close packing leading to the high Z′ structures. In the fourth one, however, the phase transition was attributed mainly to the formation (on cooling) or disruption (on heating) of O–H···O hydrogen bonds connecting the 1D backbone packing motifs, which consist of infinite chains sustained by a different type of O–H···O interactions assembled in a $R_2^2(8)$ pattern typical of carboxylic acid dimers. In the fifth example O–H···O hydrogen bonds organized as $R_2^2(10)$ dimeric motifs are present, but they are not disrupted upon the phase transition. The process mostly consists of an interconversion between an ordered low-temperature Z′ = 12 form and a disordered high temperature Z′ = 1 form.

Thus, reversibility is not solely observed in the absence of strong directional interactions, albeit they will certainly contribute, in many cases, to increase the kinetic barriers that ultimately hinder thermal polymorph interconversion in enantiotropic systems. There is

also no relationship between the stability domain of a given form and its Z′ value: high-Z′ polymorphs can correspond to either the low temperature or high temperature phase vis-a-vis their low-Z′ counterparts. It should finally be noted that reversible thermal transitions between polymorphs with the same high-Z′ have been described.[46-47]

4'-Hydroxyacetophenone (HAP), has proved to be a rich system in terms of solid form diversity, with at least two polymorphs and three hydrates identified and characterized from structural,[39, 48-53] solid state stability,[39, 51-52] and crystallization points of view.[52, 54-55] The anhydrous polymorphs also provide an opportunity to study structure-energetics relationships behind the adoption of high-*Z*' structures and their relative stability towards a *Z*' = 1 counterpart, when solid state interconversion is hindered by kinetic barriers. Indeed, DSC and XRD studies carried out at atmospheric pressure previously evidenced an irreversible phase transition between the two HAP polymorphs where packing, molecular conformation, and *Z*' simultaneously change.[39] On heating HAP form II (orthorhombic, space group $P2_12_12_1$, *Z*' = 2)[39, 48-50] from ambient temperature, an endothermic transformation into form I (monoclinic, $P2_1/c$, *Z*' = 1)[39] was observed at 351.2±2.7 K.[39] The reverse process was not detected on cooling and both forms could be stored unaltered without strict control of laboratory temperature, pressure or humidity. This robustness towards interconversion was observed, even if the available thermal energy at 298 K (*RT* = 2.5 kJ·mol^{-1}) was ~5 times larger than the difference between the lattice enthalpies of form II and form I at that temperature (0.49±0.13 kJ·mol^{-1}) determined by solution calorimetry. The reduction of the number of molecules in the asymmetric unit from *Z*' = 2 to *Z*' = 1, was accompanied by a change in molecular conformation, since the relative orientations of the OH and C=O groups switched from *Z* in form II to *E* in form I (Figure 5.1).[39]

The *Z* conformations of the two molecules in the asymmetric unit of form II are very similar in terms of distances and dihedral angles. Moreover, albeit in both cases the 1D packing motifs consisted of infinite linear chains C(8) sustained by "head-to-tail" bonding between the hydroxyl group of one molecule (donor) and the carbonyl group of an adjacent molecule (acceptor), the chains changed from helicoidal in form II to linear in form I (Figure 5.1).[39] It is finally worth mention that the higher lattice enthalpy of the low temperature form II also corresponds to a slight density advantage, since the density of form II at 298 K (1.278 g·cm^{-3}) is

2.4% larger than that of form I (1.247 g·cm^{-3}), even though the packing fractions of both polymorphs are very similar (~0.70).[39]

In this work the thermodynamics and kinetics of the solid-solid phase transition involving the two HAP polymorphs was investigated by DSC, adiabatic calorimetry and solubility measurements. The structure/energetics features behind the occurrence of the *Z*' = 2 (form II) or *Z*' = 1 (form I) structures in HAP were investigated from various angles. The conflict between achievement of close packing and maximization of lattice energy was examined

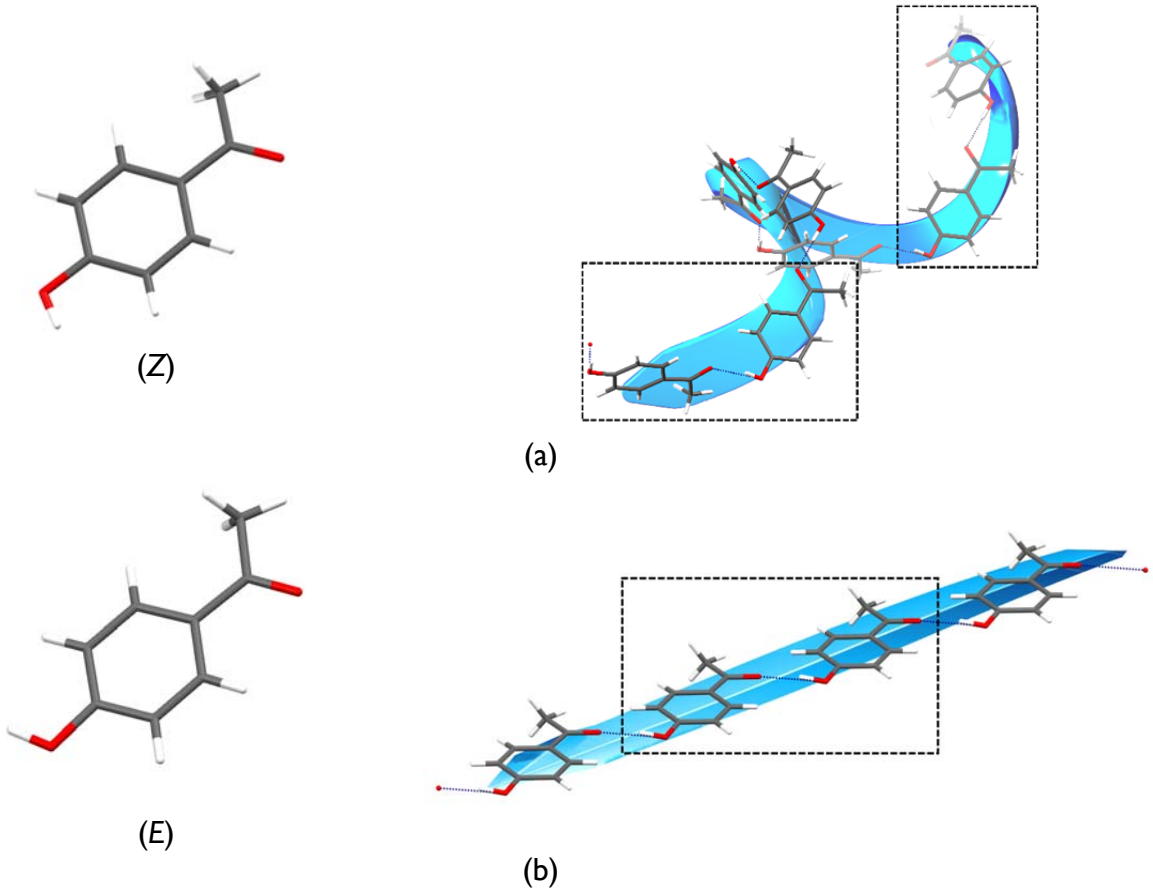

Figure 5.1 Molecular conformations and 1D packing motifs of 4'-hydroxyacetophenone polymorphs: (a) form II; (b) form I. The dashed boxes indicate the dimeric units used in the quantum chemistry calculations carried out in this work (see text).

from: (i) a comparison of the lattice energy difference between forms I and II HAP, with the relative stability of hydrogen bonded dimers representative of their head-to-tail 1D packing motifs obtained from DFT calculations and (ii) a Hirshfeld surface analysis of the relative contributions of different packing interactions. The role of enthalpic and entropic contributions in determining the preference for the *Z*' = 1 or the *Z*' = 2 polymorphs in different temperature ranges was elucidated based on DSC, adiabatic calorimetry and solubility experiments. DSC experiments also allowed to investigate the activation energy of the form II $\rightarrow$ form I transformation. The overall results provided a detailed view of the thermodynamic/kinetic profile relating forms I and II HAP and of the major energetic reasons behind the preference of Z′ = 1 or *Z*′ = 2 structures in different temperature domains. They also corroborate the conclusion,[22] that the metastability of Z′ > 1 polymorphs relative to *Z*′ = 1 forms cannot be considered universally true.

5.2 Materials and Methods

Ethanol (Panreac, mass fraction 0.999) and acetonitrile (Fisher Scientific, HPLC grade, mass fraction 0.9999) were used as received.

Form I HAP was obtained by sublimation of a commercial material (Fluka, mass fraction 0.98), at 368 K and 13 Pa. GC-MS analysis performed as previously reported[39] indicated that the purified sample had a mass fraction >0.9999. The powder pattern recorded at 298±2 K was indexed as monoclinic, space group $P2_1/c$, a = 7.704(8) Å, b = 8.337(8) Å, c = 11.268(9) Å, β = 94.98(2)°. The indexation is in agreement with previously reported data from single crystal X-ray diffraction: a = 7.7200(15) Å, b = 8.3600(17) Å, c = 11.280(2) Å, β = 95.02(3)°.[39]

Form II was prepared by magnetically stirring a suspension of form I in ethanol or acetonitrile, below 300 K, for ~1 week. This procedure was suggested by the solubility determinations described below. The powder pattern of the obtained material, recorded at 298±2 K, was indexed as orthorhombic, space group $P2_12_12_1$, a = 6.114(6) Å, b = 9.569(9) Å, c = 24.324(52) Å. These results are in agreement with previously reported single crystal X-ray diffraction data: a = 6.1097(11) Å, b = 9.5293(14) Å, c = 24.313(4) Å, β = 90.00°.[39] Large form II

single crystals (1-2 mm edge) were also obtained by the following procedure. A saturated ethanol solution of form I was prepared inside a Schlenk flask at ambient temperature (295±1 K) under magnetic stirring. The flask containing the solution was transferred to a thermostatic bath, where it was kept at 325 K for ~2 h and then cooled to 275 K at a rate of ~10 $K \cdot h^{-1}$. Crystals were collected by filtration, after ~24 h, and dried under reduced pressure. Their identification as form II HAP was carried out by powder X-ray diffraction and DRIFT spectroscopy.

The powders of forms I or II used in the DSC studies consisted of 250-88 μm (60-170 mesh) particles and were obtained by grinding and sieving the original samples. Sieving was done by means of a Scienceware mini-sieve micro sieve set (apertures 707, 500, 354, 250, 88 and 63 μm). The phase purity of the grinded/sieved materials was assessed by powder X-ray diffraction and DRIFT spectroscopy.

5.2.1 X-ray Powder Diffraction (XRPD)

The X-ray powder diffractograms were recorded on a Philips X'Pert PRO diffractometer with automatic data acquisition (X'Pert Data Collector v2.0b), operating in the θ-2θ mode. The apparatus had a vertical PW 3050/60 goniometer and a X'Celerator detector. A monochromatized Cu Kα radiation source set to 30 mA and 40 kV was used. The diffractograms were recorded at ~293 K, in the range $5° < 2\theta < 35°$ using continuous scanning mode with a step size of 0.017° (2θ) and a step time of 20 s. The samples were mounted on an aluminum sample holder. The indexation of the powder patterns was performed using the program Cellref.[56]

5.2.2 Diffuse Reflectance Infrared Fourier Transform (DRIFT) spectroscopy

DRIFT spectra were collected in the 400 - 4000 cm^{-1} range using a Nicolet 6700 spectrometer equipped with a Smart Diffuse Reflectance (SDR) kit (Thermo Electron Corp.) and a deuterated triglycine sulfate (DTGS) detector. The wavenumber scale was calibrated with

polystyrene film, the selected resolution was 2 cm^{-1} and 512 scans were used for both the background and sample runs. The background spectra were recorded with pure KBr (Sigma-Aldrich, FTIR grade). The samples were prepared by grinding the appropriate HAP and KBr quantities to obtain a spectral absorbance in a range compatible with the Kubelka-Munk transformation.[57] The amount of sample in the sample-holder was consistent with infinite thickness conditions.

5.2.3 Raman spectroscopy

Raman spectra of form II in a temperature range covering the phase transition were recorded with a Raman RXN1 Analyzer (Kaiser Optical Systems, Inc., Ecully, France) using NIR excitation at 785 nm and a sample irradiance of 6.4 $W \cdot cm^{-2}$. The spectra were collected at 30 s intervals using acquisition times of 4×4 s and a resolution of 4 cm^{-1}. A single crystal of form II was placed in a levitation device [58] and heated from 303 K to 363 K, in steps of 5 K using equilibration stages of ~600 s. The crystal temperature was maintained constant by a nitrogen steam that passed through a thermostatized oven located immediately bellow the levitation device. The oven temperature was controlled by a Eurotherm unit connected to a thermocouple, placed as close as possible to the sample.[58]

5.2.4 Hot-Stage Microscopy (HSM)

An Olympus BX51 microscope coupled with a Linkam hot stage LTS350 and an Olympus SC-30 digital camera was used for visualizing the form II → form I solid-solid phase transition of HAP. The temperature was controlled by a Linkam TMS 94 controller. The sample was placed on the hot stage, which was heated from 298 K to 373 K at 5 $K \cdot min^{-1}$. Images were recorded at regular intervals in polarized light.

5.2.5 Differential Scanning Calorimetry (DSC)

The DSC investigation of the solid-solid and fusion phase transitions observed for forms I and II HAP was carried out by using powders and single crystals.

The experiments on powders were performed on a DSC 204 F1-Phoenix from Netzsch. Heating rates of 1, 10, and 80 $K \cdot min^{-1}$ were used. The temperature and heat flow scales of the apparatus were calibrated at the same heating rates with indium (Netzsch, mass fraction: 0.99999, T_{fus} = 429.75 K, $\Delta_{fus}h^{\circ}$ = 28.6 $J \cdot g^{-1}$). The HAP samples with a mass of ~5 mg were sealed in aluminum crucibles and weighed with a precision of ±0.1 μg on a Mettler XP2U ultra-micro balance. Nitrogen (Air Liquide N45) was used as purge and protective gas, at flow rates of 20 $cm^3 \cdot min^{-1}$ and 50 $cm^3 \cdot min^{-1}$, respectively. The instrument control and data treatment procedures were carried out with the Netzsch Proteus Software V. 6.1.0.

Studies on form II HAP single crystals were performed either on the Netzsch instrument or in a TA Instruments 2920 MTDSC apparatus. In a typical experiment, a single crystal of HAP form II with 0.2-1.5 mg mass was sealed in an aluminum pan and weighed with a precision of ±0.1 μg in a Mettler UMT2 or Mettler XP2U ultra-micro balance. The Netzsch DSC was operated as described above using heating rates of 1, 5, 10, 12, 14, 16, and 20 $K \cdot min^{-1}$. In the case of the TA apparatus, helium (Air Liquide N55), at a flow rate of 30 $cm^3 \cdot min^{-1}$, was used as the purging gas. The heating rates were 8, 10, and 14 $K \cdot min^{-1}$. The temperature and heat flow scales were calibrated at the same heating rates as previously described.[59]

Low temperature annealing of powdered HAP samples was performed on the DSC 204 F1-Phoenix from Netzsch. Samples (~5 mg) of both forms I and II were sealed in aluminum crucibles and weighed with a precision of ±0.1 μg on a Mettler XP2U ultra-micro balance. The crucibles were placed in the calorimeter furnace and subjected to three consecutive heating/cooling cycles in the temperature range 213 K to 268 K. In each cycle the samples were first cooled from 268 K to 213 K at 0.2 $K \cdot min^{-1}$ and then heated from 213 K to 268 K at 0.5 $K \cdot min^{-1}$. An isothermal step of 3 hours was incorporated between each dynamic scan. The annealed samples were then analyzed in separate experiments as described above at heating rates of 0.25, 0.5, 1 and 2 $K \cdot min^{-1}$.

Experiments carried out on annealed form II powdered samples were also used to investigate the form II $\rightarrow$ form I phase transition kinetics. This study was based on the determination of the II $\rightarrow$ I conversion fraction (α) as a function of temperature (T) using:

$$\alpha = \frac{A_0^T}{A_0^\infty} \tag{5.4}$$

where A_0^T is the area of the phase transition peak up to temperature T and A_0^∞ is the total area of the peak. The full α-T curve was obtained with the Netzsch Proteus Analysis software Version 6.1.0.

Heat capacity measurements on liquid HAP, in the temperature range 385.3-400.1 K, were performed on a DSC 7 from Perkin Elmer. The procedure was described elsewhere.[23, 60] The heating rate was 2 $K \cdot min^{-1}$, the samples had ~5 mg mass and sapphire (Perkin Elmer α-Al_2O_3 disks, mass fraction: 0.9998) was used as reference. The molar heat capacity, $C_{p,m}$, at a given temperature was obtained from:

$$C_{p,m} = k \frac{M}{m\beta} \Delta\phi \tag{5.5}$$

where m and M are the mass and the molar mass of the compound, respectively, β is the heating rate, $\Delta\phi$ is the difference in heat flow rate between the main and blank runs at a given temperature, and k is a calibration factor obtained from an analogous run carried out with sapphire. Heat capacity measurements were also carried out on form I HAP to assess the accuracy of the method against adiabatic calorimetry.

5.2.6 Adiabatic calorimetry

The heat capacities of forms I and II HAP in the temperature ranges 299-373 K and 294-373 K, respectively, were obtained with a fully automated setup consisting of a vacuum adiabatic calorimeter and an AK-9.02 control and data acquisition system connected to a computer. The apparatus and method have been described.[61-63] During the calorimetric measurements the sample with a mass of 302.19 mg (form I) or 377.57 mg (form II) was contained in a cylindrical titanium cell of ~1 cm^3 internal volume, tightly fitted into a copper sleeve, surrounded by an adiabatic shield. Weightings were performed with a precision of ±0.05 mg using a Mettler balance. The adiabaticity of the calorimeter was ensured by an AK-9.02 unit, which maintained the temperature difference between the sample container and shield within ±1-3 mK, throughout an experiment. The temperature of the shield, T_{shield}, was monitored with an accuracy of ±3 mK using a rhodium-iron resistance thermometer. The temperature difference between the adiabatic shield and the cell, ΔT_{s-c}, was measured to ±0.01-0.02 K with a four-junction thermocouple. The temperature of the sample (assumed identical to that of the calorimetric cell) was obtained by combining the T_{shield} and ΔT_{s-c} values. A typical experiment consisted of six periods: (i) fore period where the sample was heated to the desired initial temperature; (ii) equilibration period to attain a steady reading at that temperature; (iii) initial baseline recording (6 min); (iv) main period (4 min), where a known electrical energy (~3 J) was supplied to the calorimeter at a rate of 0.3 $K \cdot min^{-1}$; (v) equilibration period (10 min) to attain a steady temperature reading; (vi) final baseline recording (6 min). Further data points were obtained by repeating steps (iii)-(vi). This procedure had been previously validated by measuring the heat capacity of copper (mass fraction 0.99995) and *n*-heptane (chromatographically pure). The obtained accuracy in the temperature range 80-373 K was ~0.2%.

5.2.7 Solubility measurements

Equilibrium solubility measurements on HAP, in ethanol and acetonitrile, were carried out by using the previously described set-up and gravimetric procedure.[64] The determinations were performed in the 283-312 K range, using ascending and descending temperature

sequences with ~2 K steps. The temperature of the mixture inside each glass cell was controlled to ±0.01 K by circulating water from a thermostatic bath through the cell jacket, and monitored with a resolution of ±0.01 K by a Pt100 thermometer. In a typical experiment, a suspension of HAP in 7 cm^3 of solvent was initially equilibrated at a desired temperature for one week. After the equilibration period, three samples of the supernatant liquid (3 cm^3 each) were extracted using a preheated syringe adapted to a micro filter (Whatman Puradisc 25 TF, 0.2 μm PTFE membrane). The corresponding masses of solvent and solute were determined by weighing the samples before and after being taken to dryness. Based on these determinations, the mole fraction of HAP in the saturated solution, x_{HAP}, could be determined as the mean value from the three samples. At each equilibration temperature, a sample of the solid phase was collected and analyzed for phase identification by DRIFT spectroscopy.

5.2.8 Computations

Quantum chemical calculations were used to evaluate the energetic differences between the molecular conformations of the HAP molecules in the gas phase and as they exist in the solid forms I and II. Also computed were the H-bond energies in dimmers representing the 1D packing motifs for each polymorph (Figure 5.1). All calculations were carried out with the Gaussian 09 package,[65] using the B3LYP-D3 hybrid functional,[66-69] where D3 denotes the addition of the dispersion corrections proposed by Grimme *et al*[69] to the B3LYP functional. Full (gas phase conformations) and partial (solid state conformations) geometry optimizations were performed with the cc-pVDZ basis set.[70-71] In the partial optimizations, only the hydrogen positions were allowed to relax and, in the case of HAP dimers, the relative orientation of the molecules and their intermolecular distance were kept as in the crystal structure. Single point energy calculations for each optimized structure were carried out at the B3LYP-D3/aug-cc-pVTZ level of theory.[66-71] In the case of dimmers correction for the basis set superposition error by the counterpoise method was performed.[72] No zero point energy and thermal corrections were considered.

Hirshfeld surface analysis was carried out with Crystal Explorer 3.1.[73-75] The weight-function used in the spatial partitioning and construction of molecular Hirshfeld surfaces was

determined from spherically averaged atomic electron densities calculated at the HF level using the Thakkar Slater-type basis set.[76] These calculations were performed with the TONTO quantum chemistry program distributed with Crystal Explorer.

5.3 Results and Discussion

As substantiated below, differential scanning calorimetry, adiabatic calorimetry and solubility studies showed that in the case of HAP, the thermodynamic preference for a Z' = 1 or Z' = 2 polymorph depends on the temperature range considered. Only the form II (Z' = 2) $\rightarrow$ form I (Z' = 1) transition can be observed in the solid state and, despite the high activation barrier, hot stage microscopy experiments revealed that the process can unequivocally occur under single crystal to single crystal conditions. The direct solid-solid transition is typically observed at a temperature well above (c.a. 30 K to 70 K, depending on the heating rate) that corresponding to equilibrium conditions (300.1±0.4 K, see section on solubility studies below). It is nevertheless possible to interconvert the two forms under conditions of thermodynamic control if, as in the solubility studies, the phase transition is mediated by a solvent. Important insights into the structural aspects behind the adoption of the high or low Z' structures were provided by quantum chemistry and Hirshfeld surface analysis of the main interactions involved in the molecular packing. Detailed results of the DSC, adiabatic calorimetry, solubility measurements and of the quantum chemistry calculations are given as Supporting Information. All uncertainties quoted for thermodynamic and kinetic quantities in the present work correspond to twice standard errors of the mean.

5.3.1 Differential Scanning Calorimetry

When a sample of polymorph I HAP in powder form (250-88 μm particles) was heated at different rates (1, 10, and 80 $K \cdot min^{-1}$) in the temperature range 293-418 K no phase transitions other than fusion, with onset T_{on} = 382.0±0.6 K and $\Delta_{fus}H^{o}_{m}$ = 18.1±0.2 $kJ \cdot mol^{-1}$, were observed. These results are similar to those previously obtained at 1 $K \cdot min^{-1}$

(T_{on} = 381.9±0.1 K; $\Delta_{fus}H^{o}_{m}$ = 18.08±0.07 kJ·mol^{-1}).[39] Different patterns were, however, evidenced when the experiments were repeated with form II HAP powder. As illustrated in Figure 5.2a for β = 1 K·min^{-1}, the measured curve showed the II → I phase transition at T_{on} = 356.8±4.8 K ($\Delta_{trs}H^{o}_{m}$ = 0.6±0.2 kJ·mol^{-1}), followed by fusion of form I at T_{on} = 381.71±0.04 K. No signature of the reverse I → II process was noted when a form II sample was heated above the phase transition range without melting and then cooled to 213 K. This is consistent with previous results obtained for form II at the same heating rate.[39] For β = 10 K·min^{-1}, the II → I phase transition peak was absent. In this case, fusion of form II was observed at T_{on} = 377.2±0.2 K, followed by the crystallization of metastable liquid HAP into form I, which subsequently melted at T_{on} = 381.9±0.2 K. Finally, at β = 80 K·min^{-1}, the fusions of forms II and I could not be separated. In this case only a broad peak with an onset (T_{on} = 378.8±0.2 K) corresponding to the fusion of form II and a shoulder with maximum at T_{max} = 390.1±0.8 K (a temperature consistent with form I melting) was observed.

When similar experiments were carried out with single crystals of form II (one crystal of 1-2 mm edge inside the crucible), using heating rates of 1-20 K·min^{-1}, the three following patterns were observed (Figure 5.2b). In most cases, independently of the

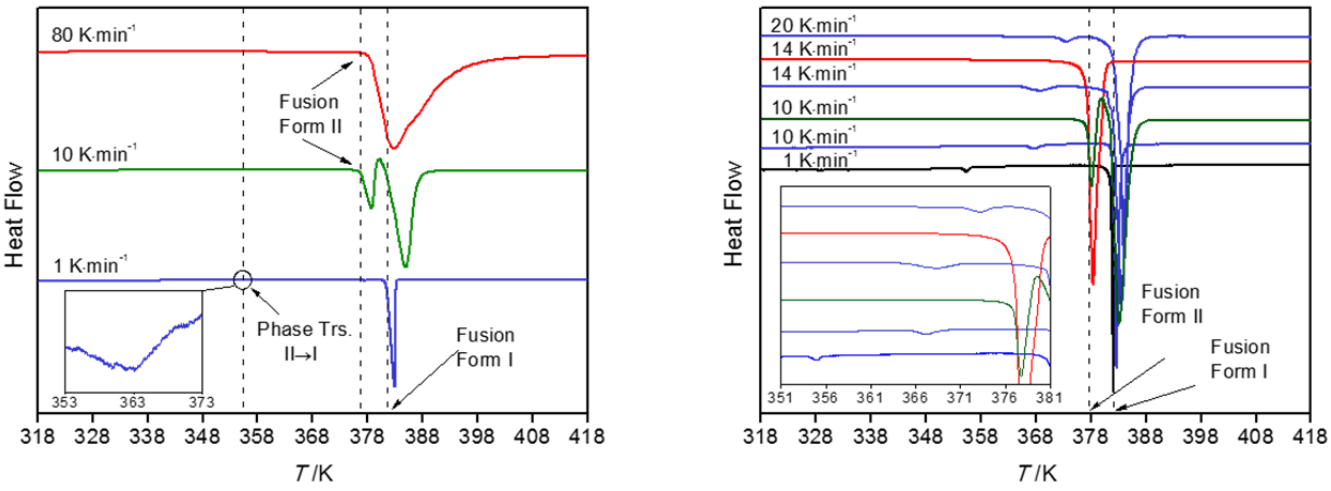

(a) (b)

Figure 5.2 Differential scanning calorimetry curves obtained at different heating rates for (a) HAP powders and (b) single crystals.

heating rate, the measured curve evidenced the II → I phase transition followed by fusion of form I. While the fusion temperature was fairly insensitive to the heating rate, with a mean value for all heating rates of 382.1±0.2 K, the onset of the phase transition increased from 351 K to 371 K on increasing β from 1 K·min^{-1} to 20 K·min^{-1}. In a few cases where β = 8, 10, or 14 K·min^{-1}, either (*i*) a single sharp peak corresponding to the fusion of form II (T_{on} = 377.7±0.2 K; $\Delta_{fus}H^{o}_{m}$ = 19.1±0.6 kJ·mol^{-1}) was detected or (*ii*), as in the case of powders, the DSC curve showed the fusion of form II followed by crystallization of the metastable liquid into form I and finally the fusion of form I.

Overall, the DSC patterns observed at different heating rates using powders and single crystals deserve the following comments: (*i*) The fact that a clean fusion of form II could only be observed with single crystals probably reflects a more hindered nucleation of form I on a form II crystal of higher perfection. This is in agreement with previous results on, for example, *p*-dichlorobenzene.[77] (*ii*) Both for single crystals and powders, whenever fusion of form II was not present, and regardless of the heating rate, the DSC curve always evidenced the II → I phase transition followed by fusion of form I. (*iii*) Increasing the heating rate shifted, however, the onset of the phase transition to a higher temperature (e.g. Figure 5.2b). This is typical of thermally induced nucleation and growth processes, where a widening of the metastable zone width is normally observed on increasing the heating/cooling rate. (*iv*) The three peak endo → exo → endo patterns shown in Figures 5.2a and 5.2b, correspond to cases where the heating rate is sufficiently high for the fusion temperature of form II to be reached (first endothermic peak), before nucleation and growth of the thermodynamically stable form I occurs inside the metastable form II. (*v*) The observation that the enthalpy of fusion obtained for form II ($\Delta_{fus}H^{o}_{m}$ = 19.1±0.6 kJ·mol^{-1}) is larger than that obtained for form I ($\Delta_{fus}H^{o}_{m}$ = 18.1±0.2 kJ·mol^{-1}) is in accordance with Burger's heat of fusion rule, which states that in an enantiotropic system the higher melting polymorph will have the lowest enthalpy of fusion.[4, 31-32] (*vi*) The fact that the II → I process was found to be endothermic, irreversible and with an onset that increased with the heating rate gave a good indication that, even at the lowest heating rate (β = 1 K·min^{-1}), the phase transition temperature (T_{on} = 356.8±4.8 K) is considerably higher than the "true" equilibrium value. Further evidence that this was indeed the

case (large metastable zone width) was provided by the adiabatic calorimetry and by the solubility results discussed in the sections below. The latter, in particular, allowed the assignment of that transition temperature to 300.1±0.4 K. This is in agreement with Burger's enthalpy of transition rule which indicates that if an endothermic solid-solid phase transition is observed in a DSC trace, then the corresponding equilibrium temperature must be at, or below, the temperature of the experimentally detected peak.[4, 31-32] It may also be recalled that, as mentioned in the Introduction section, some degree of superheating (heating mode) or supercooling (cooling mode) is always necessary for the occurrence of a nucleation and growth process involving two crystal phases. That degree is expected to significantly depend on the activation energy (E_a) of the process. The large metastable zone width found in the present work, therefore, suggested that a significant activation barrier should be associated to the II → I phase transition. This conclusion is also consistent with the notable irreversibility of the process, because the thermal energy available to overcome E_a progressively decreases as the system is being cooled below 300.1±0.4 K.

Effect of low temperature annealing. When a sample of annealed polymorph I HAP in powder form (250-88 μm particles) was heated at the rate of 1 K·min^{-1} in the temperature range 293-418 K, no phase transitions other than fusion (T_{on} = 381.52±0.06 K and $\Delta_{fus}H^o_m$ = 17.8±0.1 kJ·mol^{-1}) were observed. This observation suggests that low temperature annealing has no effect on the reversibility of phase transition as no I →II phase transition was detected.

When similar experiments were carried out with annealed polymorph II powder (250-88 μm particles), at a heating rate of 1 K·min^{-1}, a significant change in the reproducibility of the phase transition onset was observed. Figure 5.3 shows the DSC profiles of five experiments carried at 1 K·min^{-1} using non-annealed (Figure 5.3a) and annealed samples (Figure 5.3b). A much larger T_{on} dispersion is noted for the non-annealed (T_{on} = 356.8±4.8 K) than for the annealed (T_{on} = 356.9±0.8 K) samples. Also the peak profile seems to be broader and rougher in the first case. This is not unexpected since, when a substance is crystallized there are often defects within the crystals which lead to lattice strain.[78] Annealing tends to remove the lattice

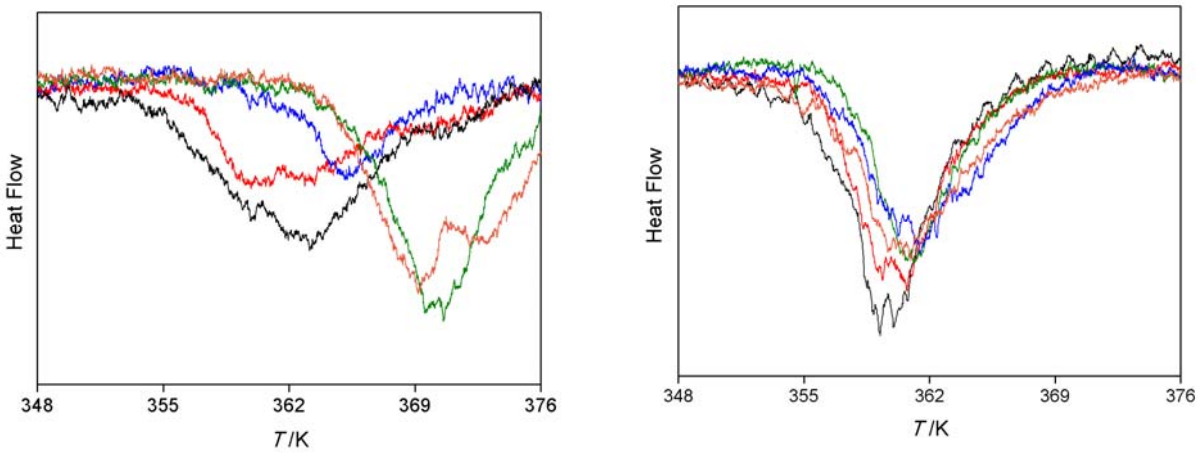

Figure 5.3 Differential scanning calorimetry curves obtained for polymorph II powder at 1 $K \cdot min^{-1}$: (a) non-annealed sample (b) annealed samples.

strain and reduce the number of defects in the crystallites and, as a result, the phase transition becomes smoother and more reproducible.

Kinetics of the form II → form I phase transition. All the DSC experiments carried out to investigate the activation barrier of the form II → form I transition were made on annealed form II powder samples. In principle, it is possible to evaluate the activation energy, E_a, of a phase transition using the conversion fraction α obtained from eq. 5.4 as a function of time (t) or temperature (T). Isothermal experiments were unsuccessful since the phase transition event has a very low enthalpy ($\Delta_{trs}H^{o}_{m}$ = 0.81±0.06 $kJ \cdot mol^{-1}$ for the annealed form II samples, see Supporting Information) and was widely spread over time so that the corresponding curve could not be accurately separated from the baseline. The kinetic analysis was therefore based on the non-isothermal experiments. Moreover all experiments were performed at heating rates of 0.25, 0.5, 1 and 2 $K \cdot min^{-1}$, because for larger heating rates the most common DSC pattern showed the fusion of form II without detection of the II → I phase transition. The obtained results are illustrated in Figure 5.4.

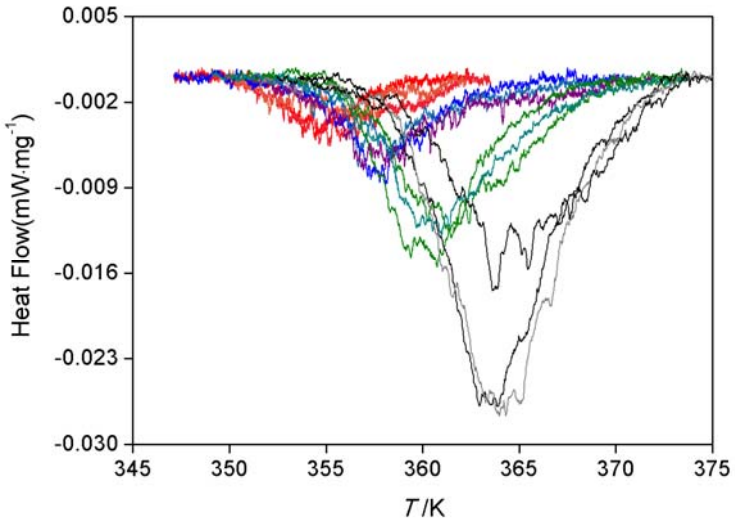

Figure 5.4 Plot of original data obtained from set of three experiments carried out on annealed powdered samples of form II at different heating rates. (From left to right: 0.25, 0.5, 1 and 2 $K \cdot min^{-1}$).

The E_a determination was based on the isoconversional approaches proposed by Starink,[79-82] and Vyazovkin,[83] (integral methods), and Friedman,[79] (differential method), which do not require any mechanistic hypothesis. The Starink procedure relies on the equation:

$$\ln\left(\frac{\beta}{T^{1.92}}\right) = C - 1.0008\frac{E_a}{RT} \qquad (5.6)$$

where, β is the heating rate, R is the gas constant, T and E_a are the temperature and activation energy at a given α, respectively, and C is a constant. Linear least squares fittings of eq. 5.6 to plots of $\ln\left(\beta / T^{1.92}\right)$ against $1/T$ for α values in the range 0.1 to 0.9 gave a series of straight lines with slopes $s = -1.0008E_a / R$. The activation energies were obtained from these slopes and can be considered constant along the full α range within the error bars of the determinations

(Figure 5.5). This supports the applicability of the isoconversional approach[84] and also suggests that the phase transition mechanism is the same throughout the conversion pathway.[85] The mean value of the results (see Supporting Information) corresponds to E_a = 240.4±13.5 kJ·mol^{-1}.

According to Vyazovkin's method the activation energy at a specific conversion fraction, α, is obtained by determining the E_a value that minimizes the equation:[83]

$$\sum_{i=1}^{n}\sum_{j\neq i}^{n}\frac{I\left(E_\alpha, T_{\alpha,i}\right)\beta_j}{I\left(E_\alpha, T_{\alpha,j}\right)\beta_i} = \min \tag{5.7}$$

where

$$I\left(E_\alpha, T_\alpha\right) = \int_0^{T_\alpha} \exp\left(\frac{-E_\alpha}{RT}\right)dT \tag{5.8}$$

In the previous equations, E_α and T_α are the activation energy and temperature corresponding to fraction α at different *i* and *j* heating rates, β. Equation 5.8 was evaluated numerically between 0.1 K and T_α, assuming that the integral between 0 and 0.1 K is equal to zero (the validity of this approximation was tested by using the program Mathematica 10). For this purpose, the trapezium rule was used with an interval length that led to a difference smaller than 10^{-6} between two consecutive iterations. The method was implemented in an Excel macro. The mean value of E_a obtained for different α (see Supporting Information) corresponds to E_a = 240.3±13.6 kJ·mol^{-1} and is virtually identical to the value obtained by Starink's method.

Friedman's differential method is based on equation:[79]

$$\ln\left(\frac{d\alpha}{dt}\right) = C - \frac{E_a}{RT} \qquad (5.9)$$

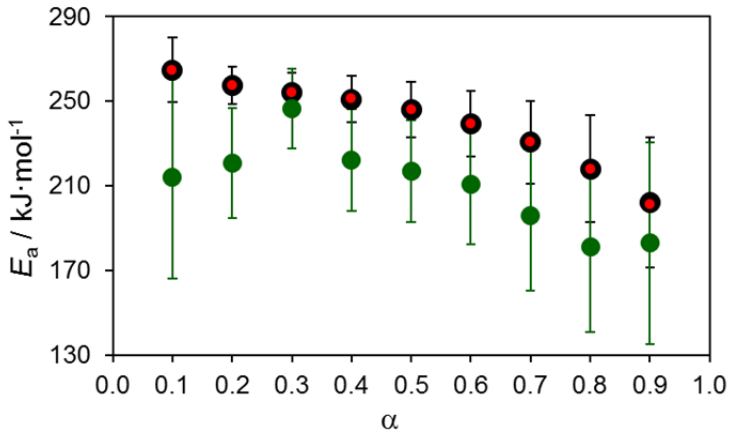

Figure 5.5 Activation energy, E_a, as a function of the conversion fraction, α, obtained from isoconversional analysis of DSC results in Figure 5.4 by using Starink's method (●),Vyazovkin's method (●) and Friedman's differential method (●).

and, in this case, the routine incorporated in the Netzsch Thermokinetics software Version 3.1 was used. The mean value of the E_a obtained for different α (see Supporting Information) corresponds to E_a = 210.2±13.8 kJ·mol^{-1}. It is therefore concluded that the three different isoconversional procedures tested in this work led to activation energies which are in agreement within their combined uncertainty intervals (Figure 5.5).

To obtain mechanistic insights the approach proposed by Khawam and Flanagan was also applied.[82] In this case, E_a values obtained by fitting various mechanistic models according to the Coats's Redfern[82] procedure are compared with the mean E_a value determined by Vyazovkin's isoconversional method. The most reliable mechanistic model is assumed to be the

one, which leads to the activation energy in better agreement with that derived from Vyazovkin's isoconversional analysis. The Avrami-Erofeev A2 and A3 nucleation and growth models were the ones that best fulfilled these criteria. (see Supporting Information). This is consistent with the above conclusion that the form II → form I transition occurs through a nucleation and growth mechanism.

The E_a results obtained for the phase transition, at different α, by the three isoconversional methods span the range 181-265 kJ·mol^{-1}, and correspond to a mean value E_a = 230.3±9.4 kJ·mol^{-1}. As can be seen in Figure 5.6, this value is considerably higher than the lattice energy of HAP as measured by the enthalpy of sublimation of form I at 298 K ($\Delta_{sub}H^{o}_{m}$ = 103.2±2.7 kJ·mol^{-1}).[39] Even the value corresponding to the lowest end of the activation energy range E_a = 195.0±13.7 kJ·mol^{-1} is larger than $\Delta_{sub}H^{o}_{m}$ =103.2±2.7 kJ·mol^{-1}. Albeit apparently strange, large activation energies have been typically obtained for polymorphic phase transitions in organic compounds using different experimental methods. Representative examples are summarized in Table 5.1**.** The origin of this finding, was, however impossible to ascertain in this thesis.

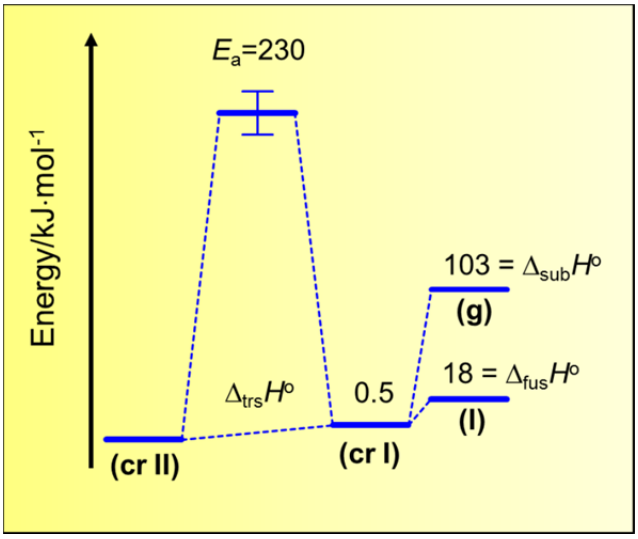

Figure 5.6 Energy profile of the crII → crI phase transition observed in HAP.

Table 5.1 Activation energies of phase transitions obtained for various organic compounds by different methods and corresponding enthalpies of sublimation.

Compound	Transition	E_a/ kJ·mol^{-1}(method)	$\Delta_{sub}H^o_m$ /kJ·mol^{-1}
FOX-7 ($C_2H_4N_4O_4$)	$\beta \rightarrow \gamma$ $\gamma \rightarrow \delta$	215.0 (DSC)[86] 647.4 (DSC)[86]	108.7[87]
Chlorothalonil ($C_8Cl_4N_2$)	$\alpha \rightarrow \beta$	650±90 (DSC)[88]	109.1[89]
Carbamazepine ($C_{15}H_{12}N_2O$)	form III → form I	344 to 368 (In-situ Raman spectroscopy)[90]	—
Mefenamic acid ($C_{15}H_{15}NO_2$)	form I → form II	299.6 (solid state infrared spectroscopy)[91] 361.5 (DSC)[92]	132.7±0.8[93]
Mebendazole ($C_{16}H_{13}N_3O_3$)	form C → form A	238±16 (variable temperature X-ray diffraction)[94]	—

5.3.2 Adiabatic calorimetry

The heat capacity measurements on forms I and II HAP by adiabatic calorimetry provided further support for the picture resulting from the DSC observations. Form I was studied in the range 299.20-369.79 K. As showed in Figure 5.7a (black solid line, open triangles), no evidence of phase transitions was obtained. Form II was subjected to the following measuring sequence: (i) heating from 294.38 K to 373.11 K; (ii) cooling to 79.12 K (without data recording) and (iii) re-heating from 79.12 K to 373.25 K. As shown in Figure 5.7a (blue solid line, open squares), when the sample was first heated from 294.38 K to 373.11 K the presence of the II → I phase transition was clearly apparent in the range 328.51-336.49 K. After the phase transition, the heat capacity curve followed that obtained for form I within ~0.15%. On re-heating the sample from 79.12 K and to 373.25 K (Figure 5.7b), the high temperature part of the recorded heat capacity curve (Figure 5.7a, red line, open circles) matched that obtained for form I (Figure 5.7a, black line, open triangles) within ~0.1%. It can be concluded

from these results that: (i) as observed in the DSC experiments, the endothermic form II → form I transition is irreversible; (ii) the onset of the phase transition is observed at T_{on} ~ 328 K, c.f. 29 K below that observed in the DSC runs corresponding to the lowest heating rate (1 K·min^{-1}); (iii) the peak corresponding to the phase transition is composed of a series of exothermic and endothermic events.

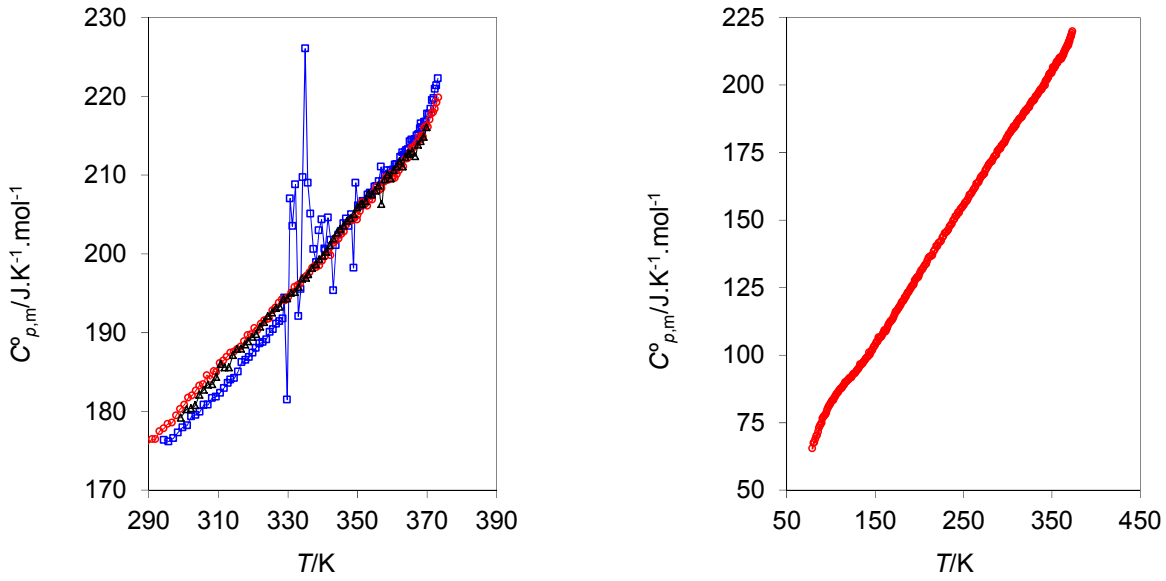

(a) (b)

Figure 5.7 Heat capacity of the two polymorphs of 4'-hydroxyacetophenone measured by adiabatic calorimetry. (a) Overlay of form I and form II data: heating of form I in the range 299.20-369.79 K (black solid line, open triangles); heating of form II from 294.38 K to 373.11 K (blue solid line, open squares) and final section of a second run where the same sample to was re-heated to 373.25 K, after cooling from 373.11 K to 79.12 K (red solid line, open circles). (b) Full data of the previous run in the range 79.12-373.25 K.

The adiabatic calorimetry experiments, where the lowest T_{on} value was observed, were carried out by a slow stepwise process in which the heating steps were separated by equilibration periods. This observation and the irreversible nature of the phase transition noted

in the calorimetric experiments suggest that the true equilibrium temperature of the form II → form I transition should be even lower than T_{on} ~ 328 K, obtained in the adiabatic calorimetry experiments. This was in fact confirmed in the equilibrium solubility studies described below, which allowed the assignment of that transition temperature to 300.1±0.4 K. The few exothermic "sparks" observed throughout the phase transition range are perhaps originated by the release of internal strains accumulated within the crystalline material. This is supported by the fact that such effect is much less pronounced in DSC experiments carried out with annealed than with non-annealed samples.

5.3.3 Solubility

As mentioned above, the results of the DSC and adiabatic calorimetry experiments suggested that, for kinetic reasons, the onset temperatures of the II → I phase transition observed for different heating regimes did not correspond to equilibrium values. The thermodynamic equilibrium temperature, T_{trs}, was, therefore, determined from solubility studies in ethanol and acetonitrile, where the nature of the solid phase in equilibrium with the solution at each temperature was monitored by DRIFT analysis.[33] These experiments allow overcoming the energy barrier hindering the direct conversion of the two solid phases, through a solution mediated process, where the phase which is metastable at a given temperature dissolves and the thermodynamically stable one subsequently precipitates.

The mole fraction (x) solubility determinations were carried out in the range 283-312 K. Linear least squares fits of eq. 5.10

$$\ln x = a + \frac{b}{(T/\mathrm{K})} \tag{5.10}$$

to the obtained x vs. T data (see Supporting Information) led to the results indicated in Table 5.2, where T_{range} denotes the temperature range of the measurements and R^2 is the regression

coefficient for 95% probability. As shown in a Table 5.2 and Figure 5.8a for all solvents the ln*x* vs. 1/*T* curves exhibit a slight slope shift at 300.1±0.4 K originated by the II → I phase transition. The occurrence of the phase transition at this temperature was confirmed by the DRIFT analysis of the solid phase in contact with the solution, as illustrated in Figure 5.8b for ethanol. The thermodynamic equilibrium temperature was therefore taken as T_{trs} = 300.1±0.4 K. This value is 28 K lower than the II → I onset temperature observed in the adiabatic calorimetry experiments and 57 K lower than the corresponding temperatures measured by DSC experiments at different heating rates.

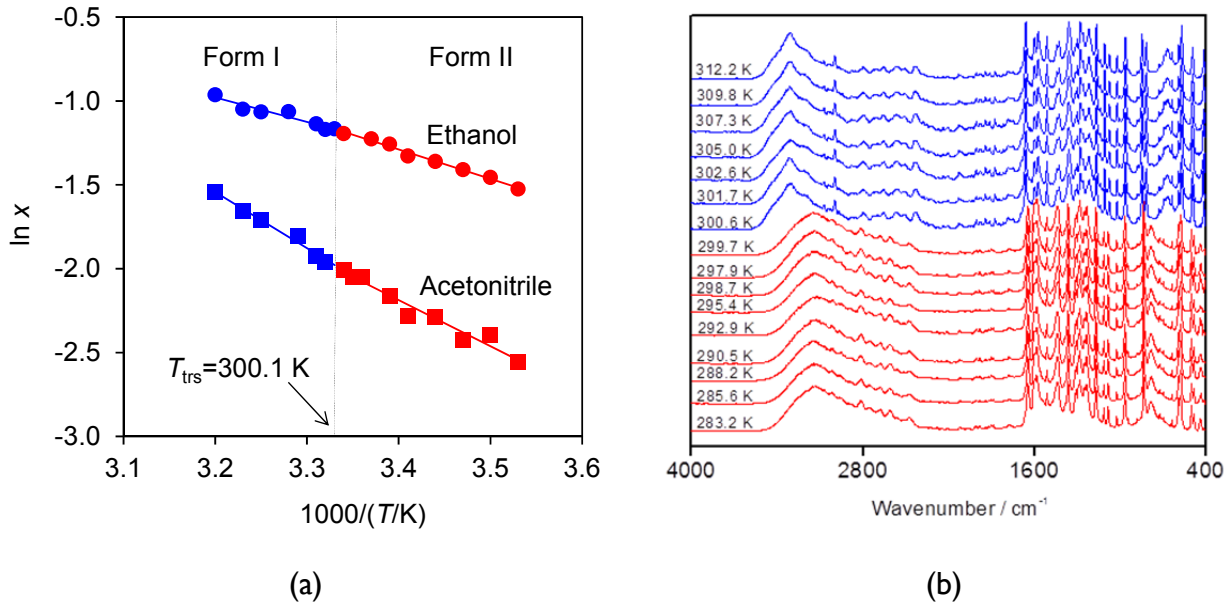

Figure 5.8 (a) Mole fraction solubilities of HAP in ethanol and acetonitrile. (b) DRIFT spectra of the solid phase in equilibrium with the solution throughout the solubility measurements in ethanol. The spectra obtained up to 299.7 K correspond to form II (red lines) and those above this temperature (in blue) refer to form I.

Table 5.2 Parameters of Eq. 5.10, corresponding temperature ranges of application (T_{range}), and regression coefficients (R^2)

Solvent	Phase	$-a$	b	T_{range}/K	R^2
ethanol	form I	1505.8±194.0	3.84±0.63	300-312	0.92
	form II	1731.9±51.4	4.60±0.18	283-299	0.99
acetonitrile	form I	3268.2±246.3	8.92±0.80	300-312	0.98
	form II	2661.6±197.4	6.86±0.67	283-299	0.96

5.3.4 Raman spectroscopy

The Raman spectra collected for a single crystal of HAP form II, suspended on an acoustic levitator, as a function of temperature are shown in Figure 5.9. The figure reveals the solid-solid phase transition to form I initiates at ~353 K. This observation is in good agreement with the DSC results presented above. The beginning of the process is signaled by the appearance of a peak at 1658 cm^{-1} (marked with an asterisk in Figure 5.9) which corresponds to the stretching frequency of the carbonyl group in form I. As in the case of infrared spectra,[53] the major spectral differences between the two phases are observed in the range 1659 cm^{-1} to 1575 cm^{-1}**.** These frequencies are related with the ν(C=O) and ring ν(C···C) normal modes, and reflect the modifications of the hydrogen bonds between the molecules (ν(C=O) which changes from 1642 cm^{-1} to 1659 cm^{-1}) and the rotation of the hydroxyl group relative to the carbonyl from *Z* to *E* conformation (ν(C···C) changes during the phase transition from 1584 cm^{-1}, 1598 cm^{-1} and 1605 cm^{-1}, to 1575 cm^{-1}, 1603 cm^{-1} and 1641 cm^{-1}).[53] The Raman spectroscopy results, therefore, suggest that the phase transition directly occurs from form II to form I, without any detectable intermediate phase (at least within the detection limit of the technique employed). This conclusion is also supported by the hot stage microscopy results discussed below.

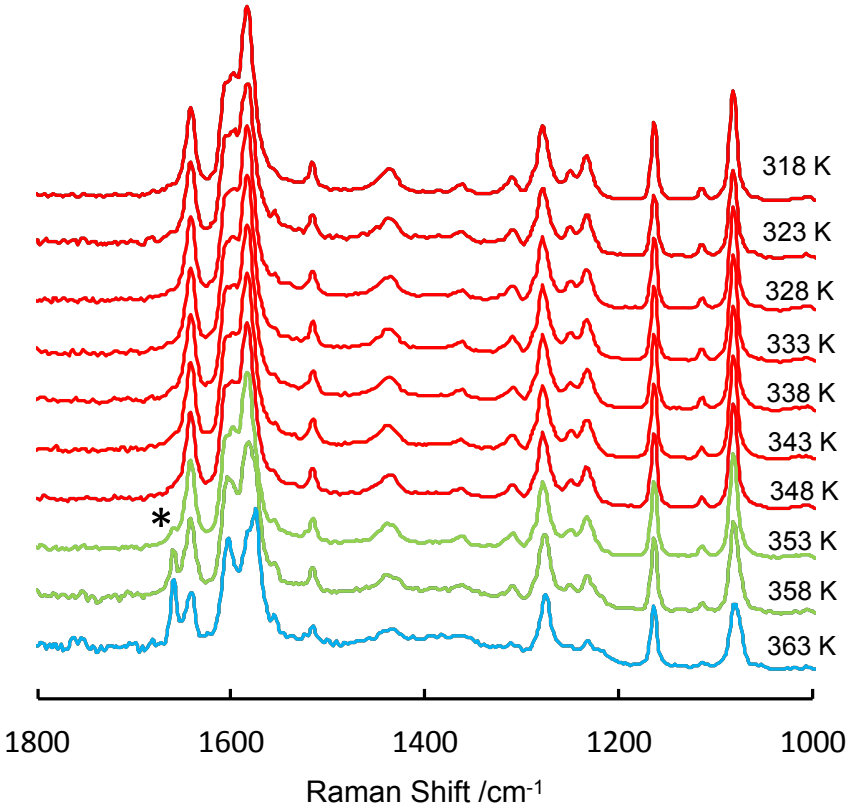

Figure 5.9 Raman spectra collected for a single crystal of 4'-hyroxyacetophenone form II as a function of temperature. The red spectra refer to form II while the blue spectrum corresponds to form I. The green spectra refer to mixtures of the two phases.

5.3.5 Hot Stage Microscopy

Observations made on a good small single crystal of HAP form II at a heating rate of 5 $K \cdot min^{-1}$ revealed a smooth movement of a well bounded interface (Figure 5.10). This interface movement represents the growth of form I within the original form II. This single crystal to single crystal phase transformation was only possible to observe in a well formed good quality crystal with a flat surface.

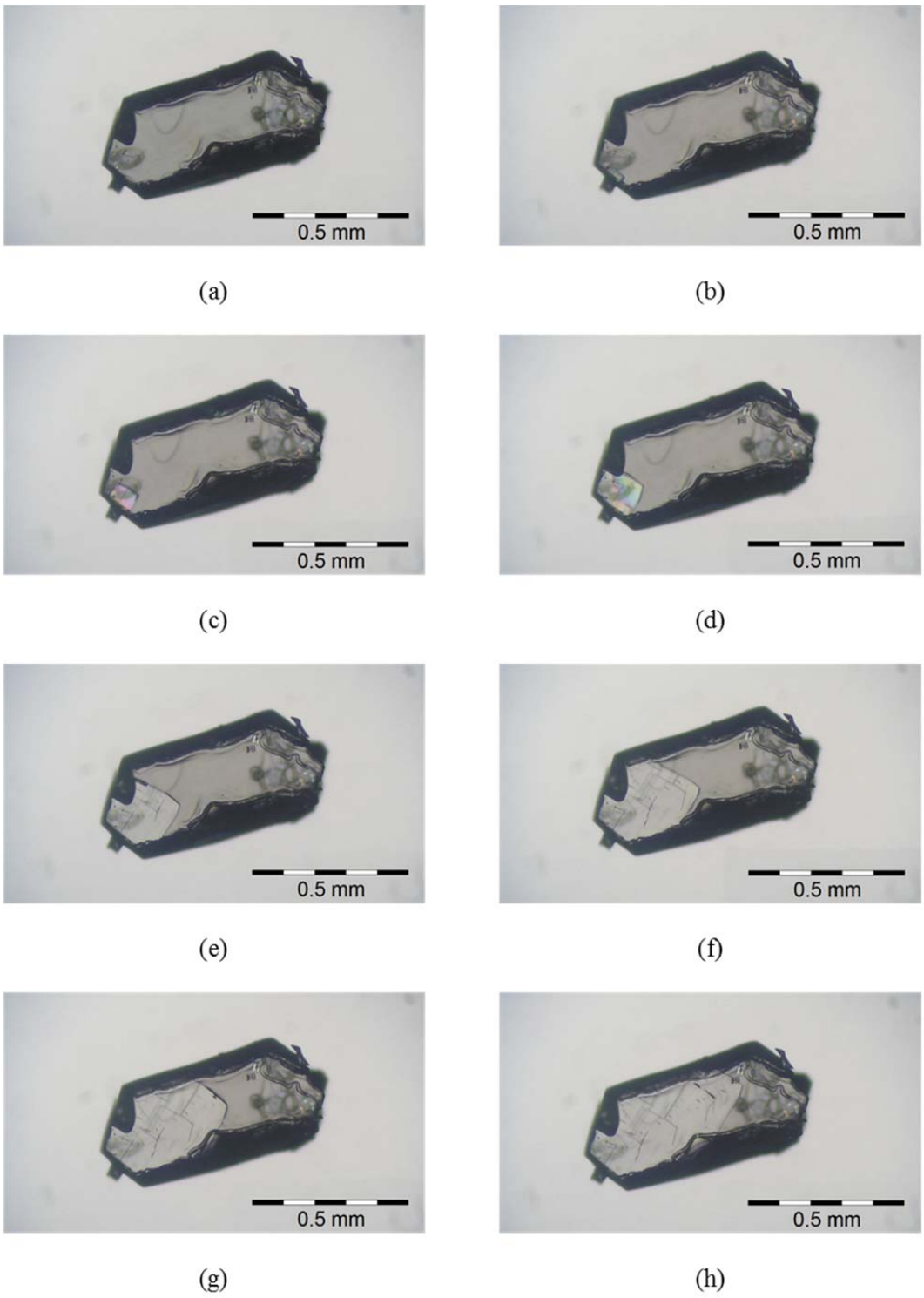

Figure 5.10 Hot-stage microscopy images of a form II → form I phase transition in 4HAP, when heated from 298 to 373 K at 5 K·min^{-1}. The images were recorded in polarized light.

The phase transition shown in Figure 5.10b occurred at ~ 370 K. This temperature is well above its equilibrium counterpart (300.1 K) determined in the solubility studies and comparable to the onset temperature T_{on} = 362.5±5.8 K of the phase transition obtained in the DSC experiments carried out with single crystals at the heating rate of 5 K·min^{-1}. This finding is in agreement with the conclusion of the DSC experiments that overheating is necessary for nucleation of form I to occur and more perfect crystals yield larger overheatings. After the interface propagation was initiated, the phase transformation was completed within a minute.

5.3.6 $\Delta_f G_m^\circ$ -*T* phase diagram

The data obtained in this work allowed us to revisit the $\Delta_f G_m^\circ$ -*T* diagram highlighting the stability domains of forms I and II HAP. Critical for the building of the $\Delta_f G_m^\circ$ -*T* diagram, using the previously reported methodology,[95] were the heat capacities of solid (forms I and II) and liquid HAP (see Supporting Information) obtained by adiabatic calorimetry and DSC, and the phase transition equilibrium temperature (T_{trs} = 300.1±0.4 K) determined from the solubility studies. All other thermodynamic data necessary for the calculations are given as Supporting Information.

The heat capacities of solid (forms I and II) and liquid HAP obtained by adiabatic calorimetry and DSC, respectively, were fitted to polynomial equations of the type:

$$C_{p,m}^\circ/\mathrm{J\cdot mol^{-1}\cdot K^{-1}} = a + b(T/\mathrm{K}) + c(T/\mathrm{K})^2 \qquad (5.11)$$

by the least squares method. The corresponding parameters, range of application and

Table 5.3 Coefficients of eq 5.11 for different HAP phases, corresponding temperature ranges of application (T_{range}), and regression coefficients (R^2)[a]

Phase	*a*	*b*	*c*	T_{range}/K	R^2
HAP, cr I	24.821±0.935	0.51426±0.00275		298-373	0.998
HAP, cr II	35.776±2.307	0.47390±0.00740		294-327	0.993
HAP, l	157.49±0.07	0.34625±0.00017		385-400	0.999
HAP, g[a]	6.8932	0.5596	-1.9376×10^{-4}	298-347	

[a]Ref 39, see text.

regression coefficients (R^2) for 95% probability are summarized in Table 5.3. Also included in Table 5.3 for comparison purposes are the previously reported parameters for the heat capacity of gaseous HAP.[39] The reliability of the $C^{\circ}_{p,m}$ measurements by DSC was tested by comparing the corresponding values obtained for form I with analogous results from adiabatic calorimetry calculated from eq 5.11 and the parameters in Table 5.3. The agreement between the two determinations in the range covered by the DSC measurements (324-374 K) was within ~1 %. The obtained $\Delta_f G^{\circ}_m$-*T* diagram is given in Figure 5.11a, showing that at ambient pressure (1 bar) form II is the stable phase up to T_{trs} = 300.1 K and, there on, form I prevails until fusion occurs at 381.9 K. The phase transition temperatures obtained in the adiabatic calorimetry (~328 K) and DSC (351 K to 371 K on increasing the heating rate from 1 K·min^{-1} to 20 K·min^{-1}) experiments, therefore, correspond to situations where a considerably metastable form II converts into form I. The change in the thermodynamic functions of the phase transition, $\Delta_{trs}G^{\circ}_m$, $\Delta_{trs}H^{\circ}_m$ and $\Delta_{trs}S^{\circ}_m$ (Figure 5.11b) also led to the important conclusion that the process is entropy driven since the enthalpy of formation of form II is always smaller than that of form I and thus the II → I process is always endothermic.

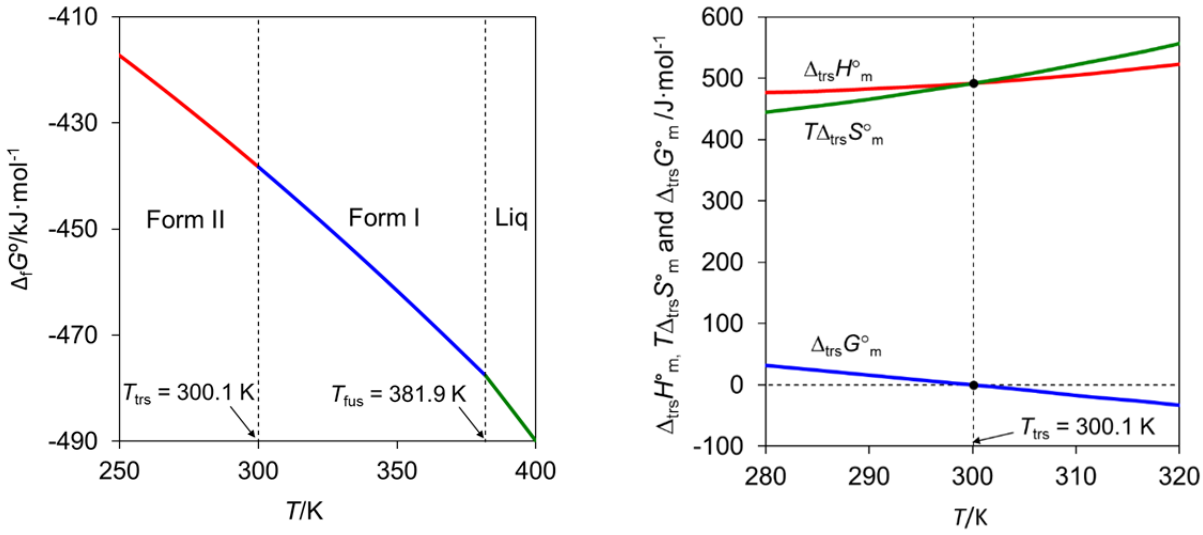

(a) (b)

Figure 5.11 (a) $\Delta_f G^\circ_m$-T diagram for the solid and liquid phases of 4'-hydroxyacetophenone at p° = 1 bar and (b) Thermodynamic functions of the form II → I phase transition.

5.3.7 Quantum Chemistry and Hirshfeld Surface Analysis Structure-Energetics Relationship

Structural insights on the relative stability of Z' = 1 (form I) and Z' = 2 (form II) structures in HAP can be obtained by analyzing the results of ab initio calculations and Hirshfeld surface analysis. The analysis of the configuration energy of the individual HAP molecules based on the DFT calculations show that, as previously determined,[39] the Z conformation is more stable than the E conformation in the gas phase, $\Delta E(Z \rightarrow E)$ = 0.72 kJ·mol^{-1}. This result contrasts with those found in solid state where, after optimization of the hydrogen positions (optimization of the hydrogen positions was performed due to the uncertainty associated with their location by single crystal X-ray diffraction analysis), $\Delta E(Z \rightarrow E)$ = –0.83 kJ·mol^{-1} and $\Delta E(Z \rightarrow E)$ = –1.78 kJ·mol^{-1}, taking into consideration the two HAP molecules in the asymmetric unit of form II. Thus, in the solid state, the two molecular conformations found in form II are

less stable than that in form I. Therefore, the higher lattice energy observed for form II should arise from the formation of stronger intermolecular interactions in solid state. Consistent with this conclusion, it is, for example, found, that the molecular arrangement in form II leads to hydrogen bonds more stable by ~8 $kJ \cdot mol^{-1}$ than in form I.

The larger lattice enthalpy of form II is also consistent with the results of Hirshfeld surface analysis of the crystal structures of form II and form I (cif temperature: 298 K). As shown in Figure 5.12 the contribution from O···H contacts is ~2% larger and that from repulsive O···O contacts smaller in form II than in form I. Thus suggests the formation of stronger H-bonds in the form II. Figure 5.12 also suggests a larger number of H···H and C···C contacts (1-2%) in the case of form I. This difference is originated by the presence in form I, of close contacts between different HAP 1D layers (i.e. the distance between layers is comparable to the sum of the Van der Waals radii of the atoms). Furthermore, the relative orientation of the molecules in the two layers allow, interactions between the quadrupole moment of the HAP aromatic ring, leading to stronger interaction energies in the 3D structure of form I than in the case of form II.

Thus, the combined results of ab initio calculations and Hirshfeld surface analysis suggest that the presence of two molecules in the unit cell allows the formation of stronger H-bonds (~8 $kJ \cdot mol^{-1}$) in form II than in the case of form I. This effect seems to overcome the stability loss resulting from the fact that the molecular conformations of the two molecules in the asymmetric unit of form II are less stable than that adopted in form I. The experimental difference of only ~0.5 $kJ \cdot mol^{-1}$ between the lattice energy of the two polymorphs, results from a less efficient packing and loss of conformational stability of the individual molecules characteristic of form II.

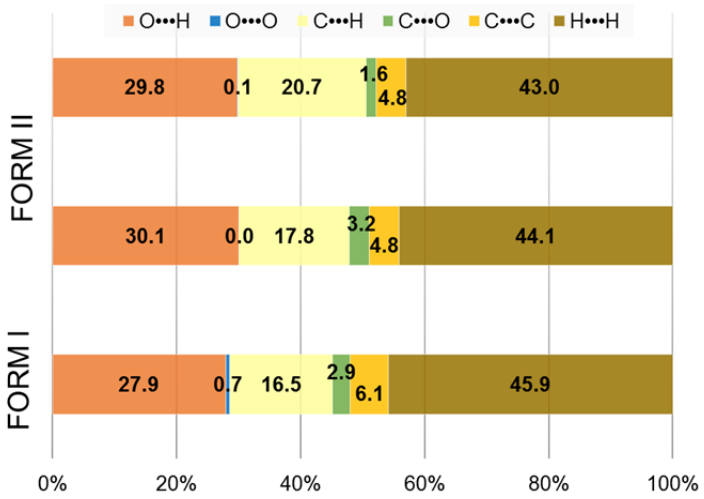

Figure 5.12 Contribution of different bonds in the two polymorphs of HAP as determined by Hirshfeld analysis.

5.4 Conclusion

DSC experiments carried out on powder and single crystals of form II showed that the II→I phase transition is hindered in crystals of higher perfection where clean fusion of form II can be observed. It was also established that annealing the samples, tends to remove lattice strain associated with crystal defects leading to a more reproducible phase transition onset. The equilibrium temperature of the II→I HAP phase transition (T_{trs} = 300.1±0.4 K) determined from solubility studies was found to be well below the corresponding onsets observed by adiabatic calorimetry (328 K) and DSC (351 K to 371 K on increasing the heating rate from 1 K·min^{-1} to 20 K·min^{-1}), despite the fact that the lattice energies of the two forms differ by only 0.49±0.13 kJ·mol^{-1}.[53] This indicates that the direct solid-solid conversion should be hindered by a considerable kinetic barrier. This barrier which was estimated from DSC kinetic studies as E_a = 230.3±9.4 kJ·mol^{-1}, allows the survival of metastable form II up to ~51 K in the case of DSC (300.1 to 351 K) and ~28 K (300.1 to 328 K) in the case of adiabatic calorimetry above the equilibrium value. This also explains why form I can be kept unchanged at ambient temperature without any strict control of storage conditions. The fact that in this work and in other published accounts of phase transition studies E_a values larger than the lattice energy of a

molecular organic solid (measured by the enthalpy of sublimation) is found, requires further investigation.

Solubility determinations also showed that at atmospheric pressure, form II HAP (orthorhombic, *Z*' = 2) is more stable than form I (monoclinic, *Z*' = 1) up to 300.1±0.4 K and that the stability is reversed above that temperature. The fact that the interconversion of the two polymorphs is possible under conditions of thermodynamic control indicates that the assumption of Z′ > 1 forms being necessarily less stable than the corresponding Z′ = 1 form cannot be universally true. The present results therefore lend quantitative support to the analogous conclusion stated in a recent review.[22] Finally, as a result of the solubility experiments a procedure for the selective and reproducible production of forms I and II HAP, which is amenable to scale-up, was developed.

The enantiotropic nature of the HAP system and the stability domains of the two polymorphs were quantitatively expressed by a $\Delta_f G_m^\circ$-*T* phase diagram. The driving force for the form II $\rightarrow$ form I transition was also identified by analyzing the enthalpy-temperature and entropy-temperature landscapes of both forms. The enthalpy of formation of form II was always found to be smaller than that of form I thus indicating that the phase transition is entropy driven.

The relative stability of the two polymorphs based on lattice energies was also tested by ab-initio calculations and Hirshfeld surface analysis. It was found that slightly higher lattice energy of form II is the result of stronger hydrogen bonds (~ 8 $kJ \cdot mol^{-1}$) than in form I due to presence of two molecules in asymmetric unit of form II. Although the molecular conformations in form II was found to be less stable than in form I due to less efficient packing and loss of stability of molecules. These conclusions also highlight the important fact that the relative stability of the polymorphs should not be considered based lattice energy alone.

Supporting Information

Table S1 Indexation of the X-ray Powder Diffraction pattern of HAP form I in the range 5°≤ 2θ≤ 35° (space group $P2_1/c$; a = 7.704(8) Å, b = 8.337(8) Å, c = 11.268(9), β = 94.98(2)°).

h	k	l	2θ (obs)/°	$\Delta 2\theta$/°
1	0	0	11.550	0.020
0	1	1	13.255	0.026
0	0	2	15.820	0.030
-1	1	1	17.150	0.029
1	1	1	18.015	-0.016
-1	0	2	18.775	0.017
0	1	2	19.090	0.028
1	0	2	20.410	0.012
0	2	0	21.325	0.009
-1	1	2	21.540	-0.059
2	0	0	23.155	-0.023
1	2	0	24.325	0.026
2	1	0	25.570	0.016
0	1	3	26.110	0.006
-2	0	2	26.990	0.007
-1	1	3	27.765	0.018
-1	2	2	28.505	-0.036
2	0	2	29.360	0.048
2	1	2	31.195	-0.061

Continued….

h	*k*	*l*	2θ (obs)/°	$\Delta 2\theta$/°
0	0	4	31.915	0.025
-1	0	4	33.025	0.005
0	1	4	33.640	-0.059

Table S2 Indexation of the X-ray Powder Diffraction pattern of HAP form II in the range 5°≤ 2θ≤ 35° (space group $P2_12_12_1$; a = 6.114(6) Å, b = 9.569(9) Å, c = c = 24.324(52) Å

h	k	l	2θ (obs)/°	$\Delta 2\theta$/°
0	1	2	11.790	0.022
0	0	4	14.635	0.068
1	0	1	14.920	-0.019
1	0	2	16.145	-0.080
1	1	0	17.230	0.020
1	1	1	17.585	-0.010
1	0	3	18.095	-0.077
0	2	1	18.915	0.011
0	2	2	19.875	-0.067
1	1	3	20.365	-0.058
0	2	3	21.550	-0.017
1	1	4	22.555	-0.064
1	2	0	23.645	0.034
1	2	2	24.715	-0.021
1	1	5	25.065	-0.112
1	2	3	26.050	-0.027
1	2	4	27.865	0.011
0	3	1	28.235	0.017
0	2	6	28.970	0.103
1	2	5	29.980	-0.017
2	1	0	30.755	0.055

Continued….

h	*k*	*l*	2θ (obs)/°	$\Delta 2\theta$/°
0	1	8	30.895	0.036
2	1	2	31.690	0.100
1	2	6	32.480	0.040
1	3	3	33.540	-0.021
0	1	9	34.460	-0.025
2	2	0	34.820	-0.004

Table S3 Molar heat capacities of solid and liquid HAP obtained by adiabatic calorimetry and DSC.[a]

Adiabatic Calorimetry				DSC			
Form I		Form II		Form I		Liquid	
(m = 302.19 mg)		(m = 377.57 mg)		(m = 5 to 6 mg)		(m = 5 to 6 mg)	
T/K	$C_{p,m}$/ J K^{-1}·mol^{-1}	T/K	$C_{p,m}$/ J K^{-1}·mol^{-1}	T/K	$C_{p,m}$/ J K^{-1}·mol^{-1}	T/K	$C_{p,m}$/ J K^{-1}·mol^{-1}
298.27	177.98	294.38	176.37	324.18	188.28±2.65 (5)	385.27	290.89±7.90 (5)
299.93	179.78	295.72	176.17	325.17	189.00±2.56 (5)	386.25	291.23±7.60 (5)
301.17	179.67	297.06	176.58	326.15	189.69±2.56 (5)	387.24	291.57±7.24 (5)
302.36	179.91	298.40	177.30	327.14	190.38±2.48 (5)	388.23	291.92±6.96 (5)
303.54	181.46	299.72	177.95	328.12	191.05±2.47 (5)	389.21	292.26±6.61 (5)
304.72	182.18	301.03	178.20	329.11	191.70±2.39 (5)	390.2	292.60±6.35 (5)
305.90	182.76	302.26	179.34	330.10	192.35±2.32 (5)	391.18	292.94±6.09 (5)
307.07	182.08	303.48	179.56	331.08	192.97±2.30 (5)	392.17	293.28±5.87 (5)
308.23	182.18	304.66	179.94	332.07	193.59±2.36 (5)	393.15	293.62±5.53 (5)
309.39	184.01	305.85	180.83	333.05	194.19±2.29 (5)	394.14	293.96±5.31 (5)
310.54	184.91	307.03	180.83	334.04	194.79±2.31 (5)	395.12	294.30±5.06 (5)
311.69	185.49	308.20	181.70	335.02	195.36±2.25 (5)	396.11	294.64±4.73 (5)
312.83	186.32	309.36	181.86	336.01	195.93±2.25 (5)	397.09	294.98±4.51 (5)
313.97	186.94	310.50	182.34	336.99	196.49±2.16 (5)	398.08	295.33±4.23 (5)
315.10	187.20	311.63	182.96	337.98	197.04±2.16 (5)	399.06	295.67±3.92 (5)
316.23	187.70	312.75	183.62	338.96	197.58±1.34 (5)	400.05	296.01±3.71 (5)
317.01	187.93	313.50	184.04	339.95	198.11±1.41 (5)		
318.13	188.46	314.59	184.21	340.93	198.63±1.51 (5)		
319.24	189.06	315.66	185.02	341.92	199.14±1.54 (5)		

Continued….

Adiabatic Calorimetry				DSC			
Form I		Form II		Form I		Liquid	
(*m* = 302.19 mg)		(*m* = 377.57 mg)		(*m* = 5 to 6 mg)		(m = 5 to 6 mg)	
T/K	$C_{p,m}$/ J K^{-1}·mol^{-1}	*T*/K	$C_{p,m}$/ J K^{-1}·mol^{-1}	*T*/K	$C_{p,m}$/ J K^{-1}·mol^{-1}	*T*/K	$C_{p,m}$/ J K^{-1}·mol^{-1}
320.35	189.71	316.72	186.23	342.90	199.64±1.61 (5)		
321.45	190.25	317.77	186.52	343.89	200.14±1.71 (5)		
322.54	190.90	318.81	186.87	344.87	200.63±1.77 (5)		
323.63	191.34	319.83	187.45	345.86	201.12±1.82 (5)		
324.72	191.65	320.84	188.06	346.84	201.59±1.71 (5)		
325.79	192.58	321.84	188.60	347.83	202.07±1.62 (5)		
326.86	192.85	322.83	188.79	348.82	202.54±1.65 (5)		
327.93	193.40	323.80	189.13	349.80	202.99±1.61 (5)		
328.99	193.05	324.76	190.08	350.79	203.45±1.65 (5)		
330.04	193.98	325.71	190.43	351.77	203.91±1.60 (5)		
331.08	195.16	326.65	191.11	352.76	204.36±1.64 (5)		
332.12	195.59	327.59	191.42	353.74	204.80±1.59 (5)		
333.16	195.96	328.51	191.78	354.73	205.25±1.63 (5)		
333.81	195.59			355.71	205.69±1.59 (5)		
334.84	196.69			356.70	206.13±2.87 (5)		
335.85	197.04			357.68	206.57±2.92 (5)		
336.86	197.44			358.67	207.01±2.97 (5)		
337.87	198.27			359.65	207.45±2.98 (5)		
338.86	198.96			360.64	207.89±3.05 (5)		
339.85	199.59			361.62	208.32±3.05 (5)		

Continued….

Adiabatic Calorimetry				DSC			
Form I (m = 302.19 mg)		Form II (m = 377.57 mg)		Form I (m = 5 to 6 mg)		Liquid (m = 5 to 6 mg)	
T/K	$C_{p,m}$/ J K^{-1}·mol^{-1}	T/K	$C_{p,m}$/ J K^{-1}·mol^{-1}	T/K	$C_{p,m}$/ J K^{-1}·mol^{-1}	T/K	$C_{p,m}$/ J K^{-1}·mol^{-1}
340.84	199.45			362.61	208.77±3.13 (5)		
341.82	200.40			363.59	209.20±3.16 (5)		
342.79	200.97			364.58	209.65±3.19 (5)		
343.76	201.04			365.56	210.09±3.21 (5)		
344.71	202.10			366.55	210.54±2.60 (5)		
345.66	203.04			367.53	210.99±2.52 (5)		
346.61	203.63			368.52	211.45±2.47 (5)		
347.55	203.93			369.51	211.91±2.44 (5)		
348.48	204.05			370.49	212.37±2.37 (5)		
348.95	203.77			371.48	212.84±2.35 (5)		
349.88	204.45			372.46	213.31±2.29 (5)		
350.79	205.79			373.45	213.79±2.31 (5)		
351.70	205.95			374.43	214.28±2.27 (5)		
352.60	206.68			375.42	214.77±2.24 (5)		
353.50	206.78			376.40	215.27±2.23 (5)		
354.38	207.54						
355.27	208.01						
356.14	207.36						
357.01	208.08						
357.87	208.48						

Continued….

Adiabatic Calorimetry				DSC			
Form I		Form II		Form I		Liquid	
(m = 302.19 mg)		(m = 377.57 mg)		(m = 5 to 6 mg)		(m = 5 to 6 mg)	
T/K	$C_{p,m}$/ J K^{-1}·mol^{-1}	T/K	$C_{p,m}$/ J K^{-1}·mol^{-1}	T/K	$C_{p,m}$/ J K^{-1}·mol^{-1}	T/K	$C_{p,m}$/ J K^{-1}·mol^{-1}
358.72	209.17						
359.57	209.84						
360.41	209.36						
361.24	210.24						
362.07	210.77						
362.35	210.64						
363.16	210.26						
363.97	211.82						
364.77	212.24						
365.57	213.60						
366.36	213.10						
367.14	213.41						
367.92	213.75						
368.69	213.85						
369.44	214.81						
370.20	215.69						
370.94	215.82						
371.68	216.67						
372.41	217.71						
373.14	218.59						

[a]In the DSC results the uncertainty corresponds to number of independent determinations is given in parenthesis.

Table S4 Molar heat capacities of form II in the phase transition range [a]

T/K	$C_{p,m}$/J·K^{-1}·mol^{-1}	T/K	$C_{p,m}$/J·K^{-1}·mol^{-1}
328.51	191.78	337.31	200.60
328.95	194.42	338.13	198.94
329.81	181.49	338.89	202.97
330.62	207.03	339.69	204.34
331.32	203.50	340.48	200.65
332.16	208.80	340.72	200.47
332.98	192.08	341.51	204.57
333.69	195.51	342.29	201.76
334.25	209.71	343.07	195.37
334.97	226.04	343.82	201.09
335.70	208.99	344.52	202.41
336.49	205.06		

[a]Heat Capacities measured by adiabatic calorimetry

Table S5 Molar heat capacities of form II after phase transition [a]

T/K	$C_{p,m}$/J·K^{-1}·mol^{-1}	T/K	$C_{p,m}$/J·K^{-1}·mol^{-1}
344.52	202.41	361.23	211.32
345.27	202.91	361.80	211.38
346.01	203.86	362.35	212.27
346.75	204.44	362.90	212.88
347.48	203.51	363.44	212.58
348.19	204.99	363.98	213.11
348.85	198.21	364.50	213.26
349.48	209.01	365.02	214.26
350.17	206.12	365.54	214.49
350.86	206.03	366.05	214.16
351.54	206.71	366.55	214.50
351.59	206.48	367.05	215.00
352.27	206.53	367.54	215.16
352.93	207.52	368.02	215.89
353.59	207.73	368.50	216.04
354.25	207.43	368.21	216.53
354.89	208.52	368.68	215.45
355.52	208.53	369.15	216.74
356.15	209.19	369.62	216.73
356.77	211.04	370.07	217.78
357.24	209.22	370.53	217.75
357.85	209.99	370.97	218.40

Continued….

T/K	$C_{p,m}$/J·K^{-1}·mol^{-1}	T/K	$C_{p,m}$/J·K^{-1}·mol^{-1}
358.46	210.58	371.41	219.49
359.05	210.13	371.85	219.76
359.64	210.59	372.27	220.92
360.22	210.64	372.69	221.36
360.80	211.29	373.11	222.26

[a]Heat Capacities measured by Adiabatic Calorimetry

Table S6 Molar heat capacities of form I from 79.12 K to 373.25 K after cooling from 373.11 K.[a]

T/K	$C_{p,m}$/J·K^{-1}·mol^{-1}	T/K	$C_{p,m}$/J·K^{-1}·mol^{-1}	T/K	$C_{p,m}$/J·K^{-1}·mol^{-1}
79.12	65.46	111.16	87.60	142.18	99.47
80.43	67.43	112.16	87.68	143.17	100.91
81.47	67.64	113.17	88.18	144.13	100.13
82.50	68.81	114.18	88.75	145.12	100.82
83.53	70.04	115.20	88.99	146.10	101.64
84.57	70.27	116.21	89.84	147.09	101.81
85.60	71.55	117.21	89.94	148.07	102.77
86.63	73.00	118.22	90.26	149.06	103.18
87.66	73.81	119.23	90.70	150.04	103.49
88.69	74.32	120.24	90.79	151.03	104.29
89.72	74.87	121.25	91.52	152.01	104.92
90.74	76.52	122.25	91.58	152.99	105.03
91.77	77.10	123.26	91.68	153.97	106.50
92.80	77.57	124.26	92.21	154.95	106.09
93.83	77.96	125.26	92.90	155.93	106.56
94.85	78.60	126.26	93.13	156.91	106.61
95.87	79.77	127.27	93.22	157.88	107.06
96.89	80.53	128.25	93.63	158.86	107.75
97.92	81.18	129.25	94.18	159.80	108.40
98.94	81.49	130.24	94.65	160.77	109.21
99.97	82.17	131.24	94.77	161.74	108.60
100.99	82.85	132.24	95.48	162.72	109.01
102.01	83.21	133.24	96.62	163.69	109.81

Continued….

T/K	$C_{p,m}$/J K^{-1}·mol^{-1}	T/K	$C_{p,m}$/J K^{-1}·mol^{-1}	T/K	$C_{p,m}$/J K^{-1}·mol^{-1}
103.03	83.32	134.23	96.28	164.65	110.70
104.05	84.22	135.23	96.63	165.62	111.47
105.07	84.62	136.22	96.96	166.59	111.92
106.08	85.28	137.22	97.58	167.56	112.50
107.10	85.81	138.21	97.94	168.52	112.60
108.12	86.19	139.20	98.53	169.49	113.04
109.13	86.76	140.19	98.81	170.45	113.58
110.15	87.24	141.19	99.23	171.41	114.24
172.37	115.06	226.23	143.48	288.53	175.54
173.34	116.04	227.61	143.98	289.74	175.79
174.30	116.11	228.99	145.09	290.95	176.47
175.21	116.45	230.27	145.42	291.92	176.46
176.17	117.08	231.64	145.76	293.12	177.46
177.13	117.49	233.02	146.45	294.32	177.81
178.09	117.97	234.39	147.51	295.50	178.41
179.04	118.49	235.76	148.11	296.69	178.56
180.00	119.37	237.12	148.60	297.86	179.49
180.95	119.79	238.48	149.82	299.04	180.30
181.91	120.01	239.84	150.26	300.21	180.83
182.86	120.44	241.20	151.31	301.37	181.71
183.81	121.42	242.54	151.60	302.44	182.02
184.75	121.43	243.89	152.74	303.51	182.64
185.70	122.13	245.23	152.62	304.57	183.26
186.65	122.94	246.58	153.99	305.62	183.44

Continued….

T/K	$C_{p,m}$/J·K^{-1}·mol^{-1}	T/K	$C_{p,m}$/J·K^{-1}·mol^{-1}	T/K	$C_{p,m}$/J·K^{-1}·mol^{-1}
187.60	123.22	247.92	154.40	306.67	184.57
188.54	123.42	249.26	154.93	307.72	184.10
189.48	124.22	250.59	155.52	308.75	185.09
190.37	124.60	251.78	156.27	309.40	184.96
191.31	125.07	253.11	156.76	310.43	186.09
192.25	125.65	254.43	157.18	311.45	186.42
193.19	125.86	255.76	158.12	312.47	186.91
194.13	126.43	257.06	159.27	313.48	187.45
195.06	127.63	258.37	159.53	314.48	187.58
196.00	127.81	259.68	160.19	315.48	187.88
196.94	128.45	260.98	161.04	316.47	188.23
197.87	128.86	262.29	161.44	317.45	188.91
198.81	128.68	263.58	162.19	318.43	189.67
199.74	129.40	264.88	163.48	319.40	189.78
200.92	130.43	266.15	163.67	320.36	190.56
202.35	131.39	267.44	164.01	321.32	190.34
203.77	131.73	268.72	165.19	322.27	191.12
205.19	132.55	270.00	165.90	323.22	191.52
206.62	133.36	271.28	166.35	324.16	191.71
207.97	133.76	272.38	166.77	324.63	191.78
209.39	134.82	273.64	167.10	325.56	192.78
210.80	135.98	274.91	168.32	326.49	193.16
212.22	136.43	276.17	168.93	327.40	193.78
213.63	136.59	277.42	169.72	328.31	194.20

Continued….

T/K	$C_{p,m}$/J·K^{-1}·mol^{-1}	T/K	$C_{p,m}$/J·K^{-1}·mol^{-1}	T/K	$C_{p,m}$/J·K^{-1}·mol^{-1}
215.04	136.94	278.68	170.44	329.21	194.06
216.45	138.32	279.92	170.99	330.11	194.47
217.85	138.99	281.17	171.53	331.00	195.06
219.25	140.35	282.41	171.75	331.88	195.78
220.66	140.30	283.64	172.55	332.76	195.98
222.05	141.50	284.87	173.39	333.63	196.22
223.45	141.81	286.09	173.91	334.50	196.84
224.84	142.25	287.32	174.07	335.35	197.18
336.21	197.62	351.41	206.52	364.39	212.07
337.05	198.22	352.13	206.23	364.97	212.66
337.89	198.51	352.84	206.09	365.55	213.42
338.18	198.27	353.54	206.90	366.12	213.51
339.01	198.52	354.23	206.87	366.69	213.74
339.84	199.08	354.92	207.89	367.25	214.12
340.65	199.62	355.60	208.52	367.80	214.83
341.46	200.20	356.28	208.05	368.34	214.51
342.26	199.80	356.94	208.30	368.88	214.84
343.05	201.34	357.60	209.09	368.64	214.97
343.84	201.62	358.26	209.77	369.18	215.97
344.63	201.93	358.91	209.37	369.71	216.20
345.40	202.52	359.55	210.13	370.23	216.07
346.17	202.79	360.18	209.80	370.75	217.03
346.93	203.70	360.12	209.51	371.26	217.76
347.69	204.14	360.75	209.62	371.77	217.97

Continued….

T/K	$C_{p,m}$/J·K^{-1}·mol^{-1}	T/K	$C_{p,m}$/J·K^{-1}·mol^{-1}	T/K	$C_{p,m}$/J·K^{-1}·mol^{-1}
348.44	204.24	361.37	210.11	372.27	218.39
349.18	204.52	361.99	210.57	372.76	219.19
349.92	204.31	362.60	211.21	373.25	219.82
350.03	204.87	363.20	211.05		
350.69	205.41	363.80	212.06		

[a] The form I sample resulted from heating the original form II sample through the II → I transition range up to 373.11 K. The present results were obtained on cooling that sample to 79.12 K and re-heating to 373.25 K.

Table S7 Comparison of the molar heat capacities of form I obtained by adiabatic calorimetry and DSC in the range 324-374 K[a]

	DSC	Adiabatic Calorimetry	
T/K	$C_{p,m}$/J·K^{-1}·mol^{-1}	$C_{p,m}$/J·K^{-1}·mol^{-1}	Δ%[b]
324	189.66	191.44	0.9
326	190.65	192.47	0.9
328	191.64	193.50	1.0
330	192.64	194.53	1.0
332	193.63	195.56	1.0
334	194.63	196.58	1.0
336	195.62	197.61	1.0
338	196.61	198.64	1.0
340	197.61	199.67	1.0
342	198.60	200.70	1.0
344	199.60	201.73	1.1
346	200.59	202.75	1.1
348	201.58	203.78	1.1
350	202.58	204.81	1.1
352	203.57	205.84	1.1
354	204.57	206.87	1.1
356	205.56	207.90	1.1
358	206.55	208.93	1.1
360	207.55	209.95	1.1
362	208.54	210.98	1.2

Continued….

	DSC	Adiabatic Calorimetry	
T/K	$C_{p,m}$/J·K^{-1}·mol^{-1}	$C_{p,m}$/J·K^{-1}·mol^{-1}	Δ%[b]
364	209.54	212.01	1.2
366	210.53	213.04	1.2
368	211.52	214.07	1.2
370	212.52	215.1	1.2
372	213.51	216.13	1.2
374	214.51	217.15	1.2

[a] Heat capacity values obtained from the following fits to the experimental data in Table S3:

Adiabatic calorimetry: $C^{\circ}_{p,m}$(cr I)/J·mol^{-1}·K^{-1} = (24.821±0.935) +(0.51426±0.00275)(T/K)

DSC: $C^{\circ}_{p,m}$(cr I)/J·mol^{-1}·K^{-1} = (157.49±0.070) +(0.34625±0.00017)(T/K)

[b] Δ% = 100×|[$C^{\circ}_{p,m}$(ad. Cal) − $C^{\circ}_{p,m}$(DSC)]/ $C^{\circ}_{p,m}$(ad. Cal)|

Table S8 Results of DSC experiments carried out at different heating rates (1 K·min^{-1}, 10 K·min^{-1}, 80 K·min^{-1}) on powder (250-88 μm particles) of (a) Form I and (b) Form II.

(a).

β = 1 K·min^{-1}			
m/mg	T_{on}/K	T_{max}/K	$\Delta_{fus}H°_m$/kJ·mol^{-1}
5.4244	381.7	382.9	18.6
5.1276	381.7	383.0	18.1
5.1422	381.6	382.9	17.9
5.4201	381.6	382.9	18.3
5.6401	381.7	383.0	17.9
$<T_{on}>$ = 381.66±0.04 K			
$<T_{max}>$ = 382.94±0.04 K			
$<\Delta_{fus}H°_m>$ = 18.2±0.3 kJ·mol^{-1}			
β = 10 K·min^{-1}			
m/mg	T_{on}/K	T_{max}/K	$\Delta_{fus}H°_m$/kJ·mol^{-1}
5.2700	381.7	385.2	17.9
5.5060	381.8	385.2	17.5
5.9634	381.9	385.4	18.3
4.9064	381.7	385.0	17.6
5.0184	381.8	385.2	17.7
$<T_{on}>$ = 381.78±0.08 K			
$<T_{max}>$ = 385.20±0.12 K			
$<\Delta_{fus}H°_m>$ = 17.8±0.3 kJ·mol^{-1}			
β = 80 K·min^{-1}			
m/mg	T_{on}/K	T_{max}/K	$\Delta_{fus}H°_m$/kJ·mol^{-1}
5.1964	382.5	391.2	18.1
5.4562	382.5	391.8	18.1
5.2827	382.5	391.4	18.3
4.8982	382.6	391.6	18.6
5.9652	382.8	392.3	18.2
$<T_{on}>$ = 382.58±0.12 K			
$<T_{max}>$ = 391.66±0.38 K			
$<\Delta_{fus}H°_m>$ = 18.2±0.2 kJ·mol^{-1}			

(b).

β = 1 K·min^{-1}

(II→I) Phase transition				Fusion (Form I)		
m/mg	T_{on}/K	T_{max}/K	$\Delta_{trs}H°_m$/kJ·mol^{-1}	T_{on}/K	T_{max}/K	$\Delta_{fus}H°_m$/kJ·mol^{-1}
4.8659	356.2	365.4	0.4	381.8	383.0	17.5
4.7836	352.0	360.1	0.5	381.8	383.1	17.3
5.5164	351.9	363.4	0.7	381.8	383.2	17.9
5.3894	359.7	370.8	0.8	381.7	383.0	17.9
5.3303	364.4	369.4	0.6	381.7	383.0	18.4
$<T_{on}>$ = 356.8±4.8 K				$<T_{on}>$ = 381.71±0.04 K		
$<T_{max}>$ = 365.8±4.0 K				$<T_{max}>$ = 383.01±0.08 K		
$<\Delta_{trs}H°_m>$ = 0.6±0.2 kJ·mol^{-1}				$<\Delta_{fus}H°_m>$ = 17.8±0.4 kJ·mol^{-1}		

β = 10 K·min^{-1}

Fusion (Form II)			Fusion (Form I)	
m/mg	T_{on}/K	T_{max}/K	T_{on}/K	T_{max}/K
5.1648	377.3	378.6	382.0	385.6
5.2425	377.2	378.4	382.0	385.8
5.4409	376.9	379.0	381.6	385.1
5.1041	377.4	378.6	382.0	385.7
5.6111	377.4	378.6	382.0	385.8
$<T_{on}>$ = 377.2±0.2 K			$<T_{on}>$ = 381.9±0.2 K	
$<T_{max}>$ = 378.6±0.2 K			$<T_{max}>$ = 385.6±0.2 K	

β = 80 K·min^{-1}

m/mg	T_{on}/K(Fusion of Form II)	T_{max}/K(Fusion of form I) shoulder
5.0519	378.8	389.9
5.1723	378.9	389.1
5.7278	378.6	389.7
5.8872	379.1	391.3
5.2875	378.8	390.3
$<T_{on}>$ = 378.8±0.2 K (Fusion of form II)		
$<T_{max}>$ = 390.1±0.8 K (Fusion of form I)		

Table S9 Results of DSC experiments carried out at different heating rates (1 K·min^{-1}, 10 K·min^{-1}, 80 K·min^{-1}) on single crystal of form II (1-2 mm edge) where (a) phase transition was observed and (b) direct fusion of form II was observed.

(a)

β = 1K·min^{-1}						
	(II→I) Phase transition			Fusion (Form I)		
m/mg	T_{on}/K	T_{max}/K	$\Delta_{trs}H°_m$/kJ·mol^{-1}	T_{on}/K	T_{max}/K	$\Delta_{fus}H°_m$/kJ·mol^{-1}
0.2086	357.3	358.15	0.73	381.85	382.15	17.51
0.3994	347.2	351.35	0.88	381.95	382.25	17.88
0.4944	344.0	349.75	0.60	381.95	382.25	15.01
0.7029	355.1	355.65	0.78	381.95	382.35	16.64
$<T_{on}>$ = 350.9±6.3 K				$<T_{on}>$ = 381.93±0.04 K		
$<T_{max}>$ = 353.7±3.9 K				$<T_{max}>$ = 382.25±0.08 K		
$<\Delta_{trs}H°_m>$ = 0.75±0.12 kJ·mol^{-1}				$<\Delta_{fus}H°_m>$ = 16.76±1.28 kJ·mol^{-1}		
β = 5 K·min^{-1}						
	(II→I) Phase transition			Fusion (Form I)		
m/mg	T_{on}/K	T_{max}/K	$\Delta_{trs}H°_m$/kJ·mol^{-1}	T_{on}/K	T_{max}/K	$\Delta_{fus}H°_m$/kJ·mol^{-1}
0.2124	368.85	369.35	0.83	382.05	382.55	18.98
0.2461	365.55	366.85	0.85	382.05	382.55	18.07
0.2049	359.05	360.85	0.73	382.05	382.55	18.04
0.3858	356.35	358.85	0.91	381.95	382.65	18.21
$<T_{on}>$ = 362.45±5.76 K				$<T_{on}>$ = 382.03±0.06 K		
$<T_{max}>$ = 363.98±4.94 K				$<T_{max}>$ = 382.58±0.04 K		
$<\Delta_{trs}H°_m>$ = 0.83±0.08 kJ·mol^{-1}				$<\Delta_{fus}H°_m>$ = 18.33±0.44 kJ·mol^{-1}		
β = 10 K·min^{-1}						
	(II→I) Phase transition			Fusion (Form I)		
m/mg	T_{on}/K	T_{max}/K	$\Delta_{trs}H°_m$/kJ·mol^{-1}	T_{on}/K	T_{max}/K	$\Delta_{fus}H°_m$/kJ·mol^{-1}
0.2340	366.35	367.65	0.89	382.15	382.85	20.04
0.2364	369.95	370.75	0.60	381.95	382.55	17.53
0.3065	366.95	369.75	0.69	382.15	383.05	17.89
$<T_{on}>$ = 367.75±2.22 K				$<T_{on}>$ = 382.08±0.14 K		
$<T_{max}>$ = 369.38±1.82 K				$<T_{max}>$ = 382.82±0.30 K		
$<\Delta_{fus}H°_m>$ = 0.73±0.18 kJ·mol^{-1}				$<\Delta_{fus}H°_m>$ = 18.49±1.56 kJ·mol^{-1}		

Continued…

β = 12 K·min^{-1}						
(II→I) Phase transition				Fusion (Form I)		
m/mg	T_{on}/K	T_{max}/K	$\Delta_{trs}H°_m$/kJ·mol^{-1}	T_{on}/K	T_{max}/K	$\Delta_{fus}H°_m$/kJ·mol^{-1}
0.3525	367.75	369.25	0.65	382.05	383.05	17.75
0.7901	367.35	369.25	0.79	382.15	383.55	18.28
0.6550	364.55	367.15	0.81	382.25	383.55	19.43
$<T_{on}>$ = 366.55±2.02 K				$<T_{on}>$ = 382.15±0.12 K		
$<T_{max}>$ = 368.55±1.40 K				$<T_{max}>$ = 383.38±0.34 K		
$<\Delta_{trs}H°_m>$ = 0.75±0.10 kJ·mol^{-1}				$<\Delta_{fus}H°_m>$ = 18.49±1.00 kJ·mol^{-1}		
β = 14 K·min^{-1}						
(II→I) Phase transition				Fusion (Form I)		
m/mg	T_{on}/K	T_{max}/K	$\Delta_{trs}H°_m$/kJ·mol^{-1}	T_{on}/K	T_{max}/K	$\Delta_{fus}H°_m$/kJ·mol^{-1}
0.9218	365.35	368.85	0.54	381.95	383.55	18.30
0.5345	366.65	369.85	0.69	382.25	383.35	16.73
0.2003	369.25	370.55	0.53	381.95	382.85	17.28
$<T_{on}>$ = 367.08±2.30 K				$<T_{on}>$ = 382.05±0.20 K		
$<T_{max}>$ = 369.75±0.98 K				$<T_{max}>$ = 383.25±0.42 K		
$<\Delta_{trs}H°_m>$ = 0.59±0.10 kJ·mol^{-1}				$<\Delta_{fus}H°_m>$ = 17.44±0.92 kJ·mol^{-1}		
β = 16 K·min^{-1}						
(II→I) Phase transition				Fusion (Form I)		
m/mg	T_{on}/K	T_{max}/K	$\Delta_{trs}H°_m$/kJ·mol^{-1}	T_{on}/K	T_{max}/K	$\Delta_{fus}H°_m$/kJ·mol^{-1}
1.0052	364.75	368.05	0.76	382.25	384.15	18.48
1.0817	369.55	372.05	0.73	383.15	384.45	18.40
0.5812	365.95	368.85	0.69	382.25	383.45	17.93
$<T_{on}>$ = 366.75±2.88 K				$<T_{on}>$ = 382.55±0.60 K		
$<T_{max}>$ = 369.65±2.44 K				$<T_{max}>$ = 384.02±0.60 K		
$<\Delta_{fus}H°_m>$ = 0.73±0.04 kJ·mol^{-1}				$<\Delta_{fus}H°_m>$ = 18.27±0.34 kJ·mol^{-1}		
β = 20 K·min^{-1}						
(II→I) Phase transition				Fusion (Form I)		
m/mg	T_{on}/K	T_{max}/K	$\Delta_{trs}H°_m$/kJ·mol^{-1}	T_{on}/K	T_{max}/K	$\Delta_{fus}H°_m$/kJ·mol^{-1}
0.6577	372.05	373.55	0.38	382.65	384.05	17.18
0.2699	372.65	375.75	0.77	382.25	383.35	19.91
0.3283	369.65	371.45	0.47	382.15	383.35	18.46
$<T_{on}>$ = 371.45±1.84 K				$<T_{on}>$ = 382.35±0.30 K		
$<T_{max}>$ = 373.58±2.48 K				$<T_{max}>$ = 383.58±0.46 K		
$<\Delta_{fus}H°_m>$ = 0.54±0.24 kJ·mol^{-1}				$<\Delta_{fus}H°_m>$ = 18.52±1.58 kJ·mol^{-1}		

(b)

β = 8 K·min^{-1}			
m/mg	T_{on}/K	T_{max}/K	$\Delta_{fus}H°_m$/kJ·mol^{-1}
1.28	377.67	378.46	19.93
0.35	377.67	378.46	18.33
1.25	377.69	378.69	19.65
1.04	377.47	378.46	19.59
$<T_{on}>$ = 377.63±0.10 K			
$<T_{max}>$ = 378.52±0.12 K			
$<\Delta_{fus}H°_m>$ = 19.38±0.72 kJ·mol^{-1}			
β = 10 K·min^{-1}			
m/mg	T_{on}/K	T_{max}/K	$\Delta_{fus}H°_m$/kJ·mol^{-1}
0.89	377.56	378.71	19.37
0.80	377.93	378.64	19.55
0.54	377.61	378.57	18.35
$<T_{on}>$ = 377.70±0.24 K			
$<T_{max}>$ = 378.64±0.08 K			
$<\Delta_{fus}H°_m>$ = 19.09±0.74 kJ·mol^{-1}			
β = 14 K·min^{-1}			
m/mg	T_{on}/K	T_{max}/K	$\Delta_{fus}H°_m$/kJ·mol^{-1}
0.19	377.72	378.57	17.50
1.48	377.91	379.09	18.82
0.29*	377.95	379.05	20.31
$<T_{on}>$ = 377.86±0.14 K			
$<T_{max}>$ = 378.90±0.34 K			
$<\Delta_{fus}H°_m>$ = 18.88±1.62 kJ·mol^{-1}			

*Obtained on Netzsch DSC 204 F1 Phoenix.

Table S10 Results of DSC experiments carried out at 1 K·min^{-1} on annealed powder (250-88 μm particles) of (a) Form I and (b) Form II.

(a)

β = 1K·min^{-1}			
m/mg	T_{on}/K	T_{max}/K	$\Delta_{fus}H°_m$/kJ·mol^{-1}
5.5934	381.55	383.0	17.92
5.8015	381.45	383.0	17.73
5.7036	381.55	382.9	17.78
$<T_{on}>$ = 381.52±0.06 K			
$<T_{max}>$ = 382.97±0.06 K			
$<\Delta_{fus}H°_m>$ = 17.81±0.12 kJ·mol^{-1}			

(b)

β = 1K·min^{-1}						
(II→I) Phase transition				Fusion (Form I)		
m/mg	T_{on}/K	T_{max}/K	$\Delta_{trs}H°_m$/kJ·mol^{-1}	T_{on}/K	T_{max}/K	$\Delta_{fus}H°_m$/kJ·mol^{-1}
5.6431	358.1	359.5	0.94	381.85	383.15	17.92
5.6144	356.4	361.0	0.77	381.75	383.15	17.99
5.3589	357.3	360.9	0.80	381.75	383.05	17.99
5.7420	355.9	361.7	0.76	381.85	383.05	17.76
5.6055	356.9	359.9	0.80	381.85	383.05	17.36
$<T_{on}>$ = 356.91±0.74 K				$<T_{on}>$ = 381.81±0.04 K		
$<T_{max}>$ = 360.60±0.80 K				$<T_{max}>$ = 383.09±0.04 K		
$<\Delta_{trs}H°_m>$ = 0.81±0.06 kJ·mol^{-1}				$<\Delta_{fus}H°_m>$ = 17.80±0.24 kJ·mol^{-1}		

Table S11 Activation energy (E_a) as a function of conversion fraction (α) obtained for annealed powder samples of form II using various isoconversional approach.

α	E_a/kJ·mol^{-1}		
	Starnik	Vyazovkin	Freidmann
0.10	264.79±15.24	264.65	214.17±25.80
0.20	257.50±8.87	257.54	220.81±19.00
0.30	254.19±9.19	254.24	246.46±23.91
0.40	251.06±11.19	251.08	222.25±24.02
0.50	246.12±13.21	246.12	217.05±28.13
0.60	239.34±15.60	239.33	210.70±35.68
0.70	230.58±19.47	230.57	195.96±40.28
0.80	218.08±25.25	217.87	181.36±47.94
0.90	202.25±30.81	201.40	182.85±41.50

Table S12 Regression coefficients, R^2 and activation energy, E_a obtained by fitting Coats-Redfern equation to non-isothermal α vs T data obtained at heating rates of (a) 0.25 $K \cdot min^{-1}$, (b) 0.5 $K \cdot min^{-1}$, (c) 1 $K \cdot min^{-1}$, (d) 2 $K \cdot min^{-1}$.

(a)

	β = 0.25 $K \cdot min^{-1}$					
Kinetic	Exp-1		Exp-2		Exp-3	
models	R^2	E_a/kJ·mol^{-1}	R^2	E_a/kJ·mol^{-1}	R^2	E_a/kJ·mol^{-1}
P2	0.9065	321.55	0.8585	205.59	0.8229	185.41
P3	0.9049	212.41	0.8549	135.09	0.8181	121.63
P4	0.9033	157.83	0.8512	99.84	0.8132	89.75
A2	0.9641	403.83	0.9373	264.98	0.9189	247.27
A3	0.9635	267.26	0.9360	174.68	0.9171	162.88
A4	0.9630	198.97	0.9346	129.53	0.9152	120.68
B1	—	—	—	—	—	—
R2	0.9375	722.57	0.9018	470.38	0.8765	431.98
R3	0.9470	750.86	0.9147	490.78	0.8921	453.26
D1	0.9088	1303.90	0.8636	840.10	0.8297	759.39
D2	0.9266	1392.70	0.8878	904.57	0.8596	825.92
D3	0.9474	1507.61	0.9156	987.47	0.8933	912.43
D4	0.9340	1430.34	0.8977	931.75	0.8716	854.27
F0/R1	0.9080	649.00	0.8619	417.10	0.8275	376.74
F1	0.9646	813.56	0.9386	535.87	0.9207	500.46
F2	0.9964	1050.16	0.9852	705.02	0.9753	678.85
F3	0.9960	1344.52	0.9936	915.18	0.9868	901.64

(b)

Kinetic	β = 0.5 K·min^{-1}					
	Exp-1		Exp-2		Exp-3	
Models	R^2	E_a/kJ·mol^{-1}	R^2	E_a/kJ·mol^{-1}	R^2	E_a/kJ·mol^{-1}
P2	0.9668	149.80	0.8170	147.17	0.7729	118.18
P3	0.9655	97.89	0.8107	96.12	0.7637	76.79
P4	0.9640	71.94	0.8041	70.59	0.7539	56.09
A2	0.9918	187.52	0.9101	196.17	0.8795	159.10
A3	0.9915	123.04	0.9076	128.79	0.8753	104.07
A4	0.9912	90.80	0.9049	95.09	0.8709	76.55
B1	—	—	—	—	—	—
R2	0.9823	339.28	0.8683	343.68	0.8328	278.63
R3	0.9862	352.24	0.8835	360.57	0.8501	292.73
D1	0.9687	616.94	0.8259	606.61	0.7859	490.70
D2	0.9774	657.75	0.8526	658.48	0.8160	534.14
D3	0.9864	710.40	0.8852	727.12	0.8527	591.45
D4	0.9808	675.00	0.8641	680.92	0.8288	552.89
F0/R1	0.9681	305.51	0.8230	300.32	0.7817	242.35
F1	0.9920	380.95	0.9126	398.32	0.8834	324.18
F2	0.9892	489.11	0.9755	543.00	0.9584	444.37
F3	0.9637	623.43	0.9968	724.70	0.9888	595.23

(c)

Kinetic	β = 1 K·min^{-1}					
	Exp-1		Exp-2		Exp-3	
Models	R^2	E_a/kJ·mol^{-1}	R^2	E_a/kJ·mol^{-1}	R^2	E_a/kJ·mol^{-1}
P2	0.8570	224.84	0.8385	172.45	0.8514	154.79
P3	0.8537	147.90	0.8336	112.96	0.8463	101.19
P4	0.8502	109.42	0.8285	83.21	0.8410	74.39
A2	0.9360	289.46	0.9300	229.71	0.9350	204.60
A3	0.9347	190.98	0.9282	151.13	0.9331	134.40
A4	0.9334	141.74	0.9264	111.85	0.9312	99.29
B1	—	—	—	—	—	—
R2	0.8996	513.09	0.8891	401.74	0.8976	359.68
R3	0.9126	535.34	0.9040	421.46	0.9112	376.85
D1	0.8619	917.33	0.8454	707.85	0.8586	637.18
D2	0.8854	986.26	0.8729	768.79	0.8831	689.94
D3	0.9135	1076.67	0.9052	848.95	0.9125	759.71
D4	0.8953	1015.84	0.8844	795.01	0.8935	712.75
F0/R1	0.8603	455.67	0.8431	350.92	0.8563	315.58
F1	0.9372	584.92	0.9317	465.44	0.9367	415.21
F2	0.9875	773.84	0.9852	633.29	0.9880	562.25
F3	0.9992	1010.21	0.9955	843.59	0.9996	746.77

(d)

Kinetic Models	β = 2 K·min^{-1} Exp-1 R^2	Exp-1 E_a/kJ·mol^{-1}	Exp-2 R^2	Exp-2 E_a/kJ·mol^{-1}	Exp-3 R^2	Exp-3 E_a/kJ·mol^{-1}
P2	0.9012	199.06	0.9419	187.90	0.9465	156.62
P3	0.8984	130.69	0.9401	123.26	0.9445	102.40
P4	0.8955	96.51	0.9382	90.94	0.9423	75.29
A2	0.9643	253.52	0.9838	233.61	0.9873	194.74
A3	0.9635	167.00	0.9834	153.73	0.9869	127.81
A4	0.9626	123.74	0.9829	113.79	0.9865	94.35
B1	—	—	—	—	—	—
R2	0.9361	452.76	0.9657	422.83	0.9702	353.65
R3	0.9464	471.49	0.9724	438.53	0.9767	366.73
D1	0.9052	814.35	0.9445	769.69	0.9494	644.57
D2	0.9247	872.94	0.9579	819.33	0.9627	686.40
D3	0.9470	949.03	0.9728	883.10	0.9771	739.50
D4	0.9327	897.85	0.9633	840.23	0.9680	703.83
F0/R1	0.9039	404.16	0.9437	381.83	0.9485	319.27
F1	0.9651	513.07	0.9842	473.25	0.9877	395.51
F2	0.9974	670.41	0.9986	603.62	0.9984	502.59
F3	0.9950	866.44	0.9845	765.28	0.9804	634.73

Table S13 Temperature dependency of the mole fraction (x_{4HAP}) solubilities of form I and II HAP in ethanol and acetonitrile[a]

	Ethanol		Acetonitrile	
	T/K	*x*	*T*/K	*x*
Form II	283.25	0.2177±0.0011(3)	283.12	0.0775±0.0007(3)
	285.68	0.2332±0.0018(3)	285.60	0.0915±0.0011(3)
	288.16	0.2442±0.0018(3)	288.08	0.0887±0.0007(3)
	290.54	0.2565±0.0008(3)	290.51	0.1018±0.0018(3)
	292.98	0.2651±0.0010(3)	292.97	0.1024±0.0001(3)
	295.38	0.2845±0.0025(3)	295.38	0.1151±0.0003(3)
	297.11	0.2935±0.0010(6)	297.88	0.1290±0.0008(3)
	299.35	0.3030±0.0016(6)	298.77	0.1291±0.0011(3)
			299.84	0.1343±0.0006(6)
Form I	300.25	0.3115±0.0020(6)	300.81	0.1406±0.0010(6)
	301.46	0.3102±0.0008(6)	301.98	0.1460±0.0012(6)
	302.42	0.3213±0.0024(6)	303.67	0.1643±0.0004(6)
	305.03	0.3450±0.0041(3)	307.26	0.1814±0.0017(3)
	307.33	0.3445±0.0009(3)	309.82	0.1908±0.0006(3)
	309.78	0.3505±0.0018(3)	312.29	0.2133±0.0014(3)
	312.18	0.3819±0.0030(3)		

[a] The indicated uncertainties correspond to twice the standard error of the mean of the number of determinations given in parenthesis.

Table S14 Coefficients of Eq S1 for different species used for the calculation of the $\Delta_f G^\circ_m$-T diagram

$$C^\circ_{p,m}/\mathrm{J\cdot mol^{-1}\cdot K^{-1}} = a(T/\mathrm{K})^4 + b(T/\mathrm{K})^3 + c(T/\mathrm{K})^2 + d(T/\mathrm{K}) + e \quad \text{(S1)}$$

Species	*a*	*b*	*c*	*d*	e
C, graphite[a]			-2.4157×10^{-5}	4.9315×10^{-2}	-4.0300
H_2, g[a]	-2.5236×10^{-10}	4.9386×10^{-7}	-3.6054×10^{-4}	1.1716×10^{-1}	14.859
N_2, g[a]		5.0282×10^{-9}	3.2928×10^{-6}	-2.8304×10^{-3}	29.538
O_2, g[a]		-4.2167×10^{-8}	6.3820×10^{-5}	-2.1853×10^{-2}	31.335
S°_m (HAP, g)[b]			1.65499×10^{-4}	0.621999	222.855

[a] These were obtained by fitting eq S1 to data retrieved from the JANAF tables.[96]
[b]Ref 39

Table S15 Auxiliary data for the calculation of the $\Delta_f G_m^\circ$ -T diagram (p° = 1 bar), for the solid and liquid phases of 4'-hydroxyacetophenone.

M	136.1479 g·mol^{-1}
R	8.314472 J·K^{-1}·mol^{-1}
p°	100000 Pa
T_{trs}(II→I)	300.1 K
$\Delta_{trs}H_m$ (II→I, $T_{trs,\ eq.}$)	0.49 kJ·mol^{-1}
T_{fus}(cr I)	381.9 K
$\Delta_{fus}H_m$ (cr I, T_{fus})	18.08 kJ·mol^{-1}
T_{fus}(cr II)	377.7
$\Delta_{fus}H_m$ (cr II, T_{fus})	19.1 kJ·mol^{-1}
$\Delta_f H_m$ (cr I, 298.15 K)	-368.9 kJ·mol^{-1}
$\Delta_f H_m$ (cr II, 298.15 K)	-369.3900 kJ·mol^{-1}
$\Delta_f H_m$ (g, 298.15 K)	-265.7 kJ·mol^{-1}
$\Delta_f H_m$ (l, $T_{fus\ l,}$)	-352.9583 kJ·mol^{-1}
T_{sat}	327.4 K
S_m^o (g, T_{sat})	444.2 J·K^{-1}·mol^{-1}
S_m^o (cr I, T_{sat})	247.3114 J·K^{-1}·mol^{-1}
S_m^o (cr II, $T_{trs,\ eq.}$)	229.4709 J·K^{-1}·mol^{-1}
S_m^o (l, $T_{fus\ l}$)	326.5026 J·K^{-1}·mol^{-1}

Tables S16 Data for the calculation of (a) $\Delta_f G_m^\circ$-T diagram (Figure 5.11a), and (b) thermodynamic functions ($\Delta_{trs} G_m^\circ$, $\Delta_{trs} H_m^\circ$ and $T\Delta_{trs} S_m^\circ$) of the form II → I phase transition.(Figure 5.11b).

(a)

T/K	$\Delta_f H_m^\circ$ (cr I)/ kJ·mol^{-1}	$\Delta_f H_m^\circ$ (cr II)/ kJ·mol^{-1}	$\Delta_f H_m^\circ$ (l)/ kJ·mol^{-1}	S_m° (g)/ J·K^{-1}·mol^{-1}	S_m° (cr I)/ J·K^{-1}·mol^{-1}	S_m° (cr II)/ J·K^{-1}·mol^{-1}	S_m° (l)/ J·K^{-1}·mol^{-1}	$\Delta_f G_m^\circ$ (cr I)/ kJ·mol^{-1}	$\Delta_f G_m^\circ$ (cr II)/ kJ·mol^{-1}	$\Delta_f G_m^\circ$ (l)/ kJ·mol^{-1}
200	-364.656	-365.234	-344.100	353.875	169.561	167.516	161.649	-398.568	-398.737	-376.430
205	-364.904	-365.469	-344.345	357.320	172.746	170.769	167.269	-400.317	-400.477	-378.635
210	-365.151	-365.703	-344.587	360.773	175.915	174.000	172.795	-402.093	-402.243	-380.874
215	-365.395	-365.935	-344.828	364.235	179.070	177.212	178.232	-403.895	-404.035	-383.148
220	-365.636	-366.165	-345.068	367.705	182.212	180.404	183.584	-405.722	-405.853	-385.457
225	-365.873	-366.392	-345.307	371.183	185.341	183.577	188.855	-407.575	-407.697	-387.799
230	-366.107	-366.617	-345.546	374.670	188.458	186.733	194.047	-409.452	-409.566	-390.176
235	-366.337	-366.840	-345.783	378.164	191.563	189.872	199.166	-411.354	-411.459	-392.587
240	-366.564	-367.060	-346.020	381.668	194.657	192.994	204.213	-413.282	-413.378	-395.031
245	-366.788	-367.278	-346.256	385.179	197.740	196.102	209.191	-415.234	-415.323	-397.508
250	-367.007	-367.492	-346.492	388.698	200.813	199.194	214.104	-417.210	-417.290	-400.018
255	-367.223	-367.704	-346.727	392.226	203.876	202.272	218.954	-419.211	-419.283	-402.561
260	-367.434	-367.912	-346.963	395.762	206.929	205.336	223.744	-421.236	-421.300	-405.137
265	-367.641	-368.118	-347.199	399.307	209.973	208.387	228.475	-423.284	-423.340	-407.745
270	-367.844	-368.320	-347.435	402.860	213.008	211.425	233.150	-425.357	-425.405	-410.385
275	-368.043	-368.519	-347.671	406.421	216.035	214.451	237.771	-427.452	-427.493	-413.058
280	-368.237	-368.714	-347.907	409.990	219.054	217.465	242.340	-429.572	-429.604	-415.762
285	-368.426	-368.905	-348.144	413.567	222.064	220.468	246.859	-431.714	-431.738	-418.499
290	-368.610	-369.093	-348.381	417.153	225.067	223.460	251.329	-433.880	-433.896	-421.267
295	-368.789	-369.276	-348.620	420.747	228.063	226.441	255.752	-436.068	-436.076	-424.067
298.15	-368.900	-369.390	-348.770	423.016	229.946	228.314	258.516	-437.459	-437.462	-425.846
300.1	-368.967	-369.460	-348.863	424.422	231.111	229.471	260.218	-438.324	-438.324	-426.955
305.6	-369.154	-369.653	-349.127	428.394	234.390	232.727	264.982	-440.783	-440.774	-430.106
311.1	-369.333	-369.840	-349.392	432.376	237.661	235.972	269.696	-443.270	-443.251	-433.295
316.6	-369.507	-370.023	-349.658	436.369	240.925	239.205	274.360	-445.783	-445.756	-436.521
322.1	-369.673	-370.201	-349.926	440.371	244.181	242.428	278.977	-448.324	-448.287	-439.785
327.6	-369.833	-370.373	-350.196	444.384	247.429	245.640	283.548	-450.891	-450.844	-443.086
333.1	-369.987	-370.540	-350.466	448.406	250.671	248.842	288.074	-453.486	-453.429	-446.424
338.6	-370.134	-370.700	-350.739	452.438	253.906	252.034	292.558	-456.106	-456.039	-449.799
344.1	-370.273	-370.855	-351.014	456.481	257.134	255.217	297.000	-458.753	-458.675	-453.212
349.6	-370.406	-371.005	-351.290	460.533	260.356	258.391	301.402	-461.427	-461.339	-456.660

Continued….

T/K	$\Delta_f H^o_m$ (cr I)/ kJ·mol^{-1}	$\Delta_f H^o_m$ (cr II)/ kJ·mol^{-1}	$\Delta_f H^o_m$ (l)/ kJ·mol^{-1}	S^o_m (g)/ J·K^{-1} ·mol^{-1}	S^o_m (cr I)/ J·K^{-1}·mol^{-1}	S^o_m (cr II)/ J·K^{-1}·mol^{-1}	S^o_m (l)/ J·K^{-1}·mol^{-1}	$\Delta_f G^o_m$ (cr I)/ kJ·mol^{-1}	$\Delta_f G^o_m$ (cr II)/ kJ·mol^{-1}	$\Delta_f G^o_m$ (l)/ kJ·mol^{-1}
355.1	-370.532	-371.149	-351.569	464.596	263.572	261.556	305.764	-464.126	-464.027	-460.146
360.6	-370.650	-371.286	-351.849	468.668	266.782	264.712	310.089	-466.852	-466.742	-463.667
366.1	-370.761	-371.418	-352.132	472.751	269.986	267.860	314.378	-469.603	-469.481	-467.226
371.6	-370.865	-371.543	-352.417	476.843	273.185	271.000	318.630	-472.380	-472.246	-470.820
377.7	-370.971	-371.674	-352.737	481.394	276.726	274.473	323.307	-475.490	-475.343	-474.850
378	-370.976	-371.681	-352.752	481.618	276.900	274.644	323.536	-475.644	-475.496	-475.049
380	-371.009	-371.723	-352.857	483.113	278.060	275.781	325.059	-476.672	-476.519	-476.379
381.9	-371.038	-371.760	-352.958	484.534	279.160	276.860	326.503	-477.650	-477.493	-477.650
385.9	-371.099	-371.839	-353.170	487.530	281.476	279.128	329.529	-479.721	-479.555	-480.335
389.9	-371.156	-371.914	-353.384	490.532	283.789	281.392	332.538	-481.805	-481.629	-483.040
393.9	-371.208	-371.986	-353.599	493.539	286.100	283.653	335.530	-483.902	-483.717	-485.764
397.9	-371.255	-372.054	-353.816	496.551	288.407	285.910	338.506	-486.013	-485.817	-488.508
401.9	-371.300	-372.119	-354.033	499.568	290.713	288.164	341.467	-488.138	-487.932	-491.268
405.9	-371.339	-372.180	-354.253	502.591	293.015	290.414	344.411	-490.274	-490.058	-494.050

(b)

T/K	$\Delta_{trs}G^{\circ}_{m}$ /J·mol^{-1}	$\Delta_{trs}H^{\circ}_{m}$ /J·mol^{-1}	$T\Delta_{trs}S^{\circ}_{m}$/J·mol^{-1}
200	169	579	409
205	160	565	405
210	150	552	402
215	140	540	400
220	131	529	398
225	122	519	397
230	114	510	397
235	105	502	398
240	96	496	399
245	89	490	401
250	80	485	405
255	72	481	409
260	64	478	414
265	56	476	420
270	48	476	427
275	41	476	436
280	32	477	445
285	24	479	455
290	16	483	466
295	8	487	479
298.15	3	490	487
300.1	0	492	492
305.6	-9	499	508
311.1	-19	507	526
316.6	-27	517	544
322.1	-37	527	565
327.6	-47	539	586
333.1	-57	552	609
338.6	-67	567	634
344.1	-78	582	660
349.6	-88	599	687
355.1	-99	617	716
360.6	-110	636	746
366.1	-122	657	778
371.6	-134	678	812
377.7	-147	704	851
378	-148	705	853
380	-153	713	866
381.9	-157	722	879
385.9	-166	740	906
389.9	-176	759	935
393.9	-185	778	964
397.9	-196	798	994
401.9	-206	819	1024
405.9	-216	841	1056

Tables S17 Electronic energy obtained from DFT calculations at the B3LYP-D3/aug-cc-pVTZ level of theory, after: full geometry optimization of a single HAP molecule in the gas phase, E_{FO}; optimizing the hydrogens positions of an isolated molecule with the molecular conformation found in solid state, E_{HO}; optimizing the hydrogen positions of a HAP dimer connected by hydrogen bonds, as found in each crystal phase, E_{HB}.

	E_{FO} /Ha	E_{HO} /Ha	E_{HB} /Ha
Form I	-460.3267289	-460.3267289	-920.6671446
Form IIa[a]	-460.3271984	-460.3264123	-920.6698137
Form IIb[a]	-460.3271984	-460.3260513	-920.6695493

[a] Form IIa and Form IIb refer to results obtained for the two HAP molecules in the asymmetric unit of form II, or to the two types of hydrogen bonds that can be found in the crystal structure of this phase.

Acknowledgements

This work was supported by Fundação para a Ciência e a Tecnologia (FCT), Portugal through project UID/MULTI/00612/2013 and grants awarded to A. Joseph (SFRH/BD/90386/2012) and C. E. S. Bernardes (SFRH/BPD/101505/2014). Thanks are also due to PARALAB (Portugal) for providing the Netzsch DSC 204 F1-Phoenix apparatus and to Dr. F. Agapito (CQB-FCUL) for helpful discussions on Hirshfeld surface analysis.and COST Action CM1402.

References

1. Desiraju, G. R. *Angew. Chem. Int. Edit.* **2007**, *46,* 8342-8356.
2. Desiraju, G. R. *J. Am. Chem. Soc.* **2013**, *135,* 9952-9967.
3. Desiraju, G. R.; Vittal, J. J.; Ramanan, A., *Crystal Engineering: A Textbook* Ed.; World Scientific Publishing Co.: Singapore, 2011.
4. Bernstein, J., *Polymorphism in Molecular Crystals*, Ed.; Oxford University Press: Oxford, 2002.
5. Brittain, H. G., *Polymorphism in Pharmaceutical Solids*, Ed.; Marcel Dekker: New York, 1999.
6. Brittain, H. G., *Polymorphism in Pharmaceutical Solids*, 2nd ed.; Ed.; Informa Healthcare: New York, 2009.
7. Griesser, U. J., *The Importance of Solvates*. Wiley-VCH Velag GmbH & Co.: Weinheim, 2006; p 211-233.
8. Das, D.; Banerjee, R.; Mondal, R.; Howard, J. A. K.; Boese, R.; Desiraju, G. R. *Chem. Comm.* **2006,** 555-557.
9. Desiraju, G. R. *CrystEngComm* **2007**, *9,* 91-92.
10. Allen, F. H. *Acta Crystallogr.* **2002**, *B58,* 380-388.
11. Brock, C. P.; Duncan, L. L. *Chem. Mater.* **1994**, *6,* 1307-1312.
12. Brock, C. P.; Patrick, B. O. *Mol. Cryst. Liq. Cryst.* **2002**, *389,* 79-85.
13. Lehmler, H. J.; Robertson, L. W.; Parkin, S.; Brock, C. P. *Acta Crystallogr.* **2002**, *B58,* 140-147.
14. Anderson, K. M.; Steed, J. W. *CrystEngComm* **2007**, *9,* 328-330.
15. Nichol, G. S.; Clegg, W. *CrystEngComm* **2007**, *9,* 959-960.
16. Janot, C., *Quasicrystals: A Primer*, 2nd ed.; Ed.; Clarendon Press: Oxford, 1994.
17. Gelbrich, T.; Braun, D. E.; Ellern, A.; Griesser, U. J. *Cryst. Growth Des.* **2013**, *13,* 1206-1217.
18. Nangia, A. *Acc. Chem. Res.* **2008**, *41,* 595-604.
19. Roy, S.; Banerjee, R.; Nangia, A.; Kruger, G. J. *Chem. Eur. J.* **2006**, *12,* 3777-3788.
20. Pidcock, E. *Acta Crystallogr.* **2006**, *B62,* 268-279.

21. Vande Velde, C. M. L.; Tylleman, B.; Zeller, M.; Sergeyev, S. *Acta Crystallogr.* **2010**, *B66,* 472-481.
22. Steed, K. M.; Steed, J. W. *Chem. Rev.* **2015**, *115,* 2895-2933.
23. Martinho Simões, J. A.; Minas da Piedade, M. E., *Molecular Energetics: Condensed-Phase Thermochemical Techniques*; Oxford University Press: New York, 2008.
24. Mnyukh, Y., *Fundamentals of Solid-State Phase Transitions, Ferromagnetism and Ferroelectricity*, Ed.; 1st Book Library Milton Keynes, 2001.
25. Westrum Jr., E. F.; McCullough, J. P., Thermodynamics of Crystals. In *Physics and Chemistry of the Organic Solid State*, Fox, D.; Labes, M. M.; Weissberger, A., Eds. Interscience: New York, 1963; Vol. I.
26. Denbigh, K., *The Principles of Chemical Equilibrium*, 4th ed.; Cambridge University Press: Cambridge, 1981.
27. Gopal, E. S. R., *Specific Heats at Low Temperatures*, Ed.; PlenumPress: New York, 1966.
28. Gavezzotti, A., Crystal Symmetry and Molecular Recognition. In *Theoretical Aspects and Computer Modelling of the Molecular Solid State*, Gavezzotti, A., Ed. John Wiley: Chichester, 1997; pp 20-21.
29. Cox, J. D.; Pilcher, G., *Thermochemistry of Organic and Organometallic Compounds*, Ed.; Academic Press: London, 1970.
30. Herbstein, F. H. *Acta Crystallogr* **2006**, *B62,* 341-383.
31. Burger, A.; Ramberger, R. *Mikrochim. Acta* **1979**, *2,* 259-271.
32. Threlfall, T. L. *Org. Process Res. Dev.* **2009**, *13,* 1224-1230.
33. Simões, R. G.; Bernardes, C. E. S.; Minas da Piedade, M. E. *Cryst. Growth Des.* **2013**, *13,* 2803-2814.
34. Zencirci, N.; Gelbrich, T.; Apperley, D. C.; Harris, R. K.; Kahlenberg, V.; Griesser, U. J. *Cryst. Growth Des.* **2010**, *10,* 302-313.
35. Zencirci, N.; Griesser, U. J.; Gelbrich, T.; Apperley, D. C.; Harris, R. K. *Mol. Pharmaceut.* **2014**, *11,* 338-350.
36. Yu, L.; Stephenson, G. A.; Mitchell, C. A.; Bunnell, C. A.; Snorek, S. V.; Bowyer, J. J.; Borchardt, T. B.; Stowell, J. G.; Byrn, S. R. *J. Am. Chem. Soc.* **2000**, *122,* 585-591.
37. Yu, L. *Accounts Chem. Res.* **2010**, *43,* 1257-1266.
38. Hean, D.; Gelbrich, T.; Griesser, U. J.; Michael, J. P.; Lemmerer, A. *CrystEngComm* **2015**, *17,* 5143-5153.
39. Bernardes, C. E. S.; Piedade, M. F. M.; Minas da Piedade, M. E. *Cryst. Growth Des.* **2008**, *8,* 2419-2430.
40. Long, S. H.; Siegler, M. A.; Mattei, A.; Li, T. L. *Cryst. Growth Des.* **2011**, *11,* 414-421.
41. Nanubolu, J. B.; Ravikumar, K.; Sridhar, B.; Sreedhar, B. *J. Mol. Struct.* **2014**, *1078,* 133-145.
42. Krishnan, B. P.; Sureshan, K. M. *J. Am. Chem. Soc.* **2015**, *137,* 1692-1696.
43. Takahashi, H.; Ito, Y. *CrystEngComm* **2010**, *12,* 1628-1634.
44. Fun, H. K.; Chantrapromma, S.; Ong, L. H. *Molecules* **2014**, *19,* 10137-10149.
45. Brandel, C.; Cartigny, Y.; Couvrat, N.; Eusébio, M. E. S.; Canotilho, J.; Petit, S.; Coquerel, G. *Chem. Mater.* **2015**, *27,* 6360-6373.
46. Batsanov, A. S.; Collings, J. C.; Ward, R. M.; Goeta, A. E.; Porrès, L.; Beeby, A.; Howard, J. A. K.; Steed, J. W.; Marder, T. B. *CrystEngComm* **2006,** *8,* 622-628.
47. Suzuki, M.; Maeda, Y.; Akita, M.; Teramae, H.; Kobayashi, K. *Cryst. Growth Des.* **2014**, *14,* 6302-6310.

48. Vainshte, B. K.; Lobanova, G. M.; Gurskaya, G. V. *Kristallografiya* **1974**, *19,* 531-538.
49. Chenthamarai, S.; Jayaraman, D.; Meera, K.; Santhanaraghavan, P.; Subramanian, C.; Bocelli, G.; Ramasamy, P. *Crystal Eng.* **2001**, *4,* 37-48.
50. Kresge, A. J.; Lough, A. J.; Zhu, Y. *Acta Crystallogr.* **2002**, *58,* o1057-o1059.
51. Bernardes, C. E. S.; Piedade, M. F. M.; Minas da Piedade, M. E. *Cryst. Growth Des.* **2010**, *10,* 3070-3076.
52. Bernardes, C. E. S.; Minas da Piedade, M. E. *Cryst. Growth Des.* **2012**, *12,* 2932-2941.
53. Bernardes, C. E. S.; Ilharco, L. M.; Minas da Piedade, M. E. *J. Mol. Struct.* **2014**, *1078,* 181-187.
54. Bernardes, C. E. S.; Matos Lopes, M. L. S.; Ascenso, J. R.; Minas da Piedade, M. E. *Cryst. Growth Des.* **2014**, *14,* 5436-5441.
55. Kulkarni, S. A.; Meekes, H.; ter Horst, J. H. *Cryst. Growth Des.* **2014**, *14,* 1493-1499.
56. Laugier, J. B., B. *Cellref V3 http://www.ccp14.ac.uk/tutorial/lmgp/cellref.htm*.
57. Kubelka, P.; Munk, F. *Zeits. f. Techn. Physik* **1931**, *12,* 593–601.
58. Gnutzmann, T.; Thi, Y. N.; Rademann, K.; Emmerling, F. *Cryst. Growth Des.* **2014**, *14,* 6445-6450.
59. Moura Ramos, J. J.; Taveira-Marques, R.; Diogo, H. P. *J. Pharm. Sci.* **2004**, *93,* 503-1507.
60. Joseph, A.; Bernardes, C. E. S.; Minas da Piedade, M. E. *J. Chem. Thermodyn.* **2012**, *55,* 23-28.
61. Krol, O. V.; Druzhinina, A. I.; Varushchenko, R. M.; Dorofeeva, O. V.; Reshetova, M. D.; Borisova, N. E. *J. Chem. Thermodyn.* **2008**, *40,* 549-557.
62. Varushchenko, R. M.; Druzhinina, A. I.; Sorkin, E. L. *J. Chem. Thermodyn.* **1997**, *29,* 623-637.
63. Varushchenko, R.; Druzhinina, A. I., *Thermodynamics of the Phase Equilibriums of Some Organic Compounds*, Ed.; InTech: Rijeka, 2011.
64. Gonçalves, E. M.; Minas da Piedade, M. E. *J. Chem. Thermodyn.* **2012**, *47,* 362-371.
65. Frisch, M. J.; Trucks, G. W.; Schlegel, H. B.; Scuseria, G. E.; Robb, M. A.; Cheeseman, J. R.; Scalmani, G.; Barone, V.; Mennucci, B.; Petersson, G. A.; Nakatsuji, H.; Caricato, M.; Li, X.; Hratchian, H. P.; Izmaylov, A. F.; Bloino, J.; Zheng, G.; Sonnenberg, J. L.; Hada, M.; Ehara, M.; Toyota, K.; Fukuda, R.; Hasegawa, J.; Ishida, M.; Nakajima, T.; Honda, Y.; Kitao, O.; Nakai, H.; Vreven, T.; Montgomery Jr., J. A.; Peralta, J. E.; Ogliaro, F.; Bearpark, M. J.; Heyd, J.; Brothers, E. N.; Kudin, K. N.; Staroverov, V. N.; Kobayashi, R.; Normand, J.; Raghavachari, K.; Rendell, A. P.; Burant, J. C.; Iyengar, S. S.; Tomasi, J.; Cossi, M.; Rega, N.; Millam, N. J.; Klene, M.; Knox, J. E.; Cross, J. B.; Bakken, V.; Adamo, C.; Jaramillo, J.; Gomperts, R.; Stratmann, R. E.; Yazyev, O.; Austin, A. J.; Cammi, R.; Pomelli, C.; Ochterski, J. W.; Martin, R. L.; Morokuma, K.; Zakrzewski, V. G.; Voth, G. A.; Salvador, P.; Dannenberg, J. J.; Dapprich, S.; Daniels, A. D.; Farkas, Ö.; Foresman, J. B.; Ortiz, J. V.; Cioslowski, J.; Fox, D. J. *Gaussian 09 D.01*, Gaussian, Inc.: Wallingford, CT, USA, 2009.
66. Koch, W.; Holthausen, M. C. A., *Chemist's Guide to Density Functional Theory*, 2nd ed.; Ed.; Wiley-VCH: Weinheim, 2002.
67. Becke, A. D. *J. Chem. Phys.* **1993**, *98,* 5648-5652.
68. Lee, C.; Yang, W.; Parr, R. G. *Phys. Rev. B* **1988**, *37,* 785-789.
69. Grimme, S.; Ehrlich, S.; Goerigk, L. *J. Comput. Chem.* **2011**, *32,* 1456-1465.
70. Dunning, T. H. *J. Chem. Phys.* **1989**, *90,* 1007-1023.
71. Kendall, R. A.; Dunning, T. H.; Harrison, R. J. *J. Chem. Phys.* **1992**, *96,* 6796-6806.
72. Boys, S. F.; Bernardi, F. *Mol. Phys.* **2002**, *100,* 65-73.

73. Wolff, S. K.; Grimwood, D. J.; McKinnon, J. J.; Turner, M. J.; Jayatilaka, D.; Spackman, M. A., *CrystalExplorer (Version 3.1)*, . University of Western Australia, 2012.
74. McKinnon, J. J.; Spackman, M. A.; Mitchell, A. S. *Acta Crystallogr.* **2004**, *B60,* 627-668.
75. Spackman, M. A.; Jayatilaka, D. *CrystEngComm* **2009**, *11,* 19-32.
76. Koga, T.; Kanayama, K.; Watanabe, S.; Thakkar, A. J. *Int. J. Quantum Chem.* **1999**, *71,* 491-497.
77. Mnyukh, Y. V.; Panfilova, N. A. *J. Phys. Chem. Solids* **1973**, *34,* 159-170.
78. Li, S. D.; Sellers, M. S.; Basaran, C.; Schultz, A. J.; Kofke, D. A. *Int J Mol Sci* **2009**, *10,* 2798-2808.
79. Vyazovkin, S.; Burnham, A. K.; Criado, J. M.; Perez-Maqueda, L. A.; Popescu, C.; Sbirrazzuoli, N. *Thermochim. Acta* **2011**, *520,* 1-19.
80. Ozawa, T. *Bull. Chem. Soc. Jp.* **1965**, *38,* 1881-+.
81. Flynn, J. H.; Wall, L. A. *J. Polym. Sci. Pol. Lett.* **1966**, *4,* 323-328.
82. Khawam, A.; Flanagan, D. R. *J. Pharm. Sci.* **2006**, *95,* 472-498.
83. Vyazovkin, S. *J Comput Chem* **1997**, *18,* 393-402.
84. Šimon, P.; Thomas, P.; Dubaj, T.; Cibulková, Z.; Peller, A.; Veverka, M. *J. Therm. Anal. Calorim.* **2014**, *115,* 853-859.
85. Vyazovkin, S.; Wight, C. A. *Int. Rev. Phys. Chem.* **1998**, *17,* 407-433.
86. Burnham, A. K.; Weese, R. K.; Wang, R.; Wang, Kwok, Q. S. M.; Jones, D. E. G. Solid-Solid Phase Transition Kinetics of FOX-7. In *NATAS Annual Conference*, Universal City, CA, United States, 2005.
87. Hu, A.; Larade, B.; Dudiy, S.; Abou-Rachid, H.; Lussier, L. S.; Guo, H. *Propell. Explos. Pyrot.* **2007,** *32,* 331-337.
88. Rong, H. R.; Gu, H. *Thermochim. Acta* **2005,** *428,* 19-23.
89. Stephenson, R. M. M., Stanislaw, *Handbook of the Thermodynamics of Organic Compounds*, Ed.; Springer Netherlands, 1987.
90. O'Brien, L. E.; Timmins, P.; Williams, A. C.; York, P. *J. Pharmaceut. Biomed.* **2004,** *36,* 335-340.
91. Gilpin, R. K.; Zhou, W. *Vib. Spectrosc.* **2005**, *37,* 53-59.
92. Umeda, T.; Ohnishi, N.; Yokoyama, T.; Kuroda, T.; Kita, Y.; Kuroda, K.; Tatsumi, E.; Matsuda, Y. *Chem. Pharm. Bull.* **1985**, *33,* 2073-2078.
93. Surov, A. O.; Terekhova, I. V.; Bauer-Brandl, A.; Perlovich, G. L. *Cryst. Growth Des.* **2009**, *9,* 3265-3272.
94. de Villiers, M. M.; Terblanche, R. J.; Liebenberg, W.; Swanepoel, E.; Dekker, T. G.; Song, M. *J. Pharmaceut. Biomed.* **2005**, *38,* 435-441.
95. Bernardes, C. E. S.; Piedade, M. F. M.; Minas da Piedade, M. E. *Cryst. Growth Des.* **2008**, *8,* 2419-2430.
96. Chase Jr., M. W., *NIST-JANAF Thermochemical Tables*, 4th ed.; Ed.; *J. Phys. Chem. Ref. Data* **1998**, Monograph 9.

Chapter 6

Kinetics and Mechanism of the Thermal Dehydration of a Robust and Yet Metastable Hemihydrate of 4-Hydroxynicotinic Acid.

Abhinav Joseph, Carlos E. S. Bernardes, Ana S. Viana, M. Fatima M. Piedade, Manuel E. Minas da Piedade

Article published on:
Cryst. Growth Des., **2015,** *15*, 3511-3524
DOI: 10.1021/acs.cgd.5b00594

This chapter is essentially focused on the kinetic analysis of the thermal dehydration of a hemihydrate of 4-hydroxynicotinic acid (4HNA·0.5H_2O). The kinetic data along with microscopic observations were used to predict the dehydration mechanism of the hydrate. Finally the kinetic and thermodynamic data from this work were combined with the thermodynamic information previously reported for this system to construct an approximate Gibbs energy profile for the dehydration of 4HNA·0.5H_2O at 298.15 K.

Synthesis and characterization of 4HNA·0.5H_2O were performed by me. I also carried out the isothermal dehydration experiments using thermogravimetric analysis (TGA) which was followed by the kinetic data analysis. The program to analyze the isokinetic effect was developed by Dr. Carlos Bernardes at our Lab. The microscopic observations involving hot stage microscopy (HSM) were carried out in collaboration with Prof. Hermínio Diogo (IST-UL). Atomic force microscopy (AFM) experiments were carried out by Dr. Ana S. Viana at FCUL. Structural analysis of the hemihydrate and anhydrous form of 4-hydroxynicotinic acid were done by Prof. Fatima at FCUL. Finally I contributed in the discussion of results and writing of the manuscript.

Abstract

Hydrates are the most common type of solvates and certainly the most important ones for industries such as pharmaceuticals which strongly rely on the development, production, and marketing of organic molecular solids. A recent study indicated that, in contrast with thermodynamic predictions, a new hemihydrate of 4-hydroxynicotinic acid ($4HNA{\cdot}0.5H_2O$) did not undergo facile spontaneous dehydration at ambient temperature and pressure. The origin of this robustness and the mechanism of dehydration were investigated in this work, through a combined approach which involved kinetic studies by thermogravimetry (TGA), crystal packing analysis based on X-ray diffraction data, and microscopic observations by hot stage microscopy (HSM), scanning electron microscopy (SEM), and atomic force microscopy (AFM).

The TGA results indicated that the resilience of $4HNA{\cdot}0.5H_2O$ to water loss is indeed of kinetic origin, c.f., due to a significant activation energy, E_a, which increased from 85 $kJ{\cdot}mol^{-1}$ to 133 $kJ{\cdot}mol^{-1}$ with the increase in particle size. This E_a range is compatible with the fact that four moderately strong hydrogen bonds (typically 20-30 $kJ{\cdot}mol^{-1}$ each) must be broken to remove water from the crystal lattice. The dehydration kinetics conforms to the Avrami-Erofeev A2 model, which assumes a nucleation and growth mechanism. Support for a nucleation and growth mechanism was also provided by the HSM, SEM, AFM observations. These observations further suggested that the reaction involves one-dimensional nucleation, which is rarely observed. Finally, a statistical analysis of Arrhenius plots for samples with different particle sizes revealed an isokinetic relationship between the activation parameters. This is consistent with the fact that the dehydration mechanism is independent of the sample particle size.

6.1 Introduction

Nicotinic acid (pyridine-3-carboxylic acid, also known as niacin or vitamin B_3) and its hydroxy derivatives (2-, 4-, 5-, and 6-hydroxynicotinic acids) have received considerable attention in recent years. This interest has been mostly driven by their biological significance[1-3] and ample industrial applications, namely as additives in food, forage or cosmetics[4-5] and, particularly, as active pharmaceutical ingredients (API).[5-10] In those applications the compounds are usually employed as solids and, in this case, it is important to investigate the possible occurrence of polymorphism (i.e. the existence of more than one crystal form) or solvate formation, and to establish as accurately as possible the relative thermodynamic and kinetic stabilities of the different solid forms isolated.[11-14] Because dissimilar crystal forms may exhibit significantly different properties (e.g. fusion temperature, compressibility, solubility, dissolution rate in a given media) the lack of control over polymorphism and solvate formation can wreak havoc with end-use applications of a compound, as illustrated by a number of striking examples,[14] such as the widely publicized ritonavir (a AIDS drug) case.[15]

Hydrates are the most commonly occurring solvates during the isolation and processing of organic molecular solids.[16-19] The evaluation of their tendency to form and to dehydrate is therefore of particular interest if tight control over the production and processing of crystalline organic products is to be achieved. Also relevant, from a more fundamental point of view, is to understand the mechanism of the dehydration process. In spite of the important efforts made to systematize the mechanisms of solid state dehydrations, the topic remains a challenge, particularly when there is no obvious relationship between the hydrate and anhydrate lattices and no evidence of reversibility.[20-22]

Recently a new hemihydrate of 4-hydroxynicotinic acid ($4HNA{\cdot}0.5H_2O$), was obtained and characterized both from structural and thermodynamic points of view.[23] No spontaneous dehydration was observed under ambient temperature, pressure, and humidity conditions. This observation was against the thermodynamic analysis of the hydrate stability, which predicted spontaneous dehydration to occur at 298 K, even for a relative humidity of 100%. Irreversible dehydration could, however, be observed at higher temperatures. It was therefore conjectured that the experimentally observed robustness of the compound at ambient temperature should

be of kinetic origin i.e. due to the existence of a sufficiently high activation barrier for the removal of the water molecules from the crystal lattice. This hypothesis was experimentally tested in the present work, based on a thermogravimetric (TGA) study of the 4HNA·0.5H_2O dehydration kinetics, under isothermal conditions, at different temperatures in the range 323-358 K. Also investigated was the influence of particle size on the rate of reaction, which evidenced an isokinetic effect involving the activation parameters. Finally, some insights into the mechanism of the dehydration process were provided by combining the kinetic information with a molecular packing analysis based on single crystal X-ray diffraction results and direct observations of crystals at different dehydration stages by hot-stage optical microscopy (HSM), scanning electron microscopy (SEM), and atomic force microscopy (AFM).

Theoretical framework of the kinetic analysis

The kinetic investigation of the dehydration of 4HNA·0.5H_2O by TGA was primarily based on the determination of the mass loss from the sample as a function of time, under isothermal conditions, and a dynamic flow of N_2/He gas. Based on the mass loss, the conversion fraction, α, at a given time *t* can be obtained as:

$$\alpha = \frac{m_o - m}{m_o - m_f} \qquad (6.1)$$

where m_o and m_f are the initial and final masses of the sample, respectively, and *m* is the mass of sample at time *t*. The rate of reaction, $v = d\alpha/dt$, can be defined by the general equation:

$$v = \frac{d\alpha}{dt} = k\, f(\alpha) \qquad (6.2)$$

where k is the temperature-dependent rate constant and $f(\alpha)$ is a function expressing the dependence of v on α.

Solid state dehydrations frequently have complex mechanisms, involving various elementary steps (e.g. nucleation of the anhydrous phase, interface advance, water vaporization and diffusion) that are difficult to discern experimentally.[20, 22, 24-25] Thus, in many instances $f(\alpha)$ does not correspond to a simple function of α (e.g. α^n where n is the reaction order). The mathematical form of $f(\alpha)$ is dictated by the mechanistic model that best describes the kinetic profile of the reaction. Table 6.1 summarizes the $f(\alpha)$ expressions for various mechanisms that are frequently implied in solid state kinetics and that were tested in the present work.[22, 24, 26-27] Integration of the rate law in eq. 6.2 leads to:

$$\int_0^{\alpha} \frac{1}{f(\alpha)} d\alpha = \int_0^{t} k dt \qquad (6.3)$$

$$g(\alpha) = kt \qquad (6.4)$$

where $g(\alpha)$ represents the function resulting from the integration of the left hand side of eq. 6.3. The mathematical forms of $g(\alpha)$ for different mechanistic models are also given in Table 6.1. In general, the mechanism of a reaction is assigned to the model that gives the best linear fit when the corresponding $g(\alpha)$ function is plotted against t.[22] As indicated by eq. 6.4 the slope of that plot yields the overall rate constant, k. The values of $g(\alpha)$ for the different models can be calculated from the experimental α vs. t plots by using the appropriate expressions in the last column of Table 6.1.

Table 6.1 Rate expressions for different reaction models.[a]

Model	Differential form	Integral form
	$f(\alpha) = \frac{1}{k}\frac{d\alpha}{dt}$	$g(\alpha) = \int_0^{\alpha} \frac{1}{f(\alpha)} d\alpha = kt$
1. *Acceleratory α-time*		
Pn.power law	$n\alpha^{(n-1)/n}$	$\alpha^{1/n}$
E1 exponential law	A	ln α
2. *Sigmoid α-time*		
A2 Avrami-Erofeev	$2(1-\alpha)[-\ln(1-\alpha)]^{1/2}$	$[-\ln(1-\alpha)]^{1/2}$
A3 Avrami-Erofeev	$3(1-\alpha)[-\ln(1-\alpha)]^{2/3}$	$[-\ln(1-\alpha)]^{1/3}$
A4 Avrami-Erofeev	$4(1-\alpha)[-\ln(1-\alpha)]^{3/4}$	$[-\ln(1-\alpha)]^{1/4}$
A*n* Avrami-Erofeev	$n(1-\alpha)[-\ln(1-\alpha)]^{(n-1)/n}$	$[-\ln(1-\alpha)]^{1/n}$
B1 Prout-Tompkins	$\alpha(1-\alpha)$	$\ln[\alpha/(1-\alpha)]$
3. *Deceleratory α-time*		
3a. *Geometrical models*		
R2 contracting area	$2(1-\alpha)^{1/2}$	$1-(1-\alpha)^{1/2}$
R3 contracting volume	$3(1-\alpha)^{2/3}$	$1-(1-\alpha)^{1/3}$
3b. *Diffusion models*		
D1 one-dimensional	0.5α	α^2
D2 two-dimensional	$[-\ln(1-\alpha)]^{-1}$	$(1-\alpha)\ln(1-\alpha)+\alpha$
D3 three-dimensional	$1.5(1-\alpha)^{2/3}[1-(1-\alpha)^{1/3}]$	$[1-(1-\alpha)^{1/3}]^2$
D4 Ginstling-Brounshtein	$1.5[(1-\alpha)^{-1/3}-1]^{-1}$	$1-(2\alpha/3)-(1-\alpha)^{2/3}$
3c. *Reaction-order models*		
F0 zero order	1	α
F1 first order	$(1-\alpha)$	$-\ln(1-\alpha)$
F2 second order	$(1-\alpha)^2$	$(1-\alpha)^{-1}-1$
F3.third order	$(1-\alpha)^3$	$0.5[(1-\alpha)^{-2}-1]$

Energetic barriers of a reaction can be inferred from the temperature dependence of the rate constant which is most often given in terms of Arrhenius equation[24, 28-29]

$$k = Ae^{-E_a/RT} \tag{6.5}$$

Here, E_a represents the overall activation energy of the process, A is the pre-exponential factor, and R = 8.3144621 J·K^{-1}·mol^{-1} [30] is the gas constant. According to Arrhenius equation a plot of $\ln k$ against $1/T$ should lead to a straight line:

$$\ln k = -\frac{a}{T} + b \tag{6.6}$$

with slope $a = E_a/R$ and ordinate $b = \ln A$. The activation parameters A and E_a are normally found by fitting eq. 6.6, to a series of k values obtained at different temperatures.

The Arrhenius parameters can be related to thermodynamic activation functions by:[28-29]

$$\Delta^{\ddagger}H^{\circ}_{m} = E_a - RT \tag{6.7}$$

$$\frac{\Delta^{\ddagger}S^{\circ}_{m}}{R} = \ln A - 1 - \ln\frac{k_B T}{h} \tag{6.8}$$

$$\Delta^{\ddagger}G^{\circ}_{m} = \Delta^{\ddagger}H^{\circ}_{m} - T\Delta^{\ddagger}S^{\circ}_{m} \tag{6.9}$$

where $\Delta^{\ddagger}H_m^{\circ}$, $\Delta^{\ddagger}S_m^{\circ}$ and $\Delta^{\ddagger}G_m^{\circ}$ are the standard molar enthalpy, entropy, and Gibbs energy of activation, respectively, k_B = 1.3806488×10^{-23} J·K^{-1} [30] is the Boltzmann constant, h = 6.62606957×10^{-34} J·s [30] represents the Planck's constant, and T is normally taken as the mean temperature of the interval covered by the experiments.

It should also be pointed out that, because restrictions to molecular motion can vary with the nature of the lattice site (e. g. surface site, defect in the bulk), a dehydration reaction is expected to occur with different activation energies depending on the spatial location of the reactive center.[31-33] As such, the activation parameters obtained through the application of Arrhenius equation, which normally refer to an overall result of several reaction steps, may change with sample characteristics such as the particle size (different surface area to bulk volume ratio) or crystallinity.

Isoconversional Method. The dependence of the activation energy on α may be evaluated by using a model-free or isoconversional approach.[34] The standard isoconversional method relies on the equation:

$$-\ln t_{\alpha} = -\frac{E_{a,\alpha}}{RT_{\alpha}} + \ln\left[\frac{A}{g(\alpha)}\right]_{\alpha} \qquad (6.10)$$

which can be derived by combining eqs. 6.4 and 6.5. The subscript "$_{\alpha}$" denotes a specific conversion fraction along the dehydration pathway. According to eq 6.10, the activation energy for a definite value of α, $E_{a,\alpha}$, may be determined from the slope of a $-\ln t_{\alpha}$ vs. $1/T_{\alpha}$ plot corresponding to that conversion fraction. The necessary (t_{α}, T_{α}) data can be obtained from a series of isothermal α-*t* curves recorded at different temperatures. It is in principle possible to calculate the frequency factor *A* from the intercept of eq. 6.10, but this requires the assumption

of a model to describe the rate characteristics of the reaction. Therefore, the model free method only yields the activation energy.

Master Plot. The assessment of the model that best describes the reaction kinetics can also be based on a so-called master plot.[35] A master plot is a reference theoretical curve that depends on the model but is generally independent of the kinetic parameters of the process (i.e., rate constant, pre-exponential factor, activation energy). The model for the reaction is selected by comparing the master plot with experimental data. One such procedure is the reduced time method,[36-37] which relies on the equation:

$$\frac{g(\alpha)}{g(0.5)} = \frac{t_{\alpha}}{t_{0.5}} \qquad (6.11)$$

Equation 6.11 can be derived from eq. 6.4 by using the data point corresponding to 50% conversion in the α-*t* curve ($t_{0.5}$, α = 0.5) as reference. The symbols $g(0.5)$ and $g(\alpha)$ refer to the values of the integral rate law calculated through a specific model in Table 6.1 for α = 0.5 and for any other conversion fraction α, respectively; $t_{0.5}$ and t_{α} are the corresponding times determined from the experimentally observed α-*t* curves. The model of choice is the one that best adjusts to a linear plot of $g(\alpha)/g(0.5)$ against $t_{\alpha}/t_{0.5}$ with unity slope and zero intercept. This test can be performed for any temperature within the range covered by the experiments.

6.2 Materials and Methods

All molar quantities used throughout this work were based on molar masses calculated from the standard atomic masses recommended by the IUPAC Commission in 2011.[38]

6.2.1 General.

Diffuse reflectance infrared Fourier-transform (DRIFT) spectroscopy measurements were performed in the range 400-4000 cm^{-1} using a Nicolet 6700 spectrometer. The resolution was 4 cm^{-1} and the samples were ~5% (w/w) 4HNA·0.5H_2O or 4HNA in KBr. The X-ray powder diffractograms were recorded on a Philips PW1730 diffractometer, with automatic data acquisition (APD Philips v.35B), operating in the θ-2θ mode. The apparatus had a vertical goniometer (PW1820), a proportional xenon detector (PW1711), and a graphite monocromator (PW1752). A Cu Kα radiation source was used. The tube amperage was 30 mA and the tube voltage 40 kV. The diffractograms were recorded in the range $5° \leq 2\theta \leq 35°$, in the continuous mode, with a step size of 0.015°(2θ), and an acquisition time of 1.5 s per step. The samples were mounted on an aluminum sample holder. The indexation of the powder patterns was performed using the program Cellref.[39] An Olympus BX51 microscope coupled with a Linkam hot stage LTS350 and Olympus SC-30 digital camera was used for visualizing the isothermal dehydration of 4HNA·0.5H_2O. Temperature was controlled by Linkam TMS 94 controller. The sample was placed on the hot stage, which was heated from 298 to 333 K at 15 $K \cdot min^{-1}$. The temperature was maintained at 333 K until completion of dehydration was observed, and images were recorded at regular intervals in polarized light. Scanning electron microscopy (SEM) images of Au/Pd-sputtered samples were recorded in vacuum, with a resolution of 2 nm, using a FEI ESEM Quanta 400 FEG apparatus. The electron beam voltage was set to 10 kV. Atomic force microscopy (AFM) images were obtained at 294±2 K, on a Nanoscope IIIa multimode microscope (Digital Instruments, Veeco). The experiments were carried out by tapping mode AFM, using etched silicon tips with a resonance frequency of ~300 kHz (TESP, Veeco). The scan frequency was 1.3-1.8 Hz. Data analysis was done with the Veeco Nanoscope 6.14 R1 software.

6.2.2 Materials

The anhydrous 4HNA sample used as starting material for the synthesis of 4HNA·0.5H_2O was prepared from 4-chloronicotinic acid (Aldrich, 96%), as described earlier.[40] The hemihydrate was obtained by a modified version of a reported procedure.[23] Approximately 1 g of 4-hydroxynicotinic acid was added to 30 cm^3 of a 1:2 (v/v) ethanol/water mixture inside a 500 cm^3 beaker and magnetically stirred, at 340 K, until complete dissolution was observed. To prevent excessive solvent evaporation the beaker was covered with aluminum foil during the heating process. The solution was cooled to ambient temperature. Several small holes were punctured in the aluminum foil and needle shaped crystals of 4HNA·H_2O were produced by slow evaporation of the solvent over a 1 month period. The ethanol/water mixture used as crystallization solvent was prepared from ethanol (Panreac, 99.9 %) and distilled and deionized water from a Milli-Q Plus system (conductivity 0.1 $\mu S \cdot cm^{-1}$).

Thermogravimetry and X-ray powder diffraction analysis confirmed that the obtained sample matched the same orthorhombic phase previously used in the thermodynamic investigation of 4HNA·0.5H_2O[23] and also in part of the kinetic studies described in this work: (i) the mass loss observed in the TGA experiments gave a molar ratio n_{H_2O} / n_{4HNA} = 0.5; (ii) the corresponding X-ray powder diffraction pattern (Figure 6.1) was indexed as orthorhombic, space group $P2_12_12$ with a = 7.217(14) Å, b = 23.709(47) Å, c = 3.699(7) Å, in good agreement with the published single crystal X-ray diffraction results: space group $P2_12_12$; a =7.235(2) Å, b = 23.717(6) Å, c = 3.706(1) Å.[23]

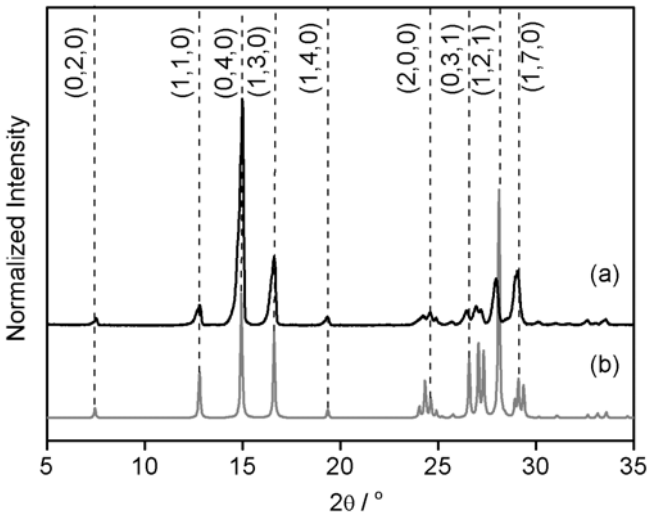

Figure 6.1 X-ray powder diffraction patterns of 4HNA·0.5H_2O: (a) experimental; (b) simulated from single crystal data.[23] Miller indices are given in parentheses.

6.2.3 Particle size fractionation

To assess the effect of crystal size on the kinetics of the dehydration process the obtained hydrate sample was sieved into different size ranges, using a mini-sieve micro sieve set (Scienceware, USA). Sieves with apertures 707, 500, 354, 250, 177, 125, 88 and 63 μm were stacked and ~1 g of 4HNA·0.5H_2O was sieved through gentle shaking by hand. Three fractions were obtained: 250-177 μm (80 mesh, sample 1), 354-250 μm (60 mesh, sample 2) and >707 μm (25 mesh, sample 3). As mentioned above the 4HNA·0.5H_2O sample from the previous thermodynamic study[23] was also used in this work. This material (sample 4) was composed of thicker crystals which, when sieved, were also found to correspond to size >707 μm. Analysis of microscopy images of samples 3 and 4 (10 crystals each) obtained with an Olympus SZX10 stereoscopic microscope using the Cell^D 2.6 software, led to Feret's mean diameters[41] in the ranges d_F = 0.05 – 0.11 mm (sample 3) and d_F = 0.17 – 0.29 mm (sample 4).

6.2.4 Thermogravimetry Analysis (TGA)

TGA experiments were carried out isothermally, in the range 323-358 K, on a Perkin Elmer TGA7 apparatus. The balance chamber was kept under a nitrogen flow (Air Liquide N45) of 38 $cm^3 \cdot min^{-1}$. The sample purge gas was helium (Air Liquide N55) at a flow rate of 22.5 $cm^3 \cdot min^{-1}$. The mass scale of the instrument was calibrated with a standard 100 mg weight and the temperature calibration was based on the measurement of the of the Curie points (T_C) of alumel alloy (Perkin-Elmer, T_C = 427.35K) and nickel (Perkin-Elmer, mass fraction 0.9999, T_C = 628.45 K) standard reference materials. The 4HNA·0.5H_2O samples with an initial mass of ~5-8 mg were placed in an open platinum crucible. Each sample was rapidly heated to the required temperature at 40 $K \cdot min^{-1}$. It was then maintained at that temperature until no further mass loss was observed, indicating that complete dehydration had been achieved.

6.2.5 Differential Scanning Calorimetry (DSC)

DSC studies on sample 2 were made on a Perkin-Elmer DSC 7 apparatus. Sealed aluminum crucibles with punctured lids containing ~1.4 - 2.2 mg of 4HNA·0.5H_2O were used. Weightings were performed with a precision of ±0.1 μg on a Mettler XP2U ultra-micro balance. The experiments were carried out in the approximate range 298-540 K, under a flow of nitrogen (Air Liquide N45) of 25 $cm^3 \cdot min^{-1}$. Heating rates β = 1, 2, 3, 4, and 5 $K \cdot min^{-1}$ were used. The temperature scale of the apparatus was calibrated at each heating rate by taking the onset of the fusion peaks of indium (Perkin Elmer; mass fraction 0.99999; T_{fus} = 429.75 K, $\Delta_{fus}h°$ = 28.45 $J \cdot g^{-1}$) and zinc (Perkin-Elmer, mass fraction 0.99999, T_{fus} = 692.65 K). The calibration of the heat flow scale was based on the area of the of the fusion peak of the indium sample.

6.3 Results and Discussion

6.3.1 Kinetics of isothermal dehydration.

As mentioned above, the isothermal TGA kinetic studies of the dehydration reaction:

$$4HNA{\cdot}0.5H_2O(cr) \rightarrow 4HNA(cr) + 0.5H_2O(g) \qquad (6.12)$$

were carried out in the temperature range 323-358 K, using samples 1-4 with different crystal sizes. All experiments gave a mass loss consistent with a 0.5:1 water/4HNA molar ratio for the hemihydrate, thus confirming that complete dehydration had been achieved. Examination of the dehydrated solid by powder X-ray diffraction and DRIFT spectroscopy (see Supporting Information for details) further indicated that the reaction led to the same monoclinic anhydrous form of 4HNA observed in the previous thermodynamic study of reaction 6.12.[23, 40]

Model Fitting Analysis. The procedure used in the analysis of the kinetic data will be illustrated for sample 3 (size > 707 μm). In this case two sets of experiments (7 and 9 runs, respectively) separated by one week and approximately covering the same temperature range were performed (see Supporting Information). The good agreement between the results of both sets evidenced the reproducibility of the $4HNA{\cdot}0.5H_2O$ dehydration kinetics. The results for set 2 are illustrated in Figure 6.2. As shown in Figure 6.2 all obtained α-*t* curves were sigmoidal and, as expected, the rate of dehydration increased with temperature. Equation 6.4 was fitted by least squares regression to the experimental α-*t* data in the range $0.01 \leq \alpha \leq 0.95$, for all models given in Table 6.1 (see Supporting Information for detailed results). The Avrami-Erofeev A2 model was the one that gave the best overall fit at all temperatures. The corresponding fittings for three temperatures within the range covered by the experiments are illustrated Figure 6.3a.

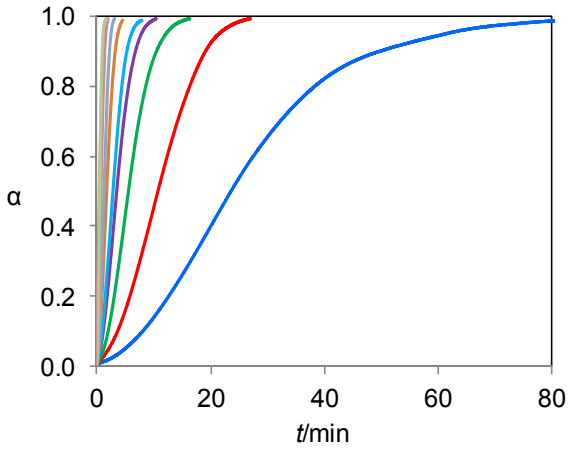

Figure 6.2 Typical conversion (α) against time (t) curves for the isothermal dehydration of 4HNA·0.5H_2O (sample 3) at (from right to left): 323.5 K, 328.4K, 333.3 K, 335.6 K, 338.6 K, 343.4 K, 347.7 K, 352.6 K and 356.7 K.

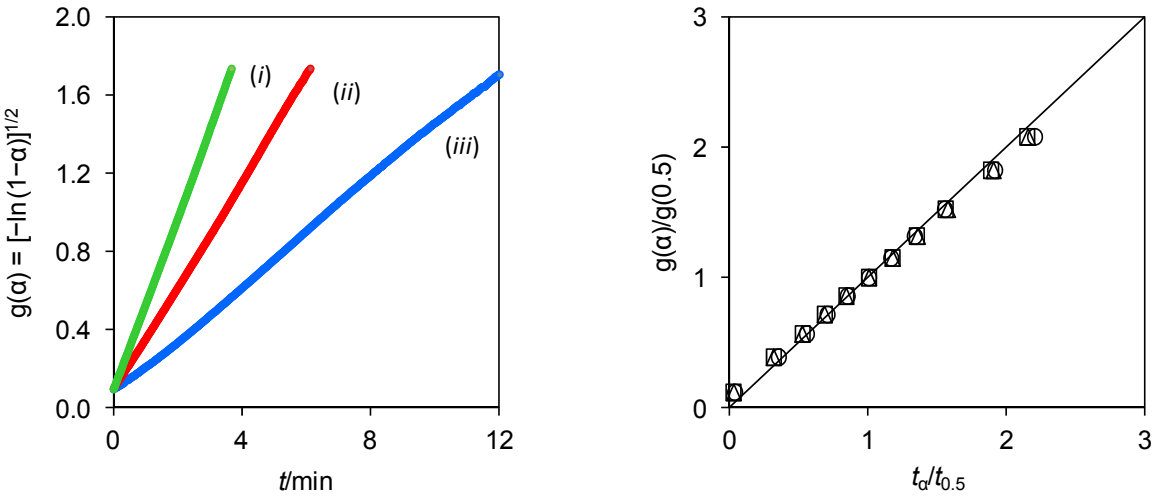

(a) (b)

Figure 6.3 Plots of (a) Avrami-Erofeev (A2) model (Table 6.1) and (b) eq. 6.11 based on TGA data obtained for sample 3 at: (*i*) 356.7 K (open triangles); (*ii*) 338.6 K (open squares); and (*iii*) 333.3 K (open circles). The fits refer to the range $0.01 \leq \alpha \leq 0.95$.

Further support that A2 was the model of choice for the dehydration of 4HNA·0.5H_2O was provided by the application of the reduced time method, which relies on eq. 6.11. Indeed the A2 model was the one that best conformed to a $g(\alpha)/g(0.5)$ against $t_\alpha / t_{0.5}$ plot with unity slope and zero intercept. The corresponding results are illustrated in Figure 6.3b for the same experimental data set shown in Figure 6.3a.

Effect of Crystal Size. The effect of crystal size on the rate of 4HNA·0.5H_2O dehydration is illustrated in Figure 6.4 for runs carried out at 348 K with samples 1-4. The results show that the dehydration rate increases as the particle size decreases. This is probably related to a more facile dehydration when crystals exhibit a larger surface to volume ratio, as previously noted, for example, in the cases of theophylline monohydrate[42] or zinc acetate dihydrate.[43] The dehydration process is likely to be favored if the water molecules evaporate from surface sites where they are least strongly bound to the crystal lattice or if the bulk sites are closer to the surface. Crystals with a larger surface to volume ratio may, therefore, exhibit a faster overall dehydration.

No significant effect of crystal size on the model fitting analysis was noted. Indeed, the Avrami-Erofeev A2 model was the one that best conformed to the experimental data regardless of the crystal size (see Supporting Information). Figure 6.5, shows the $g(\alpha)$-t and reduced time plots corresponding to the same experimental results in Figure 6.4.

Activation Parameters. The particle size seems, however, to significantly influence the activation parameters of the dehydration process. This is apparent in upper part of Table 6.2, which summarizes the results obtained through an unconstrained fitting of eq. 6.6 to the rate constants determined at various temperatures for samples 1-4 (in the case of sample 3 the results of sets 1 and 2 were combined). Note that the uncertainties assigned to the slopes $a = E_a/R$, and ordinates $b = \ln A$ of the Arrhenius relationship represent standard errors.

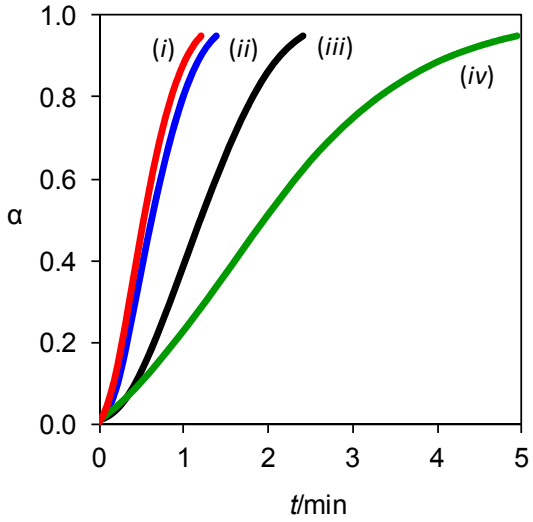

Figure 6.4 Conversion (α) against time (*t*) curves at 348 K for the dehydration of 4HNA·0.5H_2O obtained with crystals of different sizes: (*i*) sample 1; (*ii*) sample 2; (*iii*) sample 3; (*iv*) sample 4.

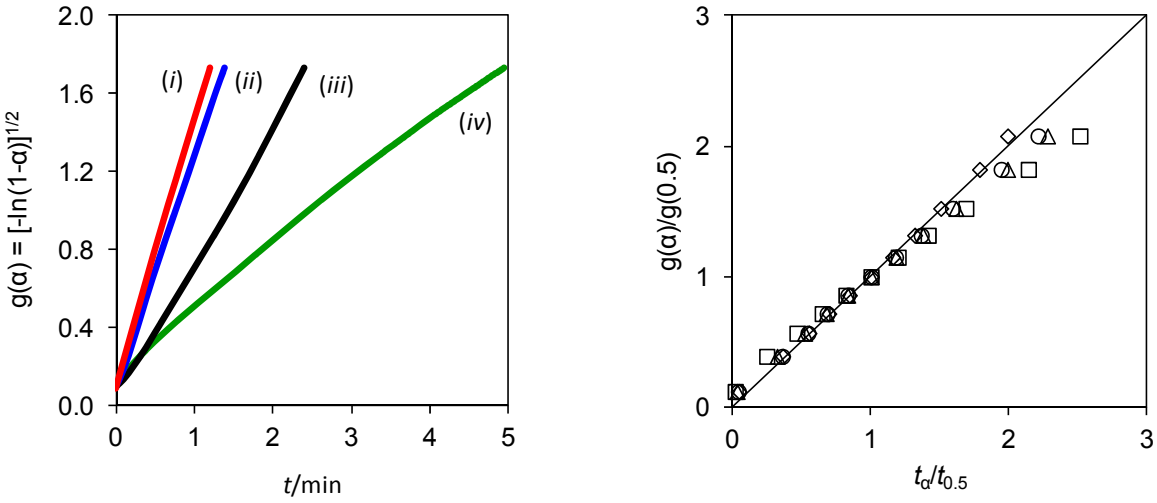

(a) (b)

Figure 6.5 Plots of (a) the Avrami-Erofeev A2 model (Table 6.1) and (b) eq. 6.11 based on the same experimental results shown in Figure 6.4. The data refer to 348 K: (*i*) sample 1 (open triangles); (*ii*) sample 2 (open circles); (*iii*) sample 3, set 2 (open diamonds); (*iv*) sample 4 (open squares).

Consistent with the rate of reaction trend illustrated in Figure 6.4, the activation energies for the dehydration of 4HNA·0.5H_2O show an increase with the increase of particle size. It is also interesting to note that the obtained E_a values cover the approximate range 85-133 kJ·mol^{-1}.This is compatible with the fact that dehydration of 4HNA·0.5H_2O implies the breaking of the four moderately strong hydrogen bonds (H-bond) sustaining water in the crystal lattice. Indeed, as previously reported[23] and illustrated in Figure 6.6, the water molecules of 4HNA·0.5H_2O are isolated from each other and hydrogen bonded to four different 4HNA molecules. In two of those bonds H_2O acts as donor to the carbonyl oxygen of the 4HNA carboxylic group ($d_{OwH\cdots O}$ = 1.775 Å) and in the other two as acceptor from the NH group of 4HNA ($d_{NH\cdots Ow}$ = 1.895 Å). These distances are characteristic of moderately strong OH···O and NH···O hydrogen bonds, with typical bond dissociation energies of 20-30 kJ·mol^{-1} each.[44-47]

Table 6.2. Arrhenius parameters for the dehydration of 4HNA·0.5H_2O crystals of different particle sizes.[a]

Sample	1	2	3[b]	4
Particle size/μm	250-177	354-250	>707[c]	>707[c]
Temperature range/K	328.7-348.0	328.2-353.5	323.5-356.7	324.7-352.1
n	5	8	14	4
	Arrhenius parameters (Unconstrained Fitting)[d]			
a	10207.2±303.4	11139.9±596.4	13255.1±489.7	15955.7±684.8
b = ln(*A*/s^{-1})	25.68±0.90	28.17±1.75	33.64±1.44	40.64±2.02
E_a /kJ·mol^{-1}	84.9±2.5	92.6±5.0	110.2±4.1	132.7±5.7
R^2	0.997	0.980	0.981	0.996
	Arrhenius parameters (Isokinetic Fitting)[d]			
a	10885.3±495.5	11681.3±666.6	13430.0±492.0	15766.8±699.7
b = ln(*A*/s^{-1})	27.69±1.47	29.71±1.97	34.15±1.44	40.08±2.06
E_a /kJ·mol^{-1}	90.5±4.1	97.1±5.5	111.7±4.1	131.1±5.8
R^2	0.993	0.979	0.981	0.996

[a] Based on rate constants given by the Avrami-Erofeev A2 model; *n* is the number of data points used in the regression and R^2 is the determination coefficient for 95% probability; . [b] Obtained by combining the results from sets 1 and 2 (see Supporting Information). [c] Feret's mean diameters: d_F = 0.05 – 0.11 mm (sample 3) and d_F = 0.17 – 0.29 mm (sample 4); [d] see text.

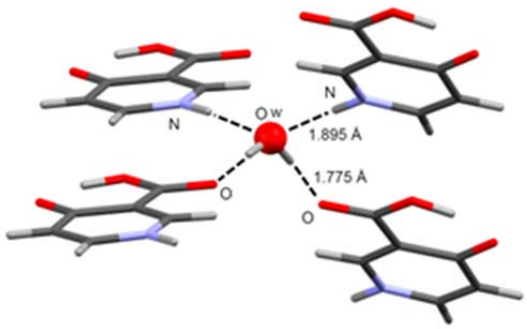

Figure 6.6 Local structure and hydrogen bonding pattern of the water molecules in the crystal lattice of 4HNA·0.5H_2O.[23]

Model Free Analysis. The variation of the activation energy with α in the range $0.1 \leq \alpha \leq 0.9$, obtained from an isoconversional analysis (eq. 6.10) of the TGA results on samples 1-4, is shown in Figure 6.7. The decrease of E_a with the decrease in particle size and thickness observed in the previous section for the overall activation energy is also noted in Figure 6.7. Moreover for samples 1-3, E_a varies in a narrow range (84-89 kJ·mol^{-1} for sample 1, 97-100 kJ·mol^{-1} for sample 2, and 109-112 kJ·mol^{-1} for sample 3) and can be considered essentially independent of α if the experimental uncertainties are taken into account. In the case of sample 4, however, above $\alpha \sim 0.4$, E_a steadily increases from 115-132 kJ·mol^{-1}. As mentioned above sample 4 is composed of thicker crystals. Hence this observation probably reflects an enhanced difficulty in removing water from the crystal lattice as the reaction progresses from surface to bulk. It should finally be noted that the mean values of the model free activation energies for the different samples in Figure 6.7 (86.3 kJ·mol^{-1} for sample 1; 98.7kJ·mol^{-1}, for sample 2; 110.3 kJ·mol^{-1} for sample 3; 121.8 kJ·mol^{-1}, for sample 4) agree with the corresponding overall results in Table 6.2, which rely on the fitting of the Avrami-Erofeev A2 model to the experimental α-*t* results. This also supports A2 as the model of choice in the case of the dehydration of 4HNA·0.5H_2O.

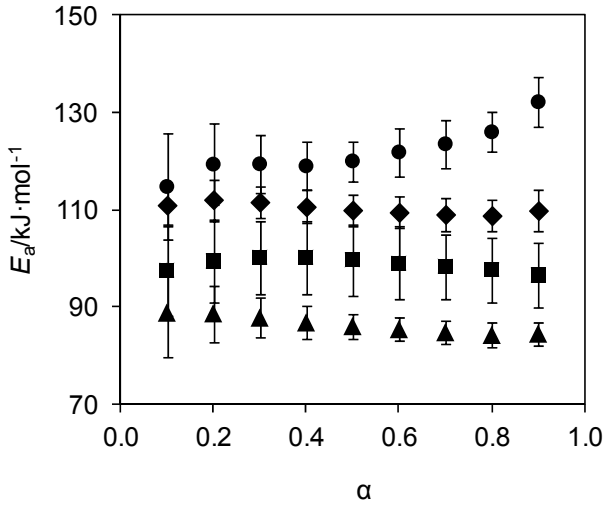

Figure 6.7 Activation energy, E_a, as a function of the conversion fraction, α, obtained from isoconversional analysis of the TGA results: (▲) sample 1; (■) sample 2; (◆) sample 3; (●) sample 4.

Isokinetic Effect. As illustrated in Figure 6.8, there is a strong correlation between the Arrhenius activation parameters obtained for the dehydration of different 4HNA·0.5H_2O samples. A least squares fit to the ln A and E_a data gave:

$$\ln A = (0.312 \pm 0.001)\, E_a - (0.80 \pm 0.13) \qquad (6.13)$$

with a correlation coefficient R^2 = 0.99998 for 95% probability. This type of linear relationship involving the activation parameters for a series of related processes is denoted compensation or isokinetic effect.[48-51] It has been observed in many kinds of chemical studies.[48-51] Although there has been a long lasting debate about the nature of the effect in different instances,[48-61] it is generally agreed that the use of plots such as those in eq. 6.13 may not be meaningful for validation of isokinetic relationships, because the two variables used in the correlation (A and E_a)are obtained from the same regression and are, therefore, interdependent. This problem

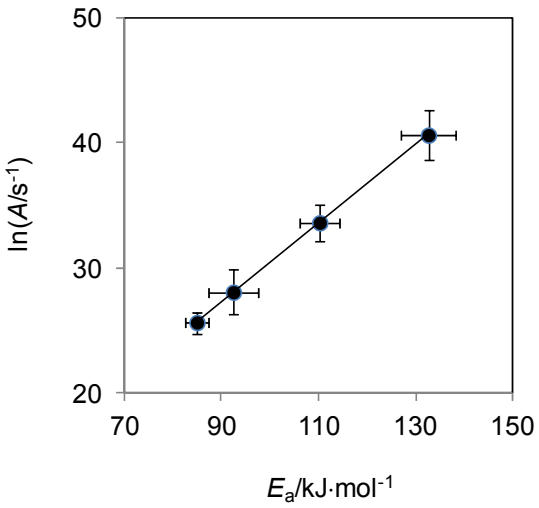

Figure 6.8 Correlation between the Arrhenius parameters for the dehydration of 4HNA·0.5H_2O samples of different particle sizes (data from Table 6.2, unconstrained fitting). The linear relationship is given by eq. 6.13 (see text).

may, however, be overcome by using the following strategy devised by Exner, which relies on the correlation of two statistically independent quantities, namely *k* and *T*.[48-49]

The values of the rate constants (k_i) and activation parameters ($E_{a,i}$ and $\ln A_i$) for each individual sample *i* are related by:

$$\ln k_i = -\frac{E_{a,i}}{RT} + \ln A_i \qquad (6.14)$$

If a linear relationship between $\ln A_i$ and $E_{a,i}$ such as that expressed by eq. 6.13 is indeed valid, then it is possible to conclude from eq. 6.14 that:

$$\ln A_i = \ln k_{iso} + \frac{E_{a,i}}{RT_{iso}} \tag{6.15}$$

where T_{iso} and k_{iso} are the so-called isokinetic temperature and rate constant, respectively. In this case T_{iso} will correspond to the hypothetical temperature at which the dehydration of 4HNA·0.5H_2O will proceed at the same rate regardless of the sample particle size. Substitution of eq. 6.15 into eq. 6.14 leads to:

$$\ln k_i = y_o - \frac{E_{a,i}}{R}\left(\frac{1}{T} - x_o\right) \tag{6.16}$$

where $y_o = \ln k_{iso}$ and $x_o = 1/T_{iso}$. According to eq. 6.16 plots of $\ln k$ vs. $1/T$ for samples 1-4 should lead to a bundle of straight lines which intersect at a common point of ordinate $\ln k_{iso}$ and abscissa $1/T_{iso}$ in the Arrhenius plane.[48-49]

To test if the isokinetic effect was statistically sound and calculate the T_{iso} and k_{iso} values, an algorithm based on the methodologies recommended by Exner,[62-63] Linert *et al.*[64] and Ouvrard *et al.*[65] was implemented in a computer program. To obtain T_{iso} and k_{iso}, $x_o = 1/T_{iso}$ was scanned from 0 K^{-1} to 0.1 K^{-1} with increments of 2×10^{-7} K^{-1}. For each x_o value a system of four eqs. 6.16 (one per sample) was fitted to the experimental data in Figure 6.9 (bottom) by least squares regression. From the obtained results, the global residual sum of squares, S_x, of the fitting was calculated and plotted against $1/T$ (Figure 6.9, top). The minimum, S_0, of that curve corresponds to x_o = 2.5379×10^{-3}, y_o = 0.06839, yielding T_{iso} = 394.0 K and

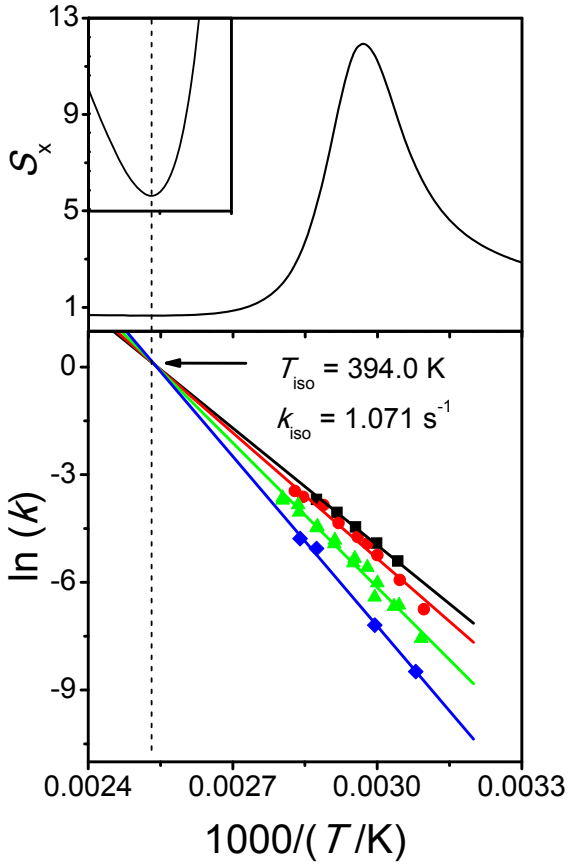

Figure 6.9 Isokinetic Arrhenius plots (bottom) for the crystals of different sizes: (■) sample 1; (●) sample 2; (▲) sample 3; (◆) sample 4. The top of the figure shows the global least residual sum of squares, S_x, for different x_o values. The minimum of the curve, shown in the inset, was ascribed as the isokinetic temperature, T_{iso}.

k_{iso} = 1.071 s^{-1} as the most probable values of the isokinetic temperature and rate constant. The slopes of the fitted lines corresponding to S_0 led to the energies of activation given in the lower part of Table 6.2 (isokinetic fitting) along with the associated ln A_i values, obtained from eq. 6.15.

The program also performed an evaluation of the statistical significance of the isokinetic effect, based on an *F*-test and on the more stringent ψ-test proposed by Exner.[66] In the *F*-test

the value of S_0 for the constrained lines was compared with the corresponding global residual sum of squares S_{00} for the unconstrained lines according to the equation:[64-65]

$$F = \frac{S_0 - S_{00}}{S_{00}} \times \frac{N-2l}{l-2} \tag{6.17}$$

where N is the number of data points and l the number of lines.

The ψ-test is based on the equation:

$$\psi = \sqrt{\frac{\sum_i (y_i - y_i')^2}{\sum_i (y_i - \bar{y})^2}} \tag{6.18}$$

where $(y_i - y_i')$ represents the difference between the experimental and calculated values of $\ln k$ and $(y_i - \bar{y})$ is the deviation between those experimental values and their mean.

The F-test led to F = 0.348. This result is lower than the reference value, F_{ref} = 19.5,[67] for a 95% confidence interval and $N-2l$ = 26 and $l-2$ = 2 degrees of freedom, thus supporting the existence of an isokinetic effect for the dehydration process studied in this work. The ψ-test gave ψ = 0.12 which is within the limits assumed by Exner for relationships fulfilled with satisfactory (ψ < 0.2) and good (ψ < 0.1) accuracy.[66] Hence, the ψ-test indicates that the statistical significance of the isokinetic effect observed in this work is, at least, satisfactory.

It may finally be pointed out that the observation of an isokinetic relationship for the

dehydration of 4HNA·0.5H_2O is consistent with the fact that the mechanism is always the same regardless of the particle size in the sample.[48]

6.3.2 Mechanism of dehydration

The kinetic analysis of the TGA experiments led to the conclusion that the Avrami-Erofeev A2 model was the one that best described the obtained α-*t* results. This model relies on the assumption that the final product is originated through a nucleation and growth process. In such case no simple structural relationship between the initial hydrate and the final anhydrous product is expected. Corroboration of this conclusion and further insights into the reaction mechanism were achieved by combining an examination of the molecular packing in 4HNA·0.5H_2O and anhydrous 4HNA based on single crystal X-ray diffraction data,[23, 40] with experimental microscopic observations of 4HNA·0.5H_2O crystals carried out by hot stage optical microscopy, scanning electron microscopy, and atomic force microscopy.

Packing Analysis. Crystal packing analyses on 4HNA and 4HNA·0.5H_2O, based on published single crystal X-ray diffraction data,[23, 40] were carried out by using the *Mercury 3.5.1* program (Build RC5).[68] This software package was also employed to perform BFDH morphology calculations on 4HNA·0.5H_2O.

The results indicate that the conformation of the 4HNA molecule is similar in the hydrate and anhydrous structures:[23, 40] in both cases the 4HNA unit (i) adopts an *oxo* form, characterized by N_{ring}–H and C_{ring}=O substituents, and (ii) exhibits an intramolecular H-bond involving the exocyclic C_{ring}=O oxygen and the OH fragment of the carboxylate group in a S(6) pattern.

As mentioned above (Figure 6.6), the water molecules in the hydrate lattice are isolated from each other and linked by four hydrogen bonds to four different 4HNA molecules: two as donor and two as acceptor.[23] The hydrate crystal packing is also characterized by two types of infinite chains where this template plays a central role (Figure 6.10): one type is sustained by a $C_{carboxylic}$=O···H–Ow···H–N_{ring} H-bond motif (recall that Ow refers to an H_2O oxygen), where

water simultaneously acts as H-bond donor and acceptor towards the N_{ring}–H and groups of adjacent 4HNA molecules, respectively. This H-bond pattern generates two linear chains $C_2^2(8)$, formed by coplanar 4HNA molecules, which have the carboxylic group aligned in the same direction (Figure 6.10a): one that grows along the diagonal of the *ac* plane and another making an angle of 53.48° with the first one.

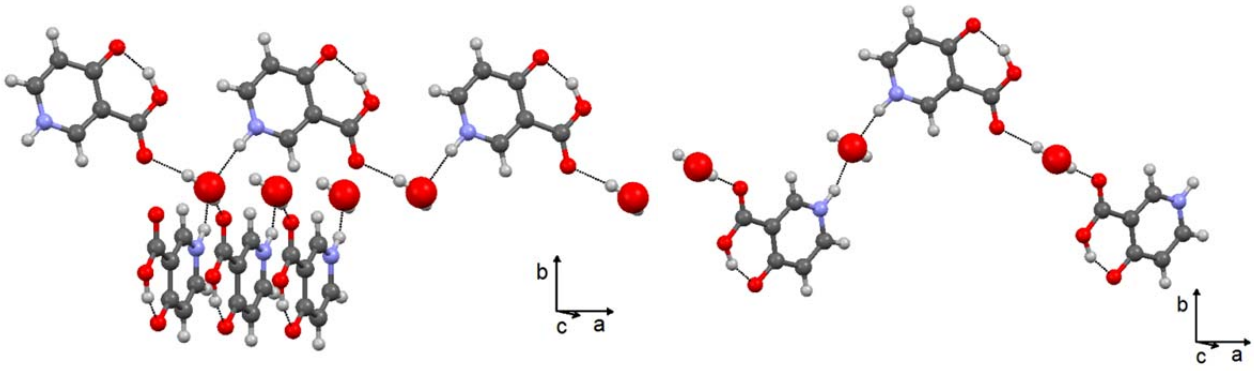

(a) (b)

Figure 6.10 Packing motifs of 4HNA·0.5H_2O: (a) the two linear chains $C_2^2(8)$ making an angle of 53.48° the *ac* plane; (b) non-linear $C_4^3(16)$ chain.

The other type of chain corresponds to a non-linear $C_4^3(16)$ pattern (Figure 6.10b) sustained by alternating N_{ring}–H···Ow···H–N_{ring} and $C_{carboxylic}$=O···H–Ow–H···O=$C_{carboxylic}$ motifs, where the 4HNA molecules make an angle of 47.5°. In this case the water molecules are consecutively acting as either H-bond donors or acceptors, while in the $C_2^2(8)$ chains each H_2O is simultaneously donor and acceptor.

The crystalline packing of anhydrous 4HNA[40] significantly differs from that of 4HNA·0.5H_2O. In this case the most prominent feature consists of infinite $C_1^1(6)$ chains sustained by C_{ring}=O···H–N_{ring} H-bonds (Figure 6.11) involving adjacent 4HNA molecules. These chains grow along the $[10\bar{2}]$ plane and the adjacent 4HNA molecules are rotated by

~171° relative to each other with a translation of 1/2 along z, because they are related to each other by a glide plane perpendicular to [010] with the glide component [0,0,1/2].

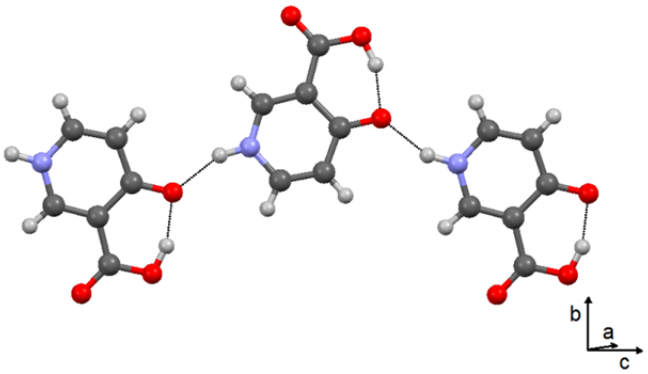

Figure 6.11 Infinite linear chain $C_1^1(6)$ in anhydrous 4HNA.

Comparison of the 4HNA·0.5H_2O and 4HNA structures suggests that albeit the conformation of the individual 4HNA molecules does not change upon dehydration (always *oxo*), the packing features of the hydrate and anhydrous phases are considerably different. In particular (i) no direct H-bonds between the 4HNA molecules exist in the hydrate form and (ii) the arrangement of two successive 4HNA molecules in the $C_2^2(8)$ and $C_4^3(16)$ chains is not favorable to the direct formation of the C_{ring}=O···H–N_{ring} H-bonds present in the anhydrous form with opposite alignment of the carboxylic groups in adjacent molecules of the chain. Thus, no packing features of the hydrate seem to be transferred to the anhydrous phase upon dehydration or, in other words, there is no evident topotatic[22] relationship between the reactant and product structures. Moreover, because the water molecules are isolated from each other and linked by four hydrogen bonds to the organic molecules, a smooth removal from the lattice must be hindered. This is further suggested by the fact that the values of the activation energies in Table 6.2 are considerable (50-78 %) when compared with the lattice enthalpy of the hydrate, $\Delta_{lat}H_m^\circ$ = 170.1±3.7 kJ·mol^{-1}, assigned to the process:[23]

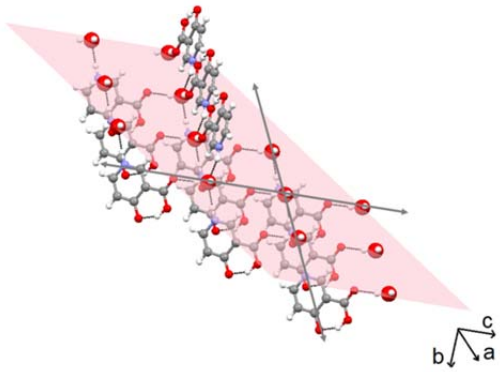

(a)

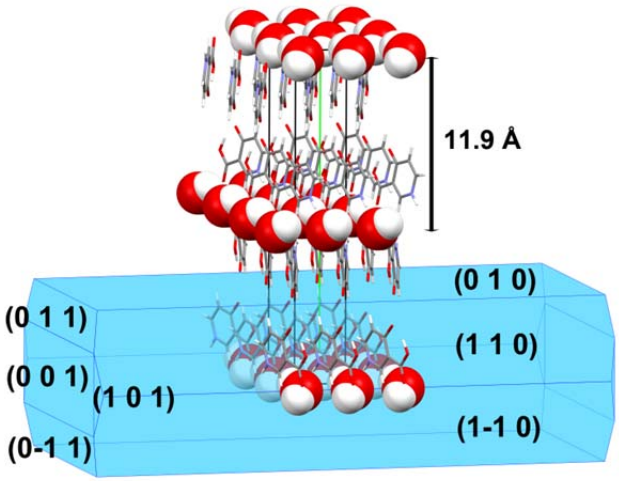

(b)

Figure 6.12 (a) Examples of most likely directions of water loss from 4HNA·0.5H_2O along the *ac* plane. (b) BFDH morphology of 4HNA·0.5H_2O calculated with the Mercury 3.5.1 software package.[68]

$$4HNA{\cdot}0.5H_2O(cr) \rightarrow 4HNA(g) + 0.5H_2O(g) \quad (6.19)$$

Dehydration, should therefore, imply a considerable structural rearrangement, involving large molecular movements, which is likely to require a nucleation and growth process. The molecular packing analysis of the hydrate also shows that the water molecules are in lattice planes parallel to the *ac* plane (Figure 6.12), thus indicating that water loss should be easier along this plane. These conclusions are consistent with the HSM, AFM and SEM observations discussed in the next sections.

Hot-Stage Optical Microscopy. Figure 6.13 shows a series of hot-stage optical microscopy images of a $4HNA{\cdot}0.5H_2O$ crystal dehydrating at 338 K. The observed up-face is assigned (010) and is, therefore, oriented parallel to the *ac* plane. This assignment was based on the comparison of the experimental and simulated powder diffractograms in Figure 6.1. The highest intensity peak in the experimental pattern (Figure 6.1a) is observed at 2θ = 14.9°, which corresponds to the (040) lattice plane parallel to the (010) face shown in Figure 6.12b. In contrast, the most intense peak in the simulated pattern corresponds to 2θ = 28.3° and lattice plane (121) (Figure 6.1b). This enhanced intensity of the (040) relative to the (121) peak in the experimental pattern is expected if a larger (010) face is formed leading to a plate-like habit. In this case the crystal morphology will favor a preferred orientation of the crystallites with the (010) face up in the analyzed powder sample and an increase of the corresponding peak intensity relative to that predicted for a randomly oriented sample. Further support to this assumption was obtained from AFM results (see below).

The HSM images revealed the initial development of a surface texture composed of needle like motifs and a progressive loss of transparency as the reaction proceeds. These motifs appear to be initially originated at sites close to the (010) face edges (e.g. red circles in Figure 6.13) and grow towards the interior of the face. The surface texture is originated by the

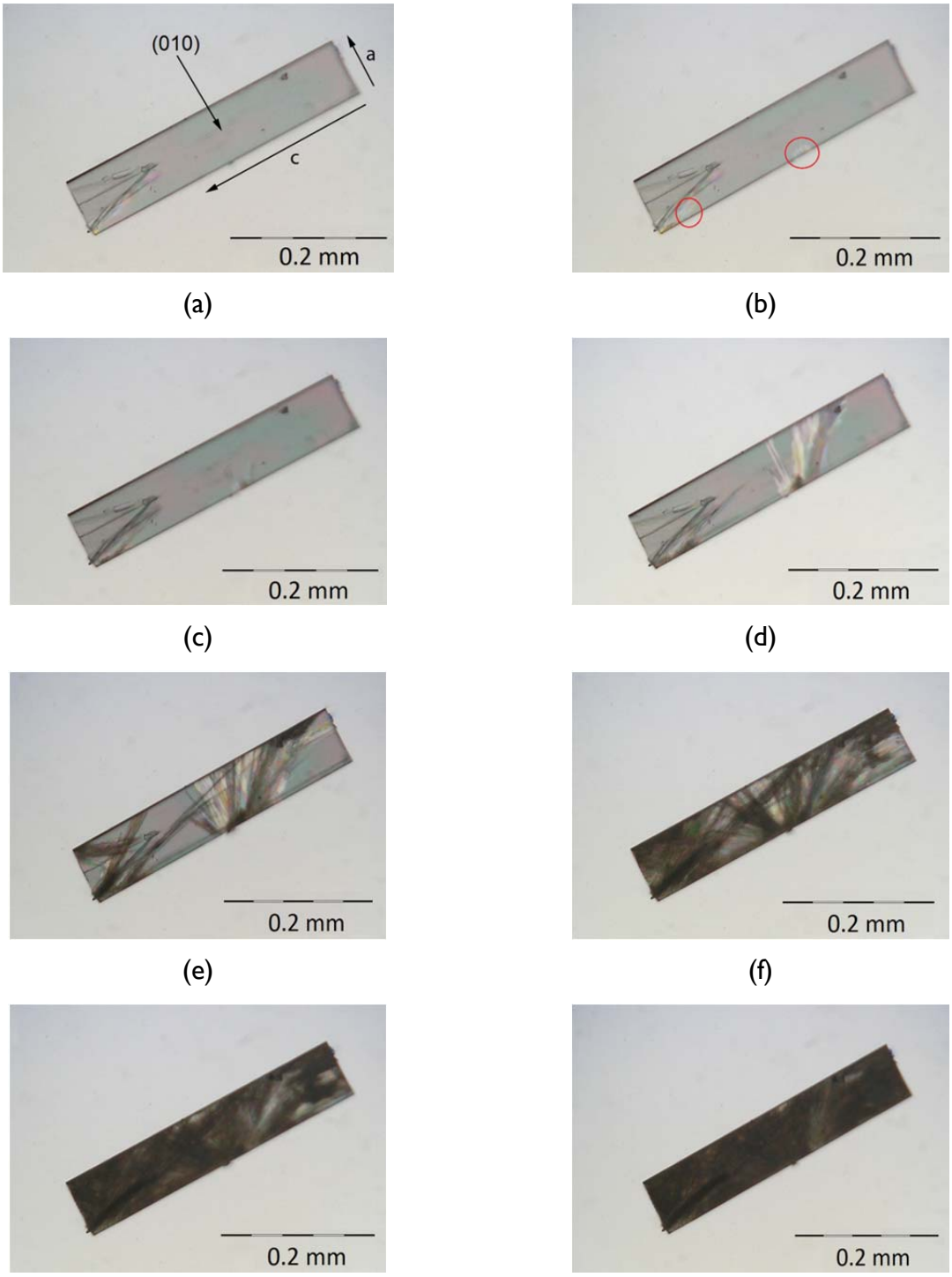

Figure 6.13 Hot-stage microscopy images of a 4HNA·0.5H_2O dehydrating at 333 K. The images were recorded in polarized light.

collapse of the hydrate structure leading to the formation cracks and anhydrous domains, which grow in number along the dehydration process (see also AFM results below). The loss of transparency is due to light scattering on the surface of the 4HNA crystallites which are numerous in the final product. The reaction is also found to occur with preservation of the original shape of the crystal, a phenomenon known as pseudomorphosis.[12] These observations are common for the dehydration of isolated site hydrates, such as 4HNA·0.5H_2O, which is normally accompanied by significant structural changes.[12] Such changes are often sufficiently large to induce a fracture of the original crystal into numerous small anhydrous crystallites, while maintaining its initial shape and leading to pseudomorphosis.

The observed pattern of crystallite development is also compatible with the above conclusions of the packing analysis. Indeed the loss of water along different directions parallel to the *ac* plane such as those illustrated in Figure 6.12 should favor the observation of random needle like growth patterns and the fragmentation of the original crystal into multiple crystallites.

Atomic Force and Scanning Electron Microscopy. AFM was used to visualize the events arising on the surface of the crystalline hydrate during the dehydration process. Figure 6.14 illustrates the topographical changes occurring on the (010) face of 4HNA·0.5H_2O crystals before and after dehydration. A scan acquired over the surface of a hydrated crystal (Figures 6.14a) revealed terraces with a vertical separation of ~12 Å (inset in Figure 6.14a), which is in agreement with d_{010} = 23.717/2 Å (= *b*/2) and corresponds to the distance between two H_2O layers (Figure 6.12b). This lends further support to the assignment of this face as (010) based on XRD data, mentioned in the HSM discussion. Figure 6.14b shows the surface of the dehydrated crystal obtained at the end of the HSM experiments (Figure 6.13h), where various domains separated by cracks are apparent. These domains are composed of numerous needle like crystallites running parallel to each other (Figure 6.14c). The crystallites are separated by 30 nm and are stacked over each other parallel to the (010) terraces. The crystallite stacks maintain the height difference of the original terraces (~12 Å). This observation suggests that the dehydrated phase is composed of multiple layers of anhydrous material.

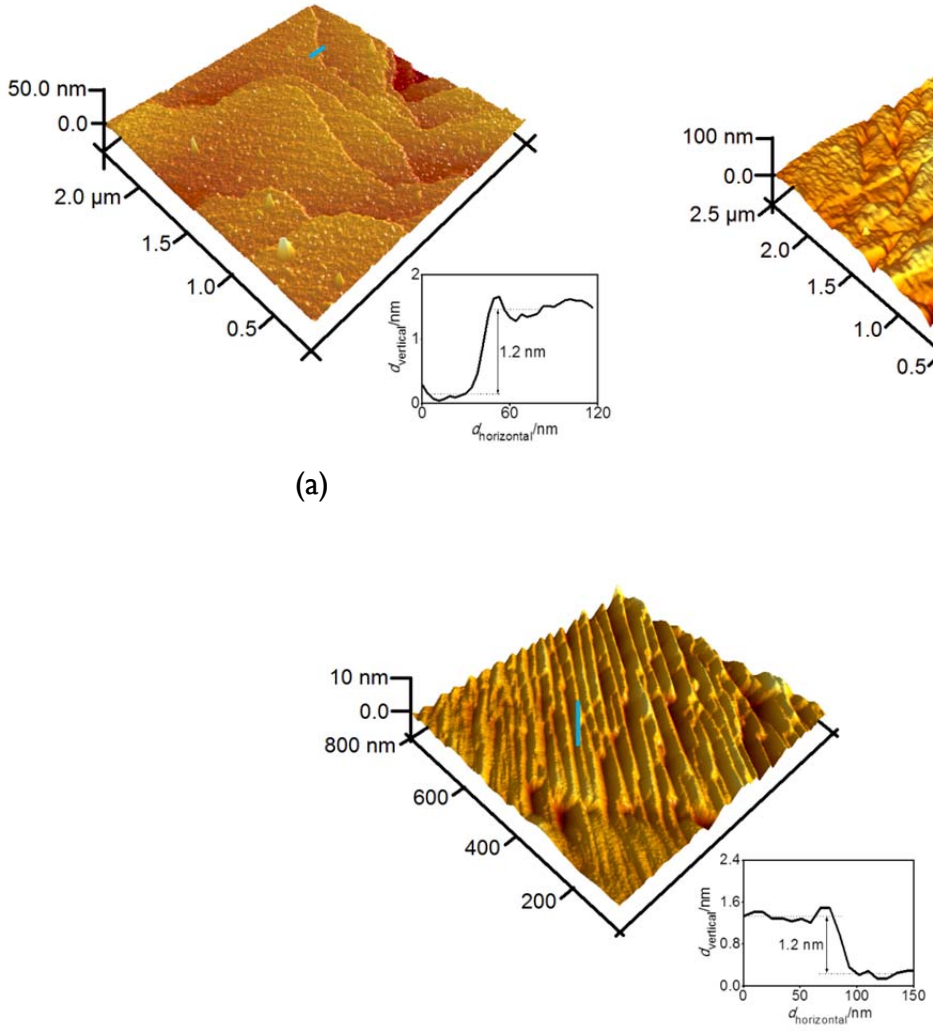

Figure 6.14 AFM images of (010) faces of 4HNA·0.5H_2O crystals at different dehydration stages, observed at room temperature: (a) before dehydration (ambient temperature) with inset showing the cross section between the two terraces marked in blue; (b) the surface the completely dehydrated crystal at the end of the HSM experiment (Figure 6.13h), showing merged crystallites interspersed with cracks; (c) a crystal removed from the TGA apparatus upon complete dehydration at 333 K, with the inset showing the vertical distance between two stacked crystallites marked by the in blue line in the main image

The change of the original hydrate into a polycrystalline material indicated by the HSM and AFM experiments is also evidenced by SEM observations. This is illustrated in Figure 6.15 where it is noted that the initial smooth surface of a hemihydrate crystal (Figure 6.15a) transformed upon dehydration into a rough polycrystalline surface (Figure 6.15b).

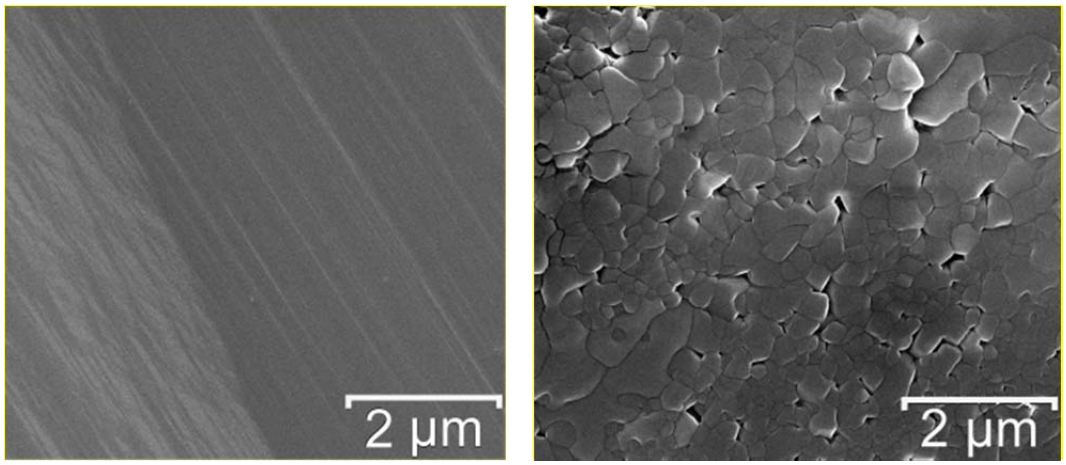

(a) (b)

Figure 6.15 SEM images of (a) the surface of a 4HNA·0.5H_2O crystal, (b) the surface of a crystal dehydrated at 353 K.

Mechanistic Model. The overall results indicate that the dehydration of 4HNA·0.5H_2O does proceed by a nucleation and growth mechanism consistent with an Avrami-Erofeev A2 kinetics. The observation of an isokinetic relationship between the Arrhenius activation parameters ($\ln A$ and E_a) obtained for the dehydration of samples with different crystal sizes also suggests that, at least in the 177 µm to >707 µm range, the reaction mechanism is independent of the particle size. The following steps can be envisaged. (i) Initially water loss occurs, at or near the crystal surface, at sites where its escape is easier c.f. terrace edges and preferably along the *ac* plane. It then propagates to zones of hydrated reactant adjoining the original water loss sites. (ii) The developed local strain within these sites leads to bond redistribution, giving rise to nuclei of the anhydrous phase. The release of water molecules, breakage of hydrogen bonds, and creation of void spaces in the crystal lattice enable the 4HNA

molecules to undergo packing changes. (iii) Nuclei growth then proceeds within the dehydrated zones originating crystallites of the anhydrous phase. Penetration of the anhydrous 4HNA crystallites into the reactant phase indicates that the advancement of the reaction interface is controlled by the formation of the solid product.[69] (iv) This process is also accompanied by the appearance of numerous cracks in the original material, exposing further surface at which the H_2O release process is facilitated. (v) With time, the dehydration process extends to the whole crystal. (vi) The continued expansion of the nuclei becomes impossible at a certain point along the reaction due to a shortage of unreacted hydrate phase and impingement of the crystallites of the product phase. This leads to a deceleration of the reaction as it approaches completion consistent with the observation of a sigmoidal α-*t* profile.

The overall transformation of the hydrate (orthorhombic; space group $P2_12_12$; a = 7.227 Å, b = 23.701 Å, c = 3.6999 Å)[23] into the anhydrous phase (monoclinic; space group $P2_1/c$; a = 3.804 Å, b = 14.582 Å, c = 10.673 Å, β = 94.254)[40] involves a unit cell volume change from V = 633.7 Å^3 to V = 590.4 Å^3, which corresponds to a volume contraction of ~7%. This contraction may contribute for the development of the numerous cracks mentioned above, that separate the particles composed of crystallites of the anhydrous form in the final polycrystalline material. The moderate volume change (7%) may also explain why disintegration of the original crystal does not occur and pseudomorphosis is observed.

It should also be pointed out that the parameter n in the $g(\alpha)$ expressions of the Avrami-Erofeev models in Table 1 is a sum of two terms:

$$n = \gamma + \delta \qquad (6.20)$$

where γ is related with the nucleation rate and δ is the nuclei growth dimension.[24] When n = 2 there are two possible interpretations, viz. that the number of nuclei increases with time and each nucleus is one-dimensional (i.e. when n = 2, γ = 1, δ = 1) or that the number of nuclei remains constant and the nuclei are two-dimensional (n = 2, γ = 0, δ = 2).[24] The observation of

the elongated structures shown in Figures 6.13 and 6.14c,d suggests that the first interpretation is the most likely, i.e. γ = 1, δ = 1 and that the reaction involves the rare case [22] of a one-dimensional nuclei growth.

Finally the overall results here obtained are compatible with a water evolution mechanism falling into a WET3 (Water Evolution Type 3) type according to Galway's [21-22] classification or Class I Destructive Crystallization (I-D.C.) type according to the classification of Petit and Coquerel.[20] WET3 includes nucleation and growth mechanisms in which a crystalline product may, or may not, be topotactically related to the reactant structure but cracking ensures release of water at the advancing interface. The I-D.C. class accommodates a process where the lattice disruption associated to dehydration leads to an amorphous intermediate which recrystallizes into the final product through nucleation and growth. One important criterion for the classification of a given reaction into this category is the observation of a significant value of the ratio *R* between the energy necessary for water release and the energy of the crystal lattice.[20] The dehydration of 4HNA·0.5H_2O fulfills this criterion since, as mentioned above, depending on the particle size, $R = E_a / \Delta_{lat}H^\circ_m$ = 0.5-0.8.

6.3.3 Energetics

As previously reported [23] well-formed crystals of sample 4 showed no signs of dehydration when left in air at ambient temperature and pressure for over four months, without any specific care for humidity control. Furthermore, no measurable heat effect was observed when the same crystals were used in an attempt to directly obtain the enthalpy of dehydration of 4HNA·0.5H_2O at 308 K and 0.13 Pa, by Calvet microcalorimetry, showing that water loss did not occur under reduced pressure. A detailed thermodynamic study of reaction 6.12 based on DSC and Calvet microcalorimetry results subsequently indicated, however, that the process should be thermodynamically favorable (exergonic, $\Delta_r G_m$(6.12) < 0) at ambient temperature and pressure (298 K, 1 bar), even for a relative humidity Φ = 100%. Evidence that the anhydrous form was more stable than the hydrated one at temperatures close to ambient was also provided by solubility tests carried out in the present work. Indeed, no hydrate

formation was noted when a saturated aqueous solution of 4HNA was kept under magnetic stirring for 1 week at 283 K, 293 K, and 303 K, even when hydrate crystals were added to the slurry (see Supporting Information). All these facts suggested that the stability of sample 4 should be of kinetic origin, viz. related to the existence of a large enough activation energy to hinder the water removal from the crystal lattice. Such conclusion is supported by the present study, which led to E_a = 132.7±5.7 kJ·mol^{-1} for the dehydration of sample 4 in the range 324.7-352.1 K (Table 6.2). The kinetic barrier for water loss from the hemihydrates was found to consistently decrease with the size of the crystallites from the same batch, namely E_a = 110.2±4.1 kJ·mol^{-1} (sample 3), 92.6±5.0 kJ·mol^{-1} (sample 2), and 84.9±2.5 kJ·mol^{-1} (sample 1).

The E_a values here obtained are all comparable to or larger than the energy/enthalpy necessary to cleave the four 20-30 kJ·mol^{-1} OH···O and NH···O H-bonds holding the water molecules in the crystal lattice of 4HNA·0.5H_2O (Figure 6.6). They are also considerably larger than the enthalpy of dehydration directly obtained for sample 4 by DSC under non-isothermal conditions, $\Delta_r H^\circ_m(6.12)$ = 24.0±0.7 kJ·mol^{-1} (β = 5 K·min^{-1}; peak limits: T_i = 345.5±1.3 K, T_f =357.6±0.5 K), or determined under isothermal conditions, at 298.15 K, from the combined results of DSC and Calvet microcalorimetry studies, $\Delta_r H^\circ_m(6.12)$ = 22.0±0.6 kJ·mol^{-1}.[23] This is not unexpected because in reaction 6.12 the energetic cost of water removal from the hemihydrate should be partially compensated by the formation of the anhydrous 4HNA lattice. The above $\Delta_r H^\circ_m(6.12)$ value at 298.15 K does, in fact, represent the difference between the lattice energies of 4HNA·0.5H_2O ($\Delta_{lat} H^\circ_m$ = 170.1±3.7 kJ·mol^{-1}, reaction 6.19)[23] and 4HNA ($\Delta_{lat} H^\circ_m$ = $\Delta_{sub} H^\circ_m$ = 148.1±3.7 kJ·mol^{-1}).[40] It is also worth noting that, in contrast with what was found for the activation parameters, no significant effect of particle size on $\Delta_r H^\circ_m(6.12)$ was observed. Indeed, five DSC experiments carried out in this work with sample 2 and using different heating rates β = 1, 2, 3, 4, and 5 K·min^{-1} (see Supporting Information) led to a mean value $\Delta_r H^\circ_m(6.12)$ = 24.5±0.9 kJ·mol^{-1}, in good agreement with $\Delta_r H^\circ_m(6.12)$ = 24.0±0.7 kJ·mol^{-1} indicated above for sample 4. The initial, T_i, and final, T_f, peak limits for sample 2

(T_i = 330.9±4.0 K, T_f = 342.9±4.2 K) were, however, significantly shifted to lower temperatures when compared with those indicated above for sample 4 (T_i = 345.5±1.3 K, T_f =357.6±0.5 K). Note that the uncertainties quoted for T_i and T_f and $\Delta_r H^\circ_m(6.12)$ are twice the standard errors of the mean of five determinations.

An approximate Gibbs energy profile for the dehydration of 4HNA·0.5H_2O at 298.15 K (Figure 6.16), can be built by combining the thermodynamic information previously reported,[23] or obtained in this work, with the present kinetic results. This is illustrated in Figure 6.16 for sample 4, where the activation barrier $\Delta^\ddagger G^\circ_m(6.12)$ = 101.6±8.1 kJ·mol^{-1} at the mean temperature of the range covered by the experiments (338.4 K) was derived from the corresponding E_a and A data in Table 6.2 (unconstrained fitting) by using eqs. 6.7-6.9. It should be pointed out that, in contrast with E_a, the $\Delta^\ddagger G^\circ_m(6.12)$ values showed little variation with the particle size ($\Delta^\ddagger G^\circ_m$ = 95.9 - 101.6 kJ·mol^{-1}). The Gibbs energy of reaction 6.12 for different relative humidity, Φ, was obtained from:

$$\Delta_r G_m(6.12) = \Delta_r G^\circ_m(6.12) + 0.5RT \ln \frac{p(H_2O)}{p^\circ} \quad (6.21)$$

$$\%\Phi = 100 \frac{p(H_2O)}{p(H_2O)_{sat}} \quad (6.22)$$

where $p(H_2O)$ is the partial pressure of water in equilibrium with the hydrate, p° = 10^5 Pa is the standard pressure and $p(H_2O)_{sat}$ = 3.17 kPa,[70] is the saturation pressure of water at 298.15 K. The standard molar Gibbs energy of reaction at 298.15 necessary for the calculation was obtained as $\Delta_r G_m(6.12)$ = 1.5±1.0 kJ·mol^{-1}, from the corresponding enthalpy,

$\Delta_r H_m^\circ(6.12)$ = 22.0±0.6 kJ·mol^{-1},[23] and entropy, $\Delta_r S_m^\circ(6.12)$ = 69.2±2.3 J·K^{-1}·mol^{-1}, terms. The latter was calculated from:

$$\Delta_r S_m^\circ(298.15\ \mathrm{K}) = \Delta_r S_m^\circ(351.6\ \mathrm{K}) + \int_{351.6\ \mathrm{K}}^{298.15\ \mathrm{K}} \frac{\Delta_r C_{p,m}^\circ}{T} \mathrm{d}T \qquad (6.23)$$

where $\Delta_r C_{p,m}^\circ$ = $C_{p,m}^\circ$(4HNA, cr) + 0.5 $C_{p,m}^\circ$(H_2O, g) − $C_{p,m}^\circ$(4HNA·0.5H_2O, g), using the published[23] $\Delta_r S_m^\circ(351.6\ \mathrm{K})$ = 68.3±2.3 J·K^{-1}·mol^{-1} and heat capacity data on 4HNA·0.5H_2O(cr), 4HNA(cr), and H_2O(g).

Figure 6.16 highlights the previous conclusion that the reaction should be thermodynamically favourable (exergonic, $\Delta_r G_m(6.12)$ < 0) at 298.15 K even for a relative humidity of 100 %. Moreover, the driving force for dehydration should increase - more negative $\Delta_r G_m(6.12)$ - with the decrease in humidity. It also shows that spontaneous dehydration is hindered by a significant activation barrier which, on absolute terms, is considerably larger than the Gibbs energies of reaction obtained for relative humidity ranging from 0.001% to 100% for which $\Delta_r G_m(6.12)$ = −17 kJ·mol^{-1} and −2.8 kJ·mol^{-1}, respectively. From a kinetic point of view, the process may become more favorable for samples consisting of smaller crystallites in view of the decrease of E_a with the particle size noted in Table 6.2.

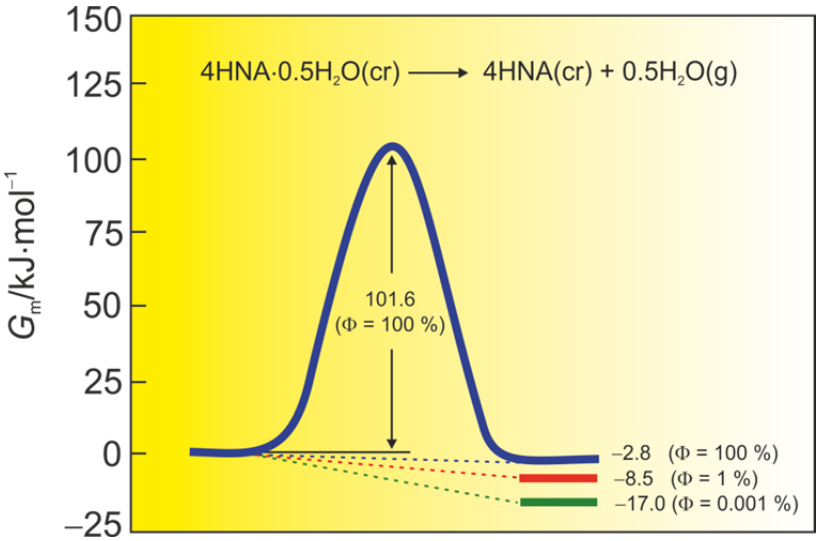

Figure 6.16 Gibbs energy profile for reaction 6.12 based on data for sample 4 (see text).

6.4 Conclusion

The present study indicates that the robustness of 4HNA·0.5H_2O towards dehydration at 298 K is indeed of kinetic origin with the activation energy of reaction 6.12 varying from 84.9 kJ·mol^{-1} to 132.7 kJ·mol^{-1} with the increase of the particle size range from 177 μm to > 707 μm. A much smaller influence of the particle size was, however, noted when the corresponding Gibbs energy of activation was considered, $\Delta^{\ddagger}G^{\circ}_{m}$ = 95.9 - 101.6 kJ·mol^{-1}. In the absence of such kinetic barriers the sample should spontaneously dehydrate, i.e. $\Delta_r G_m(6.12) < 0$, even for a relative humidity of 100%. The obtained E_a values for different particle sizes are all comparable to or larger than the energy/enthalpy necessary to cleave the four ~20-30 kJ·mol^{-1} OH···O and NH···O H-bonds holding the water molecules in the crystal lattice of 4HNA·0.5H_2O. It should also be pointed out that, in contrast with what was found for the activation parameters, no significant effect of particle size on $\Delta_r H^{\circ}_m(6.12)$ was observed. The onset of dehydration was, nevertheless, shifted to lower temperatures with the decrease of particle size, a conclusion that is in line with the kinetic observations.

Regardless of the particle size, the dehydration kinetics follows the Avrami-Erofeev A2 model, which assumes a nucleation and growth mechanism. Consistent with this particle size

independency, a statistical analysis of Arrhenius plots for samples with different particle sizes evidenced the existence of an isokinetic relationship between the activation parameters. Microscopic observations suggest that the reaction involves the rare case of a one-dimensional nuclei growth. The obtained results are consistent with a dehydration process falling into Class I Destructive Crystallization (I-D.C.) type according to the classification of Petit and Coquerel[20] or WET3 (Water Evolution Type 3) type according to Galway's [21-22] classification.

Supporting Information

Table S1 Indexation of the X-ray powder diffraction pattern of the 4HNA·0.5H_2O sample used in the thermogravimetric studies (before sieving). The pattern was recorded at 298±2 K, in the range 5° ≤ 2θ ≤ 35° (Space Group $P2_12_12$; a = 7.217(14) Å, b = 23.709(47) Å, c = 3.699(07) Å, α = β = γ =90°.

h	*k*	*l*	2θ(obs.)	2θ(calc.)	Diff.
1	1	0	12.830	12.822	-0.008
0	4	0	14.885	14.947	0.062
1	3	0	16.505	16.636	0.131
1	4	0	19.225	19.379	0.154
0	0	1	24.145	24.059	-0.086
0	1	1	24.530	24.355	-0.175
2	0	0	24.700	24.672	-0.028
2	1	0	25.085	24.961	-0.124
2	2	0	25.920	25.809	-0.111
0	3	1	26.445	26.608	0.163
1	0	1	27.005	27.089	0.084
1	1	1	27.295	27.354	0.059
1	2	1	28.140	28.134	-0.006
2	4	0	28.865	28.970	0.105
1	7	0	29.085	29.125	0.040
0	8	0	30.215	30.156	-0.059
2	5	0	31.135	31.147	0.012

Continued….

h	*k*	*l*	2θ(obs.)	2θ(calc.)	Diff.
1	8	0	32.850	32.666	-0.184
0	6	1	33.190	33.176	-0.014
2	6	0	33.555	33.635	0.080

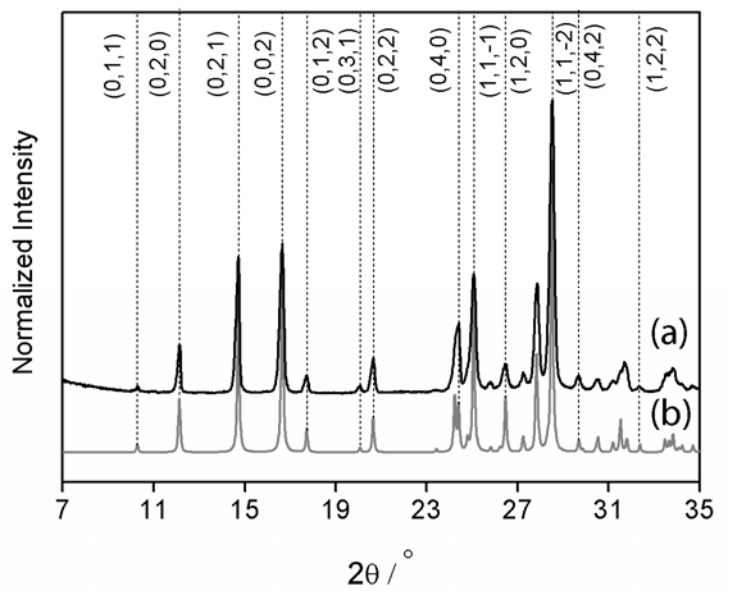

Figure S1 (a) X-ray powder diffraction pattern of a 4HNA sample resulting from the dehydration of 4HNA·0.5H_2O; (b) corresponding diffractogram simulated from single crystal X-ray diffraction data.[23] Miller indices are given in parentheses.

Table S2 Indexation of the X-ray powder diffraction pattern of the 4HNA sample in Figure S1, resulting from the dehydration of 4HNA·0.5H_2O. The pattern was recorded at 298±2 K, in the range 5° ≤ 2θ ≤ 35° (Space Group $P2_1/c$; a = 3.803(3) Å, b = 14.589(7) Å, c = 10.665(8) Å, α = γ =90°, β = 94.17°(16)

h	*k*	*l*	2θ(obs.)	2θ(calc.)	Diff.
0	1	1	10.295	10.283	0.011
0	2	0	12.150	12.123	0.027
0	2	1	14.735	14.713	0.022
0	0	2	16.670	16.656	0.014
0	1	2	17.770	17.736	0.034
0	3	1	20.075	20.061	0.014
0	2	2	20.655	20.652	0.003
1	0	0	23.385	23.435	-0.050
1	1	0	24.220	24.226	-0.006
0	4	0	24.415	24.385	0.030
-1	1	1	25.090	25.079	0.012
0	1	3	25.825	25.839	-0.014
1	2	0	26.500	26.465	0.035
-1	2	1	27.225	27.252	-0.027
-1	0	2	27.855	27.857	-0.002
-1	1	2	28.525	28.533	-0.008

Continued….

h	*k*	*l*	2θ(obs.)	2θ(calc.)	Diff.
0	4	2	29.680	29.677	0.003
1	1	2	30.530	30.524	0.007
0	3	3	31.155	31.194	-0.039
1	3	1	31.530	31.509	0.022
0	5	1	31.695	31.775	-0.080
0	5	1	31.810	31.775	0.035
1	2	2	32.370	32.361	0.009
-1	3	2	33.525	33.495	0.030
-1	1	3	33.885	33.863	0.022
0	1	4	34.235	34.249	-0.014
-1	4	1	34.675	34.705	-0.030

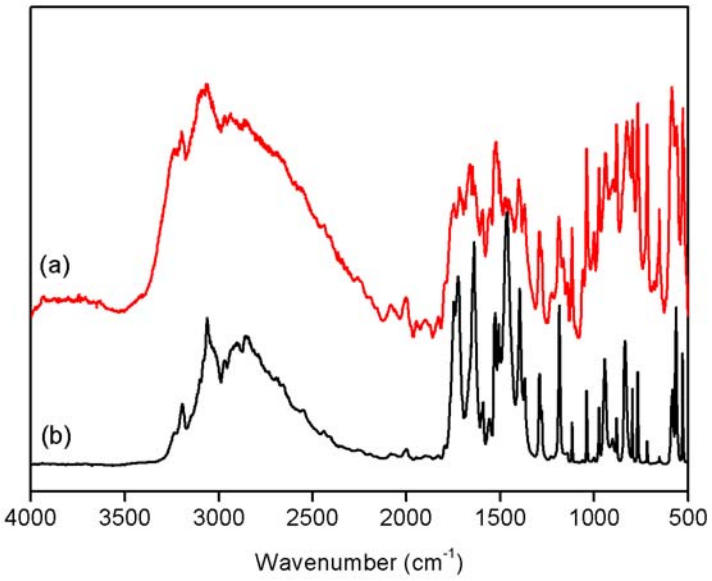

Figure S2 DRIFT spectra in KBr of (a) the original anhydrous 4HNA sample used in the preparation of 4HNA·0.5H_2O and (b) a 4HNA sample resulting from the dehydration of 4HNA·0.5H_2O.

Table S3 Regression coefficients, R^2, obtained by fitting the different kinetic models given in Table 6.1 of the main text to the α-*t* data obtained from the TGA studies of the 4HNA·0.5H_2O isothermal dehydration. (a) sample 1, 250-177 μ; (b) sample 2, 354-250 μ; (c) sample 3, >707 μ; (d) sample 4, >707 μ.

(a)

	Model								
T/K	P2	P3	P4	A2	A3	A4	B1	R2	R3
328.67	0.9715	0.93695	0.90841	0.99903	0.97861	0.95086	0.23881	0.98451	0.9762
333.51	0.96814	0.93138	0.90245	0.99851	0.97417	0.94491	0.22704	0.98832	0.97983
338.39	0.96144	0.92463	0.89637	0.99734	0.97041	0.94079	0.28285	0.99273	0.98645
342.91	0.97862	0.94457	0.91517	0.99899	0.98236	0.95504	0.1498	0.9767	0.96501
347.97	0.9613	0.92409	0.89546	0.99735	0.97014	0.94015	0.26322	0.99276	0.9862

T/K	D1	D2	D3	D4	F0/R1	F1	F2	F3
328.67	0.94822	0.91967	0.86051	0.90242	0.9919	0.9462	0.7386	0.50813
333.51	0.95135	0.91951	0.85453	0.90045	0.99529	0.94873	0.72793	0.47779
338.39	0.96343	0.93656	0.87761	0.91965	0.99414	0.96015	0.75293	0.50907
342.91	0.93027	0.89335	0.82102	0.87182	0.99141	0.92651	0.68587	0.44661
347.97	0.963	0.93509	0.87366	0.91749	0.99443	0.95879	0.74232	0.49009

(b)

	Model								
T/K	P2	P3	P4	A2	A3	A4	B1	R2	R3
322.87	0.97504	0.93827	0.90867	0.99861	0.97754	0.94871	0.16354	0.98093	0.96891
328.21	0.97186	0.93522	0.90600	0.99884	0.97635	0.94741	0.19985	0.98488	0.97474
333.26	0.95766	0.92004	0.89199	0.99598	0.96679	0.93662	0.30572	0.99492	0.98916
335.55	0.95417	0.91658	0.88882	0.99506	0.96485	0.93455	0.34044	0.99604	0.99137
337.89	0.96041	0.92350	0.89541	0.99700	0.96946	0.93976	0.28643	0.99353	0.98734
342.49	0.95304	0.91495	0.88703	0.99459	0.96359	0.93291	0.33266	0.99658	0.99174
346.24	0.96638	0.93062	0.90210	0.99855	0.97428	0.94526	0.22898	0.98996	0.98233
351.34	0.9614	0.92570	0.89777	0.99733	0.97080	0.94150	0.24611	0.99323	0.98730
353.51	0.96911	0.93677	0.90907	0.99869	0.97894	0.95200	0.23107	0.98574	0.97935

T/K	D1	D2	D3	D4	F0/R1	F1	F2	F3
322.87	0.93250	0.89174	0.81439	0.86848	0.99565	0.92916	0.67765	0.41946
328.21	0.94276	0.90717	0.83686	0.88634	0.99548	0.93959	0.70327	0.44807
333.26	0.96782	0.94088	0.88029	0.92363	0.99460	0.96348	0.75005	0.49538
335.55	0.97211	0.94797	0.89159	0.93211	0.99321	0.96829	0.76514	0.51636
337.89	0.96488	0.93761	0.87743	0.92037	0.99447	0.96092	0.74981	0.50162
342.49	0.97279	0.94752	0.88833	0.93086	0.99364	0.96776	0.75601	0.50044

Continued….

T/K	D1	D2	D3	D4	F0/R1	F1	F2	F3
346.24	0.95720	0.92718	0.86302	0.90860	0.99431	0.95255	0.73114	0.48273
351.34	0.96549	0.93868	0.87823	0.92148	0.99358	0.96133	0.74798	0.49379
353.51	0.95502	0.93132	0.87963	0.91648	0.98904	0.95423	0.76891	0.55502

(c)

SET – I

	Model								
T/K	P2	P3	P4	A2	A3	A4	B1	R2	R3
329.47	0.96203	0.92494	0.89662	0.99759	0.97140	0.94193	0.31487	0.99154	0.98483
333.89	0.95863	0.92420	0.8972	0.99616	0.97103	0.94294	0.36435	0.99112	0.98736
338.88	0.96485	0.92840	0.90005	0.99807	0.97263	0.94342	0.26289	0.99088	0.98369
343.45	0.96315	0.92650	0.89817	0.99778	0.97181	0.94244	0.28273	0.99153	0.98487
347.86	0.95805	0.91972	0.89125	0.99592	0.96638	0.93581	0.28628	0.99465	0.98819
352.30	0.96118	0.92290	0.89396	0.99671	0.96825	0.93773	0.25342	0.99300	0.98594
356.66	0.96109	0.92386	0.89526	0.99723	0.96983	0.93977	0.25930	0.99312	0.98628

T/K	D1	D2	D3	D4	F0/R1	F1	F2	F3
329.47	0.96106	0.93424	0.87694	0.91764	0.99406	0.95782	0.75845	0.53553
333.89	0.96697	0.94920	0.90760	0.93757	0.98853	0.96881	0.81097	0.61382
338.88	0.95854	0.92982	0.86860	0.91211	0.99464	0.95542	0.74234	0.49583
343.45	0.96074	0.93361	0.87507	0.91674	0.99411	0.95792	0.75218	0.51276
347.86	0.96567	0.93642	0.87225	0.91799	0.99560	0.96062	0.73833	0.47745
352.30	0.96102	0.93059	0.86612	0.91190	0.99593	0.95751	0.73717	0.47423
356.66	0.96343	0.93409	0.86963	0.91558	0.99492	0.95771	0.73348	0.47848

SET – 2

	Model								
T/K	P2	P3	P4	A2	A3	A4	B1	R2	R3
323.46	0.95212	0.91735	0.89096	0.99370	0.96528	0.93660	0.38874	0.99411	0.99210
328.39	0.97455	0.93771	0.90804	0.99873	0.97751	0.94863	0.17732	0.98147	0.97003
333.26	0.96793	0.93254	0.90426	0.99872	0.97541	0.94695	0.25059	0.98851	0.98111
335.64	0.96215	0.92502	0.89667	0.99735	0.97039	0.94072	0.28497	0.99237	0.98576
338.59	0.96699	0.92966	0.90066	0.99833	0.97357	0.94407	0.24860	0.98873	0.98001
343.36	0.96645	0.92899	0.89998	0.99817	0.97287	0.9432	0.24052	0.98936	0.98077
347.68	0.97641	0.94128	0.91202	0.99929	0.98026	0.95226	0.15842	0.98022	0.96867
352.55	0.96512	0.92749	0.89837	0.99783	0.97161	0.94156	0.22018	0.99054	0.98208
356.72	0.96115	0.92438	0.89598	0.99737	0.97036	0.94056	0.25901	0.99304	0.98649

T/K	D1	D2	D3	D4	F0/R1	F1	F2	F3
323.46	0.97469	0.95966	0.92088	0.94915	0.98736	0.97748	0.82454	0.60792
328.39	0.93493	0.89634	0.82196	0.87409	0.99512	0.93186	0.68835	0.43746
333.26	0.95467	0.92673	0.86794	0.90968	0.99350	0.95304	0.74688	0.50625
335.64	0.96180	0.93417	0.87413	0.91692	0.99466	0.95872	0.74745	0.49850
338.59	0.95216	0.91983	0.85380	0.90044	0.99565	0.94795	0.72368	0.47866
343.36	0.95315	0.92061	0.85351	0.90097	0.99587	0.94878	0.72020	0.46780

Continued….

T/K	D1	D2	D3	D4	F0/R1	F1	F2	F3
347.68	0.93416	0.89578	0.82164	0.87360	0.99406	0.93014	0.68525	0.43349
352.55	0.95519	0.92169	0.85219	0.90137	0.99628	0.94993	0.71651	0.45920
356.72	0.96387	0.93556	0.87339	0.91770	0.99444	0.95891	0.74262	0.49434

(d)

	Model								
T/K	P2	P3	P4	A2	A3	A4	B1	R2	R3
324.73	0.90478	0.87231	0.85073	0.96691	0.92894	0.90021	0.69877	0.98435	0.99168
333.91	0.92095	0.88900	0.86625	0.97589	0.94253	0.91468	0.61352	0.98610	0.99127
348.04	0.94714	0.90868	0.88124	0.99247	0.95957	0.92862	0.40602	0.99755	0.99440
352.13	0.95105	0.91465	0.88767	0.99435	0.96447	0.93474	0.38446	0.99600	0.99278

T/K	D1	D2	D3	D4	F0/R1	F1	F2	F3
324.73	0.98614	0.99176	0.98165	0.99111	0.95629	0.99874	0.91409	0.72835
333.91	0.98129	0.98380	0.97277	0.98237	0.96422	0.99453	0.91379	0.75138
348.04	0.97750	0.95686	0.90592	0.94277	0.99122	0.97502	0.78641	0.54508
352.13	0.97576	0.95607	0.90791	0.94267	0.99017	0.97366	0.79784	0.58235

Table S4 Rate constant (k) as a function of temperature (T) and corresponding Arrhenius parameters (ln A and E_a) for the two sets of experiments carried out with sample 3

SET – 1		SET – 2	
T/K	k/s^{-1}	T/K	k/s^{-1}
329.47	1.273×10^{-3}	323.46	5.233×10^{-4}
333.89	1.642×10^{-3}	328.39	1.315×10^{-3}
338.88	4.267×10^{-3}	333.26	2.447×10^{-3}
343.45	7.250×10^{-3}	335.64	3.778×10^{-3}
347.86	1.139×10^{-2}	338.59	4.828×10^{-3}
352.30	1.746×10^{-2}	343.36	8.013×10^{-3}
356.66	2.453×10^{-2}	347.68	1.183×10^{-2}
		352.55	2.158×10^{-2}
		356.72	2.608×10^{-2}
	$\ln(A/s^{-1}) = 34.28\pm2.08$		$\ln(A/s^{-1}) = 34.02\pm1.77$
	$E_a = 112.3\pm5.9$ kJ·mol^{-1}		$E_a = 111.1\pm5.0$ kJ·mol^{-1}

Table S5 Activation energy (E_a) as a function of conversion fraction (α) obtained by isothermal isoconversional approach for: (a) sample 1, 250-177 μ; (b) sample 2, 354-250 μ; (c) sample 3, >707 μ; (d) sample 4, >707 μ.

α	E_a/kJ·mol^{-1}			
	Sample 1	Sample 2	Sample 3	Sample 4
0.10	88.8±9.1	97.5±9.1	111.0±4.2	114.8±10.8
0.20	88.7±5.8	99.3±8.3	112.1±4.2	119.4±8.3
0.30	87.8±4.2	100.2±7.5	111.6±3.3	119.4±5.8
0.40	86.8±3.3	100.2±7.5	110.7±3.3	119.0±5.0
0.50	86.0±2.5	99.7±7.5	109.9±3.3	120.0±4.2
0.60	85.4±2.5	99.0±7.5	109.5±3.3	121.9±5.0
0.70	84.8±2.5	98.4±6.7	109.1±3.3	123.6±5.0
0.80	84.2±2.5	97.7±6.7	108.8±3.3	126.0±4.2
0.90	84.5±2.5	96.6±6.7	109.9±4.2	132.2±5.0

1 Differential Scanning Calorimetry (DSC)

The results of the DSC study on sample 2 dehydration according to:

$$4HNA{\cdot}0.5H_2O(cr, T_i) \rightarrow 4HNA(cr, T_f) + 0.5H_2O(g, T_f) \quad (S1)$$

are shown in Table S6. Here, m is the mass of sample, T_i and T_f are the initial and final temperatures of the dehydration step, respectively, T_{max} is the temperature corresponding to the peak maximum and Δh the specific enthalpy change associated to reaction S1. The uncertainties quoted for the mean values $<T_i>$, $<T_f>$, $<T_{max}>$, and $<\Delta_r h^\circ>$ represent twice the standard deviation of the mean. This result leads to a standard molar enthalpy $\Delta_r H_m^\circ$ = 24.49±0.94 kJ·mol^{-1}, based on a molar mass of $M(C_6H_5O_3N{\cdot}0.5H_2O)$ = 148.1164 g.mol^{-1} for the 4-hydroxynicotinic acid hemihydrate.

Table S6 Results of the DSC experiments on reaction S1.

m/mg	β/K·min^{-1}	T_i/K	T_{max}/K	T_f/K	Δh/J·g^{-1}
2.24	1	326.2	332.7	336.9	173.823
1.61	2	331.4	338.3	343.7	170.670
1.38	3	330.1	339.4	344.7	155.358
1.79	4	335.9	340.0	346.4	164.108
2.20	5	334.5	340.4	347.1	162.833

$<T_i>$ = 330.9±4.0 K

$<T_{max}>$ = 337.6±3.4 K

$<T_f>$ = 342.9±4.2

$<\Delta_r h^o>$ = 165.4±6.4 J·g^{-1}

2 Slurry/Solubility Tests

The apparatus and procedure used to obtain the solubility of 4HNA in water and demonstrate that the anhydrous 4HNA phase was more stable than 4HNA·0.5H_2O·at temperatures close to ambient were previously described.[71] A suspension of 4HNA in 10 cm^3 distilled and deionized water from a Milli-Q Plus system (conductivity 0.1 μS cm^{-1}) was kept under magnetic stirring, inside a jacketed glass cell, for 1 week. The temperature was maintained constant to ±0.1 K at 283.3 K, 293.0 K or 302.6 K by circulating water from a thermostatic bath though the cell jacket. At the end of the equilibration period the solid in contact with the solution was collected and analyzed by X-ray powder diffraction. As shown in Figure S3 the obtained powder patterns always matched that simulated for the orthorhombic

anhydrous phase previously characterized by single crystal X-ray diffraction (space group $P2_12_12$; a =7.235 Å, b = 23.717 Å, c = 3.706 Å).[23] The formation of 4HNA·0.5H_2O was never detected, even when hydrate crystals were added to the slurry during equilibration. The solution content in 4HNA was also analyzed by the solid residue method[71]

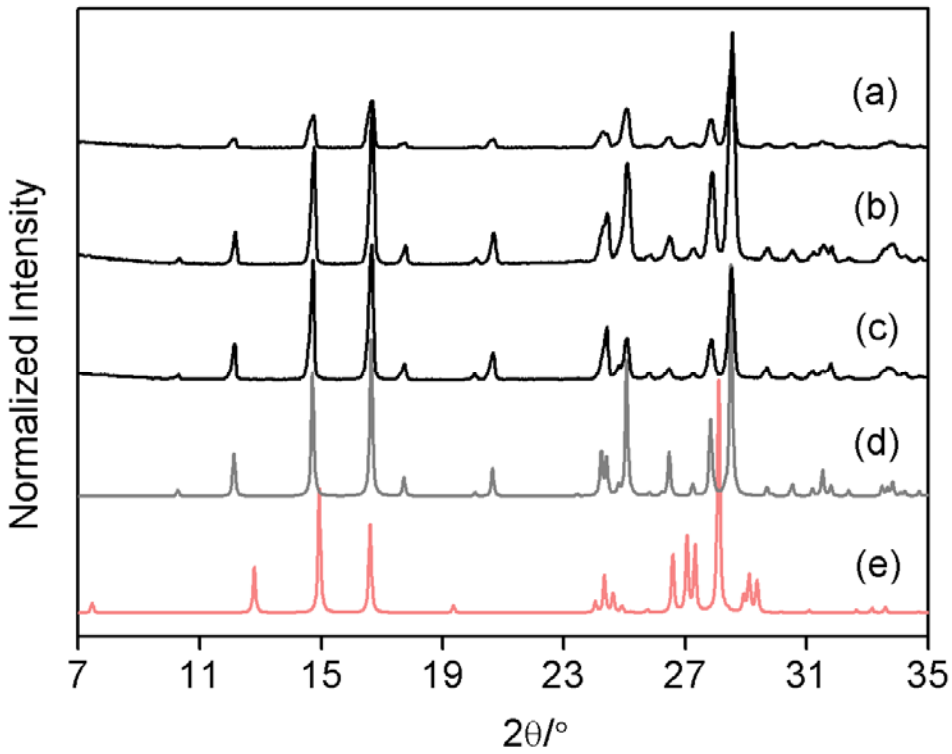

Figure S3 Comparison of the X-ray powder patterns obtained for the solid materials in contact with saturated aqueous 4HNA solutions kept at (a) 283.3 K, (b) 293.0 K, and (c) 302.6 K, with those simulated from single crystal XRD data for (d) anhydrous 4HNA[23] and (e) 4HNA·0.5H_2O.[23]

leading to the solubility data in Table S7. A linear least squares fit to a ln x_{4HNA} vs. 1/T plot based on the data in Table S7 (Figure S3) gave:

$$\ln x_{4HNA} = -(0.23 \pm 0.20) - \frac{(1884.3 \pm 58.8)}{(T/\mathrm{K})} \quad \text{(S2)}$$

with a regression coefficient R^2 = 0.9990.

Table S7 Temperature dependency of the mole fraction (x_{4HNA}) solubility of 4HNA in water[a]

T/K	$x_{4HNA} \times 10^5$
283.3	102.0±3.1 (3)
293.0	129.0±4.1 (3)
302.6	156.0±2.2 (3)

[a] The indicated uncertainties correspond to twice the standard error of the mean of the number of determinations given in parenthesis.

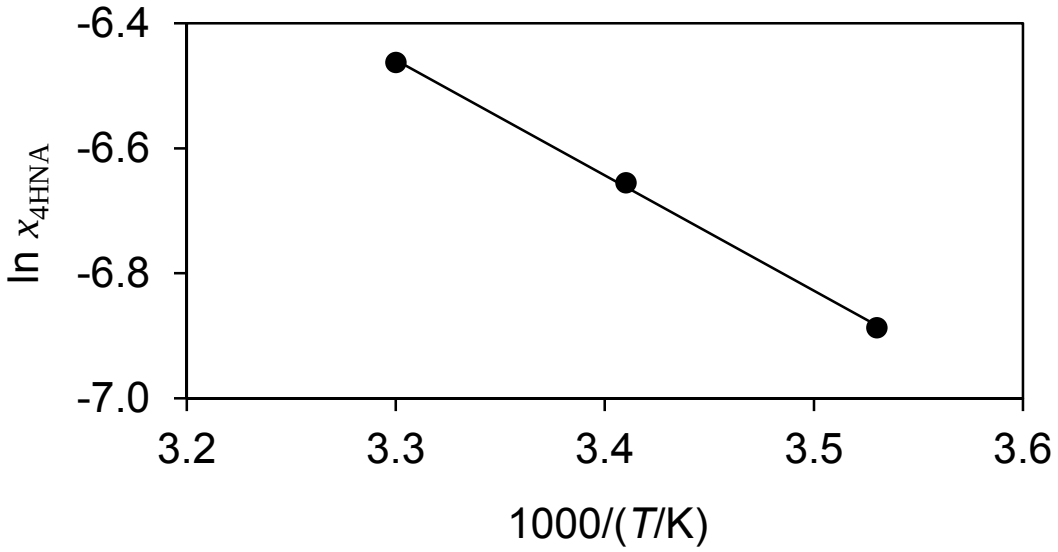

Figure S4 Temperature dependency of the mole fraction (x_{4HNA}) equilibrium solubility of 4-hydroxynicotinic acid in water.

Acknowledgements

This work was supported by Fundação para a Ciência e a Tecnologia (FCT), Portugal (Project UID/MULTI/00612/2013). PhD (SFRH/BD/90386/2012) and Post-Doctoral (SFRH/BPD/101505/2014) grants from FCT are also gratefully acknowledged by A. Joseph and C. E. S. Bernardes, respectively.

References

1. Elvehjem, C. A.; Teply, L. J. *Chem. Rev.* **1943**, *33,* 185-208.
2. Dalton C.; Quinn, J. B.; Crowley H.J., Miller O.N., *In Metabolic Effects of Nicotinic Acid and Its Derivatives*, Gey, K. F.; Carlson, L. A Eds.; Hans Huber: Bern, Switzerland 1971.
3. Miller, O. N.; Gutierrez, M.; Sullivan, A. C.; Hamilton, J. G, *In Metabolic Effects of Nicotinic Acid and Its Derivatives*, Gey, K. F.; Carlson, L. A. Eds.; Hans Huber: Bern, Switzerland, 1971.
4. Block, J. *Vitamins; In Kirk-Othmer Encyclopedia of Chemical Technology*, 5th ed.; Seidel, S. Ed.; Wiley: Hoboken, 1996; Vol. 25.
5. Carlson, L. A. *J. Intern. Med.* **2005**, *258,* 94-114.
6. Davey, R. J.; Blagden, N.; Righini, S.; Alison, H.; Quayle, M. J.; Fuller, S. *Cryst. Growth Des.* **2001**, *1,* 59-65.
7. Chuck, R. *Appl. Catal. A* **2005**, *280,* 75-82.
8. Gille, A.; Bodor, E. T.; Ahmed, K.; Offermanns, S. *Annu. Rev. Pharmacol.* **2008**, *48,* 79-106.
9. Lemke, T. L.; William, D. A.; Roche, V. F.; Zito, S. W., *Foye's Principles of Medicinal Chemistry*, 6th ed.; Lippincott Williams & Wilkins: Baltimore, 2008.
10. Li, J. J., *Triumph of the Hart. The Story of Statins*; Oxford University Press: New York, 2009.
11. Bernstein, J. *Polymorphism in Molecular Crystals*; Oxford University Press: Oxford, 2002.
12. Hilfiker, R., *Polymorphism in the Pharmaceutical Industry*; Wiley-VCH: Weinheim, 2006.
13. Brittain, H. G., *Polymorphism in Pharmaceutical Solids*, 2nd ed.; Informa Healthcare: New York.
14. Lee, A. Y.; Erdemir, D.; Myerson, A. S. *Annu. Rev. Chem. Biomol.* **2011**, *2,* 259-280.
15. Bauer, J.; Spanton, S.; Henry, R.; Quick, J.; Dziki, W.; Porter, W.; Morris, J. *Pharmaceut. Res.* **2001**, *18,* 859-866.
16. Gillon, A. L.; Feeder, N.; Davey, R. J.; Storey, R. *Cryst. Growth. Des.* **2003**, *3,* 663-673.
17. Griesser, U. J., The Importance of Solvates*; In Polymorphism in the Pharmaceutical Industry*, Hilfiker, R. Ed.; Wiley-VCH: Weinheim, 2006.
18. Infantes, L.; Fabian, L.; Motherwell, W. D. S. *CrystEngComm* **2007**, *9,* 65-71.
19. Tian, F.; Qu, H. Y.; Zimmermann, A.; Munk, T.; Jorgensen, A. C.; Rantanen, J. *J. Pharm. Pharmacol.* **2010**, *62,* 1534-1546.
20. Petit, S.; Coquerel, G. *Chem. Mater.* **1996**, *8,* 2247-2258.

21. Galway, A. K., Dehydration of Crystalline Hydrates*; In Handbook of Thermal Analysis and Calorimetry*, Gallagher, P. K., Ed.; Elsevier: Amsterdam, 2003; Vol. 2.
22. Galwey, A. K. *Thermochim. Acta.* **2000**, *355,* 181-238.
23. Matias, E. P.; Bernardes, C. E. S.; Piedade, M. F. M.; Minas da Piedade, M. E. *Cryst. Growth Des.* **2011**, *11,* 2803-2810.
24. Bamford, C. H.; Tipper, C. F. H., *Reactions in the Solid State*; Elsevier: Amsterdam, 1980; Vol. 22.
25. Galway, A. K.; Brown, M. E. Kinetic Background to Thermal Analysis and Calorimetry; In *Handbook of Thermal Analysis and Calorimetry*, Gallagher, P. K., Ed.; Elsevier: Amsterdam, 1998; Vol. 1.
26. Khawam, A.; Flanagan, D. R. *J. Pharm. Sci.* **2006**, *95,* 472-498.
27. Zhou, D. L.; Schmitt, E. A.; Zhang, G. G. Z.; Law, D.; Wight, C. A.; Vyazovkin, S.; Grant, D. J. W. *J. Pharm. Sci.* **2003**, *92,* 1367-1376.
28. Laidler, K. J., *Chemical Kinetics*, 3rd ed.; Harper and Row: New York, 1987.
29. Grunwald, E. *Thermodynamics of Molecular Species*; John Wiley: New York, 1997.
30. Mohr, P. J.; Taylor, B. N.; Newell, D. B. *J. Phys. Chem. Ref. Data* **2012**, *41*.
31. Vyazovkin, S. *New J. Chem.* **2000**, *24,* 913-917.
32. Mohr, P. J.; Taylor, B. N.; Newell, D. B. *Rev. Mod. Phys.* **2012**, *84,* 1527-1605.
33. Skrdla, P. J. *J. Phys. Chem. A* **2011**, *115,* 6413-6425.
34. Vyazovkin, S.; Wight, C. A. *Annu. Rev. Phys. Chem.* **1997**, *48,* 125-149.
35. Gotor, F. J.; Criado, J. M.; Malek, J.; Koga, N. *J. Phys. Chem. A.* **2000**, *104,* 10777-10782.
36. Sharp, J. H.; Brindley, G. W.; Achar, B. N. N. *J. Am. Ceram. Soc.* **1966**, *49,* 379-&.
37. Jones, L. F.; Dollimore, D.; Nicklin, T. *Thermochim. Acta.* **1975**, *13,* 240-245.
38. Wieser, M. E.; Holden, N.; Coplen, T. B.; Bohlke, J. K.; Berglund, M.; Brand, W. A.; De Bievre, P.; Groning, M.; Loss, R. D.; Meija, J.; Hirata, T.; Prohaska, T.; Schoenberg, R.; O'Connor, G.; Walczyk, T.; Yoneda, S.; Zhu, X. K. *Pure. Appl. Chem.* **2013**, *85,* 1047-1078.
39. Laugier, J. Bochu, B. *Cellref V3*, http://www.ccp14.ac.uk/tutorial/lmgp/cellref.htm.
40. Santos, R. C.; Figueira, R. M. B. B. M.; Piedade, M. F. M.; Diogo, H. P.; Minas da Piedade, M. E. *J. Phys. Chem. B* **2009**, *113,* 14291-14309.
41. Jillavenkatesa, A. Dapkunas, S. J.; Lum, L. S. H., *Particle Size Characterization*; National Institute of Standards and Technology: Washington, DC, 2001.
42. Agbada, C. O.; York, P. *Int. J. Pharm.* **1994**, *106,* 33-40.
43. Lente, G.; Fabian, I.; Poe, A. J. *New J. Chem.* **2005**, *29,* 759-760.
44. Pimentel, G. C.; McClellan, A. L. *The Hydrogen Bond*; W. H. Freeman and Company: San Francisco, 1960.
45. Jeffrey, G. A., *An Introduction to Hydrogen Bonding*; Oxford University Press: New York, 1997.
46. Iogansen, A. V. *Spectrochim. Acta. A* **1999**, *55,* 1585-1612.
47. Gilli, G.; Gilli, P., *The Nature of the Hydrogen Bond: Outline of a Comprhensive Hydrogen Bond Theory*; Oxford University Press: Oxford, 2009.
48. Exner, O. *Progr. Phys. Org. Chem.* **1973**, *10,* 411-482.
49. Linert, W.; Jameson, R. F. *Chem. Soc. Rev.* **1989,** *18,* 477-505.
50. Yelon, A.; Movaghar, B.; Crandall, R. S. *Rep. Prog. Phys.* **2006**, *69,* 1145-1194.
51. Liu, L.; Guo, Q. X. *Chem. Rev.* **2001**, *101,* 673-695.
52. Exner, O. *J. Phys. Org. Chem.* **1997**, *10,* 797-813.
53. Agrawal, R. K. *J. Therm. Anal.* **1986**, *31,* 73-86.

54. Zsako, J.; Somasekharan, K. N. *J. Therm. Anal.* **1987**, *32,* 1277-1281.
55. Koga, N. *Thermochim. Acta.* **1994**, *244,* 1-20.
56. Brown, M. E.; Galwey, A. K. *Thermochim. Acta.* **2002**, *387,* 173-183.
57. Pop, N.; Vlase, G.; Vlase, T.; Doca, N.; Mogos, A.; Ioitescu, A. *J. Therm. Anal. Calorim.* **2008**, *92,* 313-317.
58. Yelon, A.; Sacher, E.; Linert, W. *Catal. Lett.* **2011**, *141,* 954-957.
59. Yelon, A.; Sacher, E.; Linert, W. *Phys. Chem. Chem. Phys.* **2012**, *14,* 8232-8234.
60. Barrie, P. J. *Phys. Chem. Chem. Phys.* **2012**, *14,* 327-336.
61. Barrie, P. J. *Phys. Chem. Chem. Phys.* **2012**, *14,* 8235-8236.
62. Exner, O.; Beranek, V. *Collect. Czech. Chem. C* **1973**, *38,* 781-798.
63. Exner, O. *Collect. Czech. Chem. C* **1972,** *37,* 1425-1444.
64. Linert, W.; Soukup, R. W.; Schmid, R. *Comput. Chem.* **1982**, *6,* 47-55.
65. Ouvrard, C.; Berthelot, M.; Lamer, T.; Exner, O. *J. Chem. Inf. Comp. Sci.* **2001**, *41,* 1141-1144.
66. Exner, O. *Collect. Czech. Chem. C* **1966**, *31,* 3222-&.
67. Walpole R.E.; Myers R. H.; Myers S.L.; Ye K. *Probability and Statistics for Engineers and Scientists*, 9th ed.; Prentice Hall: Boston, 2012.
68. Macrae, C. F.; Bruno, I. J.; Chisholm, J. A.; Edgington, P. R.; McCabe, P.; Pidcock, E.; Rodriguez-Monge, L.; Taylor, R.; van de Streek, J.; Wood, P. A. *J. Appl. Crystallogr.* **2008**, *41,* 466-470.
69. Koga, N.; Tanaka, H. *Thermochim. Acta.* **2002**, *388,* 41-61.
70. Bernardes, C. E. S.; Piedade, M. F. M.; Minas da Piedade, M. E. *Cryst. Growth Des.* **2010**, *10,* 3070-3076.
71. Gonçalves, E. M.; Minas da Piedade, M. E. *J. Chem. Thermodyn.* **2012**, *47,* 362-371.

Chapter 7

Solvate Mediated Control of 5-Hydroxynicotinic Acid Molecular Conformation in the Crystalline State.

This chapter reports studies on two new solvates of 5-hydroxynicotinic acid (5HNA): a monohydrate (5HNA·H_2O), and a DMSO solvate (5HNA·DMSO). The molecular and crystal structures of the hydrate and of the DMSO solvate were obtained from single crystal X-ray diffraction (SC-XRD) analysis. The desolvation reactions of both compounds were studied by TGA, DSC and Calvet-microcalorimetry. Finally a new process to obtain highly pure 5-hydroxynicotinic acid through formation/desolvation of 5HNA·DMSO was developed.

The synthesis of the solvates and their characterization by powder X-ray diffraction, TGA, DSC, and Calvet microcalorimetry were performed by me. Single crystal X-ray diffraction analyses were performed by Prof. Fátima Piedade at IST and by Dr. Franziska Emmerling at BAM, Germany. LC-MS studies were performed by Prof. Maria da Conceição Oliveira at IST. Finally I contributed in the discussion of results and writing of manuscript.

Abstract

Two new solvates of 5-hydroxynicotinic acid (5HNA) were isolated: a monohydrate (5HNA·H_2O) and a DMSO solvate (5HNA·DMSO). Methods for the reproducible and selective preparation of both compounds were developed and their structures were obtained from single crystal X-ray diffraction (SC-XRD) analysis. Thermogravimetry (TGA) experiments confirmed the 1:1 stoichiometry deduced from SC-XRD analysis. The SC-XRD experiments further revealed that the 5HNA molecule adopts a zwitterionic conformation in 5HNA·H_2O and a hydroxyl conformation in 5HNA·DMSO. The formation of 5HNA·H_2O and 5HNA·DMSO can therefore be used to stabilize two different tautomeric forms of 5HNA.

The desolvation reactions of 5HNA·H_2O and 5HNA·DMSO were also studied by differential scanning calorimetry (DSC) and Calvet-microcalorimetry. Powder X-ray diffraction (PXRD) showed that the dehydrated and desolvated materials corresponded to the same phase. This phase was initially different from that of the original starting material but evolved over time to the latter. Finally, LC-MS analysis showed that while the purity of the starting material was 93% (mole percentage), the purities of the dehydrated and desolvated products were 99.03% and 99.95%, respectively. Solvate formation/desolvation was therefore proposed as a new and simple method to produce highly pure 5HNA.

7.1 Introduction

Tautomeric equilibria in heterocyclic organic compounds are of considerable importance in chemistry and biochemistry.[1] According to the most widely accepted definition, tautomers are structural isomers that differ only in the position of a hydrogen atom or proton.[2] Tautomeric equilibria can be influenced by micro and macro-environmental factors such as, temperature, concentrations, pH or type of solvent. Molecules with tautomeric ability are capable of adapting their structure to a specific environment and hence are referred to as the chameleons of chemistry.[3-5]

Change in structure often means change in properties. For instance, by proton transfer a basic group in a molecule may become acidic or a carbonyl group may change into a hydroxyl group and *vice versa*. In dye industry for example, the azo-hydrazone tautomerism is behind the differences in colour, tinctorial strength and toxicological profile of the dyes.[6] In biological systems, the purine and pyrimidine bases can exist in the rare tautomeric forms and their occurrence can lead to mismatch in the DNA or RNA base pairing, for eg., during RNA replication, uracil in uridine should adopts dioxo tautomeric form to compliment the amino tautomer of adenosine. However the occurrence of a rare enol tautomeric form of uracil has been reported which leads to point mutation.[7] In the case of drug molecules capable of tautomerism, it is very important to know which tautomeric form is present at each step of the drug development and metabolism. The anticoagulant drug warfarin is, for example, shown to potentially exist in solution in as many as 40 topologically distinct tautomeric forms.[3, 8] In spite of the widespread use of this drug, its mechanism of action is still unclear due to molecular level complexity involved in understanding the exact biologically active form.[3]

Tautomerism is mostly found in solution and in the gas phase, as proton transfer readily occurs in these environments. The phenomenon is often suppressed to a large extent in the solid state due to hindered proton mobility.[2, 9] Crystallization offers, therefore, a possible way to stabilize a specific tautomer and strategies to achieve this goal have attracted a broad attention both in terms of fundamental research and applications (e.g. molecular machines and switches, chemical information management systems and new generation pharmaceutics).[10] In the majority of cases, the tautomer occurring in the crystalline form corresponds to the most

stable tautomer occurring in the solution or as calculated for the gas phase.[11] When different tautomers of a given compound crystallize in different crystal forms they are called tautomeric polymorphs.[12] Though rare, a few examples of tautomeric polymorphism have been reported such as in the cases of the APIs omeprazole,[13] sulfasalazine,[14] triclabendazole,[15] ranitidine,[16] barbituric acid,[17-19] irbesarten,[20-22] 2-amino-3-hydroxy-6-phenylazopyridine,[23] 2-(2,4-dinitrobenzyl)-3-methylpyridine[24] and, recently, also in 4-hydroxynicotinic acid.[25] Tautomeric polymorphism in co-crystals has been described for the 1:1 co-crystals of piroxicam and mono-substituted benzoic acids.[12, 26-27] It was shown that different tautomers can be stabilized by interacting with different co-former molecules. This strategy was used by Cruz-Cabeza *et al.*, to crystallize a desired tautomer of 1-deazapurine (1-DAP), regardless of its relative stability, using a suitable co-former.[28] This was achieved by first investigating the most likely aggregation modes of a specific tautomer using a computational approach and then use the obtained information to guide the selection of co-formers[29] and the experimental preparation of the co-crystals.

Nicotinic acid (Pyridine-3-carboxylic acid or niacin), studied in chapter 3 of this thesis , is one of eight water-soluble B vitamins and is a compound of considerable importance in terms of chemical, dietetic and therapeutic applications.[30] The hydroxyl derivatives of nicotinic acid (2-, 4-, 5-, and 6-hydroxynicotinic acids) have also some biological activity and ample industrial applications, such as in the manufacture of pharmaceuticals, herbicides, and insecticides.[31] Our group has previously reported a number of studies on nicotinic acid and some of its derivatives, namely (i) the crystal and molecular structure and the bonding energetics of anhydrous or hydrate forms of nicotinic acid, 2-, 4-, 5-, and 6-hydroxy nicotinic acids, and 5-chloro-6-hydroxynicotinic acid;[32-34] (ii) the concentration dependence of the enthalpy of solution of nicotinic acid in water;[35] (iii) the solubility of nicotinic acid in a series of solvents differing in polarity, polarizability and hydrogen-bonding ability;[36] (iv) the influence of temperature and ionic strength on the acidity constants of nicotinic acid in aqueous solution;[37] (v) the determination of the standard molar enthalpies of formation of the three nicotinic acid species involved in aqueous protonation/deprotonation equilibria at infinite dilution;[35] and (vi) heat capacity measurements over the temperature range 296 K to 531 K and determination of the $\Delta_f G_m^\circ$ vs T phase diagram illustrating the stability domains of the solid and liquid nicotinic acid phases.[30]

These studies revealed one of the most interesting features of the hydroxynicotinic acid molecules, namely the possibility of existing as hydroxyl or oxo tautomers related by a solvent dependent equilibrium as illustrated in Scheme I for 4-hydroxynicotinic. Hydroxynicotinic acid derivatives, therefore, constitute a very interesting family of compounds to investigate how changes in the crystallization solvent and positional isomerism may be used to control conformational polymorphism in the solid state.

Scheme I

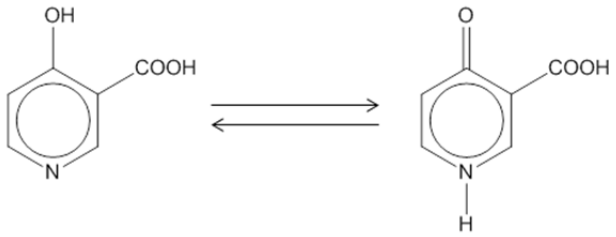

Hydroxy *Oxo*

Four polymorphic forms of 2-hydroxynicotinic acid (2HNA) have been reported and in all of them the 2HNA molecule is present in oxo form.[38] For 6-hydroxynicotinic acid (6HNA) only one crystal structure has been determined which involves the oxo tautomer.[33, 39] Five crystal structures have been published for 4-hydroxynicotinic acid (4HNA):[25] two hydrates (H-I and H-II) and three anhydrous polymorphs (form I, II and III). In hydrate H-I and anhydrous polymorphs I and II, the 4HNA molecule adopts an oxo form, whereas in hydrate H-II and anhydrous form III the zwitterionic conformation is preferred.

No crystal structure of 5-hydroxynicotinic acid (5HNA) has been reported up to now.[40] Solvated derivatives are also not known.[40] The study of 5HNA seemed, therefore, interesting, particularly because, in contrast with 2-, 4-, 6-hydroxynicotinic acids, resonance theory predicts that the oxo form will not be favored. Indeed, in the case of 5HNA, the transfer of the hydroxyl proton in the meta position to the ring nitrogen atom leads to loss of aromaticity.[41] Furthermore, considering that the behavior of hydroxynicotinic acid derivatives in the solid state parallel to that of hydroxypyridines it may be expected that, analogously to 3-hydroxypyridine (3HP), 5HNA will also preferentially crystallize in the hydroxyl form.[33]

It should nevertheless be bear in mind that the tautomer predominant in a given solvent does not necessarily correlate with the tautomer obtained in a crystallized material. In the case of nicotinic acid, for example, the zwitterionic form, **1**, dominates in aqueous media and in non-aqueous media (e.g. DMSO), the neutral form, **2**, predominates. Despite this fact the nicotinic acid molecule has been found to always crystallize as the neutral form, **2**, regardless of the solvent.

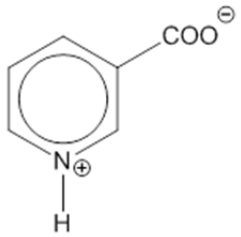

1

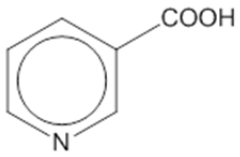

2

With this background in mind, we crystallized 5-hydroxynicotinic acid using a protic (water) and an aprotic (DMSO) solvent. These crystallization processes led to the isolation of two solvates: a monohydrate (5HNA·H_2O) and a DMSO solvate (5HNA·DMSO) displaying tautomeric differences in the 5HNA molecule. The characterization of 5HNA·H_2O and 5HNA·DMSO by XRD, TGA, DSC and Calvet microcalorimetry is described in this chapter. Unfortunately all attempts to obtain a single crystal of 5HNA suitable for a SC-XRD determination failed up to now.

7.2 Materials and Methods

7.2.1 General

The X-ray powder diffractograms were recorded in the range 5° < 2θ < 35° on a Philips X'Pert PRO diffractometer, with automatic data acquisition (X'Pert Data Collector v2.0b), operating in the θ-2θ mode. The apparatus had a vertical PW 3050/60 goniometer and a X'Celerator detector. A monochromatized Cu Kα radiation source set to 30 mA and 40 kV was used. The diffractograms were recorded at ~293 K, using the continuous scanning mode with a step size of 0.017° (2θ) and scan step of 20 s. The samples were mounted on an aluminum sample holder. The indexation of the powder patterns was performed using the program Cellref.[42] Optical microscopy images were obtained with an Olympus SZX10 stereoscopic microscope and the CellD 2.6 software.

5-Hydroxynicotinic acid (Activate Scientific GmbH, 98%) was used without further purification. The syntheses were performed with distilled and deionized water from a Milli-Q Plus system (conductivity 0.1 μs 3 cm^{-1}) and dimethyl sulfoxide (Sigma, 99.5%).

7.2.2 Concomitant crystallization of 5HNA·H_2O and 5HNA·DMSO

Solid 5HNA was added to 10 cm^3 of DMSO in a test tube, at 293 K, until saturation was achieved. The solution was filtered into another test tube sealed with a stopper. A needle was inserted through the stopper into the solution. This needle was connected to an automated burette to dispense distilled and deionized water into the DMSO solution at a programmed rate of 0.005 $cm^3 \cdot min^{-1}$ Concomitant precipitation of 5HNA·H_2O and 5HNA·DMSO crystals occurred during a week period.

7.2.3 Crystallization of 5HNA·H_2O

A suspension of 5HNA (0.07 g) in 15 cm^3 of distilled and deionized water was magnetically stirred for a week inside a Schlenk tube at 294±2 K and under nitrogen atmosphere. The mixture was heated to 353 K and the solid completely dissolved in ~30 min. The solution was filtered into another Schlenk tube, which was then immersed in a JULABO F33-ME thermostatic bath initially kept at 353 K. The system was cooled to 278 K, without stirring, at a rate of 0.25 $K \cdot min^{-1}$. Crystals of 5HNA·H_2O (Figure 7.1a) were obtained within two days.

7.2.4 Crystallization of 5HNA·DMSO

Solid 5HNA was added to 4 cm^3 of DMSO at 333 K under nitrogen atmosphere. The mixture was magnetically stirred for ~1 h to achieve saturation. The solution was filtered into another Schlenk tube, which was immersed in a JULABO F33-ME thermostatic bath initially kept at 333 K. The system was cooled to 293 K, without stirring at a rate of 0.009 $K \cdot min^{-1}$. Crystals of 5HNA·DMSO (Figure 7.1b) were obtained within two days.

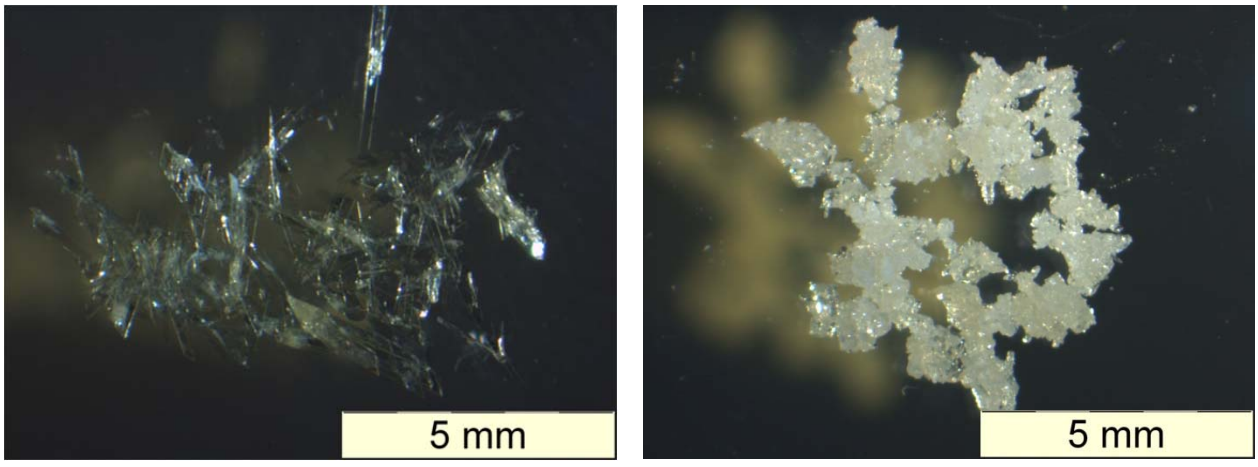

(a) (b)

Figure 7.1 Optical microscopy images of (a) 5HNA·H_2O and (b) 5HNA·DMSO.

7.2.5 Crystal structure determination

The crystal structures of the hydrate (5HNA·H_2O) and the DMSO solvate (5HNA·DMSO) were solved by single crystal X ray diffraction (SC-XRD). The experiments were carried out at 167±2 K for hydrate and at 167±2 K and 293 K for DMSO solvate, on a Bruker AXS-KAPPA APEX II area detector diffractometer. The crystals were coated with Paratone-N oil and mounted on a Kaptan loop. A graphite-monochromated Mo Kα (λ = 0.71073 Å) radiation source operating at 50 kV and 30 mA was used. The temperature scale of the apparatus was previously calibrated against a standard platinum resistance thermometer placed at the same position as the crystal. The standard temperature sensor had in turn been calibrated at an accredited facility in accordance to the International Temperature Scale ITS-90. An empirical absorption correction was applied by using Bruker SADABS[43] and the data reduction was performed with the Bruker SAINT program.[44] The structure was solved by direct methods with Bruker SHELXTL[45] and refined by full-matrix least-squares on F^2 using SHELXL97[46] programs included in WINGX-Version 1.80.05. Non-hydrogen atoms were refined with anisotropic thermal parameters. The hydrogen atoms were located in the density map and isotropic displacement parameters, U_{iso}(H), refined freely. Structural representations were prepared using Mercury 3.1.1.[47] PLATON was used for the hydrogen bond interactions.[48] A summary of the crystal data, structure solution, and refinement parameters is given in Table 7.1. The crystal structure solution for hydrate (5HNA·H_2O) was also carried out at 300 K on a Bruker AXS SMART diffractometer using Mo Kα radiation (λ = 0.71073 Å) monochromatized by a graphite crystal. Data reduction was carried out using the Bruker AXS SAINT and SADABS packages. The structure was solved by direct methods and refined by full-matrix least-squares calculations using SHELX.30 An empirical absorption correction (Ψ-scan) was applied. All non-hydrogen atoms were refined anisotropically. The hydrogen atoms were found in the Fourier Map and refined isotropically.

Table 7.1 Crystal data and structure refinement for the 5HNA·H_2O and the 5HNA·DMSO obtained in this work.

	5HNA·H_2O		5HNA·DMSO	
T/K	167	300	167 K	293 K
empirical formula	C_6 H_7 N O_4	C_6 H_7 N O_4	C_8 H_{11} N O_4 S	C_8 H_{11} N O_4 S
formula weight	157.13	157.13	217.24	217.24
wavelength, Å	0.71073	0.71073	0.71073	0.71073
Crystal system	Monoclinic	Monoclinic	Monoclinic	Monoclinic
Space group	P 2_1/c	P 2_1/c	P 2_1/c	P 2_1/c
a/Å	4.50390(10)	4.5057(15)	5.2350(3)	5.2380(2)
b/Å	16.3890(6)	16.465(6)	22.4780(13)	22.4770(11)
c/Å	8.8561(3)	9.038(3)	8.4170(5)	8.4130(4)
β/deg	91.271(2)	90.06(2)	94.301(4)	94.204(2)
V/Å^3	653.55(4)	670.5(4)	987.66(10)	987.84(8)
Z, *Z*'	4/1	4/1	4/1	4/1
ρ_{calcd}/g·cm^{-3}	1.597	1.557	1.461	1.461
μ/mm^{-1}	0.136	0.133	0.316	0.316
F(000)	328	328	456	456
θ limits/deg	2.485 to 26.419	2.474 to 27.863	2.590 to 30.561	2.591 to 28.324
Limiting índices	*-5<=h<=5*	*-5<=h<=5*	-7<=h<=7	-7<=h<=7
	-20<=k<=20	-21<=k<=21	-32<=k<=19	-29<=k<=30
	-11<=l<=10	-11<=l<=11	-12<=l<=12	-11<=l<=10
Reflections collected/ unique	5270 / 1329 [R(int) = 0.0291]	9988 / 1463 [R(int) = 0.1136]	14117 / 2999 [R(int) = 0.0502]	9632 / 2446 [R(int) = 0.0373]
Completeness to θ / %	98.8	92.8	99.4	99.9
Data / restraints / parameters	*1329 / 0 / 128*	1463 / 0 / 129	2999 / 0 / 171	2446 / 0 / 171
GOF on F^2	1.051	1.176	1.039	1.027
Final *R* indices [$I>2\sigma(I)$]	R_1 = 0.0323, wR_2 = 0.0845	R1 = 0.0653, wR2 = 0.1593	R_1 = 0.0473, wR_2 = 0.0973	R1 = 0.0305, wR2 = 0.0806
R indices (all data)	R_1 = 0.0414, wR_2 = 0.0901	R1 = 0.0871, wR2 = 0.1685	R_1 = 0.0673, wR_2 = 0.1057	R1 = 0.0331, wR2 = 0.0819
Extinction coefficient		0.074(13)		
Largest diff. peak and hole/e·Å^{-3}	0.329 and -0.224	0.253 and -0.245	0.465 and -0.272	0.404 and -0.272

7.2.6 Differential Scanning Calorimetry (DSC) and Thermogravimetry (TGA)

DSC studies were made on a Perkin-Elmer DSC 7 apparatus. Sealed aluminum crucibles with punctured lids containing ~3-4 mg of 5HNA·H_2O and ~5–6 mg of 5HNA·DMSO were used. Weightings were performed with a precision of ±0.1 μg on a Mettler XP2U ultra-micro balance. The experiments were carried out in the approximate range 300-600 K, under a flow of nitrogen (Air Liquide N45) of 25 $cm^3 \cdot min^{-1}$. Heating rate β = 5 $K \cdot min^{-1}$ was used. The temperature scale of the apparatus was calibrated at the same heating rate by taking the onset of the fusion peaks of indium (Perkin Elmer; mass fraction 0.99999; T_{fus} = 429.75 K, $\Delta_{fus}h°$ = 28.45 $J \cdot g^{-1}$) and zinc (Perkin-Elmer, mass fraction 0.99999, T_{fus} = 692.65 K). The calibration of the heat flow scale was based on the area of the indium fusion peak.

TGA experiments were carried out, in the range 325-425 K, on a Perkin Elmer TGA7 apparatus. The heating rate was β = 5 $K \cdot min^{-1}$ in all experiments. The balance chamber was kept under a nitrogen flow (Air Liquide N45) of 38 $cm^3 \cdot min^{-1}$. The sample purge gas was helium (Air Liquide N55) at a flow rate of 22.5 $cm^3 \cdot min^{-1}$. The mass scale of the instrument was calibrated with a standard 100 mg weight and the temperature calibration was based on the measurement of the of the Curie points (T_C) of alumel alloy (Perkin-Elmer, T_C = 427.35 K) and nickel (Perkin-Elmer, mass fraction 0.9999, T_C = 628.45 K) standard reference materials. The 5HNA·H_2O and 5HNA·DMSO samples with an initial mass of ~3-6 mg and ~ 5-6 mg, respectively, were placed in an open platinum crucible.

7.2.7 Calvet drop microcalorimetry

The enthalpy changes associated with dehydration of 5HNA·H_2O and desolvation of 5HNA·DMSO were determined by using an electrically calibrated Calvet microcalorimetric apparatus. The operating procedure has been previously described.[49-50] A glass capillary containing ~5-6 mg of compound in the case of 5HNA·H_2O and ~8–9 mg in the case of 5HNA·DMSO were equilibrated for 30 min at 298 K (T_i) in the drop furnace and then dropped into the calorimetric cell kept at 361 K (T_f). Following the drop, the sample and reference cells

were simultaneously evacuated to 0.13 Pa. The standard molar enthalpy of the calorimetric process, $\Delta_r H_m^\circ$ (kJ·mol^{-1}) was obtained from.

$$\Delta_r H_m^\circ = \frac{M}{m}\left[\frac{A - A_b}{\varepsilon} - \Delta H_{glass}\right] \quad (7.1)$$

where m and M are the mass and molar mass of sample, respectively, A is the area of measured curve corresponding to overall experiment, A_b is the background contribution due to pumping, ε is the energy equivalent of the calorimeter obtained from a set of electrical calibrations and ΔH_{glass} is the enthalpic contribution of the glass to the process which is given by equation.

$$\Delta H_{glass} = m_{glass} c_p^\circ(\text{glass})(T_f - T_i) \quad (7.2)$$

where m_{glass} is the mass of the glass capillary and T_i and T_f are the initial and final temperatures of the process.

7.2.8 Liquid Chromatography, with Diode Array Detection and Electrospray Ionisation Mass Spectrometry (LC-DAD-ESI/MS) analysis

The 5HNA starting material and the dehydrated and desolvated products of 5HNA·H_2O and 5HNA·DMSO, respectively, were analyzed in aqueous solution by LC-MS. The LC/MS system included a HPLC Dionex Ultimate 3000 composed of a binary pump HPG3200, an Autosampler WPS300 with a column oven TCC3000, a DAD 3000 coupled in-line to a LCQ Fleet ion trap mass spectrometer equipped with an ESI ion source (Thermo Scientific). Separations were carried out with a Phenomenex Luna C18 (2) column (150 mm×2 mm, 3 μm)

at 308 K. An injection volume of 10 µL was delivered at a flow rate of 200 $\mu L \cdot min^{-1}$ using a linear gradient from 50 to 80 % in (A) 0.1 %(v/v) of formic acid in water and (B) acetonitrile. This was followed by a 4 min linear gradient to 100% acetonitrile, and then the column was re-equilibrated with 50 % of (A) for 10 min. The DAD was monitored in the range of 200-600 nm.

The mass spectrometer was operated in the ESI positive/negative ion modes, with the following optimized parameters: ion spray voltage, ±4.5 kV; capillary voltage, 16/-18 V; tube lens offset, -63/58 V, sheath gas (N_2), 80 arbitrary units; auxiliary gas, 5 arbitrary units; capillary temperature, 573 K. Spectra typically correspond to the average of 20–35 scans, and were recorded in the range between 50-500 Da. Data acquisition and processing were performed using the Xcalibur software.

7.3 Results and Discussion

7.3.1 Structure

Single crystal X-ray diffraction analysis indicated that two previously unknown 5HNA forms were obtained in this work using two preparation methods (Table 7.1). The first procedure led to concomitant formation of a monohydrate (5HNA·H_2O) and a DMSO solvate (5HNA·DMSO). The same compounds were selectively and reproducibly obtained using separate synthetic routes. The 5HNA molecule adopts a zwitterionic conformation in 5HNA·H_2O and a hydroxyl conformation in 5HNA·DMSO (Figure 7.2). The geometrical parameters of the 5HNA molecules are summarized in Table 7.2 and the hydrogen bond distances and angles relevant for a packing analysis of the hydrate (5HNA·H_2O) and DMSO solvate (5HNA·DMSO) are indicated in Table 7.3.

The fact that a zwitterionic 5HNA conformation is found in 5HNA·H_2O and a hydroxyl conformation is preferred in 5HNA·DMSO suggests a direct relationship between the dominant species in solution and that present in the crystallized material. Indeed, on one hand, a

speciation analysis carried out for a saturated aqueous 5HNA solution (pH = 3.488 obtained in this work; *T* = 295 K; see Supporting Information) indicated that the molecule is primarily in a zwitterionic form (91%). On the other hand, by analogy with the nicotinic acid case mentioned in the Introduction it can be concluded that the hydroxy form is likely to be preferred in DMSO.

As shown in Table 7.2 the bond distances and angles in the two solvates are similar except for the region of the carboxylic group where larger differences are found. This is not unexpected considering the different conformations of the 5HNA molecule.: (i) the C6-O2 distance is 0.06 Å larger in 5HNA·H_2O than in the 5HNA·DMSO reflecting loss of double bond character in the zwitterionic conformation relative to the hydroxyl counterpart; (ii) the C6-O3 distance is 0.04 Å shorter in hydrate than in the DMSO solvate reflecting the expected opposite trend.

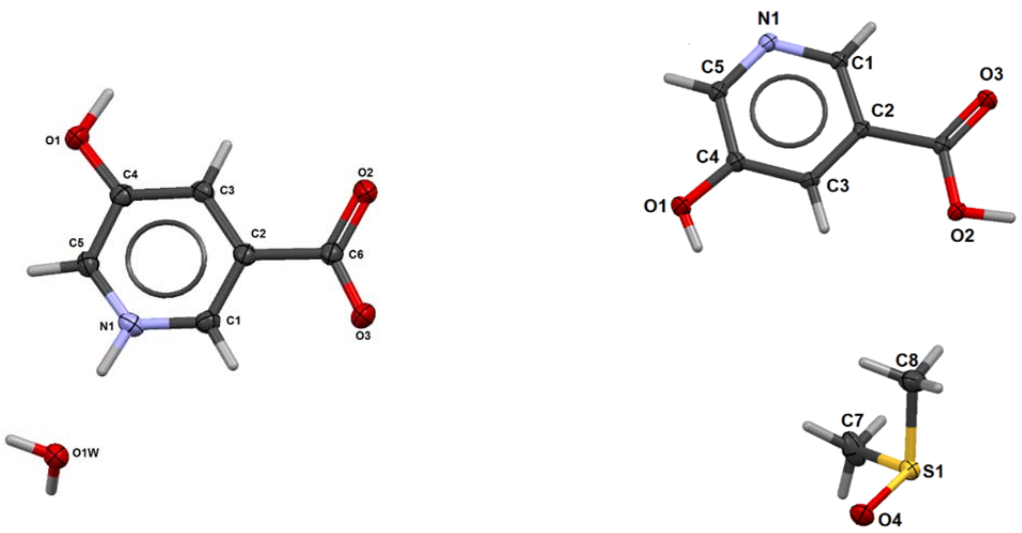

(a) (b)

Figure 7.2 Raster3D drawing and atom labeling scheme of (a) 5HNA and water molecules in 5HNA·H_2O and (b) 5HNA and DMSO molecules in the 5HNA·DMSO.

Table 7.2 Bond distances and angles for the hydrate (5HNA·H_2O) and DMSO solvate (5HNA·DMSO).

	Hydrate (163 K)	Hydrate (300 K)	DMSO solvate (163 K)	DMSO solvate (293K)
Bond Distances/Å				
O(1)-C(4)	1.3313(17)	1.326(3)	1.344(2)	1.3462(14)
O(2)-C(6)	1.2523(16)	1.241(3)	1.3111(18)	1.3104(13)
O(3)-C(6)	1.2528(16)	1.256(3)	1.2152(19)	1.2184(14)
N(1)-C(1)	1.3399(18)	1.346(3)	1.3396(19)	1.3358(14)
N(1)-C(5)	1.3401(18)	1.312(4)	1.333(2)	1.3363(15)
C(1)-C(2)	1.379(2)	1.393(3)	1.389(2)	1.3883(15)
C(3)-C(2)	1.3796(19)	1.369(4)	1.3899(15)	1.3899(15)
C(4)-C(3)	1.4056(19)	1.407(3)	1.3925(15)	1.3925(15)
C(5)-C(4)	1.3899(19)	1.399(3)	1.393(2)	1.3934(16)
C(6)-C(2)	1.5133(18)	1.520(3)	1.500(2)	1.4981(15)
S(1)-O(4)			1.5181(12)	1.5192(9)
S(1)-C(8)			1.778(2)	1.7823(15)
S(1)-C(7)			1.7826(19)	1.7757(14)
Bond Angles/degrees				
C(1)-N(1)-C(5)	122.90(12)	123.8(2)	119.4(12)	119.29(10)
N(1)-C(1)-C(2)	119.42(13)	118.7(3)	121.89(14)	121.94(11)
N(1)-C(5)-C(4)	120.14(12)	119.9(2)	122.73(14)	122.43(10)
O(1)-C(4)-C(5)	117.95(12)	117.8(2)	117.56(14)	117.38(10)
O(1)-C(4)-C(3)	124.18(12)	124.2(2)	124.29(14)	124.27(11)
O(2)-C(6)-O(3)	125.60(12)	125.9(2)	124.81(14)	124.72(10)
O(2)-C(6)-C(2)	118.74(12)	118.4(2)	113.43(13)	113.64(10)
O(3)-C(6)-C(2)	115.65(11)	115.7(2)	121.75(14)	121.63(10)
C(1)-C(2)-C(6)	118.56(12)	118.3(2)	118.63(14)	118.84(10)
C(1)-C(2)-C(3)	119.53(12)	119.5(2)	119.25(14)	119.15(10)
C(2)-C(3)-C(4)	120.14(12)	120.1(2)	118.86(14)	118.81(10)
C(3)-C(2)-C(6)	121.88(12)	122.2(2)	122.12(13)	122.01(10)
C(5)-C(4)-C(3)	117.86(13)	117.9(2)	118.16(15)	118.36(11)
O(4)-S(1)-C(8)			105.50(9)	105.53(6)
O(4)-S(1)-C(7)			105.53(9)	105.56(6)
C(8)-S(1)-C(7)			98.19(11)	98.23(8)

Table 7.3 Hydrogen bond distances and angles for the hydrate (5HNA·H_2O) and DMSO solvate (5HNA·DMSO) (D = donor; A = acceptor).

	H···A	D···A	D–H···A
	Hydrate (150 K)		
N(1)–H(1N)···O(1W)	1.71	2.6922	174
O1–H10···O3	1.57	2.5206	179
O1W–H1W···O2	1.89	2.7152	163
O1W–H2W···O2	1.87	2.7817	174
C1–H1···O1W	2.58	3.4564	161
C3–H3···O3	2.53	3.1716	126
	Hydrate (300 K)		
N(1)–H(1N)···O(1W)	1.63	2.7130	167
O1–H10···O3	1.40	2.5198	173
O1W–H1W···O2	1.90	2.7140	148
O1W–H2W···O2	1.87	2.8078	154
C1–H1···O1W	2.49	3.4564	163
C3–H3···O3	2.50	3.1716	126
C5–H5···O1	2.51	3.4646	150
	DMSO solvate (150 K)		
O(1)–H(10)···S(1)	2.84	3.5491	148
O(1) –H(10)···O(4)	1.81	2.6148	177
O(2)–H(20)···N(1)	1.63	2.5943	173
C(5)–H(5)···O(3)	2.58	3.2590	129
C(7)–H(7C)···O(3)	2.44	3.2512	146
C(8)–H(8A)···O(4)	2.55	3.4719	162
C(8)–H(8C)···O(3)	2.58	3.3579	139
C(8)–H(8C)···O(2)	2.57	3.3045	134
	DMSO solvate (293 K)		
O(1)–H(10)···S(1)	2.83	3.5470	148
O(1) –H(10)···O(4)	1.81	2.6123	175
O(2)–H(20)···N(1)	1.59	2.5923	174
C(5)–H(5)···O(3)	2.56	3.2524	129
C(7)–H(7C)···O(3)	2.43	3. 2490	144
C(8)–H(8A)···O(4)	2.51	3.4691	162
C(8)–H(8C)···O(3)	2.60	3. 3076	133
C(8)–H(8C)···O(2)	2.59	3.3602	144

In the 5HNA·H_2O the water molecules are isolated from one another (isolated site hydrate). Each water molecule takes part in three hydrogen bonds involving three 5HNA molecules (Figure 7.3): two different hydrogen bonds as donor to one of the oxygens of the carboxylic group ($d_{O1WH\cdots O2}$ = 1.87 Å and $d_{O1WH\cdots O2}$ = 1.89 Å), and one as acceptor from the N-H group ($d_{N1H\cdots O1W}$ = 1.71 Å).

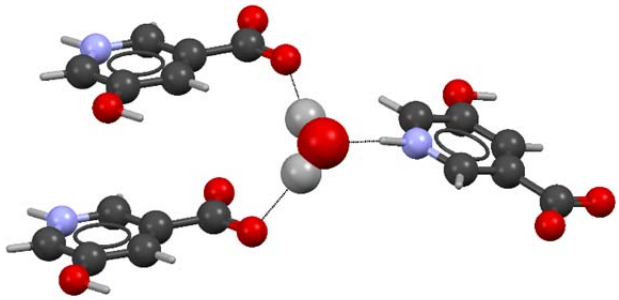

Figure 7.3 Local structure of 5HNA molecules around a water molecule in 5HNA·H_2O.

The structure of 5HNA·H_2O is very similar to that of the 4HNA hydrate H-II (monoclinic, $P2_1/c$) which is different from the 4HNA hemi hydrate H-I (orthorhombic, $P2_12_12$) studied in chapter 6 of this thesis.[25] Both 5HNA·H_2O and the 4HNA hydrate H-II, have a zwitterionic molecular conformation and the hydroxynicotinic acid molecule forms three hydrogen bonds with the water molecule with similar values namely: 2.692 Å vs. 2.68 Å in the case of N(1)–H(N)···O(W); 2.71 Å vs 2.74 Å and 2.78 Å vs 2.83 Å for the two O(W)–H(W)···Ocarboxylic bonds (5HNA vs 4HNA).

As shown in Figure 7.4, the 5HNA molecule in 5HNA·H_2O, forms non-linear $C_1^1(7)$ chains between adjacent 5HNA molecules along the (102) plane, through a O-H···$O_{carboxylic}$ hydrogen bond ($d_{O1H\cdots O3}$ = 1.57 Å), which is also sustained by a non-classical hydrogen bond C3-H···O3 ($d_{C3H\cdots O3}$ = 2.53 Å). The non linearity of these chains is reflected by the ~21° angle between the planes sustaining two adjacent 5HNA molecules.

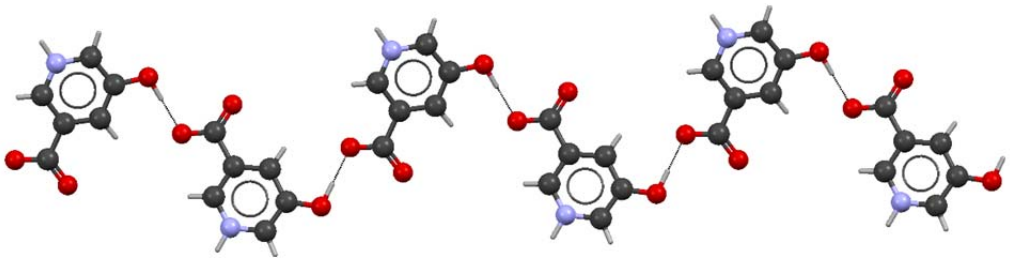

Figure 7.4 The non-linear $C_1^1(7)$ chains of adjacent 5HNA molecules along the (102) plane in 5HNA·H_2O.

In the case of the DMSO solvate, the packing shows an infinite $C_1^1(6)$ linear chain along the (102) plane, like in the hydrate form. This chain is supported by $O_{carboxylic}$-H···N ($d_{O2H\cdots N1}$ = 1.63 Å) hydrogen bonds (Figure 7.5). The solvent molecule links to the 5HNA unit through a $D_1^1(2)$ motif (Figure 7.6). This motif grows along the *b* axis via nonclassical hydrogen bonds, namely C5-H···O3 ($d_{C5H\cdots O3}$ = 2.58 Å), C7-H···O3 ($d_{C7H\cdots O3}$ = 2.44 Å), C8-H···O4 ($d_{C8H\cdots O4}$ = 2.55 Å) and C8-H···O2 ($d_{C8H\cdots O2}$ = 2.57 Å). The 3D packing is finally completed by linking adjacent 2D frameworks of this type through another nonclassical hydrogen bond C8-H···O3 ($d_{C8H\cdots O3}$ = 2.58 Å).

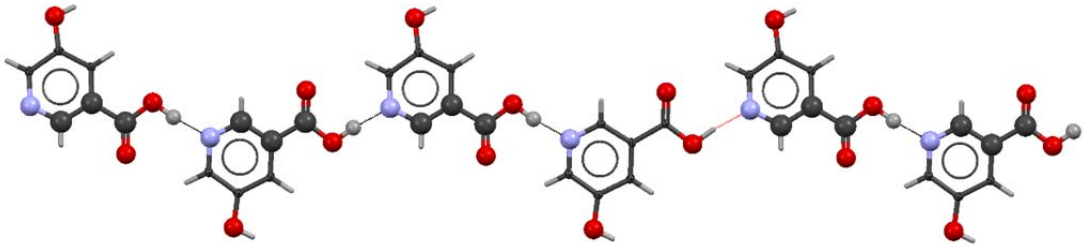

Figure 7.5 The non-linear $C_1^1(6)$ chains of adjacent 5HNA molecules along the (102) plane in 5HNA·DMSO.

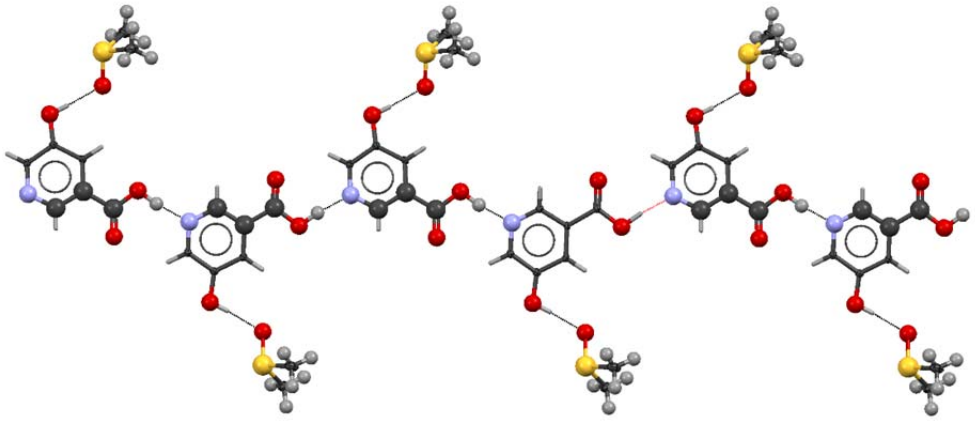

Figure 7.6 The attachment of DMSO molecules to 5HNA through a $D_1^1(2)$ motif.

Finally the comparison of powder diffraction pattern of 5HNA·H_2O and 5HNA·DMSO with the powder pattern simulated from the respective single crystal data (obtained for ~ 298 K) indicated that they correspond to the same phase characterized by single crystal X-ray diffraction. The obtained powder pattern for 5HNA·H_2O was indexed as space group $P2_1/c$ with a = 4.506(4) Å, b = 16.462(9) Å, c = 9.061(6) Å, and β = 90.24(3)°. Similarly for 5HNA·DMSO the powder pattern was indexed as $P2_1/c$ with a = 5.221(9) Å, b = 22.529 (24) Å, and c = 8.418(11) Å and β = 90.20(0)° (see Supporting Information). The results are in agreement with the results in Table 7.1.

7.3.2 Thermal analysis of dehydration and desolvation process.

Figure 7.7a shows an overlay of typical TGA and DSC curves obtained for 5HNA·H_2O in the temperature range of the dehydration process. The TGA results indicated that the dehydration reaction involves a single step with onset at T_i = 370.2±2.7 K and end at T_f = 387.5±3.4 K. The H_2O/5HNA molar ratio calculated for the 5HNA·H_2O was n =0.96±0.01.This value is compatible with the stoichiometry (n = 1) determined for

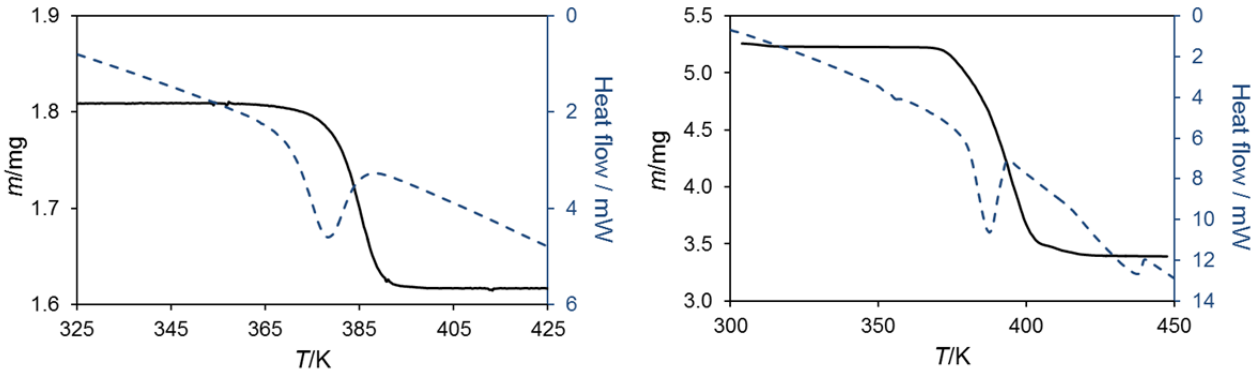

Figure 7.7 TGA (solid line) and DSC (dashed line) curves obtained at β = 5 K·min^{-1} for (a) the dehydration of 5HNA·H_2O and (b) the desolvation of 5HNA·DMSO.

5HNA·H_2O by SC-XRD. The uncertainties assigned to T_i, T_f and n correspond to twice the standard error of the mean of ten determinations.

The TGA analysis of 5HNA·DMSO showed the onset of desolvation at T_i = 389.7±1.2 K and end at T_f = 410.6±0.7 K (Figure 7.7b). As can be seen in the TGA/DSC overlay the desolvation process is composed of two steps. The DMSO/5HNA molar ratio calculated for the solvate was n = 1.01±0.02 which is in excellent agreement with the conclusion of SC-XRD analysis. The uncertainties assigned to T_i, T_f and n were calculated as for 5HNA·H_2O.

The dehydrated and desolvated products obtained from TGA analysis of 5HNA·H_2O and 5HNA·DMSO respectively, were analyzed by powder X-ray diffraction within 24 hrs of the TGA experiments. As can be seen in Figure 7.8, the corresponding powder patterns did not match that of the starting material (the original 5HNA sample), indicating that they correspond to different phases. However comparing the dehydrated and desolvated phases (after ~ 24 hrs), it can be said that they are not very different except that the dehydrated product seems more amorphous than desolvated product. A new PXRD analysis carried out on the same samples after five months indicated that the dehydrated and desolvated materials had fully transformed to the same phase as the starting material (Figure 7.8).

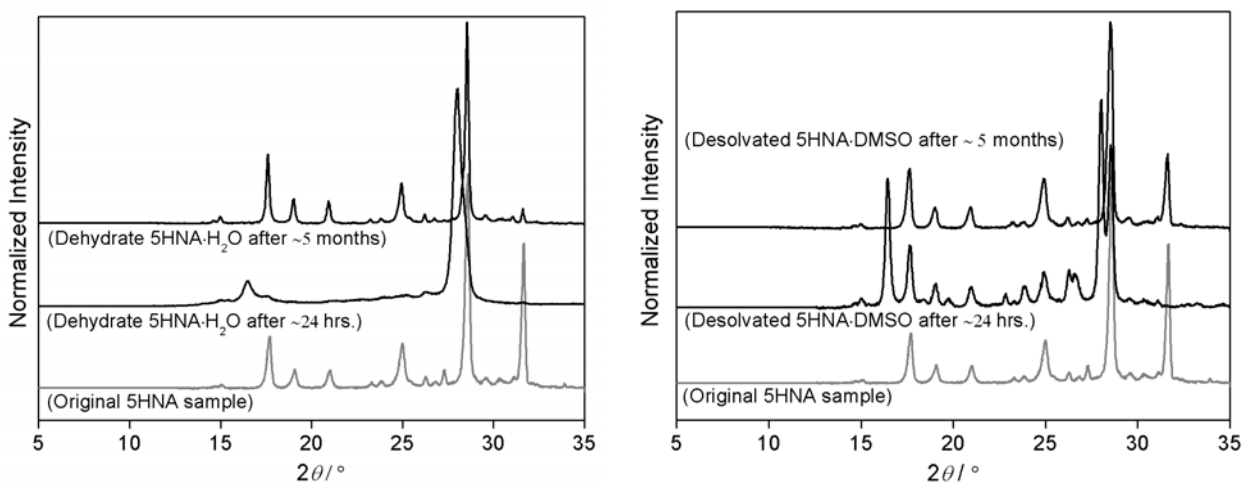

Figure 7.8 Comparison of the powder diffraction patterns of the original 5HNA sample with those obtained for the products of TGA analysis after ~ 24 hours and after ~ 5 months (same sample) of (a) dehydrated 5HNA·H_2O and (b) desolvated 5HNA·DMSO.

7.3.2.1 Thermodynamics of dehydration and desolvation process.

As illustrated in Figure 7.9a, in addition to dehydration peak (I), no other peaks except that corresponding to fusion (II) was detected in the DSC curve obtained for 5HNA·H_2O in the temperature range 300-600 K. The fusion of dehydrated 5HNA (peak II) occurs at T_{max} = 577.7 K and is followed by thermal decomposition, which was also observed in the TGA analysis of 5HNA sample (Figure 7.9c). It should be noted that fusion of the 5HNA starting material occurs at a significantly lower temperature (T_{max} = 563.3 K), a result which probably reflects the considerably lower purity of starting material (93%), when compared to that of the dehydrated material (99.03%) (see section 7.3.3 on purity analysis by LC-MS).

Dehydration (peak I) occurred at T_i = 369.9±2.0 K, T_{max} = 378.6±0.5 K and T_f = 384.7±1.2 K. The corresponding enthalpy was $\Delta_r H_m^o(\text{exp})$ = 55.9±1.8 kJ·mol^{-1}. The onset temperature of the dehydration process (T_i) measured by DSC is in agreement with that obtained in the TGA experiments (Figure 7.7a).

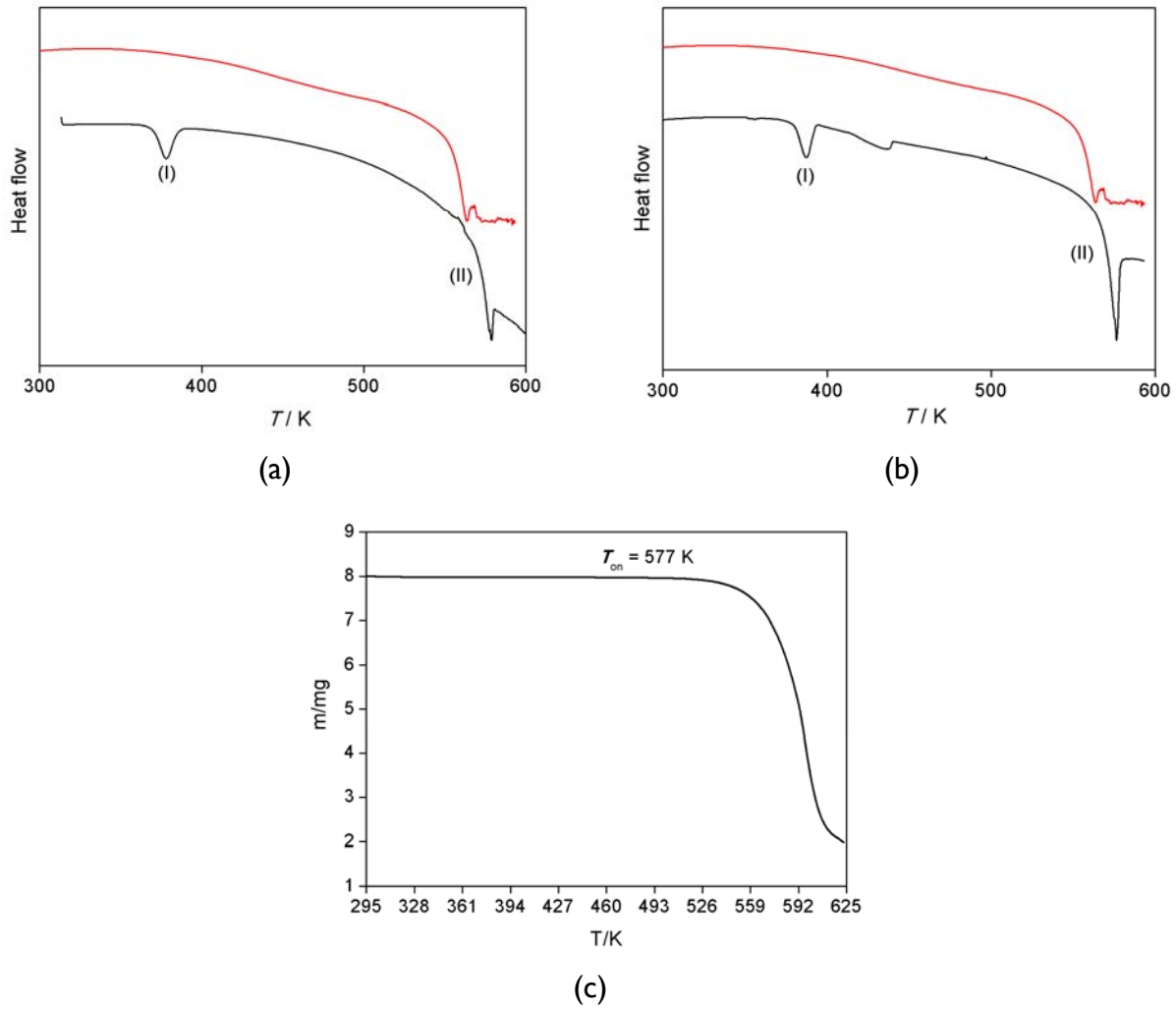

Figure 7.9 DSC measuring curve obtained at β = 5 K·min^{-1} for (a) 5HNA·H_2O and (b) 5HNA·DMSO. The DSC measuring curve of original 5HNA sample is represented in red line. (c) Observation of 5HNA decomposition in the TGA curve obtained on a desolvated 5HNA·DMSO sample.

The dehydration reaction was also investigated by Calvet microcalorimetry. In this case, T_i = 298.1±0.1 K, T_f = 361.7±0.2 K and $\Delta_r H_m^\circ$(exp) = 63.9±1.4 kJ·mol^{-1}. The uncertainties indicated for T_i, T_{max}, T_f and $\Delta_r H_m^\circ$(exp) in the case of DSC and Calvet microcalorimetry experiments, are twice the standard error of the mean of five determinations.

In the DSC curve of 5HNA·DMSO (Figure 7.9b), the desolvation process (peak I) is followed by fusion of 5HNA (peak II). Thermal decomposition was also observed in this case. The fusion of 5HNA occurs at T_{max} = 579.4 K. Analogously to the fusion of 5HNA after dehydration, the 5HNA fusion peak after desolvation is also sharper and occurs at higher temperature than for the original 5HNA sample. This can also be attributed to the increase in purity of 5HNA after the desolvation process (see section 7.3.3 on purity analysis by LC-MS). The fusion temperature of 5HNA obtained after desolvation is higher than that obtained after dehydration reflecting an even higher purity.

The fusion process was accompanied by sample decomposition, which led to the sample overflow from the crucible. Thus all DSC experiments were stopped before fusion in order to prevent cell damage.

The DSC profile of 5HNA·DMSO desolvation (Peak I in Figure 7.9b) is composed of two peaks (Figure 7.10) corresponding to a two-step process as also evidenced by the TGA analysis (Figure 7.7b): peak (i) with T_i = 389.4±3.1 K, T_{max} = 394.9±2.8 K, T_f = 399.8±1.4 K and peak (ii) with T_i = 403.7±4.7 K, T_{max} = 441.8±4.3 K, T_f = 459.6±9.6 K. It was not possible to obtain reliable enthalpy of desolvation from the DSC curves since there was considerable shift in the baseline. Thus the overall enthalpy associated with the desolvation process was obtained only by Calvet microcalorimetry. This led to $\Delta_r H_m^\circ(\text{exp})$ = 100.3±2.8 kJ·mol^{-1} for T_i = 297.96±0.04 K and T_f = 361.42±0.05 K. The uncertainties indicated for T_i, T_{max}, and T_f for both DSC and Calvet-microcalorimetry are twice the standard errors of the mean of five determinations. The uncertainty assigned to $\Delta_r H_m^\circ(\text{exp})$ obtained from Calvet is twice the overall standard error of the mean including the contribution from the calibration.

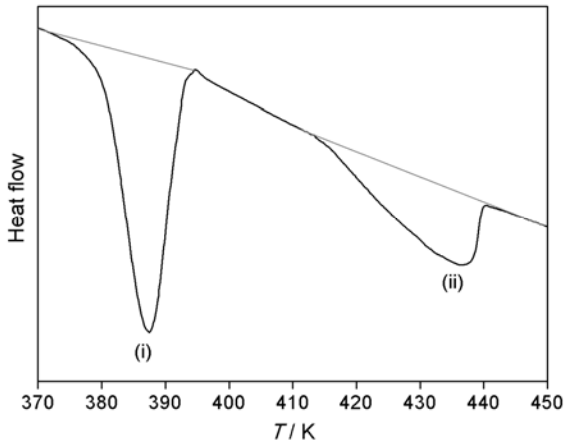

Figure 7.10 DSC profile of desolvation process in the temperature range 370-450 K.

The dehydration and desolvation reactions observed by DSC and Calvet-microcalorimetry refer to eq. 7.3 in Scheme 2, where S represents water or DMSO.

Scheme 2

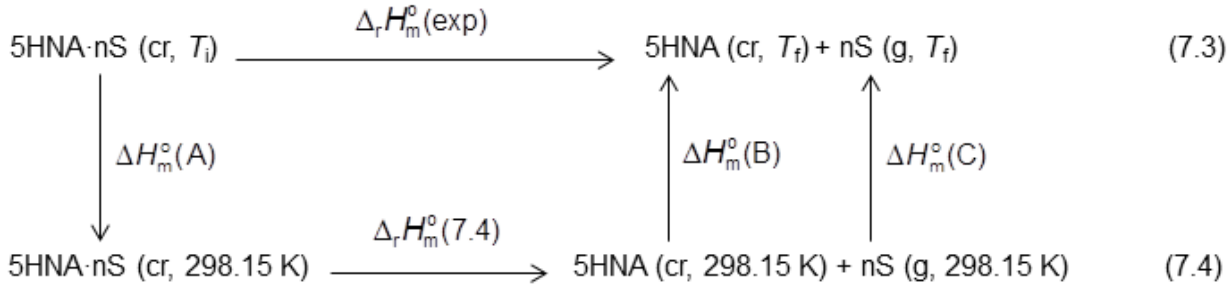

According to Scheme 2, the corresponding enthalpy under isothermal conditions at 298.15 K, $\Delta_r H_m^\circ(7.4)$, is related to the experimentally determined value, $\Delta_r H_m^\circ(\text{exp})$, by:

$$\Delta_r H_m^\circ(7.4) = \Delta_r H_m^\circ(\text{exp}) - \Delta H_m^\circ(\text{A}) - \Delta H_m^\circ(\text{B}) - \text{n}\Delta H_m^\circ(\text{C}) \tag{7.5}$$

$$= \Delta_r H_m^\circ(\text{exp}) + \int_{298.15\ \text{K}}^{T_i} C_{p,m}^\circ(5\text{HNA}\cdot\text{nS, cr})\text{d}T$$

$$+ \int_{T_f}^{298.15\text{K}} C_{p,m}^\circ(5\text{HNA, cr})\text{d}T + \text{n}\int_{T_f}^{298.15\text{K}} C_{p,m}^\circ(\text{S, g})\text{d}T \tag{7.6}$$

For $5\text{HNA}\cdot\text{H}_2\text{O}$, the standard molar heat capacities in eq. 7.6 are given by ($C_{p,m}^\circ$ in $\text{J}\cdot\text{K}^{-1}\cdot\text{mol}^{-1}$ and T in K):

$$C_{p,m}^\circ(\text{H}_2\text{O, g}) = 1.8177\times10^{-5}\ T^2\text{-}6.4164\times10^{-3}T\text{+}33.898 \tag{7.7}$$

$$C_{p,m}^\circ(5\text{HNA, cr}) = 0.43400T\text{+}23.501 \tag{7.8}$$

$$C_{p,m}^\circ(5\text{HNA}\cdot\text{H}_2\text{O, cr}) = 0.56583T\ \text{+}25.3795 \tag{7.9}$$

Equations 7.7[51] and 7.8[33] are valid for the temperature ranges 200-400 K and 288-474 K, respectively. Equation 7.9 can be derived by assuming that $C_{p,m}^\circ(5\text{HNA}\cdot\text{H}_2\text{O, cr}) = C_{p,m}^\circ(5\text{HNA, cr}) + C_{p,m}^\circ(\text{H}_2\text{O, cr})$ and using $C_{p,m}^\circ(5\text{HNA, cr})$ given by eq. 7.10 and $C_{p,m}^\circ(\text{H}_2\text{O, cr})$ given by:[34]

$$C^{\circ}_{p,m}(H_2O, cr) = 0.13183T+1.8785 \quad (7.10)$$

Conversion of $\Delta_r H^{\circ}_m(\exp)$ to the corresponding enthalpy under isothermal conditions at 298.15 K by using eqs 7.6-7.9 led to $\Delta_r H^{\circ}_m(7.4)$ = 53.5±1.8 kJ·mol^{-1} using the DSC results and $\Delta_r H^{\circ}_m(7.4)$ = 51.1±1.4 kJ·mol^{-1} using the Calvet microcalorimetry results. Both values are in excellent agreement within their combined uncertainty intervals. Note that the obtained enthalpy of dehydration of 5HNA·H_2O is not far from twice the enthalpy of dehydration of the hemihydrate 4HNA·0.5H_2O for which $\Delta_r H^{\circ}_m$ = 22.0±0.6 kJ·mol^{-1}.[34] This is not unexpected since the H_2O/4HNA molar ratio for 4HNA·0.5H_2O is half the H_2O/5HNA molar ratio of 5HNA·DMSO.

Similarly for 5HNA·DMSO, the standard molar heat capacities in eq. 7.6 are given by ($C^{\circ}_{p,m}$ in J·K^{-1}·mol^{-1} and T in K):

$$C^{\circ}_{p,m}(DMSO, g) = -1.1399\times10^{-4}\,T^2+2.5105\times10^{-1}T+24.800 \quad (7.11)$$

$$C^{\circ}_{p,m}(5HNA\cdot DMSO, cr) = 0.74489T +49.636 \quad (7.12)$$

Equation 7.11 was obtained from a least square fit to published, $C^{\circ}_{p,m}(DMSO, g)$ data in the temperature range 200-500 K.[52] Equation 7.12 was derived based on the approximation $C^{\circ}_{p,m}(5HNA\cdot DMSO, cr) = C^{\circ}_{p,m}(5HNA, cr) + C^{\circ}_{p,m}(DMSO, cr)$ by using $C^{\circ}_{p,m}(5HNA, cr)$ given by eq. 7.8 and $C^{\circ}_{p,m}(DMSO, cr)$ given by:

$$C^{\circ}_{p,m}(\text{DMSO, cr}) = 0.31089T+26.135 \qquad (7.13)$$

Equation 7.13 was obtained by a least square fit to reported $C^{\circ}_{p,m}$(DMSO, cr) results in the range 150-220 K[53] and was assumed to hold for metastable solid DMSO above 220 K.

Conversion of $\Delta_r H^{\circ}_m$(exp) obtained for by Calvet microcalorimetry to isothermal conditions, at 298.15 K, by using eqs 7.6, 7.8 and 7.11-7.12 led to $\Delta_r H^{\circ}_m(7.4)$ = 83.7±2.8 kJ·mol^{-1}.

From the $\Delta_r H^{\circ}_m(7.4)$ values indicated above it was possible to derive the enthalpies of formation of 5HNA·H_2O and 5HNA·DMSO at 298.15 K as $\Delta_f H^{\circ}_m(5\text{HNA}\cdot H_2O, \text{cr})$ = -830.5±4.9 kJ·mol^{-1} and $\Delta_f H^{\circ}_m(5\text{HNA}\cdot\text{DMSO, cr})$ = -771.8±5.7 kJ·mol^{-1} by using equation:

$$\Delta_f H^{\circ}_m(5\text{HNA}\cdot n\text{S, cr}) = \Delta_f H^{\circ}_m(5\text{HNA, cr}) + n\Delta_f H^{\circ}_m(\text{S, g}) - \Delta_r H^{\circ}_m(7.4) \qquad (7.14)$$

where $\Delta_f H^{\circ}_m$(5HNA, cr) = -537.6±4.7 kJ·mol^{-1},[33] $\Delta_f H^{\circ}_m(H_2O, \text{g})$ = -241.83±0.03 kJ·mol^{-1} [54] and $\Delta_f H^{\circ}_m$(DMSO, g) = -150.5±1.5 kJ·mol^{-1} [55].

The obtained $\Delta_r H^{\circ}_m(7.4)$ data allow also the evaluation of the lattice enthalpies of 5HNA·H_2O and 5HNA·DMSO, at 298.15 K, as measured by the enthalpy of reaction,

$$5\text{HNA}\cdot n\text{S(cr)} = 5\text{HNA(g)} + n\text{S(g)} \qquad (7.15)$$

which can be derived from:

$$\Delta_{lat}H^{o}_{m}(5HNA \cdot nS, cr) = \Delta_{r}H^{o}_{m}(7.4) + \Delta_{sub}H^{o}_{m}(5HNA) \quad (7.16)$$

using $\Delta_{sub}H^{o}_{m}(5HNA) = 149.8\pm7.1$ kJ·mol^{-1}.[33] It is, therefore, possible to conclude that $\Delta_{lat}H^{o}_{m}(5HNA \cdot H_2O, cr) = 200.9\pm7.2$ kJ·mol^{-1} and $\Delta_{lat}H^{o}_{m}(5HNA \cdot DMSO, cr) = 233.5\pm7.6$ kJ·mol^{-1}. These lattice energies are approximately additive, since they are comparable to the sum of the enthalpies of sublimation of the hydrate/solvate precursors, namely, $\Delta_{sub}H^{o}_{m}(5HNA) + \Delta_{sub}H^{o}_{m}(H_2O) = 200.7\pm7.1$ kJ·mol^{-1} and $\Delta_{sub}H^{o}_{m}(5HNA) + \Delta_{sub}H^{o}_{m}(DMSO) = 217.0\pm7.1$ kJ·mol^{-1}. The additive calculations were based on the enthalpy of sublimation of 5HNA mentioned above and on $\Delta_{sub}H^{o}_{m}(H_2O) = 50.90\pm0.02$ kJ·mol^{-1} [34] and $\Delta_{sub}H^{o}_{m}(DMSO) = 67.20\pm0.04$ kJ·mol^{-1} at 298 K. The latter value was derived from:

$$\Delta_{sub}H^{o}_{m}(DMSO) = \Delta_{sub}H^{o}_{m}(DMSO, 282.2\ K) + \int_{282.2\ K}^{298.15\ K} \Delta C^{o}_{p,m}(DMSO, g)dT \quad (7.17)$$

where $\Delta_{sub}H^{o}_{m}(DMSO, 282.2\ K) = 67.65$ kJ·mol^{-1} is the enthalpy of sublimation of DMSO at 282.2 K obtained by fitting Clausius-Clapeyron equation to reported vapor pressure vs. temperature data for crystalline DMSO in the temperature range 273-290 K.[52]

The enthalpy of desolvation of 5HNA·DMSO (83.7±2.8 kJ·mol^{-1}) was found to be higher than the enthalpy of dehydration of 5HNA·H_2O (53.5±1.8 kJ·mol^{-1}) at 298.15 K. This is an interesting result given the fact that desolvation of 5HNA·DMSO involves breaking only one hydrogen bond, while three hydrogen bonds must be cleaved to release H_2O from 5HNA·H_2O. Furthermore, the crystal lattice of 5HNA·H_2O is more closely packed when compared to that

of 5HNA·DMSO. It can therefore be concluded that the larger enthalpy of desolvation observed for 5HNA·DMSO relative to 5HNA·H_2O is necessarily due to stronger van der Walls interactions.

7.3.3 Liquid Chromatography, with Diode Array Detection and Electrospray Ionisation Mass Spectrometry (LC-DAD-ESI/MS) analysis

The dehydrated and desolvated samples obtained from 5HNA·H_2O and 5HNA·DMSO, respectively, and the 5HNA starting material from Activate Scientific were analyzed for chemical purity by LC-MS. The results are given in Table 7.4 where R_t is the retention time and *A* represents the peak area corresponding to a given molar percentage.

Table 7.4 LC-MS analysis of original 5HNA sample and that obtained after dehydration and desolvation.

5HNA (Activate Scientific, GmbH)		
R_t/min	*A*	Molar %
1.92	7226497	93.67
2.23	444819	5.77
3.06	12462	0.16
3.31	30878	0.40
Desolvated 5HNA·DMSO		
R_t/min	*A*	Molar %
1.92	37552783	99.95
2.23		
3.06		
3.31	18986	0.05
Dehydrated 5HNA·H_2O		
R_t/min	*A*	Molar %
1.92	23472428	99.03
2.23	198625	0.84
3.06	6589	0.03
3.31	23893	0.10

The peaks detected at R_t = 2.23 min for the original 5HNA sample and the dehydrated material are probably due to a tautomeric form of 5HNA since in the mass spectra a peak corresponding to 5HNA, *m*/*z* 138 (-)ESI or *m*/*z* 140 (+) ESI was only detected for this R_t fraction. This "impurity" seems to be eliminated in the desolvated 5HNA·DMSO sample and significantly reduced in dehydrated 5HNA·H_2O sample. The small contaminants at R_t = 3.06 and R_t = 3.31 min were not identified in the mass spectra.

Table 7.4 shows that the purity of 5HNA increases from 93.67% to 99.95% when the starting material is transformed into 5HNA·DMSO which is then desolvated. A slightly less pure sample (99.03%) is produced through the analogous 5HNA·H_2O hydrate pathway. It can therefore be concluded that highly pure 5HNA can be produced through solvate formation/desolvation.

Supporting information

Speciation of Aqueous 5-Hydroxynicotinic acid at 295K for Different pH. 5-Hydroxynicotinic acid is an amphiprotic system where four differently charged species may be present in equilibrium (Scheme S1). Their molar fractions $x_{(5HNA)^+}$, $x_{(5HNA)^0}$, $x_{(5HNA)^-}$ and $x_{(5HNA)^{2-}}$ at a given pH, can be approximately predicted from the corresponding acidity constants at 295 K, pK_{a1} = 1.90±0.5, pK_{a2} = 4.66±0.05, pK_{a3} = 8.62±0.04 [56] by using:[57]

$$x_{(5HNA)^+} = \frac{[H^+]^3}{\alpha} \quad \text{(S1)}$$

$$x_{(5HNA)^0} = \frac{K_{a1}[H^+]^2}{\alpha} \quad \text{(S2)}$$

$$x_{(5HNA)^-} = \frac{K_{a1}K_{a2}[H^+]}{\alpha} \quad \text{(S3)}$$

$$x_{(5HNA)^{2-}} = 1 - x_{(5HNA)^+} - x_{(5HNA)^0} - x_{(5HNA)^-} \quad \text{(S5)}$$

$$\alpha = [H^+]^3 + K_{a1}[H^+]^2 + K_{a1}K_{a2}[H^+]^3 + K_{a1}K_{a2}K_{a3} \quad \text{(S6)}$$

The obtained results are shown in Figure S1 and summarized in Table S1 where the data in boldface font correspond to the pH obtained in this work for a saturated 5HNA solution at 295 K.

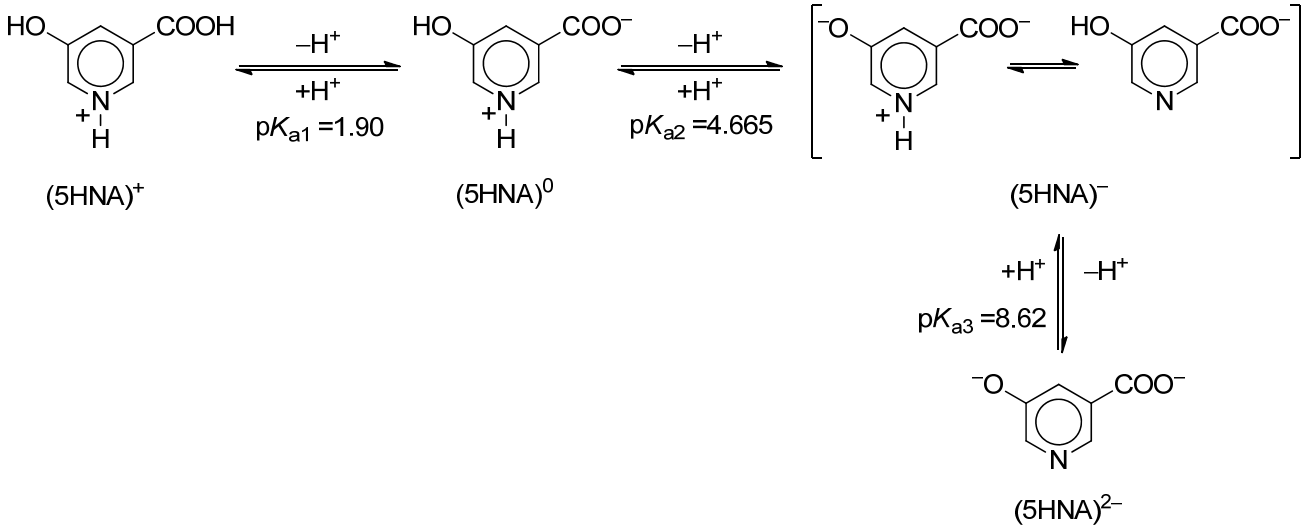

Scheme S1

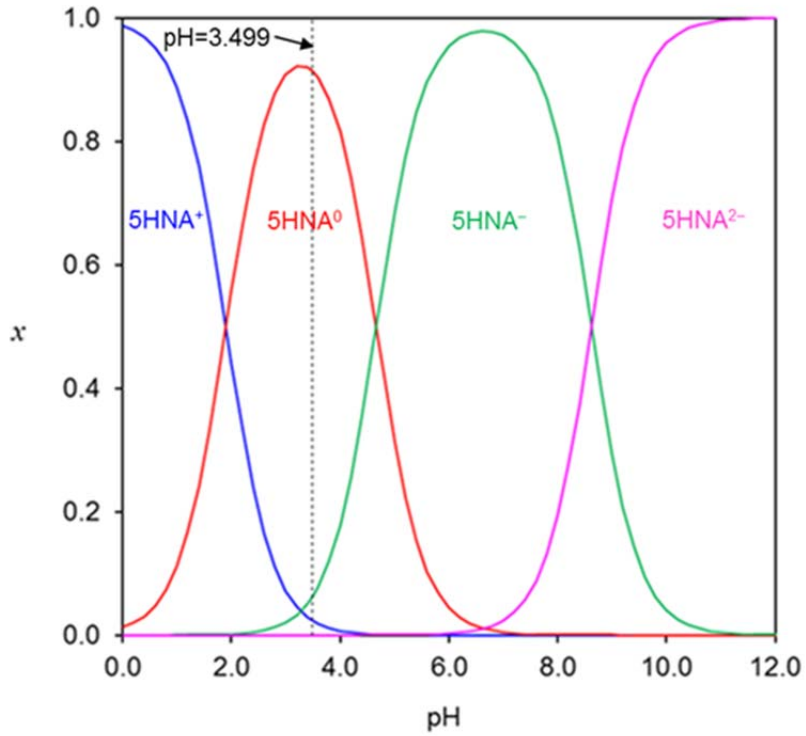

Figure S1 Molar fractions of the 5-Hydroxynicotinic acid species present in aqueous solution for different pHs, at 295 K

Table S1 Molar Fractions of the 5-Hydroxynicotinic Acid Species Present in Aqueous Solution for Different pHs, at 295 K

pH	$x_{(5HNA)^+}$	$x_{(5HNA)^0}$	$x_{(5HNA)^-}$	$x_{(5HNA)^{2-}}$
0.0	0.9876	0.0124	0.0000	0.0000
0.2	0.9804	0.0196	0.0000	0.0000
0.4	0.9693	0.0307	0.0000	0.0000
0.6	0.9523	0.0477	0.0000	0.0000
0.8	0.9264	0.0736	0.0000	0.0000
1.0	0.8882	0.1118	0.0000	0.0000
1.2	0.8336	0.1663	0.0001	0.0000
1.4	0.7596	0.2402	0.0001	0.0001
1.6	0.6659	0.3338	0.0003	0.0000
1.8	0.5570	0.4424	0.0006	0.0000
2.0	0.4421	0.5566	0.0012	0.0001
2.2	0.3331	0.6646	0.0023	0.0000
2.4	0.2393	0.7566	0.0042	-0.0001
2.6	0.1651	0.8277	0.0072	0.0000
2.8	0.1105	0.8774	0.0121	0.0000
3.0	0.0721	0.9080	0.0199	0.0000
3.2	0.0462	0.9218	0.0320	0.0000
3.4	0.0291	0.9203	0.0506	0.0000
3.499	**0.0230**	**0.9139**	**0.0631**	**0.0000**
3.6	0.0180	0.9033	0.0787	0.0000
3.8	0.0109	0.8691	0.1200	0.0000
4.0	0.0065	0.8152	0.1783	0.0000
4.2	0.0037	0.7398	0.2565	0.0000
4.4	0.0020	0.6440	0.3539	0.0001
4.6	0.0011	0.5339	0.4650	0.0000
4.8	0.0005	0.4198	0.5795	0.0002
5.0	0.0002	0.3136	0.6860	0.0002
5.2	0.0001	0.2238	0.7758	0.0003
5.4	0.0000	0.1539	0.8456	0.0005
5.6	0.0000	0.1029	0.8962	0.0009
5.8	0.0000	0.0675	0.9311	0.0014
6.0	0.0000	0.0436	0.9541	0.0023
6.2	0.0000	0.0279	0.9684	0.0037

Continued….

pH	$x_{(5HNA)^+}$	$x_{(5HNA)^0}$	$x_{(5HNA)^-}$	$x_{(5HNA)^{2-}}$
6.4	0.0000	0.0178	0.9763	0.0059
6.6	0.0000	0.0112	0.9794	0.0094
6.8	0.0000	0.0071	0.9781	0.0148
7.0	0.0000	0.0044	0.9722	0.0234
7.2	0.0000	0.0028	0.9607	0.0365
7.4	0.0000	0.0017	0.9416	0.0567
7.6	0.0000	0.0010	0.9119	0.0871
7.8	0.0000	0.0006	0.8680	0.1314
8.0	0.0000	0.0004	0.8062	0.1934
8.2	0.0000	0.0002	0.7244	0.2754
8.4	0.0000	0.0001	0.6239	0.3760
8.6	0.0000	0.0001	0.5115	0.4884
8.8	0.0000	0.0000	0.3978	0.6022
9.0	0.0000	0.0000	0.2942	0.7058
9.2	0.0000	0.0000	0.2082	0.7918
9.4	0.0000	0.0000	0.1423	0.8577
9.6	0.0000	0.0000	0.0948	0.9052
9.8	0.0000	0.0000	0.0620	0.9380
10.0	0.0000	0.0000	0.0400	0.9600
10.2	0.0000	0.0000	0.0256	0.9744
10.4	0.0000	0.0000	0.0163	0.9837
10.6	0.0000	0.0000	0.0104	0.9896
10.8	0.0000	0.0000	0.0066	0.9934
11.0	0.0000	0.0000	0.0042	0.9958
11.2	0.0000	0.0000	0.0026	0.9974
11.4	0.0000	0.0000	0.0017	0.9983
11.6	0.0000	0.0000	0.0010	0.9990
11.8	0.0000	0.0000	0.0007	0.9993
12.0	0.0000	0.0000	0.0004	0.9996
12.2	0.0000	0.0000	0.0003	0.9997
12.4	0.0000	0.0000	0.0002	0.9998
12.6	0.0000	0.0000	0.0001	0.9999
12.8	0.0000	0.0000	0.0001	0.9999
13.0	0.0000	0.0000	0.0000	1.0000
13.2	0.0000	0.0000	0.0000	1.0000

Continued….

pH	$x_{(5HNA)^+}$	$x_{(5HNA)^0}$	$x_{(5HNA)^-}$	$x_{(5HNA)^{2-}}$
13.4	0.0000	0.0000	0.0000	1.0000
13.6	0.0000	0.0000	0.0000	1.0000
13.8	0.0000	0.0000	0.0000	1.0000
14.0	0.0000	0.0000	0.0000	1.0000

Table S2 Indexation of the X-ray powder diffraction pattern of 5HNA·H_2O recorded at 295±2 K, in the range 5°≤ 2θ ≤ 35°; space group $P2_1/c$; a = 4.506(4) Å, b = 16.462(9) Å, c = 9.061(6) Å and β = 90.24(3)°.

h	*k*	*l*	2θ(obs.)	2θ(calc.)	Diff.
0	2	0	10.760	10.740	0.019
0	1	1	11.140	11.137	0.003
0	2	1	14.475	14.527	-0.052
0	3	1	18.875	18.892	-0.017
0	0	2	19.595	19.578	0.017
0	1	2	20.305	20.314	-0.009
0	4	0	21.570	21.576	-0.006
0	2	2	22.360	22.382	-0.022
1	1	1	22.695	22.709	-0.014
0	4	1	23.640	23.726	-0.086
0	4	1	23.730	23.726	0.004
1	2	1	24.565	24.586	-0.021
0	3	2	25.475	25.475	0.000
1	3	0	25.545	25.560	-0.015
-1	3	1	27.390	27.387	0.003
1	0	2	27.975	27.962	0.013
1	1	2	28.525	28.493	0.032
0	4	2	29.290	29.295	-0.005
-1	2	2	29.940	29.923	0.017
1	2	2	30.025	30.033	-0.008
0	2	3	31.530	31.527	0.003
0	6	0	32.670	32.612	0.059
0	5	2	33.650	33.623	0.027

Table S3 Indexation of the X-ray powder diffraction pattern of 5HNA·DMSO recorded at 295±2 K, in the range 5°≤ 2θ ≤ 35°; space group $P2_1/c$; a = 5.221(9) Å, b = 22.529 (24) Å, c = 8.418(11) Å and β = 90.20(0)°

h	*k*	*l*	2θ(obs.)	2θ(calc.)	Diff.
0	2	0	7.950	7.842	0.108
0	3	1	15.830	15.821	0.009
0	4	1	18.895	18.959	-0.064
-1	1	1	19.825	19.775	0.050
-1	2	1	20.945	20.931	0.0145
0	5	1	22.365	22.376	-0.011
-1	3	1	22.755	22.732	0.0231
1	4	0	23.130	23.247	-0.117
0	6	0	23.710	23.677	0.033
-1	4	1	25.065	25.0477	0.017
0	6	1	25.935	25.975	-0.040
-1	0	2	26.250	26.256	-0.006
-1	1	2	26.535	26.557	-0.022
-1	2	2	27.428	27.440	-0.017
-1	3	2	28.840	28.862	-0.022
-1	4	2	30.720	30.749	-0.029
1	6	1	31.745	31.654	0.091
1	4	2	32.515	32.489	0.026
0	2	3	32.980	32.955	0.025
-1	7	1	34.005	34.025	-0.020

Thermogravimetry (TGA). The results of the determination of the molar fraction *n* of water and DMSO in 5HNA·*n*H_2O and 5HNA·*n*DMSO by TGA at a heating rate β = 5 K·min^{-1} are summarized in Tables S4 and S5. Here, T_i and T_f are the initial and final temperatures of the mass loss step, m_i is the initial mass of sample, and Δm is the observed mass loss. The uncertainties quoted for $<T_i>$, $<T_f>$ and $<n>$represent twice the standard deviation of the mean.

Table S4 Amounts of substance *n* of water in 5HNA·*n*H_2O obtained by TGA

T_i/K	T_f/K	m_i/mg	Δm/mg	*n*
372.5	390.1	3.330704	0.367238	0.96
372.3	390.2	4.744623	0.526373	0.96
370.7	389.3	4.869117	0.541364	0.97
372.3	390.7	4.446754	0.495290	0.97
370.4	388.2	3.856289	0.413084	0.93
375.6	394.2	5.510496	0.614892	0.97
374.8	392.2	4.964419	0.539943	0.94
363.4	380.4	6.477902	0.722817	0.97
364.5	381.4	6.166906	0.678637	0.95
365.4	378.3	6.446660	0.707354	0.95
372.5	390.1	3.330704	0.367238	0.96
372.3	390.2	4.744623	0.526373	0.96

$<T_i>$ = 370.2±2.7 K; $<T_f>$ = 387.5±3.4 K

$<n>$ = 0.96±0.01

Table S5 Amounts of Substance *n* of DMSO in 5HNA·*n*DMSO obtained by TGA

T_i/K	T_f/K	m_i/mg	Δm/mg	*n*
390.6	410.9	6.131532	2.238005	1.02
388.8	410.7	5.558332	2.013057	1.01
389.9	409.6	5.853685	2.111103	1.00
387.9	411.6	6.345128	2.290331	1.01
391.2	410.4	6.937745	2.536834	1.03

$\langle T_i \rangle$ = 389.7±1.2 K; $\langle T_f \rangle$ = 410.6±0.7 K

$\langle n \rangle$ = 1.01±0.02

Differential Scanning Calorimetry (DSC). The results of the DSC study of 5HNA·H_2O and 5HNA·H_2O according to:

$$5HNA \cdot nS(cr, T_i) \rightarrow 5HNA(cr, T_f) + nS(g, T_f) \quad (S7)$$

are shown in Table S6 and S7. Here, *m* is the mass of sample, T_i and T_f are the initial and final temperatures of the dehydration step, respectively, T_{max} is the temperature corresponding to the peak maximum and Δh (eq S7) is the specific enthalpy change. The uncertainties quoted for $\langle T_i \rangle$, $\langle T_f \rangle$, $\langle T_{max} \rangle$, and $\langle \Delta_r h$ (eq S7)$\rangle$ represent twice the standard deviation of the mean.

Table S6 Results of the DSC experiments on 5HNA·H_2O.

m/mg	T_i/K	T_{max}/K	T_f/K	Δh (eq S7)/J·g^{-1}
3.639	368.7	378.9	385.6	362.89
4.295	373.4	379.1	384.7	338.55
4.435	370.9	377.7	382.4	352.49
3.123	368.7	378.8	385.5	353.52
3.140	367.9	378.6	385.4	371.90

$<T_i>$ = 369.9±2.0 K; $<T_{max}>$ = 378.6±0.5 K; $<T_f>$ = 384.7.±1.2 K

$<\Delta_r h$ (eq S7)> = 355.9±11.2 J·g^{-1}

$M(C_6H_5O_3N\cdot H_2O)$ = 148.1164 g.mol^{-1}

$<\Delta_r H_m$ (eq S7)> = 55.9±1.8 kJ·mol^{-1}

Table S7 Results of the DSC experiments on 5HNA·DMSO.

	Peak (i)			Peak (ii)		
m/mg	T_i/K	T_{max}/K	T_f/K	T_i/K	T_{max}/K	T_f/K
6.330	390.7	396.5	400.4	401.3	449.4	477.6
5.589	387.6	393.1	399.7	413.0	440.3	453.1
5.208	384.9	391.0	397.7	400.3	437.8	450.5
6.407	394.3	399.3	401.9	403.0	443.6	460.8
5.891	389.3	394.5	399.5	400.9	438.1	456.1

Peak (i): $<T_i>$ = 389.4±3.1 K; $<T_{max}>$ = 394.9±2.8 K; $<T_f>$ = 399.8.±1.4 K

Peak (ii): $<T_i>$ = 403.7±4.7 K; $<T_{max}>$ = 441.8±4.3 K; $<T_f>$ = 459.6.±9.6 K

Calvet microcalorimetry. The Calvet microcalorimetry study of reaction S7 for 5HNA·nH$_2$O and 5HNA·nDMSO led to the results in Tables S8 and S9. Here m_s and m_c are the masses of sample and of the glass capillary tube, respectively; A is the area of the measuring curve corresponding to the over-all calorimetric experiment; A_b is the area of the pumping background contribution to the calorimetric process, which was determined in a series separate experiments; ε is the energy equivalent of the calorimeter obtained from a set of electrical calibrations; T_f is the temperature of the calorimetric cell; T_i is the initial temperature of the sample before being dropped into the calorimetric cell; The term Δh (eq S7) represents the specific enthalpy of the process in eq S1, and was calculated from:

$$\Delta h(\text{eq S7}) = \frac{1}{m_s}\left[\frac{A - A_b}{\varepsilon} - m_c c_{p,c} \Delta T\right] \qquad \text{(S8)}$$

were $\Delta T = T_f - T_i$ and $c_{p,c}$ = 0.787 J·g^{-1} is the average massic heat capacity of the capillary tube at constant pressure in the ΔT range. The value of $c_{p,c}$ was determined in an independent experiment where empty glass capillaries were dropped into the calorimeter. The results in Tables S8 and S9 lead to Δh(eq S7) = 406.50±3.14 J·g^{-1} for 5HNA·nH$_2$O and Δh(eq S7) = 461.76±6.47 J·g^{-1} for 5HNA·nDMSO where the uncertainty quoted represent standard deviations of the mean. These values correspond to $\Delta_r H^\circ_m$(eq S7) = 63.9±1.4 kJ·mol^{-1} for 5HNA·nH$_2$O and $\Delta_r H^\circ_m$(eq S7) = 100.3±2.8 kJ·mol^{-1} for 5HNA·nDMSO, where the assigned uncertainties correspond to twice the over-all standard error of the mean which includes contributions from the main experiment and the calibration.

Table S8 Results of the Calvet Microcalorimetry Experiments on 5HNA·H_2O.

m_s/mg	m_c/mg	A/mV·s	T_i/K	T_f/K	Δh (eq S7)/J·g^{-1}
5.320	40.190	262.564	297.983	361.485	403.637
5.318	42.005	270.866	298.032	361.486	411.481
5.918	40.580	276.989	298.035	361.845	396.130
5.918	40.145	279.341	298.236	361.801	407.296
6.838	40.542	307.422	298.238	361.801	413.947

A_b = –2.724 mV·s

ε = 63.833±0.07 mV·W^{-1}

$<T_i>$ = 298.10±0.10 K; $<T_f>$ = 361.68±0.16 K

$<\Delta_r h$ (eq S7)> = 406.50±3.14 J·g^{-1}

$\sigma_{over\text{-}all}$ = 3.18 J·g^{-1}

$M(C_6H_5O_3N \cdot H_2O)$ = 157.1241 g.mol^{-1}

$<\Delta_r H_m$ (eq S7)> = 63.9±1.4 kJ·mol^{-1}

Table S9 Results of the Calvet Microcalorimetry Experiments on 5HNA·DMSO.

m_s/mg	m_c/mg	A/mV·s	T_i/K	T_f/K	Δh (eq S7)/J·g^{-1}
8.148	40.577	356.301	297.979	361.361	441.878
9.975	42.018	433.827	297.972	361.377	475.407
9.038	40.594	398.609	298.019	361.392	471.634
8.635	42.012	380.170	297.900	361.476	451.251
9.142	41.543	403.375	297.922	361.472	468.612

A_b = –2.724 mV·s

ε = 63.833±0.07 mV·W^{-1}

$<T_i>$ = 297.96±0.04 K; $<T_f>$ = 361.42±0.05 K

$<\Delta_r h$ (eq S7)> = 461.76±6.47 J·g^{-1}

$\sigma_{over\text{-}all}$ = 6.49 J·g^{-1}

$M(C_6H_5O_3N \cdot C_2H_6OS)$ = 217.2422 g.mol^{-1}

$<\Delta_r H_m$ (eq S7)> = 100.3±2.8 kJ·mol^{-1}

Acknowledgements

This work was supported by the FCT doctoral grant (SFRH/ BD/90386/2012) awarded to A. Joseph.

References

1. Gao, J. L.; Shao, L. *J. Phys. Chem.* **1994**, *98,* 13772-13779.
2. Wojnarowska, Z.; Wlodarczyk, P.; Kaminski, K.; Grzybowska, K.; Hawelek, L.; Paluch, M. *J. Chem. Phys.* **2010**, *133*.
3. Guasch, L.; Peach, M. L.; Nicklaus, M. C. *J Org Chem* **2015,** *80,* 9900-9909.
4. Martin, Y. C. *J. Comput. Aid. Mol. Des.* **2010**, *24,* 473-474.
5. Taylor, P. J.; van der Zwan, G.; Antonov, L. Tautomerism: Introduction, History, and Recent Developments in Experimental and Theoretical Methods, In *Tautomerism: Methods and Theories*; Antonov, L., Ed.; Wiley-VCH:Weinheim 2014.
6. Hunger, K., *Industrial Dyes: Chemistry, Properties, Applications*; Wiley-VCH:Weinheim, 2003.
7. Tian, S. X.; Zhang, C. F.; Zhang, Z. J.; Chen, X. J.; Xu, K. Z. *Chem. Phys.* **1999**, *242,* 217-225.
8. Porter, W. R. *J. Comput. Aid. Mol. Des.* **2010**, *24,* 553-573.
9. Wehrle, B.; Limbach, H. H. *Chem. Phys.* **1989**, *136,* 223-247.
10. Juribasic, M.; Bregovic, N.; Stilinovic, V.; Tomisic, V.; Cindric, M.; Sket, P.; Plavec, J.; Rubcic, M.; Uzarevic, K. *Chem-Eur J.* **2014**, *20,* 17333-17345.
11. Cruz-Cabeza, A. J.; Groom, C. R. *Crystengcomm* **2011**, *13,* 93-98.
12. Aitipamula, S., Polymorphism in Molecular Crystals and Cocrystals. In *Advances in Organic Crystal Chemistry;* Tamura, R.; Miyata M., Eds.; Springer: Japan, 2015.
13. Bhatt, P. M.; Desiraju, G. R. *Chem. Commun.* **2007**, 2057-2059.
14. Blake, A. J.; Lin, X.; Schroder, M.; Wilson, C.; Yuan, R. X. *Acta Crystallogr. C* **2004**, *60,* O226-O228.
15. Tothadi, S.; Bhogala, B. R.; Gorantla, A. R.; Thakur, T. S.; Jetti, R. K. R.; Desiraju, G. R. *Chem. Asian. J.* **2011**, *7,* 330-342
16. Mirmehrabi, M.; Rohani, S.; Murthy, K. S. K.; Radatus, B. *J. Cryst. Growth* **2004**, *260,* 517-526.
17. Chierotti, M. R.; Gobetto, R.; Pellegrino, L.; Milone, L.; Venturello, P. *Cryst. Growth Des.* **2008**, *8,* 1454-1457.
18. Chierotti, M. R.; Ferrero, L.; Garino, N.; Gobetto, R.; Pellegrino, L.; Braga, D.; Grepioni, F.; Maini, L. *Chem-Eur. J.* **2010**, *16,* 4347-4358.
19. Schmidt, M. U.; Bruning, J.; Glinnemann, J.; Hutzler, M. W.; Morschel, P.; Ivashevskaya, S. N.; van de Streek, J.; Braga, D.; Maini, L.; Chierotti, M. R.; Gobetto, R. *Angew. Chem. Int. Edit.* **2011**, *50,* 7924-7926.
20. Bauer, M.; Harris, R. K.; Rao, R. C.; Apperley, D. C.; Rodger, C. A. *J. Chem. Soc. Perk. T. 2* **1998**, 475-481.

21. Bocskei, Z.; Simon, K.; Rao, R.; Caron, A.; Rodger, C. A.; Bauer, M. *Acta. Crystallogr. C* **1998**, *54,* 808-810.
22. Garcia, M. A.; Lopez, C.; Claramunt, R. M.; Kenz, A.; Pierrot, M.; Elguero, J. *Helv. Chim. Acta.* **2002**, *85,* 2763-2776.
23. Desiraju, G. R. *J. Chem. Soc. Perk. T. 2* **1983,** 1025-1030.
24. Schmidt, A.; Kababya, S.; Appel, M.; Khatib, S.; Botoshansky, M.; Eichen, Y. *J. Am. Chem. Soc* .**1999**, *121,* 11291-11299.
25. Long, S., Zhang, M.; Zhou, P.; Yu, F.; Parkin, S; Li, T. *Cryst. Growth Des.* **2016**, 16, 2573-2580.
26. Childs, S. L.; Hardcastle, K. I. *Cryst. Growth Des.* **2007**, *7,* 1291-1304.
27. Wales, C.; Thomas, L. H.; Wilson, C. C. *CrystEngComm* **2012**, *14,* 7264-7274.
28. Epa, K.; Aakeroy, C. B.; Desper, J.; Rayat, S.; Chandra, K. L.; Cruz-Cabeza, A. J. *Chem. Commun.* **2013**, *49,* 7929-7931.
29. Desiraju, G. R. *Angew. Chem. Int. Edit.* **2007**, *46,* 8342-8356.
30. Joseph, A.; Bernardes, C. E. S.; Minas da Piedade, M. E. *J. Chem. Thermodyn.* **2012**, *55,* 23-28.
31. Joseph A.; Bernardes. C. E. S.; Viana A. S.; Piedade M.F.M.; Minas da Piedade M.E. *Cryst. Growth Des.* **2015**, *15,* 3511-3524.
32. Gonçalves, E. M.; Bernardes, C. E. S.; Diogo, H. P.; Minas da Piedade, M. E. *J. Phys. Chem. B* **2010**, *114,* 5475-5485.
33. Santos, R. C.; Figueira, R. M. B. B. M.; Piedade, M. F. M.; Diogo, H. P.; Minas da Piedade, M. E. *J. Phys. Chem. B* **2009,** *113,* 14291-14309.
34. Matias, E. P.; Bernardes, C. E. S.; Piedade, M. F. M.; Minas da Piedade, M. E. *Crys. Growth Des.* **2011**, *11,* 2803-2810.
35. Gonçalves, E. M.; Rego, T. S.; Minas da Piedade, M. E. *J. Chem. Thermodyn.* **2011**, *43,* 974-979.
36. Gonçalves, E. M.; Minas da Piedade, M. E. *J. Chem. Thermodyn.* **2012**, *47,* 362-371.
37. Gonçalves, E. M.; Joseph, A.; Conceição, A. C. L.; Minas da Piedade, M. E. *J. Chem. Eng. Data* **2011**, *56,* 2964-2970.
38. Long, S.; Zhou, P.; Theiss, K. L.; Siegler, M. A.; Li, T. *Crystengcomm* **2015**, *17,* 5195-5205.
39. Gupta, S. L.; Long, S. H.; Li, T. *Acta Crystallogr. E* **2007**, *63,* O2784-U1783.
40. Allen, F. H. *Acta Crystallogr.* **2002,** *B58,* 380-388.
41. Dewick, P. M., *Essentials of Organic Chemsitry*, John Wiley & Sons Ltd.:England, 2006.
42. Laugier, J. B., B. *Cellref V3;* http://www.ccp14.ac.uk/ tutorial/lmgp/cellref.htm.
43. *SADABS; Area-Detector Absorption Correction*, Bruker AXS Inc.: Madison, WI, 2004.
44. *SAINT: Area-Detector Integration Software (version7.23)*, Bruker AXS Inc.: Madison, WI, 2004.
45. Sheldrick, G. M. *Acta Crystallogr A* **2008**, *64,* 112-122.
46. Sheldrick, G. M. *SHELXL-97: Program for the Refinement of Crystal Structure*, University of Gottingen: Gottingen, Germany, 1997.
47. Macrae, C. F.; Edgington, P. R.; McCabe, P.; Pidcock, E.; Shields, G. P.; Taylor, R.; Towler, M.; van De Streek, J. *J. Appl. Crystallogr.* **2006**, *39,* 453-457.
48. Spek, A. L. *Acta Crystallogr. D* **2009**, *65,* 148-155.
49. Kiyobayashi, T.; Minas da Piedade, M. E. *J. Chem. Thermodyn.* **2001**, *33,* 11-21.
50. Bernardes, C. E. S.; Santos, L. M. N. B. F.; Minas da Piedade, M. E. *Meas. Sci. Technol.* **2006**, *17,* 1405-1408.

51. Bernardes, C. E. S.; Piedade, M. F. M.; Minas da Piedade, M. E. *Cryst. Growth Des.* **2010**, *10,* 3070-3076.
52. Fulem, M.; Ruzicka, K.; Ruzicka, M. *Fluid Phase Equilibr.* **2011**, *303,* 205-216.
53. Clever, H. L. *J. Phys. Chem.* **1970**, *74,* 1309-&.
54. *ATcT Thermochemical Data Based on the Core (Argonne) Thermochemical Network*, v. 1.118, http://ATcT.anl.gov.
55. Masuda, N.; Nagano, Y.; Sakiyama, M. *J. Chem. Thermodyn.* **1994**, *26,* 971-975.
56. Lezina, V. P.; Stepanyants, A. U.; Golovkina, N. I.; Smirnov, L. D. *Bull. Acad. Sci. USSR Div. Chem. Sci.* **1980**, *29,* 85-92.
57. Atkins, P. W.; de Paula, J., *Physical Chemistry for the Life Sciences*, 5th ed.; Oxford University Press: Oxford, 2006; p 181-190.